Faculty of Aerospace Engineering

Dynamic Inversion Flight Control Law Design for Fixed-Wing Aircraft

Design and Flight Testing of Incremental Nonlinear Dynamic Inversion based Control Laws for a Passenger Aircraft

Fabian Grondman

September 28, 2018

TU Delft Delft University of Technology

Challenge the future

Dynamic Inversion Flight Control Law Design for Fixed-Wing Aircraft

Design and Flight Testing of Incremental Nonlinear Dynamic Inversion based Control Laws for a Passenger Aircraft

Master of Science Thesis

For obtaining the degree of Master of Science in Aerospace Engineering
at Delft University of Technology

Fabian Grondman

September 28, 2018

Faculty of Aerospace Engineering · Delft University of Technology

Delft University of Technology

Deutsches Zentrum
für Luft- und Raumfahrt
German Aerospace Center

Delft University Of Technology
Department Of
Control and Simulation

The undersigned hereby certify that they have read and recommend to the Faculty of Aerospace Engineering for acceptance a thesis entitled **"Dynamic Inversion Flight Control Law Design for Fixed-Wing Aircraft"** by **Fabian Grondman** in partial fulfillment of the requirements for the degree of **Master of Science**.

Dated: September 28, 2018

Readers:

dr. Q. P. Chu

dr. ir. E. van Kampen

dr. ir. G. H. N. Looye

dr. E. N. van Doornbos

Abstract

This thesis describes the design, implementation and flight testing of flight control laws based on Incremental Nonlinear Dynamic Inversion (INDI). The method compares commanded and measured accelerations to compute increments on the current control deflections. This results in highly robust control solutions with respect to model uncertainties as well as changes in aircraft dynamic characteristics of failure cases during flight. At the same time, the complexity of the algorithms is similar to classical ones. The key for practical implementation is in ensuring synchronization between angular acceleration and control deflection measurements or estimates. The underlying theory and practical design methods of INDI are very well understood, but implementation and testing has remained limited to sub-scale UAVs. The main contributions of this thesis are: 1) the design and validation of manual attitude control functions for a Cessna Citation II experimental aircraft, covering control structure design, application of INDI, design optimization, robustness analyses, software implementation, ground and flight testing; 2) a novel method based on the complimentary filtering technique to obtain more accurate angular acceleration estimates from angular rate measurements; 3) mathematical proof that the inversion error of INDI due to neglecting the so-called system dynamics increment increases with the combined actuator, sensor and sampling delay. The flight tests were highly successful and marked the first successful demonstration of INDI on a CS-25 certified aircraft. The flight test results proved that INDI clearly outperforms "classical" NDI and provided valuable lessons-learnt for future applications.

Acknowledgments

Allereerst wil ik mijn dank betuigen aan Gertjan Looye, die als initiatiefnemer fungeerde van dit onderzoeksproject en optrad als dagelijkse begeleider namens DLR. Gertjan bood mij de unieke mogelijkheid om incrementele regelwetten te testen op de PH-LAB. Zijn uitstekende begeleiding, terugkoppeling en kennis van de regeltechniek waren van onschatbare waarde tijdens het project, en voor het schrijven van deze scriptie. Ook gaat mijn dank uit naar Richard Kuchar. Richard was mij tot uitstekende hulp tijdens de voorbereiding en uitvoering van de testvluchten.

Daarnaast gaat mijn dank uit aan Ping Chu, die als dagelijkse begeleider optrad namens de TU Delft. Zijn passie voor de incrementele regeltechniek werkt aanstekelijk. Verder zou ik Erik-Jan van Kampen willen danken voor de waardevolle terugkoppeling tijdens de telefonische besprekingen.

Ik zou Alexander in 't Veld en Hans Mulder willen danken voor de planning en coördinatie van de testvluchten en, als evaluatie piloten, voor de waardevolle terugkoppeling tijdens de debriefings. Verder zou ik Olaf Stroosma en Ferdinand Postema willen danken voor de goede ondersteuning met betrekking tot DUECA en de vluchttestinstrumentatie. Ook zou ik Menno Klaassen en het onderhoudsteam van de PH-LAB willen danken voor de algemene ondersteuning tijdens de vlucht campagne.

Contents

List of Tables

List of Figures

Acronyms

A/C	Aircraft
AC	Attitude Control
ACT	Actuators
AHRS	Attitude Heading and Reference System
AP	Autopilot
ATTAS	Advanced Technologies Testing Aircraft
BEW	Basic Empty Weight
DADC	Digital Air Data Computer
DASMAT	Delft University Aircraft Simulation Model and Analysis Tool
DLR	German Aerospace Institute
DOF	Degrees-Of-Freedom
DUECA	Delft University Environment for Communication and Activation
FASER	Free-flying Aircraft for Sub-scale Experimental Research
FBW	Fly-By-Wire
FMS	Flight Management System
FTIS	Flight Test Instrumentation System
IBS	Incremental BackStepping
INDI	Incremental Nonlinear Dynamic Inversion
LC	Linear Controllers
LOC-I	Loss Of Control In-flight
LPV	Linear Parameter-Varying
LQG	Linear Quadratic Gaussian
LQR	Linear Quadratic Regulator
MEMS	Microelectromechanical systems
MOPS	Multi-Objective-Parameter-Optimization
MRAC	Model Reference Adaptive Control
MTOW	Maximum Take-Off Weight

NDI	Nonlinear Dynamic Inversion
NED	North-East-Down
NN	Neural Networks
PCH	Pseudo Control Hedging
PI	Proportional-Integral
PID	Proportional-Integral-Derivative
PIO	Pilot Induced Oscillations
RCAH	Rate Control Attitude Hold
RRMSE	Relative Root Mean Square Error
SR	Institute of System Dynamics and Control
TC	Turn Compensation
UAV	Unmanned Aerial Vehicle
V&V	Verification & Validation

List of Symbols

Greek Symbols

ΔC	Uncertainty level C
ΔJ	Uncertainty level J
$\Delta \tau$	Uncertainty level τ
$\Delta \theta$	Updated dropback
α	Aerodynamic angle of attack
β	Aerodynamic angle of sideslip
χ	Course angle
$\boldsymbol{\delta}$	Control surface deflection vector
δ	Control surface deflection scalar
γ	Flight path climb angle
$\boldsymbol{\nu}$	Virtual control vector
ν	Virtual control scalar
$\boldsymbol{\omega}$	Angular rate vector
ω	Frequency
ϕ	Roll angle
ψ	Yaw angle
ρ	Air density
τ	Time constant, time delay
θ	Pitch angle
ζ	Damping ratio

Roman Symbols

A	Specific force along body axis
C	Dimensionless coefficient
DB	Dropback
$\boldsymbol{F}$	Force
J	Moment of inertia
$\boldsymbol{J}$	Inertia matrix
K	Gain
$\boldsymbol{M}$	Moment
M	Mach number
$N1$	Fan speed
S	Wing surface area
T	Temperature
$\boldsymbol{T}$	Tuning parameters
V	Airspeed
$\boldsymbol{V}$	Velocity vector
a	Linear acceleration along body axis
b	Wing span
c	Criterion
$\bar{c}$	Mean Aerodynamic Chord
d	Demand value
g	Gravity constant
h	Altitude
m	Mass
n	Load factor
$\boldsymbol{p}$	Model parameters
p	Angular rate around body x-axis, pressure
q	Angular rate around body y-axis
r	Angular rate around body z-axis
$\boldsymbol{r}$	Position vector
t	Time
u	Translational velocity along body x-axis, input scalar
$\boldsymbol{u}$	Input vector

v	Translational velocity along body y-axis
w	Translational velocity along body z-axis
$\boldsymbol{x}$	State vector
$\boldsymbol{y}$	Output vector

Subscripts

0	Initial value, current point in time
A	Aerodynamic
D	Force along the stability x-axis
E	Earth
I	Integrator
L	Force along the stability z-axis
P	Proportional
T	Thrust
Y	Force along the stability y-axis
act	Actuator
$ahrs$	Attitude Heading and Reference System
ap	Autopilot
a	Aerodynamic, airframe, air-mass, aileron
b	Body
cas	Calibrated airspeed
cg	Center of gravity
com	Command
c	Control effectors
d	Datum
est	Estimation
e	Elevator
fbw	Fly-By-Wire
fil	Filter
h	Hedge
i	Inertial
l	Moment around the body x-axis
m	Moment around the body y-axis
max	Maximum

min	Minimum
n	Moment around the body z-axis, natural
o	Other
plt	Pilot
ref	Reference
r	Rudder
$snsr$	Sensor
ss	Steady-state
$stbd$	Starboard
$sync$	Synchronization
s	Stability, servo motor
tas	True airspeed
tc	Turn Compensation
tot	Total
t	Trim
x	X-axis
y	Y-axis
z	Z-axis

Superscripts

b	Body
cg	Center of gratify
s	Stability

Chapter 1

Introduction

This chapter presents the introduction corresponding to the Master of Science Thesis: *Dynamic Inversion Flight Control Law Design for Fixed-Wing Aircraft: Design and Flight Testing of Incremental Nonlinear Dynamic Inversion based Control Laws for a Passenger Aircraft.* This research project has been made possible by the collaborative effort of the Control & Simulation department of the faculty of Aerospace Engineering of Delft University of Technology and the Institute of System Dynamics and Control (SR) of the German Aerospace Institute (DLR). The remainder of the chapter contains the project motivation (Section 1-1), the current advances in flight control law design (Section 1-2), the research objective and questions (Section 1-3) and finally the report outline (Section 1-4).

1-1 Project motivation

Aircraft accident and incident statistics reveal that Loss of Control in flight (LOC-I) is one of the most significant contributors to fatal aircraft accidents in recent times [15, 27]. A recent survey conducted by Boeing shows that LOC-I accounted for 23% of all fatal commercial jet aircraft accidents between 2005 and 2014 [8]. If solely counting the number of fatalities this number rises to 41%. LOC-I is one of the most complex accident categories usually involving multiple events leading up to the accident such as pilot error, system failures and vehicle upsets due to external disturbances. Reducing this accident category has become an industry priority.

Modern Fly-By-Wire (FBW) flight control systems provide augmented stability and control in nominal conditions. In case of severe or unforeseen failures or changes in aircraft behaviour (e.g. due to icing), the control system will howhever revert back to reversionary modes or even direct control [24]. This implies that the control law functionality is partly reduced or abandoned. This behaviour is undesirable as the pilot work load is not only increased due to failure, but also due to aircraft control. Developments subsequently focus on maintaining functionality, even in case of such failures. Research in this field includes reliable fault detection

and diagnosis, and control reconfiguration [23, 24]. One aspect is the adaptation of flight control laws to unforeseen circumstances and failures.

Current fight control techniques are most often based on classical control. In recent years, however, modern methods such as Nonlinear Dynamic Inversion (NDI) find more and more applications [6, 71]. NDI is an attractive control strategy for adaptation as it globally linearises the system dynamics and decouples the control axes [19]. Moreover, it is clear which parameters and parts require adaptation in case of changed aircraft behaviour. However, extension to fault tolerance requires failures and model changes to be completely identified online [40].

Incremental Nonlinear Dynamic Inversion (INDI) retains the advantages of NDI but attempts to solve the identification problem by reduced model-dependency. By feeding back synchronous measurement or estimation of control deflection and angular acceleration, the required model knowledge is reduced to the control effectiveness. Implementation was initially considered problematic, but due to synchronization, the control laws run reliably at sample times as in current control computers. The method first appeared in literature as simplified Nonlinear Dynamic Inversion [63, 62, 3] before being formalized as Incremental Nonlinear Dynamic Inversion by Sieberling et al. [58]. INDI has found several applications ranging from fixed-wing aircraft and spacecraft [58, 1] to helicopters and quadcopters [59, 44, 61].

A first succesful demonstration of INDI was performed by the German Aerospace Center (DLR) in cooperation with Delft University of Technology (TU Delft) at the University of Minnesota [69]. Control laws based on INDI were implemented and tested on the FASER, a sub-scale fixed-wing UAV. Recently, DLR and TU Delft also flight tested an Incremental Backstepping (IBS) variant on this platform [66]. INDI has been succesfully implemented and tested on a quadcopter as well [61]. Due to the promising results obtained on small-scale UAVs, the next logical step is to demonstrate INDI on a CS-25 certified aircraft.

The objective of this thesis is to design, implement and flight test manual flight control laws based on INDI for a small passenger aircraft. The Cessna Citation II PH-LAB, a modified business jet operated by the faculty of Aerospace Engineering of TU Delft, will serve as the application platform. With its newly certified FBW system [73], the PH-LAB is a highly promising platform for testing of advanced flight control laws.

This thesis builds upon earlier research conducted by DLR. Over the years, DLR has done flight experiments with various control laws based on classical NDI [42, 37, 38, 39]. Various functions have been tested (manual controls, autopilot functions) in various scenarios (engine failures, actuator failures, wake vortices, etc.). These experiments were conducted using the now-retired VFW-16 ATTAS testbed. Ultimately, this research contributes in improving the environmental performance, economy and safety of future aircraft generations.

1-2 Current advances in flight control law design

Up until a few decades ago control laws used in flight control systems were mostly based on classical linear control [6, 5]. These methods divide the nonlinear control task into a number of linear sub-problems, assuming the validity of a linearised model within a small region of the operating range [19, 2]. In other words, the flight envelope is partitioned into several smaller regions with separately designed linear controllers. By interpolating or "scheduling"

Figure 1-1: Cessna Citation II PH-LAB

the separate linear controllers, satisfactory performance can be obtained for the complete flight envelope. This operation is referred to as gain sheduling.

Gain scheduling is still a much used control strategy in flight control industry due to simplicity and low computational cost. Nevertheless, this method has some inherent drawbacks. First and foremost, the performance and stability cannot be guaranteed at operating conditions outside the design points [60]. In practice this implies degradaded performance at high angle of attack flight and under system failures. Sheduling of multivariable controllers also tends to be a tedious and time-consuming process [19, 2]. Furthermore, the solution is exclusive to each design problem requiring costly iterations in case of (life-cycle) design changes. The transferability of the control solution between different airframes is therefore limited as well.

Due to the disadvantages associated with classical control, advanced multivariable control techniques have become the norm in industry in recent time [6, 5]. Examples include Linear Quadratic Regulator/Gaussian (LQR/LQG), eigenstructure assignment, H_∞ loop shaping, μ-synthesis, Linear Parameter-Varying (LPV), Neural Networks (NN) and Nonlinear Dynamic Inversion (NDI). NDI is currently the most used modern control method having been successfully applied to several aircraft [6, 5], most notably the Lockheed Martin F-35 Lightning II [71]. To limit the scope and retain relevance to the current research project, the discussion will be limited to NDI and its variants.

1-2-1 Nonlinear Dynamic Inversion

Nonlinear Dynamic Inversion (NDI), a special case of feedback linearization, was developed in the late 1960s to alleviate issues associated with classical control techniques [60, 19]. NDI is fundamentally different in that it uses the inverse vehicle model and full state feedback to globally linearise the system dynamics [60, 19]. In addition, NDI fully decouples the control variables in a multivariable system and isolates the flying quality part of the system from the part that depends on the airframe and engine dynamics [71]. The desired closed-loop response of the system can be imposed via conventional linear control techniques. Compared

to classical methods, NDI improves nonlinear flight regime performance, reduces development time, is more flexible to (life-cycle) design changes and can be more easily re-used in different airframes [71, 4].

The main disadvantage of NDI lies in the required complete and accurate knowledge of the vehicle model and state [60, 19]. Model mismatch implies incorrect inversion still resulting in nonlinear closed-loop behavior. NDI is therefore not inherently robust to model uncertainties and system failures. Similarly, errors in measurement (e.g. delays, noise and bias) result in incomplete cancellation of the dynamics. Loss of performance due to these disadvantages can be significant in practice, as numerous flight tests have demonstrated [42, 70, 71, 38]. An additional disadvantage of NDI is that the physical relations need to be suitable for inversion [60, 19]. The required mathematical inversion may result in singularities within the control law, leading to infeasible control inputs. NDI cannot be directly applied to systems with unstable inverse dynamics, i.e. non-minimum phase systems. An example of such a system is the vertical acceleration response to an elevator input for aircraft with a tailplane.

Robustness to model mismatch is a major challenge in the design of NDI control laws. A common approach is to combine NDI with robust control methods such as μ-synthesis or H_∞ loop shaping [2]. These methods do howhever not take into account all uncertainties or use lumped uncertainties introducing conservatism [58]. An alternative approach was proposed by Looye and Joos [41], where robustness to model uncertainty was addressed via multi-objective optimization in combination with a multi-model approach. More recent developments have focused on adding adaptive elements to NDI such as Neural Networks (NN) [31, 9] or Model Reference Adaptive Control (MRAC) [25, 56]. Although improvements in robustness were observed in flight tests, the increased complexity and nonlinearity of these methods are a significant hurdle for certification [28].

1-2-2 Incremental Nonlinear Dynamic Inversion

Incremental Nonlinear Dynamic Inversion (INDI), initially known as enhanced or simplified NDI, was conceptualised in the late 1990s as a further development of NDI [63]. First referred to as an incremental control method in [14], INDI computes the control increment with respect to the previous point in time rather than the total control input. In general, INDI retains the advantages and disadvantages of NDI but replaces part of the vehicle model with state derivative feedback. As a result, INDI improves upon robustness to model mismatch compared to NDI [58] and is comparable to classical methods in terms of complexity. The latter is a significant advantage with respect to certification, verficication and validation [26].

Applications of INDI to fixed-wing aircraft were already described in [63, 3]. A first demonstration was performed by Smith and Berry [62], who flight tested a longditudinal pitch rate controller based upon INDI on the VAAC Harrier. The flight test revealed however issues in obtaining accurate angular acceleration feedback. The measured angular accelerations proved to be of poor quality and feedback of the filtered derivatives of the angular rates resulted in oscillations in the closed-loop response. Bacon et al. [3] proposed washout filters as a technique to obtain accurate angular accelerations from rate gyro measurements. In addition, it was noted that uncertainties in the actuator feedback loop could drive the actuator into saturation. The INDI controller developed in [16] did not proof robust to uncertainties in the control effectiveness matrix.

Chen and Zhang [14] used a Taylor series expansion of the system dynamics to arrive at more general form of INDI. This approach was adopted by Delft University of Technology in [58] and formalized as Incremental Nonlinear Dynamic Inversion (INDI). Sieberling et al. [58] provided mathmatical proof that INDI is more robust to model mismatch compared to NDI and demonstrated that all uncertainties in the system are eliminated given that the sign of the control effectiveness is known. Note that INDI is a special case of Lyapunov-based incremental control [33]. Application of INDI has not been limited to fixed-wing aircraft, in [1] the method was applied to spacecraft and performed favorably compared to NDI under time delays, model uncertainties and external disturbances. INDI has also been succesfully applied to several types of rotorcraft [59, 18, 44, 61]. Similar to NDI, actuator saturation is a concern for INDI. Simplício et al. [59] applied Pseudo Control Hedging (PCH) to INDI in order to alleviate actuator saturation issues.

Important advances were made by Smeur et al. [61] who developed a method to correctly take into account delays that occur from obtaining angular accelerations from angular rate measurements. An adaptive INDI controller was developed with online control effectiveness estimation, further reducing model dependency. The controller was successfully flight tested on a quadcopter and outperformed classical PID, displaying excellent disturbance rejection capabilities. Two successful demonstrations of INDI were reported in recent unpublished literature [69, 66]. Both were performed on a sub-scale fixed-wing Unmanned Aerial Vehicle (UAV). Vlaar [69] mentioned that unsynchronized delays between angular acceleration and control deflection feedback result in significant performance degration within INDI controllers. A practical solution to this problem was eventually proposed. Van Ekeren [66] reported that certain assumptions made in the derivation of INDI are not always valid for fixed-wing aircraft resulting in tracking errors. The size of these errors are related to the combined delay of actuators, sensors and sampling. Van 't Veld [68] worked towards the implementation of discrete-time INDI on CS-25 certified aircraft. Stability analysis revealed that a surplus of delay in the angular acceleration feedback results in relatively fast system instability. A real-time time delay identification algorithm was proposed to synchronize angular acceleration and control deflection feedback.

1-2-3 Challenges

One of the main challenges in the development of new control techiques is to demonstrate applicaliblity on a physical platform, considering the high cost associated with flight testing. INDI control laws have been implemeted and tested on a ground-attack aircraft [62], however at the time not all implementation issues had been identified. More recently, INDI has been successfully flight tested on a quadcopter [61] and a fixed-wing UAV [69, 66]. The latter results were howhever never published in peer-reviewed literature. The underlying theory and practical design methods of INDI are very well understood, but implementation and testing has remained limited to the examples above. Qualitative flight tests, especially on CS-25 certified aircraft, would be a highly valuable contribution to the ongoing development of INDI.

Part of demonstrating the advantages of new control techniques lies in rigorous comparison with established control methods. NDI is currently the most appropriate candidate for this, considering it is the most applied modern control technique [6, 5]. Although INDI has been quantitatively compared to NDI in simulation based research, the literature containing flight

test results use classical linear control techniques as baseline. The current research would be particularly benefited by simulation and flight test results that directly compare INDI with NDI control laws .

A point that has not been addressed extensively in the literature is the optimization of the free control law parameters, particularly for industry-like performance and robustness specifications. It would be valuable to demonstrate the applicability of established optimization methods to INDI.

Adaptation of the remaining model parameters online as demonstrated by Smeur et al. [61] is not considered a priority for the current project. Although this is an important step towards the goal of making INDI completely model independent and for the extension to fault tolerance, these adaptive elements tend to be difficult to certify [28].

Recent developments suggest that implementation issues can arise due to (slow) actuator and sensor dynamics and feedback signal synchronization mismatches [69, 61, 66, 68]. These issues have surfaced in simulations and have been been addressed to a certain extent. Nevertheless, this indicates that there exist a gap in the theory of INDI concerning actuator and sensor dynamics.

More specific implementation challenges are related to the angular acceleration feedback required for INDI. Angular accelerometers are not commonly found in current generation aerospace vehicles. Existing estimation methods are sub-optimal, typically relying on differentiation and low-pass filtering of angular rate measurements [62, 69, 61, 66]. To ensure general applicability of INDI there exist a need to obtain low-noise, low-lag angular acceleration estimates from angular rate measurements.

1-3 Research objective and questions

The research objective presented in Section 1-1 is to proof the concept of Incremental Nonlinear Dynamic Inversion on a CS-25 certified aircraft in flight. In order to achieve this, the project will draw from know-how in the fields of control theory, control design and testing and control law implementation from both the Control & Simulation department of the faculty of Aerospace Engineering of Delft University of Technology and the Institute of System Dynamics and Control (SR) of the German Aerospace Institute (DLR). For comparison, also control laws based on classical NDI will be developed. This controller will serve as baseline throughout the project.

Considering the high cost associated with flight testing, the risk of redesign should be minimized. For this reason, the development of a rigorous design, implementation and Validation & Verification (V&V) procedure is part of the project. Of particular importance to address are the specific implementation aspects of INDI, but also the limitations of the PH-LAB experimental aircraft require thorough consideration.

Following the research objective, the main research question is formulated as follows:

What are the required steps to successfully design and implement INDI control laws for the manual attitude control of passenger aircraft?

The main research question is sub-divided into multiple sub-questions:

1. What are the practical issues in design and implementation of (I)NDI control laws?
2. What are the limiting factors of the PH-LAB concerning design and implementation of (I)NDI control laws?
3. What measures are required to minimize loss of performance (w.r.t. above sub-questions)?
4. Does the use of INDI result in a more satisfactory control design for the PH-LAB compared to classical NDI in terms of industry-like performance and robustness specifications?

1-4 Report outline

This thesis consist of two parts, see Figure 1-2. Part II contains all the preliminary studies and covers the so-called *offline design* phase where the actual design of control laws takes place. Part I contains the research paper and covers the *assessment and clearance*, *rig testing* and *flight testing* of the control laws designed in Part II. Note that the research paper also covers the *offline design*, but in a more concise manner.

The outline of Part II is as follows. **Chapter 2** provides a concise review of the theory of Nonlinear Dynamic Inversion, Incremental Nonlinear Dynamic Inversion and Pseudo Control Hedging. In **Chapter 3** the literature is reviewed for effects encountered in practice that violate the fundamental assumptions made for (I)NDI and result in significant performance loss within the control laws. Also specific implementation aspects of INDI related to obtaining accurate angular accelerations and synchronization of feedback signals will be discussed. Note that the results of this chapter are not included in the research paper. **Chapter 4** provides a brief analysis of the PH-LAB FBW system. The focus of this chapter is on quantifying the limitations imposed on the input response by the FBW system. **Chapter 5** provides a brief analysis of the PH-LAB sensors. The focus of this chapter is on quantifying the relevant measurement errors. **Chapter 6** covers the modeling of the aircraft and relevant subsystems and prepares the models for the assessment of the numerical design criteria. **Chapter 7** covers the design and integration of the individual controller functions. This includes the construction of the actual synthesis of the controller components and signal processing algorithms. **Chapter 8** covers the formulation of the design specifications and overall optimization of the integrated control system developed in Chapter 7. For the tuning of the control laws multi-objective optimization is used. This thesis is finalized in **Chapter 9**, providing the conclusions and recommendations. Note that the flight test cards of flight #2 and #3 can be found in Appendix A and B. The corresponding flight test results are documented in Appendix C and D.

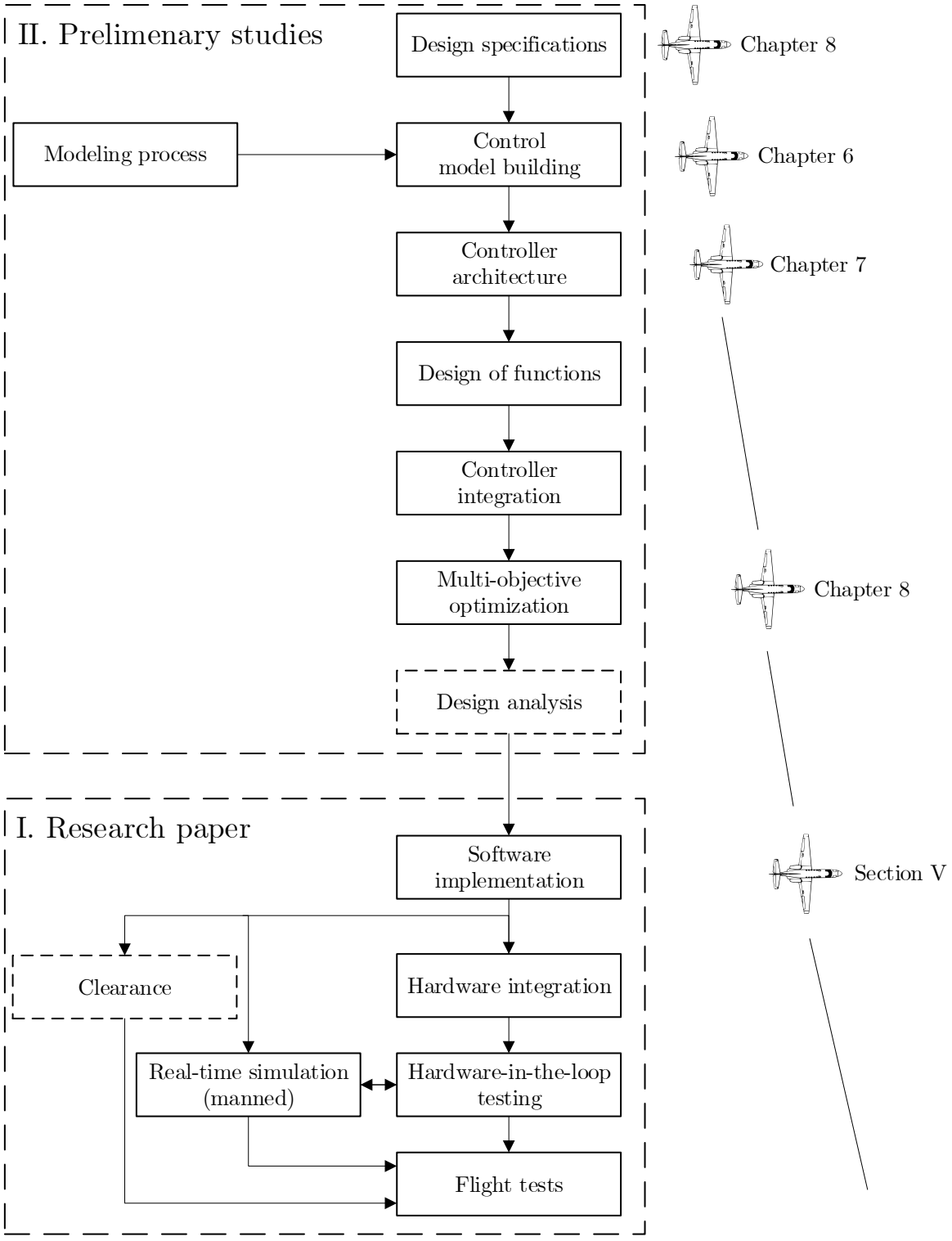

Figure 1-2: DLR-SR design process for flight control laws [43]

Part I

Research paper

Design and Flight Testing of Incremental Nonlinear Dynamic Inversion based Control Laws for a Passenger Aircraft

F. Grondman,* G.H.N. Looye,† R. Kuchar,‡ Q.P. Chu§ and E. van Kampen¶

German Aerospace Center DLR, Münchener Straße 20, 82234 Weßling, Germany

Delft University of Technology, P.O. Box 5058, 2626HS Delft, The Netherlands

This paper describes the design, implementation and flight testing of flight control laws based on Incremental Nonlinear Dynamic Inversion (INDI). The method compares commanded and measured accelerations to compute increments on the current control deflections. This results in highly robust control solutions with respect to model uncertainties as well as changes in aircraft dynamic characteristics of failure cases during flight. At the same time, the complexity of the algorithms is similar to classical ones. The key for practical implementation is in ensuring synchronization between angular acceleration and control deflection measurements or estimates. The underlying theory and practical design methods of INDI are very well understood, but implementation and testing has remained limited to sub-scale UAVs. The main contribution of this paper is to present the design and validation of manual attitude control functions for a Cessna Citation II experimental aircraft, covering control structure design, application of INDI, design optimization, robustness analyses, software implementation, ground and flight testing. For comparison, also control laws based on classical Nonlinear Dynamic Inversion were implemented and flown. The flight tests were highly successful and marked the first successful demonstration of INDI on a CS-25 certified aircraft. The flight test results proved that INDI clearly outperforms NDI and provided valuable lessons-learnt for future applications.

Nomenclature

A_x, A_y, A_z	Specific forces along body X/Y/Z axis, g
C	Dimensionless coefficient
$\boldsymbol{F}$	Force, N
$\boldsymbol{J}$	Inertia matrix, kg·m^2
J	Moment of Inertia, kg·m^2
K	Gain
$\boldsymbol{M}$	Moment, Nm
M	Mach number
$N1$	Fan speed, s^{-1}
S	Wing surface area, m^2
$\boldsymbol{V}$	Velocity vector, m/s
V	Airspeed, m/s
a_x, a_y, a_z	Linear accelerations along body X/Y/Z axis, m/s^2
b	Wing span, m^2
$\bar{c}$	Mean aerodynamic chord, m

*Graduate student, Faculty of Aerospace Engineering, Control and Simulation Division, Delft University of Technology

†Head, Department of Aircraft Systems Dynamics, Institute of System Dynamics and Control, German Aerospace Institute

‡Research associate, Department of Aircraft Systems Dynamics, Institute of System Dynamics and Control, German Aerospace Institute

§Associate Professor, Faculty of Aerospace Engineering, Control and Simulation Division, Delft University of Technology

¶Assistant Professor, Faculty of Aerospace Engineering, Control and Simulation Division, Delft University of Technology

g	Gravity constant, m/s^2
h	Altitude, m
m	Mass, kg
$\boldsymbol{p}$	Model parameters
p, q, r	Roll, pitch and yaw rate around the body X/Y/Z axis, rad/s
$\boldsymbol{r}$	Position vector, m
t	Time, s
$\boldsymbol{u}$	Input vector
u, v, w	Velocity components along body X/Y/Z axis, m/s
$\boldsymbol{x}$	State vector
$\boldsymbol{y}$	Output vector
Symbol	
α, β, γ	Angle of attack, angle of sideslip and flight path angle, rad
$\boldsymbol{\delta}$	Control surface deflection vector, rad
δ	Control surface deflection scalar, rad
ζ	Damping ratio
ϕ, θ, ψ	Roll, pitch and yaw angle, rad
$\boldsymbol{\nu}$	Virtual control vector
ν	Virtual control scalar
ρ	Air density, kg/m^3
τ	Time constant, time delay, s
$\boldsymbol{\omega}$	Angular rate vector, rad/s
ω	Frequency, rad/s
Subscript	
0	Current point in time
A	Aerodynamic
D, Y, L	Force along the stability X/Y/Z axis, N
E	Earth
I	Integrator
T	Thrust
a	Airframe, air-mass
a, e, r	Aileron, elevator, rudder
act	Actuator
b	Body
c	Control effectors
est	Estimate
fbw	Fly-By-Wire
fil	Filter
h	Hedge
i	Inertial
l, m, n	Moment around the body X/Y/Z axis, Nm
min, max	Minimum, maximum
o	Other
plt, com, ref	Pilot, command, reference
s	Stability
$sync$	Synchronization
tas, cas	True airspeed, calibrated airspeed
tc	Turn compensation
Superscript	
b	Body
cg	Center of gravity
s	Stability

I. Introduction

Current fight control techniques are most often based on classical control. In recent years, however, modern methods such as Nonlinear Dynamic Inversion (NDI) find more and more applications[1,2]

Modern Fly-By-Wire (FBW) flight control systems provide augmented stability and control in nominal conditions. In case of severe or unforeseen failures or changes in aircraft behaviour (e.g. due to icing), the control system will howhever revert back to reversionary modes or even direct control.[3] This implies that the control law functionality is partly reduced or abandoned. This behaviour is undesirable as the pilot work load is not only increased due to failure, but also due to aircraft control. Developments subsequently focus on maintaining functionality, even in case of such failures. Research in this field includes reliable fault detection and diagnosis, and control reconfiguration.[3,4] One aspect is the adaptation of flight control laws to unforeseen circumstances and failures.

NDI is an attractive control strategy for adaptation as it globally linearises the system dynamics and decouples the control axes.[5] Moreover, it is clear which parameters and parts require adaptation in case of changed aircraft behaviour. However, extension to fault tolerance requires failures and model changes to be completely identified online.[6]

Incremental Nonlinear Dynamic Inversion (INDI) retains the advantages of NDI but attempts to solve the identification problem by reduced model-dependency. By feeding back synchronous measurement or estimation of control deflection and angular acceleration, the required model knowledge is reduced to the control effectiveness. Implementation was initially considered problematic, but due to synchronization, the control laws run reliably at sample times as in current control computers.

The method first appeared in literature as simplified Nonlinear Dynamic Inversion[7–9] before being formalized as Incremental Nonlinear Dynamic Inversion by Sierbling et al.[10] INDI has found several applications ranging from fixed-wing aircraft and spacecraft[10,11] to helicopters and quadcopters.[12–14]

A first succesful demonstration of INDI was performed by the German Aerospace Center (DLR) in cooperation with Delft University of Technology (TU Delft) at the University of Minnesota.[15] Control laws based on INDI were implemented and tested on the FASER, a sub-scale fixed-wing UAV. Recently, DLR and TU Delft also flight tested an Incremental Backstepping (IBS) variant on this platform.[16] INDI has been succesfully implemented and tested on a quadcopter as well.[14] Due to the promising results obtained on sub-scale UAVs, the next logical step is to demonstrate INDI on a CS-25 certified aircraft.

The main contribution of this paper is to present the design and validation of manual attitude control functions for a Cessna Citation II experimental aircraft, covering control structure design, application of INDI, design optimization, robustness analyses, software implementation, ground and flight testing. For comparison, also control laws based on classical NDI are implemented and flown. The Cessna Citation II PH-LAB is a modified business jet operated by the faculty of Aerospace Engineering of TU Delft. With its newly certified Fly-By-Wire system,[17] the PH-LAB is a highly promising platform for testing advanced flight control laws.

The manual flight control functions presented in this paper combine Rate Control Attitude Hold (RCAH) and Attitude Control (AC) for pitch and roll with sideslip augmentation.[18] An additional feature is Pseudo Control Hedging (PCH),[19] used for adaptation of the reference model output in case of actuator saturation. Note that these control laws build upon earlier research conducted by DLR. Over the years, DLR has done flight experiments with various control laws based on classical NDI.[18,20–22] These experiments were conducted using the now-retired VFW-16 ATTAS testbed.

The outline of this paper is as follows. In Section II, the theory of NDI, INDI and PCH will be briefly reviewed. Thereafter, Section III discusses the PH-LAB research aircraft and corresponding model used for the analysis and synthesis of the control laws. The control law design is presented in Section IV, including inner and outer loop, signal processing algorithms and parameter optimization. The resulting control design is validated in Section V, presenting the simulator assessment and clearance, rig testing and flight tests. Finally, the paper is concluded in Section VI.

II. Incremental Nonlinear Dynamic Inversion

A. Nonlinear Dynamic Inversion

The general idea of NDI is to compensate the nonlinear system dynamics by means of feedback of the inverse model equations such that the closed loop system appears in a linear form. The desired closed loop response can then be imposed via conventional linear controllers.[5]

It is assumed that the model of the nonlinear system has the following control-affine form:

$$\dot{\boldsymbol{x}} = \boldsymbol{f}(\boldsymbol{x}, \boldsymbol{p}) + \boldsymbol{G}(\boldsymbol{x}, \boldsymbol{p})\boldsymbol{u} \tag{1}$$

$$\boldsymbol{y} = \boldsymbol{h}(\boldsymbol{x}, \boldsymbol{p}) \tag{2}$$

$$\boldsymbol{y}_o = \boldsymbol{h}_o(\boldsymbol{x}, \boldsymbol{p}) \tag{3}$$

Where $\boldsymbol{x} \in \mathbb{R}^n$ is the state vector, $\boldsymbol{u} \in \mathbb{R}^m$ the input vector containing only inputs that may be used by the controller, $\boldsymbol{y} \in \mathbb{R}^m$ the output vector containing the outputs to be controlled (i.e. control variables), $\boldsymbol{y}_o$ contains any other outputs of the system, $\boldsymbol{f}$, $\boldsymbol{h}$ and $\boldsymbol{h}_o$ are smooth vector fields, $\boldsymbol{G} \in \mathbb{R}^{n \times m}$ is a matrix with columns of smooth vector fields and $\boldsymbol{p}$ contains the model parameters.

Differentiation of the output equation $\boldsymbol{h}$ results in:

$$\dot{\boldsymbol{y}} = \frac{\partial \boldsymbol{h}(\boldsymbol{x}, \boldsymbol{p})}{\partial \boldsymbol{x}} \frac{\mathrm{d}\boldsymbol{x}}{\mathrm{d}t} = \nabla \boldsymbol{h}(\boldsymbol{x}, \boldsymbol{p})\big(\boldsymbol{f}(\boldsymbol{x}, \boldsymbol{p}) + \boldsymbol{G}(\boldsymbol{x}, \boldsymbol{p})\boldsymbol{u}\big) = L_{\boldsymbol{f}}\boldsymbol{h}(\boldsymbol{x}, \boldsymbol{p}) + L_{\boldsymbol{G}}\boldsymbol{h}(\boldsymbol{x}, \boldsymbol{p})\boldsymbol{u} \tag{4}$$

Where $L_{\boldsymbol{f}}\boldsymbol{h}$ and $L_{\boldsymbol{G}}\boldsymbol{h}$ are the first-order Lie derivatives along $\boldsymbol{f}$ and $\boldsymbol{G}$, respectively. It is assumed that $L_{\boldsymbol{G}}\boldsymbol{h}$ is non-singular and that each output has an order of 1 relative to at minimum one of the inputs (i.e. $L_{\boldsymbol{G}}\boldsymbol{h} \neq 0$). In this case NDI can be applied to Equation (4).[5] Defining the virtual control input as $\boldsymbol{\nu} = \dot{\boldsymbol{y}}$ and inverting Equation (4), the following control law is obtained:

$$\boldsymbol{u} = \big(L_{\boldsymbol{G}}\boldsymbol{h}(\hat{\boldsymbol{x}}, \boldsymbol{p}^*)\big)^{-1}\big(\boldsymbol{\nu} - L_{\boldsymbol{f}}\boldsymbol{h}(\hat{\boldsymbol{x}}, \boldsymbol{p}^*)\big) \tag{5}$$

The vectors $\hat{\boldsymbol{x}}$ and $\boldsymbol{p}^*$ contain the computed or estimated states from $\boldsymbol{y}$ and $\boldsymbol{y}_o$, and the assumed values for the model parameters, respectively. Substituting the control law (Equation (5)) into Equation (4):

$$\dot{\boldsymbol{y}} = L_{\boldsymbol{f}}\boldsymbol{h}(\boldsymbol{x}, \boldsymbol{p}) + L_{\boldsymbol{G}}\boldsymbol{h}(\boldsymbol{x}, \boldsymbol{p})\Big(\big(L_{\boldsymbol{G}}\boldsymbol{h}(\hat{\boldsymbol{x}}, \boldsymbol{p}^*)\big)^{-1}\big(\boldsymbol{\nu} - L_{\boldsymbol{f}}\boldsymbol{h}(\hat{\boldsymbol{x}}, \boldsymbol{p}^*)\big)\Big) \tag{6}$$

When $\boldsymbol{x}$ and $\boldsymbol{p}$ are exactly known ($\hat{\boldsymbol{x}} = \boldsymbol{x}$ and $\boldsymbol{p}^* = \boldsymbol{p}$), Equation (6) reduces to:

$$\dot{\boldsymbol{y}} = \boldsymbol{\nu} \quad \Leftrightarrow \quad \boldsymbol{y}(t) = \int_0^t \boldsymbol{\nu}(\tau)\mathrm{d}\tau \tag{7}$$

The resulting control law linearises the system dynamics, reducing the input-output response to a set of integrators. Note that for stability, the relation between $\boldsymbol{y}$ and $\boldsymbol{u}$ has to be minimum phase.[5]

B. Incremental Nonlinear Dynamic Inversion

The incremental form of NDI computes the control increment with respect to the condition of the system one incremental time instance in the past. The fundamental difference with classical NDI is that the control-independent part of the model equations is replaced by state derivative feedback, resulting in a more robust control solution with respect to model mismatch ($\boldsymbol{p}^* \neq \boldsymbol{p}$).[10]

As a first step, the nonlinear system in Equation (1) is approximated by a first-order Taylor series expansion around the current point in time '0':

$$\dot{\boldsymbol{x}} \approx \dot{\boldsymbol{x}}_0 + \frac{\partial}{\partial \boldsymbol{x}}\big(\boldsymbol{f}(\boldsymbol{x}, \boldsymbol{p}) + \boldsymbol{G}(\boldsymbol{x}, \boldsymbol{p})\boldsymbol{u}\big)\Big|_{\substack{\boldsymbol{x}=\boldsymbol{x}_0 \\ \boldsymbol{u}=\boldsymbol{u}_0}} \underbrace{(\boldsymbol{x} - \boldsymbol{x}_0)}_{\Delta \boldsymbol{x}} + \frac{\partial}{\partial \boldsymbol{u}}\big(\boldsymbol{f}(\boldsymbol{x}, \boldsymbol{p}) + \boldsymbol{G}(\boldsymbol{x}, \boldsymbol{p})\boldsymbol{u}\big)\Big|_{\substack{\boldsymbol{x}=\boldsymbol{x}_0 \\ \boldsymbol{u}=\boldsymbol{u}_0}} \underbrace{(\boldsymbol{u} - \boldsymbol{u}_0)}_{\Delta \boldsymbol{u}} \tag{8}$$

The variables with subscript '0' should be interpreted as an incremental time instance before the equivalent variables without subscript. It assumed that the time-scale separation principle holds for Equation (8). For

very small time increments and instantaneous control effectors, the change in input is much faster than the change in state (i.e. $\boldsymbol{x} - \boldsymbol{x}_0 \approx 0$ while $\boldsymbol{u} - \boldsymbol{u}_0 \neq 0$). Assuming $\boldsymbol{x} - \boldsymbol{x}_0 = 0$, Equation (8) reduces to:

$$\dot{\boldsymbol{x}} \approx \dot{\boldsymbol{x}}_0 + \boldsymbol{G}(\boldsymbol{x}_0, \boldsymbol{p})\Delta\boldsymbol{u} \tag{9}$$

It is assumed that $\boldsymbol{G}$ is non-singular and that $\boldsymbol{y} = \boldsymbol{x}$. In this case INDI can be applied to Equation (9).[10] Defining the virtual control input as $\boldsymbol{\nu} = \dot{\boldsymbol{x}}$ and inverting Equation (9), the following control law is obtained:

$$\Delta\boldsymbol{u} = \boldsymbol{G}^{-1}(\hat{\boldsymbol{x}}_0, \boldsymbol{p}^*)(\boldsymbol{\nu} - \hat{\dot{\boldsymbol{x}}}_0) \tag{10}$$

The vector $\hat{\dot{\boldsymbol{x}}}_0$ contains the state derivatives computed or estimated from $\boldsymbol{y}$ or $\boldsymbol{y}_o$, respectively. Substituting the control law (Equation (10)) into Equation (9):

$$\dot{\boldsymbol{x}} \approx \dot{\boldsymbol{x}}_0 + \boldsymbol{G}(\boldsymbol{x}_0, \boldsymbol{p})\big(\boldsymbol{G}^{-1}(\hat{\boldsymbol{x}}_0, \boldsymbol{p}^*)(\boldsymbol{\nu} - \hat{\dot{\boldsymbol{x}}}_0)\big) \tag{11}$$

In the ideal case ($\hat{\boldsymbol{x}}_0 = \boldsymbol{x}_0$, $\hat{\dot{\boldsymbol{x}}}_0 = \dot{\boldsymbol{x}}_0$ and $\boldsymbol{p}^* = \boldsymbol{p}$), the input-output response approximates to a set of integrators:

$$\dot{\boldsymbol{x}} \approx \boldsymbol{\nu} \quad \Leftrightarrow \quad \boldsymbol{x}(t) \approx \int_0^t \boldsymbol{\nu}(\tau)\mathrm{d}\tau \tag{12}$$

The total input $\boldsymbol{u}$ is obtained by adding the current input $\boldsymbol{u}_0$ to the control increment $\Delta\boldsymbol{u}$. Note that the control law should be sampled with a sufficiently high frequency (100 Hz in this application) and requires synchronization between $\boldsymbol{u}_0$ and $\dot{\boldsymbol{x}}_0$.[12,14]

C. Pseudo Control Hedging

(I)NDI inverts the dynamics of the nonlinear system but not of the input. Actuator dynamics are usually considered time-scale separated from the aircraft dynamics. Saturation caused by the physical limits on actuator position and rate may howhever result in invertibility and controllability issues, violating conditions necessary for dynamic inversion.

Pseudo Control Hedging (PCH) aims to compensate for actuator dynamics by means of modification of the reference model dynamics.[19] PCH scales down (hedges) the reference model signal by an estimate of the response deficiency of the system $\boldsymbol{\nu}_h$, effectively hiding the actuator dynamics from the error dynamics. The virtual control hedge $\boldsymbol{\nu}_h$ is computed by subtracting the commanded virtual control $\boldsymbol{\nu}$ from the actual virtual control $\hat{\boldsymbol{\nu}}$:

$$\boldsymbol{\nu}_h = \boldsymbol{\nu} - \hat{\boldsymbol{\nu}} \tag{13}$$

This concept can be applied to the (I)NDI control laws formulated in Equations (5) and (10). Due to actuator limitations, the commanded control deflections $\boldsymbol{u}$ are not identical to the actual control deflections $\boldsymbol{\delta}$. Rearranging Equations (5) and (10) for $\boldsymbol{\nu}$, $\hat{\boldsymbol{\nu}}$ is obtained by inserting $\boldsymbol{\delta}$ for $\boldsymbol{u}$. For NDI the virtual control hedge is then obtained as follows:

$$\boldsymbol{\nu}_h = L_{\boldsymbol{f}}\boldsymbol{h}(\boldsymbol{x}, \boldsymbol{p}) + L_{\boldsymbol{G}}\boldsymbol{h}(\boldsymbol{x}, \boldsymbol{p})\boldsymbol{u} - \big(L_{\boldsymbol{f}}\boldsymbol{h}(\boldsymbol{x}, \boldsymbol{p}) + L_{\boldsymbol{G}}\boldsymbol{h}(\boldsymbol{x}, \boldsymbol{p})\boldsymbol{\delta}\big) \tag{14}$$

$$\boldsymbol{\nu}_h = L_{\boldsymbol{G}}\boldsymbol{h}(\hat{\boldsymbol{x}}, \boldsymbol{p}^*)(\boldsymbol{u} - \hat{\boldsymbol{\delta}}) \tag{15}$$

A similar result is obtained for INDI:[12]

$$\boldsymbol{\nu}_h = \dot{\boldsymbol{x}}_0 + \boldsymbol{G}(\boldsymbol{x}_0, \boldsymbol{p})(\boldsymbol{u} - \boldsymbol{\delta}_0) - \big(\dot{\boldsymbol{x}}_0 + \boldsymbol{G}(\boldsymbol{x}_0, \boldsymbol{p})(\boldsymbol{\delta} - \boldsymbol{\delta}_0)\big) \tag{16}$$

$$\boldsymbol{\nu}_h = \boldsymbol{G}(\hat{\boldsymbol{x}}_0, \boldsymbol{p}^*)(\boldsymbol{u} - \hat{\boldsymbol{\delta}}) \tag{17}$$

Note that $\boldsymbol{\nu}_h$ only depends on the control effectiveness and that $\boldsymbol{\delta}$ is assumed observable. For a conventional first-order reference model, the hedged output is obtained as follows:

$$\boldsymbol{x}_{ref} = \frac{1}{s}\big(\boldsymbol{K}_{ref}(\boldsymbol{x}_{com} - \boldsymbol{x}_{ref}) - \boldsymbol{\nu}_h\big) \tag{18}$$

Where $\boldsymbol{K}_{ref}$ is the diagonal gain matrix. Note that if $\hat{\boldsymbol{x}}_0 \neq \boldsymbol{x}_0$, $\boldsymbol{p}^* \neq \boldsymbol{p}$ or $\hat{\boldsymbol{\delta}} \neq \boldsymbol{\delta}$, PCH will introduce additional uncertainties into the closed loop system.

III. Research platform

A. Cessna Citation II PH-LAB

The Cessna Citation II PH-LAB is the main research aircraft operated by the Faculty of Aerospace Engineering of Delft University of Technology. Originally designed as a 8-passenger business jet, the PH-LAB has been extensively modified to serve as a multipurpose airborne research platform. The aircraft is powered by two Pratt and Whitney JT15D-4 turbofan engines each providing 11 kN of thrust. The maximum cruise speed is 385 kt and the operating ceiling is 43,000 ft. The PH-LAB is certificated to operate in the restricted category allowing a MTOW of 6622 kg. The aircraft is equipped with numerous facilitates to accommodate flight testing including a Fly-By-Wire (FBW) system,[17] Flight Test Instrumentation System (FTIS), and various sensors.

Figure 1. Laboratory aircraft PH-LAB

Figure 2. Experimental pilot station PH-LAB

1. *FBW system*[17]

The mechanical flight control system of the PH-LAB has been supplemented with an in-house developed electric FBW system. The FBW system is based on the analog autopilot of the aircraft, inheriting all of the safety features and performance limitations associated with this system. The autopilot computer has been modified to accept signals from an experimental FBW computer. Each control channel can be separately controlled by the original autopilot or the FBW computer. The FTIS acts as the main communication hub between the various components of the FBW system. Synchronization and communication between the FTIS and the various software is obtained via the Delft University Environment for Communication and Actuation (DUECA).[23] An important limitation of the FBW system is the restricted control authority due to torque limitations imposed on the actuator servo motors.

A simple controller implemented in the FBW system allows direct command over the deflection angle of the control surfaces. The controller uses a proportional element with the servo motor position as feedback. Note that the transmission ratio between servo motor position and control surface deflection is a function of the force on the actuator cables due to cable stretch.[24] Under quasi-steady airspeed and altitude this ratio can howhever be approximated by a constant.[17]

The starboard cockpit position is designated as the experimental pilot station and equipped with a force sensing side-stick allowing two-axis manual control over the FBW system, see Figure 2. A programmable display provides visualization of the flight instruments and task specific information. Note that no manipulator is available to control the third axis via the FBW system.

2. *Sensors*

Inertial and air data are available from the Attitude Heading and Reference System (AHRS) and Digital Air Data Computer (DADC). The PH-LAB is also equipped with control surface deflection sensors. For this flight test campaign, the aircraft is fitted with an air data boom with vane-type angle of attack and sideslip sensors. Note that the angle of attack is also measured by a body-mounted vane sensor. All sensors all connected to the FTIS allowing in-flight monitoring, recording and processing.

The sensor characteristics of the relevant signals have been determined following flight data analysis, see Table 1. Frequency analysis revealed that the airflow direction sensors pick up a 10 Hz disturbance induced by the excitation of the structural eigenmodes of the air data boom. Note that some of the values in Table 1 have been taken from Van 't Veld.[25]

Table 1. Sensor characteristics PH-LAB

Signal	Noise (σ^2)	Bias	Resolution	Delay [ms]	Sampling freq. [Hz]
$p, q, r, \dot{\theta}, \dot{\phi}, \dot{\psi}$ [rad/s]	$4.0 \cdot 10^{-7}$	$3.0 \cdot 10^{-5}$	$6.8 \cdot 10^{-7}$	90	52
θ, ϕ [rad]	$1.0 \cdot 10^{-9}$	$4.0 \cdot 10^{-3}$	$9.6 \cdot 10^{-7}$	90	52
A_x, A_y, A_z [g]	$1.5 \cdot 10^{-5}$	$2.5 \cdot 10^{-3}$	$1.2 \cdot 10^{-4}$	117	52
V_{tas}, V_{cas} [m/s]	$8.5 \cdot 10^{-4}$	2.5	$3.2 \cdot 10^{-2}$	300	16, 8
h [m]	$4.5 \cdot 10^{-3}$	$8.0 \cdot 10^{-3}$	$3.0 \cdot 10^{-1}$	300	16
$\dot{h}$ [m/s]	$5.5 \cdot 10^{-4}$	$4.5 \cdot 10^{-2}$	$8.1 \cdot 10^{-2}$	300	16
M [-]	$1.0 \cdot 10^{-8}$	$7.0 \cdot 10^{-7}$	$6.3 \cdot 10^{-5}$	300	8
$\delta_a, \delta_e, \delta_r$ [rad]	$5.5 \cdot 10^{-7}$	$2.4 \cdot 10^{-3}$	-	$\sim$0	100
$\alpha_{boom}, \beta_{boom}$ [rad]	$7.5 \cdot 10^{-8}$	$1.8 \cdot 10^{-3}$	$9.6 \cdot 10^{-5}$	100	100
α_{body} [rad]	$4.0 \cdot 10^{-10}$	-	$1.0 \cdot 10^{-5}$	280	1000

B. Aircraft model DASMAT

The aircraft model is a high fidelity 6-DOF nonlinear model of the Cessna Citation I. The model was developed in the Delft University Aircraft Simulation Model and Analysis Tool (DASMAT).[26] The Cessna Citation II is a more recent iteration of the Cessna Citation I with increased seating capacity and improved flight performance. The Citation II features more powerful engines, a longer fuselage and longer wings. Despite these differences, the Citation I DASMAT model fits reasonably well to flight data of the Citation II.[27] The Relative Root Mean Square Error (RRMSE) for the longitudinal force and moment coefficients equate to 9% and 13%, respectively. For the lateral force and moment coefficients the RRMSE equals 7% and 9%, respectively.

1. Model equations

The combined translational and rotational dynamics of a rigid-body aircraft over a flat non-rotating earth are described by the Newton-Euler equations:

$$\dot{\boldsymbol{V}} = m^{-1}\big(\boldsymbol{F}_A(\boldsymbol{x}, \boldsymbol{u}, \boldsymbol{p}) + \boldsymbol{F}_T(\boldsymbol{x}, \boldsymbol{u}_o, \boldsymbol{p})\big) - \boldsymbol{\omega} \times \boldsymbol{V} + \mathbb{T}_{bE} \begin{bmatrix} 0 & 0 & g \end{bmatrix}^{\mathrm{T}} \tag{19}$$

$$\dot{\boldsymbol{\omega}} = \boldsymbol{J}(\boldsymbol{p})\big(\boldsymbol{M}_A(\boldsymbol{x}, \boldsymbol{u}, \boldsymbol{p}) + \boldsymbol{M}_T(\boldsymbol{x}, \boldsymbol{u}_o, \boldsymbol{p}) - \boldsymbol{\omega} \times \boldsymbol{J}(\boldsymbol{p})\boldsymbol{\omega}\big) \tag{20}$$

Where $\boldsymbol{V} = [u, v, w]^{\mathrm{T}}$ are the inertial translational velocities and $\boldsymbol{\omega} = [p, q, r]^{\mathrm{T}}$ the angular rates, both in body axis. $\boldsymbol{F}_A$ and $\boldsymbol{M}_A$ are the aerodynamic forces and moments respectively, $\boldsymbol{F}_T$ and $\boldsymbol{M}_T$ are the forces and moments induced by the thrust. The vectors $\boldsymbol{u}$, $\boldsymbol{u}_o$, $\boldsymbol{x}$ and $\boldsymbol{p}$ are the aerodynamic controls, the throttle settings, the air-mass referenced aircraft states and the model parameters, respectively. $\mathbb{T}_{bE}$ is the transformation matrix from the NED frame to the body frame. The aircraft mass is denoted by m and assumed constant, g is the gravitational constant and $\boldsymbol{J}$ the inertia tensor:

$$\boldsymbol{J}(\boldsymbol{p}) = \begin{bmatrix} J_{xx} & 0 & -J_{xz} \\ 0 & J_{yy} & 0 \\ -J_{xz} & 0 & J_{zz} \end{bmatrix} \tag{21}$$

Note that it is assumed that the aircraft is symmetrical in the xy-plane i.e. $J_{xy} = J_{yz} = 0$. The rotational kinematic motion can be expressed in terms of the Euler angular rates following transformation of the body angular rates:

$$\begin{bmatrix}\dot{\phi}\\ \dot{\theta}\\ \dot{\psi}\end{bmatrix} = \mathbb{T}_{\Phi b}\begin{bmatrix}p\\ q\\ r\end{bmatrix} \quad \text{with} \quad \mathbb{T}_{\Phi b} = \begin{bmatrix}1 & \sin(\phi)\tan(\theta) & \cos(\phi)\tan(\theta)\\ 0 & \cos(\phi) & -\sin(\phi)\\ 0 & \sin(\phi)\sec(\theta) & \cos(\phi)\sec(\theta)\end{bmatrix} \tag{22}$$

The aerodynamic forces and moments are defined in terms of their respective coefficients in the stability reference frame:

$$\boldsymbol{F}_A^{s,cg_{ref}}(\boldsymbol{x},\boldsymbol{u},\boldsymbol{p}) = \frac{1}{2}\rho V_{tas}^2 S\begin{bmatrix}-C_D\\ C_Y\\ -C_L\end{bmatrix} \tag{23}$$

$$\boldsymbol{M}_A^{s,cg_{ref}}(\boldsymbol{x},\boldsymbol{u},\boldsymbol{p}) = \frac{1}{2}\rho V_{tas}^2 S\begin{bmatrix}bC_l\\ cC_m\\ bC_n\end{bmatrix} \tag{24}$$

Where ρ is the air density, V_{tas} the true airspeed, b the wing span, $\bar{c}$ the mean aerodynamic chord and S the wing surface area. C_D, C_Y and C_L are the non-dimensional drag, side force and lift coefficients respectively and C_l, C_m and C_n are the non-dimensional moment coefficients. The aerodynamic coefficients are defined in the stability reference frame with cg_{ref} as origin, the aft limit of the aircraft center of gravity. The force and moment equations in body axis with the center of gravity cg as origin are defined as follows:

$$\boldsymbol{F}_A^{b,cg}(\boldsymbol{x},\boldsymbol{u},\boldsymbol{p}) = \mathbb{T}_{sb}^{-1}\boldsymbol{F}_A^{s,cg_{ref}}(\boldsymbol{x},\boldsymbol{u},\boldsymbol{p}) \tag{25}$$

$$\boldsymbol{M}_A^{b,cg}(\boldsymbol{x},\boldsymbol{u},\boldsymbol{p}) = \mathbb{T}_{sb}^{-1}\boldsymbol{M}_A^{s,cg_{ref}}(\boldsymbol{x},\boldsymbol{u},\boldsymbol{p}) + (\boldsymbol{r}_{cg_{ref}} - \boldsymbol{r}_{cg}) \times \boldsymbol{F}_A^{b,cg}(\boldsymbol{x},\boldsymbol{u},\boldsymbol{p}) \tag{26}$$

Where $\mathbb{T}_{sb}$ is the rotation matrix from the body to the stability reference frame, $\boldsymbol{r}_{cg_{ref}}$ and $\boldsymbol{r}_{cg}$ are the reference and actual position of the center of gravity, respectively.

2. Aerodynamic model

The non-dimensional aerodynamic force and moment coefficients are modeled as ordinary polynomials. As an example, the lateral moment coefficients are parametrized as follows:

$$C_l = C_{l_\beta}\beta + C_{l_{\delta_a}}\delta_a + C_{l_{\delta_r}}\delta_r + C_{l_p}\frac{pb}{2V_{tas}} + C_{l_r}\frac{rb}{2V_{tas}} \tag{27}$$

$$C_n = C_{n_\beta}\beta + C_{n_{\delta_a}}\delta_a + C_{n_{\delta_r}}\delta_r + C_{n_p}\frac{pb}{2V_{tas}} + C_{n_r}\frac{rb}{2V_{tas}} \tag{28}$$

Terms like C_{l_β} may in turn depend on the angle of attack, Mach number, altitude etc. Multiplicative uncertainties are added to the aerodynamic coefficients and the rotational inertia. As an example, the perturbed side force coefficient $\widetilde{C}_Y$ is defined as follows:

$$\widetilde{C}_Y = C_Y(1 + \Delta C_Y) \tag{29}$$

Where C_Y is the nominal value of the side force coefficient and ΔC_Y the corresponding tolerance parameter. These are up to 10% for the longitudinal coefficients and up to 30% for the lateral coefficients following standard practice, see Table 2.

3. Mass model

A highly accurate mass model for the Cessna Citation II is adopted from De Visser.[28] The model is based on the weight and balance calculation procedure of the Citation II and takes into account the mass and position of passengers, payload and fuel. The contribution of the fuel mass is updated by means of feedback of the used fuel and a model of the geometry of the fuel tanks.

4. Sensor models

The following sensor characteristics are modeled: noise, bias, delay and quantization effects (see Table 1). The noise is modeled as a zero-mean Gaussian process. In addition, kinematic position errors are applied on the specific force and airflow direction signals. The disturbances induced by the flexibility of the air data boom are modeled as a 10 Hz sinusoidal signal.

5. Actuator model

A first-order model of the PH-LAB actuator system was developed using available flight data. The flight data contains responses to a series of open loop 3211 and doublet commands applied by the autopilot on elevator and aileron. Besides a first-order lag component, the model includes actuator position and rate limits, and a transport delay:

$$\dot{\delta}(t) = S_{\dot{\delta}}\Big(K_{fbw}\omega_{act}u(t-\tau_{act}) - \omega_{act}S_{\delta}\big(\delta(t)\big)\Big) \qquad (30)$$

Where S_{δ} and $S_{\dot{\delta}}$ are the saturation function for actuator position and rate, respectively. K_{fbw} is the FBW input-output gain i.e. the transmission ratio between servo motor position and control surface deflection. The actuator bandwidth ω_{act} and transport delay τ_{act} are determined by fitting the measured control deflections to the general step input time response of a first-order system. A nonlinear least square curve-fitting method was used to find the optimum fit. For each step input command the maximum rate of deflection $\dot{\delta}_{max}$ was determined as well.

Table 2. PH-LAB parameter uncertainty ranges

Symbol	Minimum	Nominal	Maximum
$\Delta\tau_{sync}$	-0.3	0	0.3
ΔJ_{xx}	-0.1	0	0.1
ΔJ_{yy}	-0.1	0	0.1
ΔJ_{yy}	-0.1	0	0.1
ΔJ_{xz}	-0.3	0	0.3
ΔC_D	-0.1	0	0.1
ΔC_L	-0.3	0	0.3
ΔC_Y	-0.1	0	0.1
ΔC_{l_β}	-0.3	0	0.3
ΔC_{m_0}	-0.1	0	0.1
ΔC_{n_β}	-0.3	0	0.3
ΔC_{l_p}	-0.3	0	0.3
ΔC_{l_r}	-0.3	0	0.3
ΔC_{m_q}	-0.1	0	0.1
ΔC_{n_p}	-0.3	0	0.3
ΔC_{n_r}	-0.3	0	0.3
$\Delta C_{l_{\delta_a}}$	-0.3	0	0.3
$\Delta C_{l_{\delta_r}}$	-0.3	0	0.3
$\Delta C_{m_{\delta_e}}$	-0.1	0	0.1
$\Delta C_{n_{\delta_a}}$	-0.3	0	0.3
$\Delta C_{n_{\delta_r}}$	-0.3	0	0.3

Table 3. Actuator model parameters

	δ_{max} [deg]	δ_{min} [deg]	K_{fbw} [-]	$\dot{\delta}_{max}$ [deg/s]	τ_{act} [ms]	ω_{act} [rad/s]
Aileron	15	-19	0.70	19.7 ($\sigma = 4.81$)	39.8 ($\sigma = 7.91$)	12.4 ($\sigma = 2.30$)
Elevator	15	-17	0.60			
Rudder	22	-22	0.55			

IV. Control law design

For the controller developed in this paper two control objectives are formulated: Rate Control Attitude Hold (RCAH) and Attitude Control (AC).[18] RCAH is governed between $\pm 27°$ and $\pm 15°$ for roll and pitch, respectively. AC is governed outside this range up to $\pm 35°$ and $\pm 20°$ for roll and pitch, respectively. The lateral tracking task includes the angle of sideslip as well. The general controller structure can be found in Figure 3.

A. Inner loop

(I)NDI is applied to the rotational dynamics of the aircraft. The control variables $\boldsymbol{y}$ are set equal to the body angular rates $\boldsymbol{\omega} = [p, q, r]^{\mathrm{T}}$. The aileron, elevator and rudder deflection are selected as input, i.e. $\boldsymbol{u} = [\delta_a, \delta_e, \delta_r]^{\mathrm{T}}$.

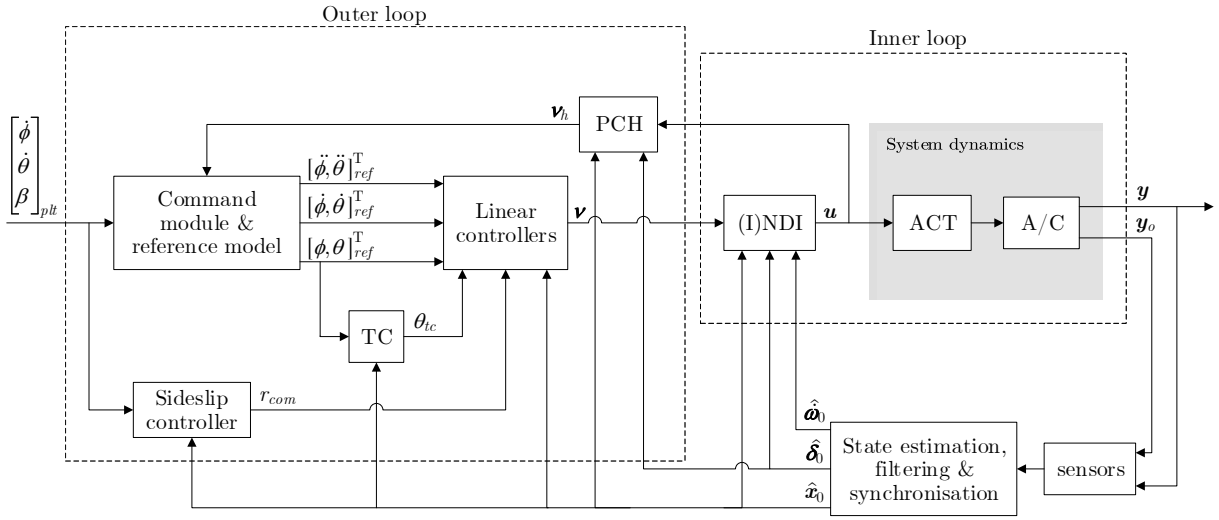

Figure 3. General controller structure

1. Angular rate NDI

The analytic relationship between the body angular rates and control surface deflections arises directly from Euler's rotation equations, see Equation (20). Neglecting the moment induced by the thrust $\boldsymbol{M}_T$, the aerodynamic moment $\boldsymbol{M}_A$ can be split into into an airframe dependent part $\boldsymbol{M}_a$ and a part dependent on the control effectors $\boldsymbol{M}_c$. These are assumed to be of the following form:

$$\boldsymbol{M}_a(\boldsymbol{x},\boldsymbol{p}) = \frac{1}{2}\rho V_{tas}^2 S \begin{bmatrix} bC_{l_a} \\ \bar{c}C_{m_a} \\ bC_{n_a} \end{bmatrix} \tag{31}$$

$$\frac{\partial \boldsymbol{M}_c(\boldsymbol{x},\boldsymbol{p},\boldsymbol{u})}{\partial \boldsymbol{u}} = \boldsymbol{M}_{c_{\boldsymbol{\delta}}}(\boldsymbol{x},\boldsymbol{p}) = \frac{1}{2}\rho V_{tas}^2 S \begin{bmatrix} bC_{l_{\delta_a}} & 0 & bC_{l_{\delta_r}} \\ 0 & \bar{c}C_{m_{\delta_e}} & 0 \\ bC_{n_{\delta_a}} & 0 & bC_{n_{\delta_r}} \end{bmatrix} \tag{32}$$

Note that it is assumed that $\boldsymbol{M}_c$ is linear in $\boldsymbol{u}$. Equation (20) can be rewritten as follows:

$$\dot{\boldsymbol{\omega}} = \boldsymbol{J}^{-1}(\boldsymbol{p})\big(\boldsymbol{M}_a(\boldsymbol{x},\boldsymbol{p}) + \boldsymbol{M}_{c_{\boldsymbol{\delta}}}(\boldsymbol{x},\boldsymbol{p})\boldsymbol{u} - \boldsymbol{\omega}\times\boldsymbol{J}(\boldsymbol{p})\boldsymbol{\omega}\big) \tag{33}$$

Applying dynamic inversion to Equation (33), the following control law is obtained:

$$\boldsymbol{u} = \underbrace{\boldsymbol{M}_{c_{\boldsymbol{\delta}}}^{-1}(\hat{\boldsymbol{x}},\boldsymbol{p}^*)\boldsymbol{J}(\boldsymbol{p}^*)}_{(L_{\boldsymbol{G}}\boldsymbol{h})^{-1}}\Big(\boldsymbol{\nu} - \underbrace{\boldsymbol{J}^{-1}(\boldsymbol{p}^*)\big(\boldsymbol{M}_a(\hat{\boldsymbol{x}},\boldsymbol{p}^*) - \boldsymbol{\omega}\times\boldsymbol{J}(\boldsymbol{p}^*)\boldsymbol{\omega}\big)}_{L_{\boldsymbol{f}}\boldsymbol{h}}\Big) \tag{34}$$

2. Angular rate INDI

The incremental form of Euler's rotation equation is obtained following a first-order Taylor expansion of Equation (33) around the current point in time '0':

$$\begin{aligned}\dot{\boldsymbol{\omega}} \approx \dot{\boldsymbol{\omega}}_0 &+ \frac{\partial}{\partial\boldsymbol{\omega}}\Big(\boldsymbol{J}^{-1}(\boldsymbol{p})\big(\boldsymbol{M}_a(\boldsymbol{x},\boldsymbol{p}) + \boldsymbol{M}_{c_{\boldsymbol{\delta}}}(\boldsymbol{x},\boldsymbol{p})\boldsymbol{u} - \boldsymbol{\omega}\times\boldsymbol{J}(\boldsymbol{p})\boldsymbol{\omega}\big)\Big)\Big|_{\substack{\boldsymbol{\omega}=\boldsymbol{\omega}_0\\ \boldsymbol{u}=\boldsymbol{u}_0}} \underbrace{(\boldsymbol{\omega}-\boldsymbol{\omega}_0)}_{\Delta\boldsymbol{\omega}} \\ &+ \frac{\partial}{\partial\boldsymbol{u}}\Big(\boldsymbol{J}^{-1}(\boldsymbol{p})\big(\boldsymbol{M}_a(\boldsymbol{x},\boldsymbol{p}) + \boldsymbol{M}_{c_{\boldsymbol{\delta}}}(\boldsymbol{x},\boldsymbol{p})\boldsymbol{u} - \boldsymbol{\omega}\times\boldsymbol{J}(\boldsymbol{p})\boldsymbol{\omega}\big)\Big)\Big|_{\substack{\boldsymbol{\omega}=\boldsymbol{\omega}_0\\ \boldsymbol{u}=\boldsymbol{u}_0}} \underbrace{(\boldsymbol{u}-\boldsymbol{u}_0)}_{\Delta\boldsymbol{u}}\end{aligned} \tag{35}$$

Again assuming $\boldsymbol{\omega} - \boldsymbol{\omega}_0 = 0$, Equation (35) reduces to:

$$\dot{\boldsymbol{\omega}} \approx \dot{\boldsymbol{\omega}}_0 + \boldsymbol{J}^{-1}(\boldsymbol{p})\boldsymbol{M}_{c_{\boldsymbol{\delta}}}(\boldsymbol{x}_0, \boldsymbol{p})\Delta\boldsymbol{u} \tag{36}$$

Applying dynamic inversion to Equation (36) and adding the current control surface deflections $\boldsymbol{\delta}_0$, the following control law is obtained:

$$\boldsymbol{u} = \underbrace{\boldsymbol{M}_{c_{\boldsymbol{\delta}}}^{-1}(\hat{\boldsymbol{x}}_0, \boldsymbol{p}^*)\boldsymbol{J}(\boldsymbol{p}^*)}_{\boldsymbol{G}^{-1}}(\boldsymbol{\nu} - \underbrace{\hat{\dot{\boldsymbol{\omega}}}_0}_{\hat{\boldsymbol{x}}_0}) + \hat{\boldsymbol{\delta}}_0 \tag{37}$$

B. Outer loop[18]

The outer loop consists of the following components: command module & reference model, sideslip controller, Turn Compensation (TC), linear controllers and Pseudo Control Hedging (PCH).

1. *Command module & reference model*

The command module and reference model serve as attitude flight envelope protection and command filter, respectively. Furthermore, the command module blends two different control methods: rate control attitude hold (RCAH) and attitude control (AC). RCAH is active between 27° and −27° for roll and between 15° and −15° for pitch. When these limits are reached the feedforward term is deactivated and the pilot command signal is directly added to the saturated signal, see Figure 4. This way the attitude angles are directly governed by the pilot command input. AC is active up to ±35° for roll and ±20° for pitch, these are the limit values of the system. Note that for zero pilot input command in AC mode, the system will always command the aircraft back to the RCAH attitude limits. The purpose of this setup is to reduce violent behavior when the roll and pitch limits of the system are reached. The gain K_2 in the command module is required to achieve a smooth transition between AC and RACH. The reference model is conventional second-order system smoothing the command signals to values achievable by the aircraft, see Equation (38).

$$H_{ref}(s) = \frac{K_1 K_2}{s^2 + K_1 s + K_1 K_2} = \frac{\omega_{n_{ref}}^2}{s^2 + 2\zeta_{ref}\omega_{n_{ref}} s + \omega_{n_{ref}}^2} \tag{38}$$

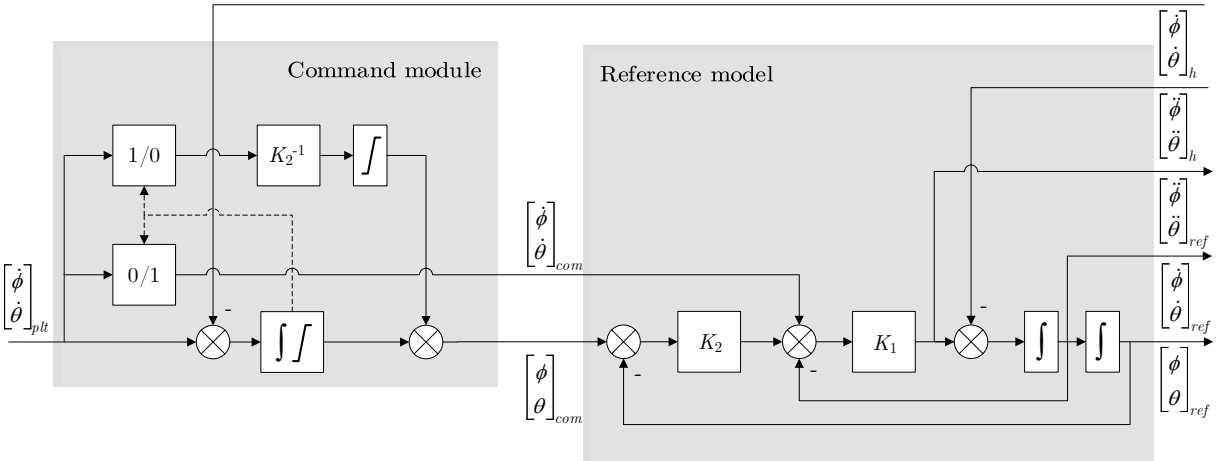

Figure 4. Command module & reference model[18]

2. *Sideslip controller*

For manual control, the angle of sideslip is preferred as outer loop control variable. Furthermore, as there is no means to manually control the yaw axis due to absence of a yaw input device, coordinated flight is only possible by means of direct sideslip augmentation. The control setup therefore includes a sideslip controller:

$$r_{com} = \frac{1}{V_{tas}}(wp - A_y) - \left(\frac{1}{s}K_{\beta_I}(\beta_{plt} - \beta) - K_\beta \beta\right) \quad \text{with} \quad w \approx V_{tas}\alpha \tag{39}$$

3. Turn Compensation

The control setup includes a turn compensation (TC) module with the following control law:

$$\theta_{tc} = \big(\cos(\phi_{ref}) - 1\big)\frac{mg}{\frac{1}{2}\rho_0 V_{cas}^2 S C_{L_\alpha}} \tag{40}$$

4. Linear controllers

The linear controllers are defined in Equations (41) to (43). For the pitch and roll channel, the controllers operate up to the 2nd order time derivative.

$$\nu_{\dot\phi} = \left(K_\phi + \frac{K_{\phi_I}}{s}\right)(\phi_{ref} - \phi) + K_{\dot\phi}(\dot\phi_{ref} - \dot\phi) + K_{\ddot\phi}\ddot\phi_{ref} \tag{41}$$

$$\nu_{\dot\theta} = \left(K_\theta + \frac{K_{\theta_I}}{s}\right)(\theta_{ref} + \theta_{tc} - \theta) + K_{\dot\theta}(\dot\theta_{ref} - \dot\theta) + K_{\ddot\theta}\ddot\theta_{ref} \tag{42}$$

$$\nu_r = K_r(r_{com} - r) \tag{43}$$

Kinematic inversion of Equations (41) and (42) immediately results in:

$$\begin{bmatrix}\nu_p\\ \nu_q\\ \nu_r\end{bmatrix} = \mathbb{T}_{\Phi b}^{-1}\begin{bmatrix}\nu_{\dot\phi}\\ \nu_{\dot\theta}\\ \nu_{\dot\psi}\end{bmatrix} - \dot{\mathbb{T}}_{\Phi b}\begin{bmatrix}p\\ q\\ r\end{bmatrix} \tag{44}$$

5. Pseudo Control Hedging

Pseudo Control Hedging is implemented slightly differently as in Lombaearts and Looye,[18] where hedging was only activated upon saturation of the actuator model. As the PH-LAB actuator model does not include speed dependent position limiting, activation upon model saturation is not desirable. In this setup, upon manual activation, compensation will be provided irrespective of actuator saturation.

Consider again Equation (17), substituting the above result obtained for $\boldsymbol{G}$, the virtual control hedge $\boldsymbol{\nu}_h$ is obtained as follows:

$$\boldsymbol{\nu}_h = \underbrace{\boldsymbol{M}_{c_{\boldsymbol{\delta}}}(\hat{\boldsymbol{x}}_0, \boldsymbol{p}^*)\boldsymbol{J}^{-1}(\boldsymbol{p}^*)}_{\boldsymbol{G}}(\boldsymbol{u} - \hat{\boldsymbol{\delta}}) \tag{45}$$

Kinematic inversion of Equation (45) immediately results in:

$$\begin{bmatrix}\nu_{\dot\phi}\\ \nu_{\dot\theta}\\ \nu_{\dot\psi}\end{bmatrix}_h = \mathbb{T}_{\Phi b}\begin{bmatrix}\nu_p\\ \nu_q\\ \nu_r\end{bmatrix}_h + \dot{\mathbb{T}}_{\Phi b}\begin{bmatrix}p\\ q\\ r\end{bmatrix} \tag{46}$$

The compensation signal is subtracted from the reference signal $[\ddot\phi_{ref}, \ddot\theta_{ref}]^{\mathrm{T}}$, see Figure 4. The command module also requires hedging as the commanded attitude $[\phi_{com}, \theta_{com}]^{\mathrm{T}}$ is obtained via integration of the pilot rate command $[\dot\phi_{plt}, \dot\theta_{plt}]^{\mathrm{T}}$, leaving the commanded attitude unhedged would lead to undesired overshoot.

C. State estimation, filtering and synchronisation

Good quality sensor signals are imperative to (I)NDI control. Not all signals provided by the PH-LAB sensor systems are processed and might contain disturbances that would propagate through the control laws without filtering. Inertial sensors are sensitive to structural vibrations while air data sensors pick up atmospheric turbulence. The flexibility of the PH-LAB air data boom also adds a 10 Hz disturbance to the airflow direction signals. The filtering techniques proposed here are in part taken from Looye and Joos.[29]

The angular acceleration signals require additional attention as these are obtained via differentiation. Careful filtering of the angular rates is necessary to reduce sensor noise. The angular rate and control deflection signals also require synchronization.

1. Inertial data

The angular rates are filtered with a second-order low-pass filter:[9]

$$H_{fil}(s) = \frac{\omega_{n_{fil}}^2}{s^2 + 2\zeta_{fil}\omega_{n_{fil}} + \omega_{n_{fil}}^2} \tag{47}$$

The natural frequency $\omega_{n_{fil}}$ is set equal to 20 rad/s and the damping ratio ζ_{fil} is unity. The remainder of the inertial signals are filtered using first-order low-pass filters with a time constant of 50 ms.

2. Air data

All DADC and airflow direction signals are combined with inertial measurements using a first-order complementary filter:

$$\hat{x} = \frac{1}{\tau_{fil}s + 1}x + \frac{\tau_{fil}s}{\tau_{fil}s + 1}x_i \tag{48}$$

Where x_i is the inertial equivalent of air data signal x. The filter time constant τ_{fil} is set equal to 1 s. Note that for some signals the derivative of the inertial signal is used as high-pass signal.

The inertial speed $\dot{V}_i$ is calculated from the linear accelerations:

$$\dot{V}_i = \begin{bmatrix} a_x & a_y & a_z \end{bmatrix} \begin{bmatrix} \cos(\alpha)\cos(\beta) \\ \sin(\beta) \\ \sin(\alpha)\cos(\beta) \end{bmatrix} \quad \text{with} \quad \begin{bmatrix} a_x \\ a_y \\ a_z \end{bmatrix} = g \left(\begin{bmatrix} A_x \\ A_y \\ A_z \end{bmatrix} + \begin{bmatrix} -\sin(\theta) \\ \cos(\theta)\sin(\phi) \\ \cos(\theta)\cos(\phi) \end{bmatrix} \right) \tag{49}$$

The derivative of the inertial vertical speed $\ddot{h}_i$ is also obtained from the linear accelerations:

$$\ddot{h}_i = \begin{bmatrix} a_x & a_y & a_z \end{bmatrix} \begin{bmatrix} \sin(\theta) \\ -\cos(\theta)\sin(\phi) \\ -\cos(\theta)\cos(\phi) \end{bmatrix} \tag{50}$$

The altitude h is complemented with the complementary filtered vertical speed $\hat{\dot{h}}$. An approximation is used for the inertial Mach number M_i:

$$M_i \approx \frac{V_{tas}}{20.05\sqrt{(288.2 - 0.0065h)}} \tag{51}$$

The inertial angle of attack α_i is computed as follows:

$$\alpha_i = \theta - \gamma_a \quad \text{with} \quad \gamma_a \approx \frac{\dot{h}}{V_{tas}} \tag{52}$$

The derivative of the inertial angle of sideslip $\dot{\beta}_i$ is obtained as follows:

$$\dot{\beta}_i = \frac{A_y g + g\sin(\phi)\cos(\theta)}{V_{tas}} - r\cos(\alpha) + p\sin(\alpha) \tag{53}$$

3. Control deflections

Synchronization between control deflection and angular acceleration feedback is achieved by applying equivalent filtering and artificially adding the surplus of angular rate delay to the control deflection signal:[14,15]

$$\hat{\boldsymbol{\delta}}_0 = H_{fil}(s)H_{sync}(s)\boldsymbol{\delta} \tag{54}$$

Where H_{sync} is the frequency-domain equivalent of a pure time delay τ_{sync} corresponding to the surplus of angular rate delay. To account for variations in delay (e.g. due to sampling or unmodeled delays), a multiplicative uncertainty is added to τ_{sync}. Alternatively, the synchronized control deflections may be estimated using actuator models:

$$\hat{\boldsymbol{\delta}}_{0_{est}} = \frac{z^{-1}H_{act}(s)H_{fil}(s)H_{sync}(s)}{1 - z^{-1}H_{act}(s)H_{fil}(s)H_{sync}(s)}\Delta\boldsymbol{u} \tag{55}$$

Where H_{act} represents the actuator dynamics i.e. the frequency-domain equivalent of Equation (30). Note that z^{-1} is the increment delay, strictly this term is required as $\Delta\boldsymbol{u}$ is one incremental time step ahead of $\boldsymbol{\delta}_0$.

D. Design optimization

For the tuning of the control laws multi-objective optimization is used. The Institute of System Dynamics and Control (SR) of the German Aerospace Institute (DLR) developed the Multi-Objective Parameter Synthesis (MOPS) tool specifically for this purpose.[30] Robustness is addressed via a multi-model approach and unspecific robustness criteria.[29] The tuning of the lateral and longitudinal controller parameters are performed separately, the discussion will be limited to the lateral case only.

1. Design criteria

Multi-objective optimization requires a set of computable criteria that can be used for optimization. The design criteria for the lateral synthesis parameters are defined in Table 4. These are computed from three nonlinear simulations and a linear analysis of the closed-loop system. Simulations 1 and 2 are used to evaluate the reference tracking with criteria concerning overshoot, rise time, settling time and control effort. Simulation 3 is used to assess the disturbance rejection by means of a cross-wind step.

The criteria are formulated as min-max optimization problems and scaled such that a value smaller than 1 is considered satisfactory. The criteria corresponding to the nonlinear simulations are scaled by division of the corresponding demand value. The criteria corresponding to the linear analysis are scaled using 'good-bad' values.[30] With this scaling type, it is demanded that the criterion is at least equal to the 'bad-low' value. The region between 'bad-low' and 'good-low' is considered acceptable with linearly decreasing scaling. Values larger than 'good low' are considered equally good and are subsequently scaled to 0. Notice that for some of the criteria in Table 4 an inequality constraint is used such that no further optimization is performed after the demand value is obtained.

2. Robustness

The robustness of the control law is addressed in two ways. A multi-model approach is used to achieve robustness to parametric uncertainties. The multi-model setup is created by adding a number of model cases with worst-case parameter combinations to the nominal case. These worst-cases are defined with respect to one of the design criteria defined in Table 4. The optimization process addresses the criteria simultaneously for all model cases allowing for trade-off between criteria under worst-case and nominal parameter conditions. Note that this approach implicitly assumes that the controller is also robust to model cases in between those addressed. To this end also local robustness margins are included as optimization criteria. These are the minimum phase and gain margins at the sensor and actuator positions listed in Table 4. Note that the local robustness criteria are also intended to achieve robustness to unspecified uncertainties (e.g. unmodeled dynamics and time delays).

Table 4. Design criteria lateral part

Name	Description	Calculation	Bad-low	Good-low	Demand	Type
Simulation 1: Box-cart: $\dot{\phi}_{plt} = 5$ °/s at $t = 1$ till $t = 6$ s						
osdphi [-]	Overshoot $\dot{\phi}$		-	-	0.5	c
rtdphi [s]	Rise time $\dot{\phi}$	0%→100%	-	-	0.75	c
stdphi [s]	Settling time $\dot{\phi}$	0.1°	-	-	4	m
osphi [-]	Overshoot ϕ		-	-	0.1	c
rtphi [s]	Rise time ϕ	0%→100%	-	-	5	c
stphi [s]	Settling time ϕ	0.1°	-	-	4	m
maxdda [deg/s]	Maximum $\dot{\delta}_a$	$\max\lvert\dot{\delta}_a\rvert$	-	-	40	m
errbeta [deg]	Error β	$\int_0^T \lvert\beta\rvert \mathrm{d}t/T$	-	-	0.5	m
Simulation 2: Step $\beta_{plt} = 5°$ at $t = 1$ s						
osbeta [-]	Overshoot β		-	-	0.01	c
rtbeta [s]	Rise time β	10%→90%	-	-	4	m
stbeta [s]	Settling time β	0.1°	-	-	5	m
maxddr [deg/s]	Maximum $\dot{\delta}_r$	$\max\lvert\dot{\delta}_r\rvert$	-	-	20	m
errphi [deg]	Error ϕ	$\int_0^T \lvert\phi\rvert \mathrm{d}t/T$	-	-	0.5	m
Simulation 3: Wind step $v_{wind} = 16$ m/s at $t = 1$ s						
maxphi [deg]	Maximum ϕ	$\max\lvert\phi\rvert$	-	-	6.7	m
maxdr [deg]	Maximum δ_r	$\max\lvert\delta_r\rvert$	-	-	22	m
Linear analysis:						
gmda [dB]	Gain margin δ_a		4	6	-	m
pmda [deg]	Phase margin δ_a		30	60	-	c
gmdr [dB]	Gain margin δ_r		4	6	-	m
pmdr [deg]	Phase margin δ_r		30	60	-	c
gmp [dB]	Gain margin p		4	6	-	m
pmp [deg]	Phase margin p		30	60	-	c
gmr [dB]	Gain margin r		4	6	-	m
pmr [deg]	Phase margin r		30	60	-	c
m=minimize, c=inequality constraint						

3. Parameter synthesis

The parameter synthesis was performed in three successive steps. First the linear controller gains and reference model parameters were optimized. With the resulting tuning parameter set, a worst-case analyses was performed. Note that it was assumed that the worst-cases are to be found at the extremities of the parameter space. To this end, minimum or maximum values were selected for the parametric model uncertainties. The criteria were evaluated for all parameter combinations. To limit the number of combinations for NDI, tolerances on the moment of inertia and less relevant aerodynamic coefficients were left out.

The two criteria that proofed most sensitive to parameter variations were added as separate model cases to the nominal model to form a multi-model set. An additional parameter synthesis was performed for this set of model-cases. The results can be found in Table 5. Note that the maximum uncertainty on the lateral moment coefficients has been slightly relieved to 20%, else a satisfactory design for the NDI controller could not be realized.

4. Assessment

The best-compromise solution for INDI and NDI will now be compared. Notice in Table 5 that for INDI a significantly lower integrator gain K_{ϕ_I} was selected by the optimizer compared to NDI. This behaviour can be attributed to the incremental nature of INDI as the calculated increment is added to the current

input, basically acting as an integral term. Further notice that for the worst cases the optimizer pushed the synchronization uncertainty $\Delta\tau_{sync}$ to its minimum value. This behaviour was expected considering that a surplus of state derivative delay results in relatively fast system instability.[25] Steady-state offsets in the angular rate tracking were effectively regulated by the linear controllers. The steady errors in the sideslip tracking are the result of measurement bias. The settling time calculation was subsequently relieved to 0.2°. Note that the noise was deactivated during the optimization as this would cause inconsistencies between the different evaluations. For the NDI worst cases the criteria corresponding to *stdphi*, *stphi*, *osbeta* and *errphi* had to be relieved.

The responses corresponding to the nonlinear simulations can be found in Figures 5 to 7. Note that the blue lines represent the responses of the nominal case and the grey area contains the responses of the worst cases. This area should be interpreted as the design uncertainty. As expected, the responses corresponding to the INDI controller show less sensitivity to parameter variations, with smaller deviations between the cases. The difference is most prominent in Figure 6. The NDI controller is unable to regulate the roll angle error under sideslip for uncertain parameter conditions, with errors up to 1.4°. The incremental controller has superior disturbance rejection compared to NDI, with faster attenuation and lower overshoot in the attitude response, see Figure 7. This result conforms to observations made by Acquentella et al.[11]

Table 5. Synthesis parameters lateral part

Tuning parameter	INDI			NDI		
Linear controller gains:						
K_ϕ	5.51			7.91		
K_{ϕ_I}	1.34			7.02		
$K_{\dot{\phi}}$	4.80			6.48		
$K_{\ddot{\phi}}$	1.05			0.941		
K_r	1.62			3.22		
K_β	1.93			1.55		
K_{β_I}	0.977			0.709		
Reference model parameters:						
ζ_{ref}	1.00			0.741		
$\omega_{n_{ref}}$	1.35			1.27		
Uncertain model parameters:						
	nominal	worst gmda	worst pmp	nominal	worst gmda	worst gmp
$\Delta\tau_{sync}$	0	-0.3	-0.3	0	0	0
ΔJ_{xx}	0	-0.1	-0.1	0	0	0
ΔJ_{zz}	0	-0.1	-0.1	0	0	0
ΔJ_{xz}	0	0.3	-0.3	0	0	0
ΔC_Y	0	0.3	-0.3	0	0.3	0.3
ΔC_{l_β}	0	0	0	0	-0.2	-0.2
$\Delta C_{l_{\delta_a}}$	0	-0.2	0.2	0	0.2	0.2
$\Delta C_{l_{\delta_r}}$	0	0.2	0.2	0	0	0
ΔC_{l_p}	0	0	0	0	-0.2	0.2
ΔC_{l_r}	0	0	0	0	-0.2	-0.2
ΔC_{n_β}	0	0	0	0	-0.2	-0.2
$\Delta C_{n_{\delta_r}}$	0	0.2	0.2	0	0.2	0.2
$\Delta C_{n_{\delta_a}}$	0	0.2	0.2	0	0	0
ΔC_{n_p}	0	0	0	0	-0.2	-0.2
ΔC_{n_r}	0	0	0	0	0.2	-0.2

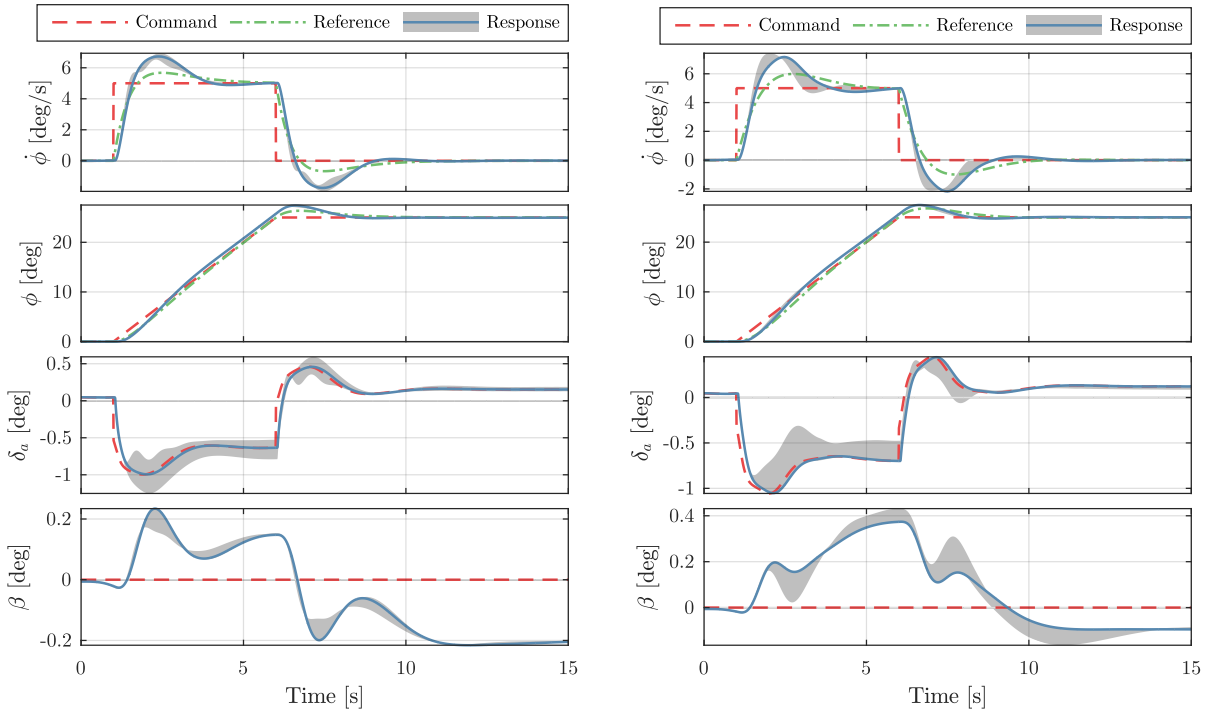

(a) INDI (b) NDI

Figure 5. Simulation 1: tracking response to 5°/s roll rate box-cart

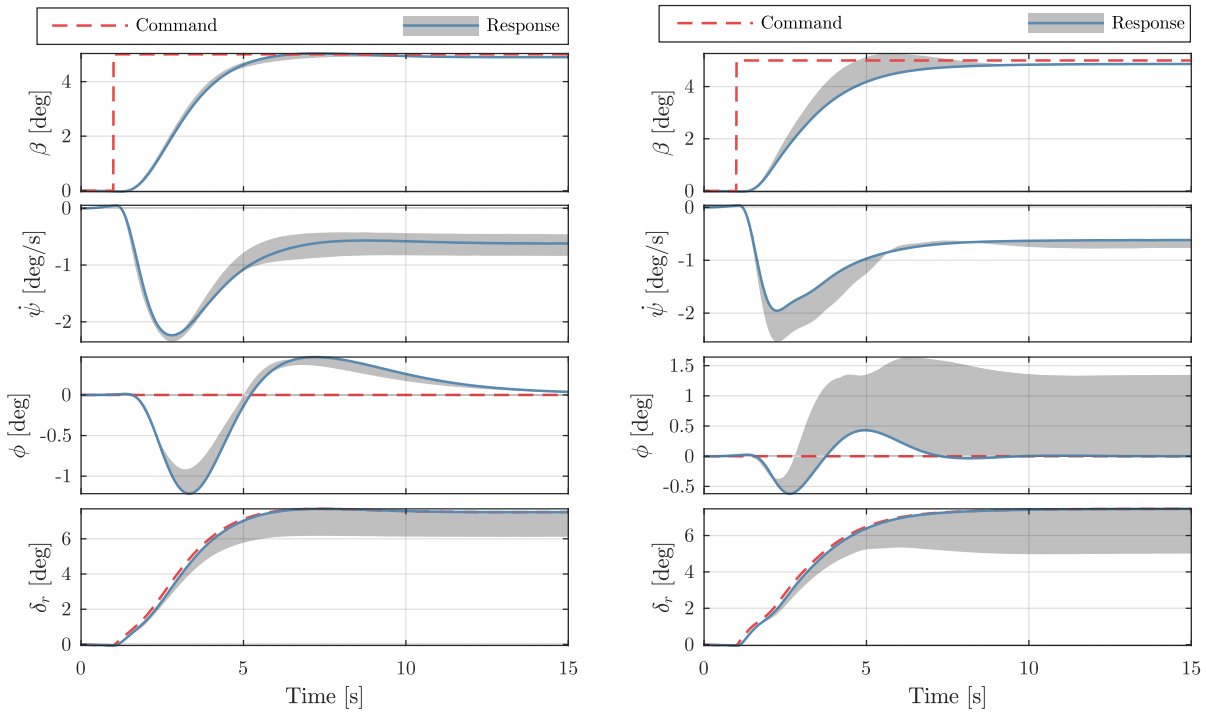

(a) INDI (b) NDI

Figure 6. Simulation 2: tracking response to 5° sideslip step

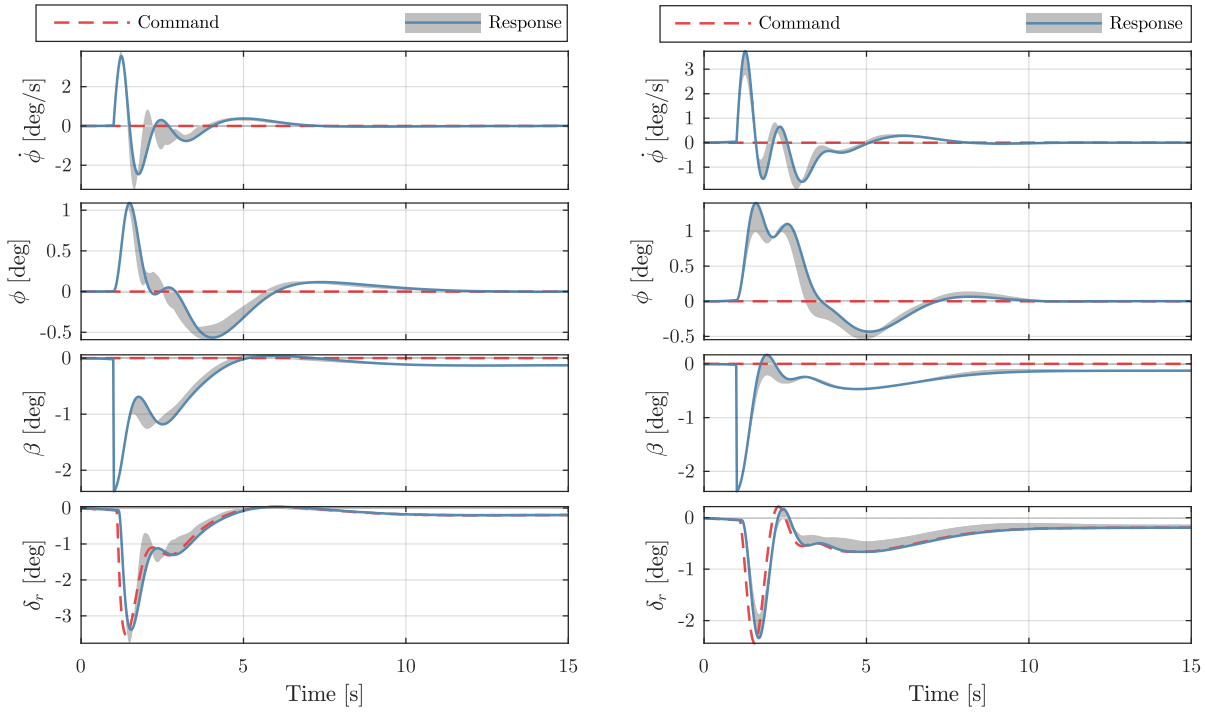

(a) INDI (b) NDI

Figure 7. Simulation 3: tracking response to 16 m/s cross-wind step

V. Control law validation

A. Simulator assessment and clearance

For the assessment and clearance of the experimental controller, use was made of the robotic motion simulator operated by the Institute of System Dynamics and Control (SR) of the German Aerospace Institute (DLR).[31] The simulator utilizes a serial kinematics industrial robot arm to generate motion cues to the attached simulator pod, greatly enlarging the motion capability compared to conventional hexapod simulators. The simulator pod is fully modular allowing use of various instrument consoles. The set-up of the cockpit includes a certified side-stick, dual throttle control system and rudder pedals. Complete three-dimensional cockpit visualization is provided via a virtual reality headset.

Specific attention was paid to the controller behavior at initialization and during switching between different controller modes. These operations should be free of any transients. The pilot-in-the-loop allowed a qualitative assessment of the overall dynamics and handling qualities of the system.

Figure 8. Robotic Motion Simulator DLR

B. Rig testing

Extensive rig testing was performed on the "iron bird" of the PH-LAB. This system includes the actual FBW hardware components and is used to validate proper functioning in interaction of the experimental controller with the system hardware. For software implementation, the Delft University Environment for Communication and Activation (DUECA)[23] is used. This framework allows straightforward implementation of controllers developed in the MATLAB/Simulink environment.

C. Flight tests

Over the course of five days, three successive flight test were performed to validate the incremental controller. All flights departed from and terminated at Amsterdam Airport Schiphol (AMS) and the experiments were executed in designated areas within Dutch airspace, see Figure 9.

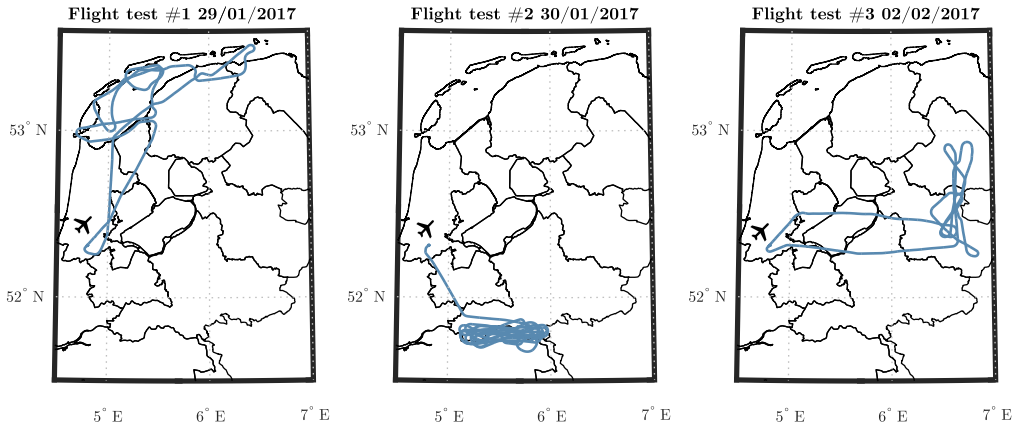

Figure 9. Flight track of test flights

1. *Experimental setup*

The aircraft was configured in a clean setup during the flight tests with gear, flaps and spoilers retracted. The experiments were repeated for two flight conditions: 200 KIAS FL150 and 240 KIAS FL150. The automatic elevator trim was deactivated during most of the experiments. Since the PH-LAB is not fitted with an autothrottle, the safety pilot was tasked to monitor and correct the airspeed manually. The experiments were performed throughout the whole flight.

The experiments focused on a series of pitch and roll attitude captures of varying magnitude and command intensity. In addition, a number of simulated engine failures were executed as well. Some turbulent air layers were encountered during the flight tests hence the controller response to turbulence could be verified. Finally, the incremental controller was used during an instrument approach and was active down to an altitude of 2000 ft.

For safety reasons, the attitude captures were first executed using a conservative setup with restricted control authority and a conservative parameter set. Artificial limits on the control signals allow maximum control deflection changes of $\pm 1^\circ$ around the trim condition. The conservative parameters are obtained by multiplying the inverse of the control effectiveness by a factor 2.

To enhance safety, situational awareness and efficiency, a strict procedure was maintained during the execution of the experiments. First the safety pilot would trim the aircraft for the desired airspeed in horizontal flight. At the same time the flight test engineer would select the desired controller configuration in the FBW computer. Conformation from both the safety pilot and flight test engineer would trigger the evaluation pilot to enable the FBW system and start the experiment. Initialization was executed with "hands-of-stick" to prevent undesirable initial control inputs.

The primary flight display was slightly modified with the addition of a marker displaying the commanded roll angle ϕ_{com}. This to enhance the situational awareness of the evaluation pilot.

2. Results

Before each flight, extensive ground testing was performed to validate proper functioning in interaction of the experimental controller with the aircraft systems. The first flight test was mainly used for familiarization due to limited experience with the test platform. Some issues were experienced due to hysteresis of the sidestick. Due to initialization problems with the actuator models, it turned out to be more effective to use measured control deflections. The FBW input-output gain K_{fbw} proofed to be smaller than estimated, resulting in a slight reduction in control effectiveness with a more conservative response as a result. As expected, the INDI control signals turned out to be noisier compared to the NDI control signals.

The response at 200 KIAS and 240 KIAS was similar albeit the latter airspeed proofed to be too close to the never-exceed-speed of the aircraft and some of the experiments had to be aborted prematurely. In the preceding experiments the airspeed was reduced to 220 KIAS. The conservative setup resulted in an overall slower response as expected. Deflection limiting did not have a perceivable effect on the pitch response as the maximum deflection changes were below the 1° limit value.

The authority of the FBW system proofed to be limited in the pitch channel with maximum pitch rates below 1°/s. No satisfactory pitch tracking could initially be achieved, with moderate pitch rate commands often resulting in large overshoots and excitation of the phugoid mode of the aircraft. The overshoot tendency was caused by the large difference between the pitch rate commanded by the pilot $\dot{\theta}_{com}$ and subsequent aircraft response. When the evaluation pilot aimed for a certain pitch attitude, command was withdrawn as soon as the aircraft reached the desired pitch attitude. However, the commanded pitch attitude θ_{com} is obtained via integration of $\dot{\theta}_{com}$ and does not take into account possible offsets between commanded and actual pitch rate. As a result, the integrated pilot rate command would exceed the desired pitch attitude causing a perceived overshoot. As no marker for θ_{com} was available on the primary flight display, the pilot had no knowledge about the commanded pitch attitude making accurate pitch attitude captures difficult to execute. Due to limited repeatability options, a successful series of pitch attitude captures could not be realized. The remainder of the discussion will therefore be limited to the lateral tracking task only.

In Figure 10 the lateral tracking response is visualized for a typical part of the flight with various roll attitude captures. Both controller types displayed favorable tracking behavior and were able to follow the imposed dynamics with small overshoot values of 1°. Notice the "jumps" in the roll command signal around 4052 s and 4070 s for the INDI controller, and around 2349 s and 2370 s for the NDI controller. At these instances the roll angle exceeded ±27° and the command module subsequently switches from RCAH to AC. The reference model ensures a smooth transition between these control laws as seen in the reference signal. AC is governed up to the roll angle limit of ±31°. Despite the higher control authority compared to the pitch channel, moderate roll commands still resulted in actuator saturation.

In Figure 11 the lateral tracking response for several roll attitude captures is visualized with PCH activated. The major difference compared to the response of the non-hedging controller is the slower response of the reference signal and the tight coupling with the aircraft response. The reference signal does not fall outside the performance envelope of the aircraft. PCH significantly reduces the saturation effect on the aileron deflections δ_a. Howhever, more noise is propagated through the control laws. The steady-state offset between command and reference/response roll angle is the result of a steady difference between the commanded and actual control deflection due to the mismatch of K_{fbw}. PCH adapts the reference model to this difference resulting in a steady error between the command and reference signal. This behavior can be avoided using actuator models instead of measured deflections.

The simulated engine failures were handled well by both the INDI and NDI controller, see Figure 12. Some oscillations were observed in the roll channel for NDI, the use of the conservative setup might have initiated this behavior. A more aggressive engine failure was simulated with the INDI controller in the loop, with an additional reversing of the differential thrust at 4550 s. The controller compensated for the asymmetric thrust in a smooth and jolt free manner. The evaluation pilot was able to perform small roll maneuvers without issues.

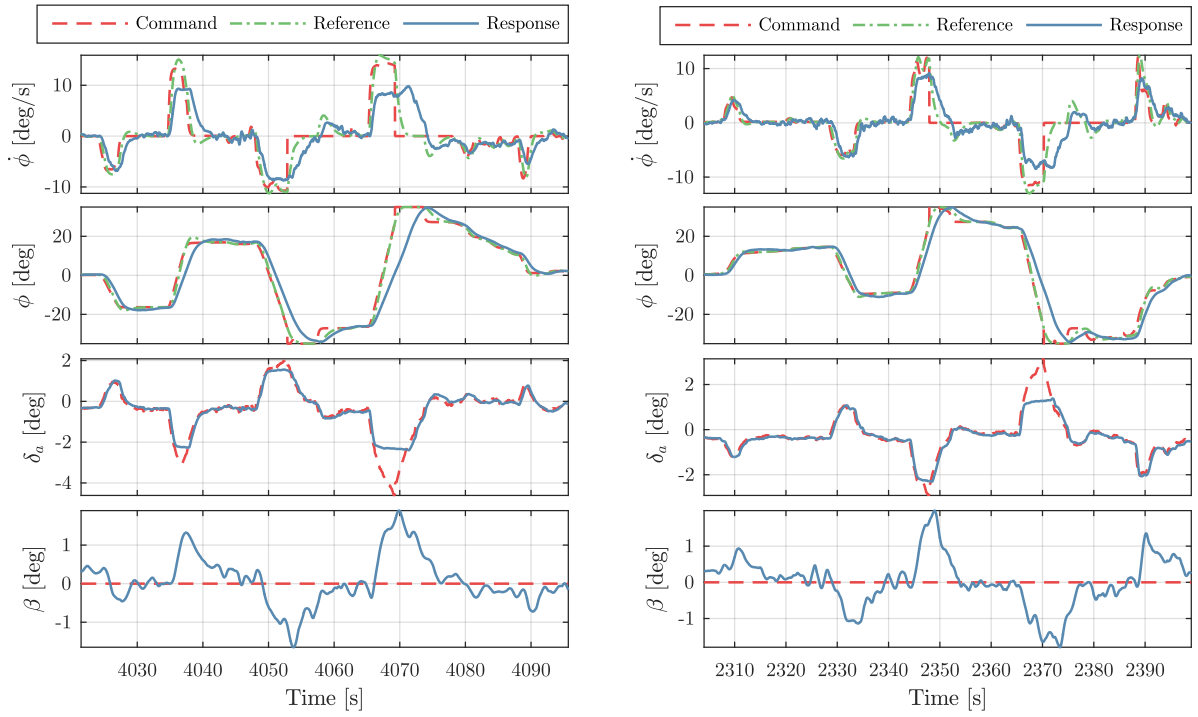

(a) INDI (nominal setup)

(b) NDI (nominal setup)

Figure 10. Lateral tracking response roll attitude captures (200 KIAS FL150)

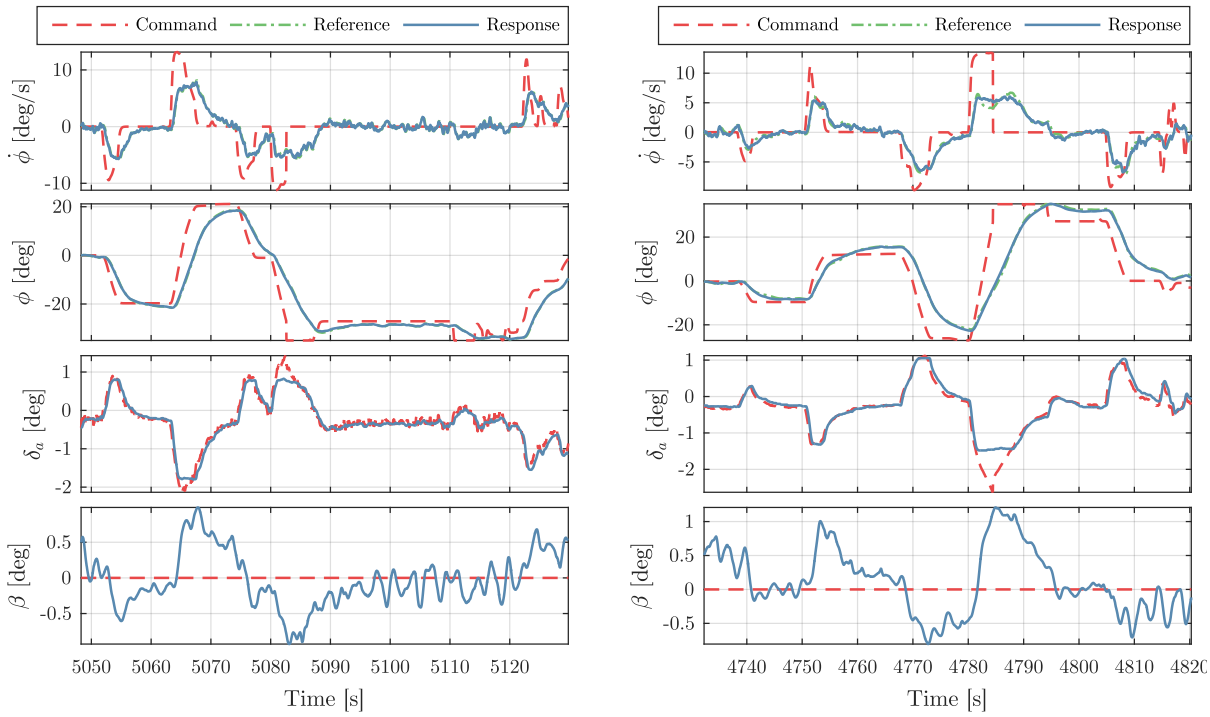

(a) INDI (nominal setup)

(b) NDI (nominal setup)

Figure 11. Lateral tracking response roll attitude captures with PCH activated (200 KIAS FL150)

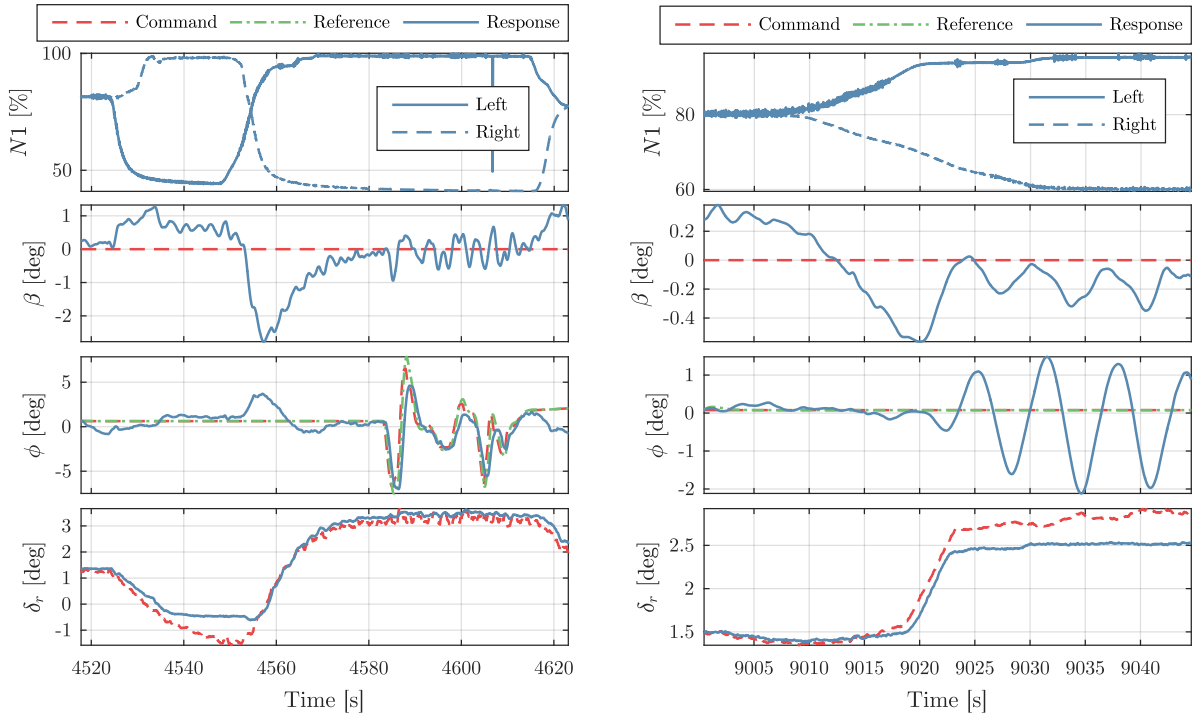

(a) INDI (nominal setup)

(b) NDI (conservative setup)

Figure 12. Lateral tracking response simulated engine failure (200 KIAS FL150)

VI. Conclusion

This paper presented the design and validation of manual attitude control functions based on Incremental Nonlinear Dynamic Inversion (INDI) for a Cessna Citation II experimental aircraft, covering control structure design, application of INDI, design optimization, robustness analyses, software implementation, ground and flight testing. For comparison, also control laws based on classical Nonlinear Dynamic Inversion (NDI) were implemented and flown.

Extensive robustness analysis revealed that INDI provides a highly robust control solution with respect to model uncertainties compared to classical NDI, even in presence of unsynchronized angular acceleration and control deflection feedback. Under the combined effect of actuators, sensors, filters, wind disturbance and model and synchronization mismatches, INDI provided a better compromise between command response, disturbance rejection and robustness compared to classical NDI.

Qualitative flight test with the INDI and NDI attitude control laws were performed on the Cessna Citation II PH-LAB, marking the first successful demonstration of INDI on a CS-25 certified aircraft. In presence of limited authority, uncertain control effectiveness and simulated engine failures, the system dynamics were canceled well by both controllers. The imposed reference dynamics were accurately tracked with nominal control effectiveness parameters, validating the simulation results.

Pseudo Control Hedging (PCH) proofed to be a valuable addition to INDI in reducing the effects of actuator saturation. To limit additional noise and uncertainties in the closed-loop system, activation of PCH only upon actuator saturation is suggested for future applications. This can for example be achieved via a simple algorithm that detects an offset between commanded and actual control deflection. For control deflection feedback, models might be preferred over measurements in certain cases as PCH adapts the reference model to any bias between commanded and actual control deflection.

A point of attention are the relatively high noise levels in the control signals of INDI. This may cause excessive wear on the actuators. Fortunately, low-noise angular acceleration measurement or estimation methods are already available in the form of angular accelerometers, linear accelerometer pairs or complimentary filters.[32]

The PH-LAB and the experimental on-board infrastructure proofed to be a reliable and efficient platform

for the testing of advanced flight control laws. For future applications it is advised that the servo motor position controller is replaced with a control law that uses the control surface deflections as feedback. This will mitigate issues with varying control effectiveness. Reducing the (electronic) torque limitations on the servo motors would also be a valuable addition to improve control authority.

Acknowledgments

The authors would like to thank the following persons from Delft University of Technology: Alexander in 't Veld, Ferdinand Postema, Hans Mulder, Menno Klaassen and Olaf Stroosma. Their support and guidance during the project is highly appreciated!

References

[1]Balas, G. J., "Flight control law design: An industry perspective," *European Journal of Control*, Vol. 9, No. 2-3, 2003, pp. 207–226.

[2]Walker, G. P. and Allen, D. A., "X-35B STOVL flight control law design and flying qualities," *Biennial International Powered Lift Conference and Exhibit*, 2002, pp. 5–7.

[3]Goupil, P., Boada-Bauxell, J., Marcos, A., Cortet, E., Kerr, M., and Costa, H., "AIRBUS efforts towards advanced real-time fault diagnosis and fault tolerant control," *IFAC Proceedings Volumes*, Vol. 47, No. 3, 2014, pp. 3471–3476.

[4]Goupil, P. and Marcos, A., "Advanced diagnosis for sustainable flight guidance and control: The European ADDSAFE project," Tech. rep., SAE technical paper, 2011.

[5]Enns, D., Bugajski, D., Hendrick, R., and Stein, G., "Dynamic inversion: an evolving methodology for flight control design," *International Journal of Control*, Vol. 59, No. 1, 1994, pp. 71–91.

[6]Lombaerts, T., Looye, G., Chu, Q., and Mulder, J., "Design and simulation of fault tolerant flight control based on a physical approach," *Aerospace Science and Technology*, Vol. 23, No. 1, 2012, pp. 151–171.

[7]Smith, P. R., "A Simplified Approach to Nonlinear Dynamic Inversion Based Flight Control," *AIAA Atmospheric Flight Mechanics Conference and Exhibit*, 1998, pp. 762–770.

[8]Smith, P. and Berry, A., "Flight test experience of a non-linear dynamic inversion control law on the VAAC Harrier," *Atmospheric Flight Mechanics Conference*, 2000, p. 3914.

[9]Bacon, B., Ostroff, A. J., and Joshi, S., "Reconfigurable NDI Controller Using Inertial Sensor Failure Detection & Isolation," *Aerospace and Electronic Systems, IEEE Transactions on*, Vol. 37, No. 4, 2001, pp. 1373–1383.

[10]Sieberling, S., Chu, Q. P., and Mulder, J. A., "Robust Flight Control Using Incremental Nonlinear Dynamic Inversion and Angular Acceleration Prediction," *Journal of Guidance, Control, and Dynamics*, Vol. 33, No. 6, 2010, pp. 1732–1742.

[11]Acquatella, P., Falkena, W., van Kampen, E.-J., and Chu, Q. P., "Robust nonlinear spacecraft attitude control using incremental nonlinear dynamic inversion," *AIAA Guidance, Navigation, and Control Conference*, 2012, pp. 1–20.

[12]Simplício, P., Pavel, M., Van Kampen, E., and Chu, Q., "An acceleration measurements-based approach for helicopter nonlinear flight control using Incremental Nonlinear Dynamic Inversion," *Control Engineering Practice*, Vol. 21, No. 8, 2013, pp. 1065–1077.

[13]Lu, P. and van Kampen, E.-J., "Active fault-tolerant control for quadrotors subjected to a complete rotor failure," *Intelligent Robots and Systems (IROS), 2015 IEEE/RSJ International Conference on*, IEEE, 2015, pp. 4698–4703.

[14]Smeur, E. J., Chu, Q., and de Croon, G. C., "Adaptive incremental nonlinear dynamic inversion for attitude control of micro air vehicles," *Journal of Guidance, Control, and Dynamics*, 2015.

[15]Vlaar, C., *Incremental Nonlinear Dynamic Inversion Flight Control: Implementation and Flight Test on a Fixed Wing UAV*, Master's thesis, Delft University of Technology, Faculty of Aerospace Engineering, 2014.

[16]van Ekeren, W., Looye, G., Kuchar, R. O., Chu, Q. P., and Van Kampen, E.-J., "Design, Implementation and Flight-Tests of Incremental Nonlinear Flight Control Methods," *2018 AIAA Guidance, Navigation, and Control Conference*, 2018, p. 0384.

[17]Zaal, P., Pool, D., Veld, A. I. t., Postema, F., Mulder, M., Paassen, M. V., and Mulder, J., "Design and Certification of a Fly-by-Wire System with Minimal Impact on the Original Flight Controls," *AIAA Guidance, Navigation, and Control Conference*, Oct 2009.

[18]Lombaerts, T. and Looye, G., "Design and flight testing of manual nonlinear flight control laws," *AIAA Guidance, Navigation, and Control Conference*, Aug 2011.

[19]Johnson, E. N. and Calise, A. J., "Pseudo-control hedging: A new method for adaptive control," *Advances in navigation guidance and control technology workshop*, 2000, pp. 1–2.

[20]Looye, G., Willemsen, D., Bauschar, J., and Moennich, W., "Flight testing robust autoland control laws," *AIAA Guidance, Navigation, and Control Conference and Exhibit*, Jun 2001.

[21]Lombaerts, T. and Looye, G., "Design and flight testing of nonlinear autoflight control laws," *AIAA Guidance, Navigation, and Control Conference*, 2012, p. 4982.

[22]Lombaerts, T. and Looye, G., "Design and Flight Testing of Nonlinear Autoflight Control Laws Incorporating Direct Lift Control," *Advances in Aerospace Guidance, Navigation and Control*, 2013, pp. 549568.

[23]van Paassen, M. M., Stroosma, O., and Delatour, J., "DUECA - Data-Driven Activation in Distributed Real-Time Computation," *Proceedings of the AIAA Modeling and Simulation Technologies Conference and Exhibit, Denver (CO)*, No. AIAA-2000-4503, Aug. 2000.

[24]Mulder, M., Lubbers, B., Zaal, P., Paassen, M. V., and Mulder, J., "Aerodynamic Hinge Moment Coefficient Estimation Using Automatic Fly-by-Wire Control Inputs," *AIAA Modeling and Simulation Technologies Conference*, Oct 2009.

[25]van't Veld, R., Van Kampen, E.-J., and Chu, Q. P., "Stability and Robustness Analysis and Improvements for Incremental Nonlinear Dynamic Inversion Control," *2018 AIAA Guidance, Navigation, and Control Conference*, 2018, p. 1127.

[26]Linden, C. A. A. M. v. d., *DASMAT-Delft University aircraft simulation model and analysis tool: a Matlab/Simulink environment for flight dynamics and control analysis*, Delft University Press, 1998.

[27]van den Hoek, M. A., de Visser, C. C., and Pool, D. M., "Identification of a Cessna Citation II Model Based on Flight Test Data," *Proceedings of the 4th CEAS Specialist Conference on Guidance, Navigation & Control, Warsaw, Poland*, 2017.

[28]de Visser, C. C., *Global Nonlinear Model Identification with Multivariate Splines*, Phd thesis, Delft University of Technology, Faculty of Aerospace Engineering, June 2011.

[29]Looye, G. and Joos, H.-D., "Design of robust dynamic inversion control laws using multi-objective optimization," *Proceedings of the AIAA Guidance, Navigation and Control Conference*, 2001.

[30]Joos, H.-D., "A methodology for multi-objective design assessment and flight control synthesis tuning," *Aerospace Science and Technology*, Vol. 3, No. 3, 1999, pp. 161–176.

[31]Bellmann, T., Heindl, J., Hellerer, M., Kuchar, R., Sharma, K., and Hirzinger, G., "The dlr robot motion simulator part i: Design and setup," *Robotics and Automation (ICRA), 2011 IEEE International Conference on*, IEEE, 2011, pp. 4694–4701.

[32]Grondman, F., *Dynamic Inversion Flight Control Law Design for Fixed-Wing Aircraft: Design and Flight Testing of Incremental Nonlinear Dynamic Inversion based Control Laws for a Passenger Aicraft*, Master's thesis, Delft University of Technology, Faculty of Aerospace Engineering, 2018.

Part II

Preliminary studies

Chapter 2

(I)NDI theory

This chapter provides a concise review of the theory of Nonlinear Dynamic Inversion (Section 2-1), Incremental Nonlinear Dynamic Inversion (Section 2-2) and Pseudo Control Hedging (Section 2-3). Note that the symbolic derivation approach is in part inspired by Looye [43]. For a more detailed review readers are referred to Slotine [60] or Enns et al. [19] for Nonlinear Dynamic Inversion, Chen and Zhang [14] or Sieberling et al. [58] for Incremental Nonlinear Dynamic Inversion and Johnson and Calise [30] for Pseudo Control Hedging.

2-1 Nonlinear Dynamic Inversion

The general idea of NDI is to compensate the nonlinear system dynamics by means of feedback of the inverse model equations such that the closed loop system appears in a linear form. The desired closed loop response can then be imposed via conventional linear controllers [60, 19].

It is assumed that the model of the nonlinear system has the following control-affine form:

$$\dot{\boldsymbol{x}} = \boldsymbol{f}(\boldsymbol{x}, \boldsymbol{p}) + \boldsymbol{G}(\boldsymbol{x}, \boldsymbol{p})\boldsymbol{u} \tag{2-1}$$

$$\boldsymbol{y} = \boldsymbol{h}(\boldsymbol{x}, \boldsymbol{p}) \tag{2-2}$$

$$\boldsymbol{y}_o = \boldsymbol{h}_o(\boldsymbol{x}, \boldsymbol{p}) \tag{2-3}$$

Where $\boldsymbol{x} \in \mathbb{R}^n$ is the state vector, $\boldsymbol{u} \in \mathbb{R}^m$ the input vector containing only inputs that may be used by the controller, $\boldsymbol{y} \in \mathbb{R}^m$ the output vector containing the outputs to be controlled (i.e. control variables), $\boldsymbol{y}_o$ contains any other outputs of the system, $\boldsymbol{f}$, $\boldsymbol{h}$ and $\boldsymbol{h}_o$ are smooth vector fields, $\boldsymbol{G} \in \mathbb{R}^{n \times m}$ is a matrix with columns of smooth vector fields and $\boldsymbol{p}$ contains the model parameters.

Differentiation of the output equation $\boldsymbol{h}$ results in:

$$\dot{\boldsymbol{y}} = \frac{\partial \boldsymbol{h}(\boldsymbol{x},\boldsymbol{p})}{\partial \boldsymbol{x}} \frac{\mathrm{d}\boldsymbol{x}}{\mathrm{d}t} = \nabla \boldsymbol{h}(\boldsymbol{x},\boldsymbol{p})\big(\boldsymbol{f}(\boldsymbol{x},\boldsymbol{p}) + \boldsymbol{G}(\boldsymbol{x},\boldsymbol{p})\boldsymbol{u}\big) = L_{\boldsymbol{f}}\boldsymbol{h}(\boldsymbol{x},\boldsymbol{p}) + L_{\boldsymbol{G}}\boldsymbol{h}(\boldsymbol{x},\boldsymbol{p})\boldsymbol{u} \tag{2-4}$$

Where $L_{\boldsymbol{f}}\boldsymbol{h}$ and $L_{\boldsymbol{G}}\boldsymbol{h}$ are the first-order Lie derivatives along $\boldsymbol{f}$ and $\boldsymbol{G}$, respectively. It is assumed that $L_{\boldsymbol{G}}\boldsymbol{h}$ is non-singular and that each output has an order of 1 relative to at minimum one of the inputs (i.e. $L_{\boldsymbol{G}}\boldsymbol{h} \neq 0$). In this case NDI can be applied to Equation (2-4) [60, 19]. Defining the virtual control input as $\boldsymbol{\nu} = \dot{\boldsymbol{y}}$ and inverting Equation (2-4), the following control law is obtained:

$$\boldsymbol{u} = \big(L_{\boldsymbol{G}}\boldsymbol{h}(\hat{\boldsymbol{x}},\boldsymbol{p}^*)\big)^{-1}\big(\boldsymbol{\nu} - L_{\boldsymbol{f}}\boldsymbol{h}(\hat{\boldsymbol{x}},\boldsymbol{p}^*)\big) \tag{2-5}$$

The vectors $\hat{\boldsymbol{x}}$ and $\boldsymbol{p}^*$ contain the computed or estimated states from $\boldsymbol{y}$ and $\boldsymbol{y}_o$, and the assumed values for the model parameters, respectively. Substituting the control law (Equation (2-5)) into Equation (2-4):

$$\dot{\boldsymbol{y}} = L_{\boldsymbol{f}}\boldsymbol{h}(\boldsymbol{x},\boldsymbol{p}) + L_{\boldsymbol{G}}\boldsymbol{h}(\boldsymbol{x},\boldsymbol{p})\Big(\big(L_{\boldsymbol{G}}\boldsymbol{h}(\hat{\boldsymbol{x}},\boldsymbol{p}^*)\big)^{-1}\big(\boldsymbol{\nu} - L_{\boldsymbol{f}}\boldsymbol{h}(\hat{\boldsymbol{x}},\boldsymbol{p}^*)\big)\Big) \tag{2-6}$$

When $\boldsymbol{x}$ and $\boldsymbol{p}$ are exactly known ($\hat{\boldsymbol{x}} = \boldsymbol{x}$ and $\boldsymbol{p}^* = \boldsymbol{p}$), Equation (2-6) reduces to:

$$\dot{\boldsymbol{y}} = \boldsymbol{\nu} \quad \Leftrightarrow \quad \boldsymbol{y}(t) = \int_0^t \boldsymbol{\nu}(\tau)\mathrm{d}\tau \tag{2-7}$$

The resulting control law linearises the system dynamics, reducing the input-output response to a set of integrators. Note that for stability, the relation between $\boldsymbol{y}$ and $\boldsymbol{u}$ has to be minimum phase [19].

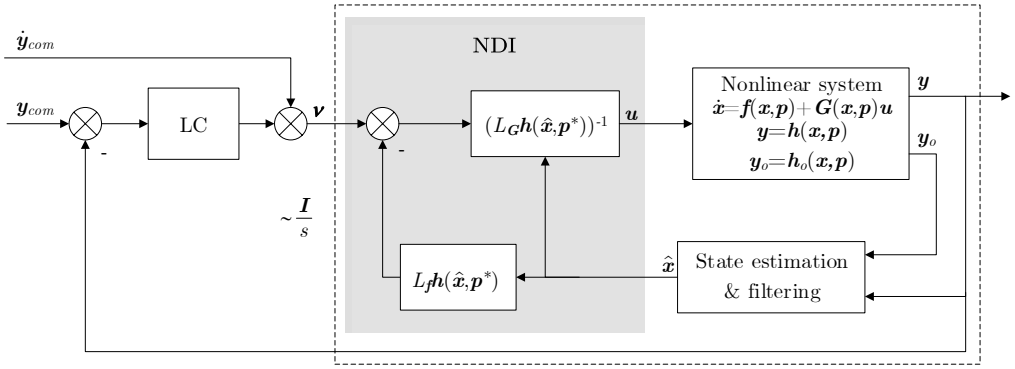

Figure 2-1: Closed loop system Nonlinear Dynamic Inversion

2-2 Incremental Nonlinear Dynamic Inversion

The incremental form of NDI computes the control increment with respect to the condition of the system one incremental time instance in the past. The fundamental difference with

classical NDI is that the control-independent part of the model equations is replaced by state derivative feedback, resulting in a more robust control solution with respect to model mismatch ($\boldsymbol{p}^* \neq \boldsymbol{p}$) [14, 58].

As a first step, the nonlinear system in Equation (2-1) is approximated by a first-order Taylor series expansion around the current point in time '0':

$$\dot{\boldsymbol{x}} \approx \dot{\boldsymbol{x}}_0 + \frac{\partial}{\partial \boldsymbol{x}}\big(\boldsymbol{f}(\boldsymbol{x},\boldsymbol{p}) + \boldsymbol{G}(\boldsymbol{x},\boldsymbol{p})\boldsymbol{u}\big)\Big|_{\substack{\boldsymbol{x}=\boldsymbol{x}_0 \\ \boldsymbol{u}=\boldsymbol{u}_0}} \underbrace{(\boldsymbol{x}-\boldsymbol{x}_0)}_{\Delta \boldsymbol{x}} + \frac{\partial}{\partial \boldsymbol{u}}\big(\boldsymbol{f}(\boldsymbol{x},\boldsymbol{p}) + \boldsymbol{G}(\boldsymbol{x},\boldsymbol{p})\boldsymbol{u}\big)\Big|_{\substack{\boldsymbol{x}=\boldsymbol{x}_0 \\ \boldsymbol{u}=\boldsymbol{u}_0}} \underbrace{(\boldsymbol{u}-\boldsymbol{u}_0)}_{\Delta \boldsymbol{u}} \tag{2-8}$$

The variables with subscript '0' should be interpreted as an incremental time instance before the equivalent variables without subscript. It assumed that the time-scale separation principle holds for Equation (2-8). For very small time increments and instantaneous control effectors, the change in input is much faster than the change in state (i.e. $\boldsymbol{x}-\boldsymbol{x}_0 \approx 0$ while $\boldsymbol{u}-\boldsymbol{u}_0 \neq 0$). Assuming $\boldsymbol{x}-\boldsymbol{x}_0 = 0$, Equation (2-8) reduces to:

$$\dot{\boldsymbol{x}} \approx \dot{\boldsymbol{x}}_0 + \boldsymbol{G}(\boldsymbol{x}_0,\boldsymbol{p})\Delta \boldsymbol{u} \tag{2-9}$$

It is assumed that $\boldsymbol{G}$ is non-singular and that $\boldsymbol{y} = \boldsymbol{x}$. In this case INDI can be applied to Equation (2-9) [14, 58]. Defining the virtual control input as $\boldsymbol{\nu} = \dot{\boldsymbol{x}}$ and inverting Equation (2-9), the following control law is obtained:

$$\Delta \boldsymbol{u} = \boldsymbol{G}^{-1}(\hat{\boldsymbol{x}}_0,\boldsymbol{p}^*)(\boldsymbol{\nu} - \hat{\dot{\boldsymbol{x}}}_0) \tag{2-10}$$

The vector $\hat{\dot{\boldsymbol{x}}}_0$ contains the state derivatives computed or estimated from $\boldsymbol{y}$ or $\boldsymbol{y}_o$, respectively. Substituting the control law (Equation (2-10)) into Equation (2-9):

$$\dot{\boldsymbol{x}} \approx \dot{\boldsymbol{x}}_0 + \boldsymbol{G}(\boldsymbol{x}_0,\boldsymbol{p})\big(\boldsymbol{G}^{-1}(\hat{\boldsymbol{x}}_0,\boldsymbol{p}^*)(\boldsymbol{\nu} - \hat{\dot{\boldsymbol{x}}}_0)\big) \tag{2-11}$$

In the ideal case ($\hat{\boldsymbol{x}}_0 = \boldsymbol{x}_0$, $\hat{\dot{\boldsymbol{x}}}_0 = \dot{\boldsymbol{x}}_0$ and $\boldsymbol{p}^* = \boldsymbol{p}$), the input-output response approximates to a set of integrators:

$$\dot{\boldsymbol{x}} \approx \boldsymbol{\nu} \quad \Leftrightarrow \quad \boldsymbol{x}(t) \approx \int_0^t \boldsymbol{\nu}(\tau)\mathrm{d}\tau \tag{2-12}$$

The total input $\boldsymbol{u}$ is obtained by adding the current input $\boldsymbol{u}_0$ to the control increment $\Delta \boldsymbol{u}$. Note that the control law should be sampled with a sufficiently high frequency and requires synchronization between $\boldsymbol{u}_0$ and $\dot{\boldsymbol{x}}_0$ [59, 61].

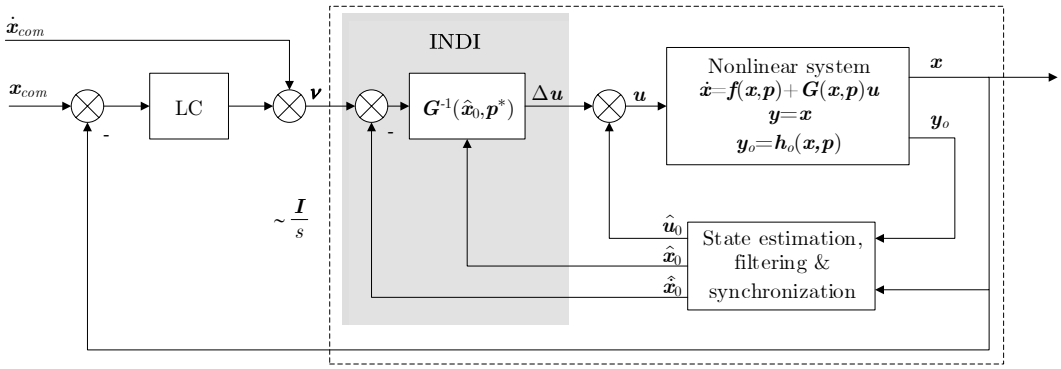

Figure 2-2: Closed loop system Incremental Nonlinear Dynamic Inversion

2-3 Pseudo Control Hedging

(I)NDI inverts the dynamics of the nonlinear system but not of the input. Actuator dynamics are usually considered time-scale separated from the aircraft dynamics. Saturation caused by the physical limits on actuator position and rate may howhever result in invertibility and controllability issues, violating conditions necessary for dynamic inversion.

Pseudo Control Hedging (PCH) aims to compensate for actuator dynamics by means of modification of the reference model dynamics [30]. PCH scales down (hedges) the reference model signal by an estimate of the response deficiency of the system $\boldsymbol{\nu}_h$, effectively hiding the actuator dynamics from the error dynamics. The virtual control hedge $\boldsymbol{\nu}_h$ is computed by subtracting the commanded virtual control $\boldsymbol{\nu}$ from the actual virtual control $\hat{\boldsymbol{\nu}}$:

$$\boldsymbol{\nu}_h = \boldsymbol{\nu} - \hat{\boldsymbol{\nu}} \tag{2-13}$$

This concept can be applied to the (I)NDI control laws formulated in Equations (2-5) and (2-10). Due to actuator limitations, the commanded control deflections $\boldsymbol{u}$ are not identical to the actual control deflections $\boldsymbol{\delta}$. Rearranging Equations (2-5) and (2-10) for $\boldsymbol{\nu}$, $\hat{\boldsymbol{\nu}}$ is obtained by inserting $\boldsymbol{\delta}$ for $\boldsymbol{u}$. For NDI the virtual control hedge is then obtained as follows:

$$\boldsymbol{\nu}_h = L_{\boldsymbol{f}}\boldsymbol{h}(\boldsymbol{x},\boldsymbol{p}) + L_{\boldsymbol{G}}\boldsymbol{h}(\boldsymbol{x},\boldsymbol{p})\boldsymbol{u} - \left(L_{\boldsymbol{f}}\boldsymbol{h}(\boldsymbol{x},\boldsymbol{p}) + L_{\boldsymbol{G}}\boldsymbol{h}(\boldsymbol{x},\boldsymbol{p})\boldsymbol{\delta}\right) \tag{2-14}$$

$$\boldsymbol{\nu}_h = L_{\boldsymbol{G}}\boldsymbol{h}(\hat{\boldsymbol{x}},\boldsymbol{p}^*)(\boldsymbol{u} - \hat{\boldsymbol{\delta}}) \tag{2-15}$$

A similar result is obtained for INDI [59]:

$$\boldsymbol{\nu}_h = \dot{\boldsymbol{x}}_0 + \boldsymbol{G}(\boldsymbol{x}_0,\boldsymbol{p})(\boldsymbol{u} - \boldsymbol{\delta}_0) - \left(\dot{\boldsymbol{x}}_0 + \boldsymbol{G}(\boldsymbol{x}_0,\boldsymbol{p})(\boldsymbol{\delta} - \boldsymbol{\delta}_0)\right) \tag{2-16}$$

$$\boldsymbol{\nu}_h = \boldsymbol{G}(\hat{\boldsymbol{x}}_0,\boldsymbol{p}^*)(\boldsymbol{u} - \hat{\boldsymbol{\delta}}) \tag{2-17}$$

Note that $\boldsymbol{\nu}_h$ only depends on the control effectiveness and that $\boldsymbol{\delta}$ is assumed observable. For a conventional first-order reference model, the hedged output is obtained as follows:

$$\boldsymbol{x}_{ref} = \frac{1}{s}\left(\boldsymbol{K}_{ref}(\boldsymbol{x}_{com} - \boldsymbol{x}_{ref}) - \boldsymbol{\nu}_h\right) \tag{2-18}$$

Where $\boldsymbol{K}_{ref}$ is the diagonal gain matrix. Note that if $\hat{\boldsymbol{x}}_0 \neq \boldsymbol{x}_0$, $\boldsymbol{p}^* \neq \boldsymbol{p}$ or $\hat{\boldsymbol{\delta}} \neq \boldsymbol{\delta}$, PCH will introduce additional uncertainties into the closed loop system.

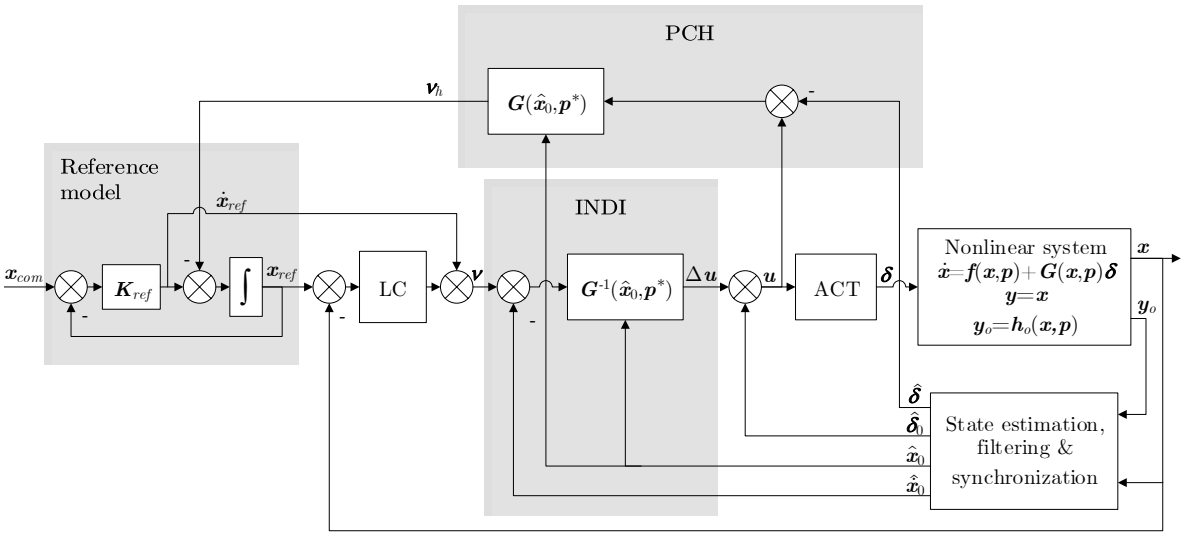

Figure 2-3: Closed loop system Incremental Nonlinear Dynamic Inversion with Pseudo Control Hedging

Chapter 3

(I)NDI implementation aspects

The application of (I)NDI is restricted to nonlinear systems under the assumptions made in Chapter 2. Some of these do however not fully hold in practice and may result in loss of performance within the control laws. The synthesis model for example will only have a finite accuracy but also subsystems such as actuators and sensors add dynamics to the overall system. The successful implementation of (I)NDI control laws depends to a significant degree on careful modeling and offline assessment of these effects.

This chapter will review the literature on (I)NDI for effects that violate the fundamental assumptions made for (I)NDI and have resulted in significant performance degradation within the control laws. Due to the practical nature of this research project, strategies proposed in literature that limit loss of performance due to these effects are of particular interest. In addition, INDI specific implementation aspects related to obtaining accurate angular accelerations and synchronous feedback signals will be discussed as well. A novel method based on the complimentary filtering technique to obtain accurate angular accelerations from angular rate measurements will be developed and proposed as alternative to conventional washout filters. Finally, an extensive mathematical analysis will be performed on the influence of actuator and sensor dynamics on the closed loop response of INDI.

The following effects will be reviewed: model mismatches (Section 3-1), actuator dynamics and saturation (Section 3-2), sensor deviations (Section 3-3), flight control computer sampling (Section 3-4) and atmospheric disturbances (Section 3-5). In Section 3-6 techniques are presented to obtain accurate angular acceleration observations. Section 3-7 discusses the issue of synchronization of feedback signals. Finally, some conclusions and recommendations will be provided in Section 3-8

3-1 Model mismatches

The NDI control law derived in Chapter 2 assumes that the model of the nonlinear system is exactly known. In practice there is always a degree of uncertainty attached to synthesis models.

Miller [47] remarked that a small model deviation in the pitch control effectiveness resulted in a perceivable change in the pitch handling qualities during a flight test of a baseline NDI controller. Robustness to these model uncertainties is typically addressed in the systhesis of the linear controller parameters using for example μ-synthesis, H_∞ loop shaping [2] or multi-model multi-objective optimization [41].

More serious model mismatches due to for example system failures require however a form of online control law adaptation. Howhever, flight tests of NDI controllers with adaptive elements reveal that robustness to larger model mismatch is still not guaranteed. In [10] a simulated failure resulted in increased Pilot Induced Oscillation (PIO) tendency for a NDI controller with Neural Networks. Similarly in [9], reduced controller performance was observed when the vehicle dynamics were artificially destabilized.

Despite the reduced model dependency of INDI, mismatches in the control-dependent part of the model may still result in performance loss. Smith and Berry [62] observed that increasing or decreasing control effectiveness caused significant changes in the aircraft behavior during a flight test of pitch rate controller based on INDI. Smeur et al. [61] demonstrated in a flight test that INDI with online control effectiveness estimation can successfully reject a change in mass distribution.

3-2 Actuator dynamics and saturation

The dynamic inversion control laws are derived without any consideration to the input behavior, represented by the actuators. Fundamental to INDI is the assumption of instantanious control effectors, see Section 3-7 for a mathematical analysis of the effect of actuator dynamics on the closed loop response of INDI. The dynamic response of actuators is generally very fast in comparison to the dynamics of the vehicle. Nevertheless, at high speed and for large aircraft in general, the actuators must provide large hinge moments for control hence cannot be considered instantaneous [36]. Although NDI has proven to cope with non-instantaneous control effectors, actuators will in general increase the natural frequency and reduce the damping of the closed loop response [47]. This behavior is due to lag between the commanded control deflection and the actual control deflection resulting in overshoot tendencies of the controlled variables. The input commands are typically tailored by command filters or reference models. These generate reference signals that can be effectively tracked without exceeding the aircraft capabilities. By detuning the natural frequencies of these models, the effect of actuator lag can be effectively accounted for [47].

A secondary issue observed due to assumed ideal actuators is saturation. This is caused by the physical limits on position and rate of the control effectors. When the system runs into these limits the affinity in control assumption does no longer hold, violating conditions necessary for dynamic inversion. Several attempts have been made to limit the effects of actuator saturation. A seamingly straightforward solution is to scale down the command inputs to values achievable by the aircraft. This can for example be achieved by including (rate) limiters in the command path. This approach may howhever result in a conservative design as the aircraft limit performance varies with flight condition. In [53] a control allocation algorithm was used in combination with INDI that adaptively penalizes the control effectors as they approach their saturation limits. Howhever, this method cannot guaruantee that saturation limits will not be violated and its adaptive nature might limit certifiability [28].

A solution that has been proven effective is Pseudo Control Hedging (PCH) [30]. This technique aims to compensate for actuator limitations by means of modification of the reference model dynamics. PCH scales down (hedges) the reference model signal by an estimate of the response deficiency of the system, effectively hiding the actuator dynamics from the error dynamics. This technique has an advantage over other adaptation methods in terms of certifiability, as the adaptation is made in a reference model rather than directly in an adaptive control law. PCH is effective in reducing the duration and magnitude of actuator saturation but cannot fully elimanate it [35]. PCH has been succesfully flight tested in combination with NDI [37, 38] and has been adapted for INDI as well [59, 68]. In [68] PCH was shown effective in reducing oscillatory tracking behavior in combination with INDI and was also successfully used as anti-windup technique for the outer linear controllers.

3-3 Sensor deviations

Dynamic inversion relies on full state feedback and assumes ideal sensor measurements. Modern passenger aircraft are equipped with various inertial and air data sensors allowing straightforward calculation of the aircraft states. Sensor accuracy is nevertheless limited due to various (physical) processes resulting in systematic or random measurement errors [34, 46]. The quality of measurement is in particular important for the control variables [49].

Delay and lag

Time delays and phase lags have been responsible for setbacks in many recently developed flight control systems [49]. A notable example is the Lockheed Martin F-35 Lightning II, where large time delays in the NDI based control system resulted in Pilot Induces Oscillations (PIO) [71]. Also Burken et al. [11] reported that even small delays within the control system can result in significantly degraded closed loop performance. Vlaar [69] noted that differences in time delay between angular acceleration and control deflection feedback are detrimental to INDI controller performance. This behaviour was also observed in other research on INDI [58, 61, 68]. See Section 3-7 for a mathematical analysis of the effect of sensor dynamics on the closed loop response of INDI.

Noise

Sensor noise within feedback signals will propagate through the control laws without further processing. In [38] measurement noise in feedback signals was responsible for a serious setback in the development of an autoflight NDI controller. Flight testing could only be continued after a partial redesign. Flight test conducted by Smith and Berry [62] already revealed that INDI is sensitive to measurement noise in the angular acceleration feedback. This issue was confirmed in simulation based research as well [3, 21, 68]. In general, sensor noise can be reduced via filtering at the expense of the dynamic behavior of the sensor.

Bias

Systematic biases in sensor measurements may result in performance degradation within (I)NDI controllers. In [29] it was reported that biases in feedback measurements contributed to tracking errors within a NDI controller with Neural Networks during flight test. Measurement bias has also been included in various simulation based research on INDI [3, 21, 1, 68]. Bacon et al. [3] already reported that uncertainties in the actuator feedback accumulate and

could drive the control into saturation. Van 't Veld [68] noted that biased control deflection measurements result in steady-state tracking errors within INDI controllers. Steady-state errors within the control variables can be compensated for using outer linear controllers with integral action.

Quantization errors

Quantization errors are the result of discrezitation. All sensor measurements have to be discretized in order to be used by the digital flight control system. In [42], problems were reported due to quantized measurements during the development of a NDI autoland controller. These effects were not included in the simulation model. Similarly, in [29] performance degradation due to quantized measurements was observed during flight testing of a NDI controller with Neural Networks. In [37, 38, 39] quantization errors were applied on some of the feedback signals in the simulation model. Howhever, no further remarks were made about the effect on the control performance. Note that similar errors arise due to the limited physical resolution of the sensor. The lower resolution of the two should therefore be included in the simulation model.

3-4 Flight control computer sampling

For the derivation of the incremental control law, very small time increments are assumed. This implies that the control law to be implemented on the flight control computer should be sampled with a sufficiently high frequency. Low sampling frequecies have shown to degrade the control performance to a significant degree [59, 68, 66]. In [59] performance degradation was observed below sampling frequencies of 60 Hz. However, no issues where reported by Vlaar [69] who succesfully flight tested INDI based controllers running at 50 Hz. The effect of sampling frequency on the closed loop stability of discrete-time INDI was analyzed in detail in the work of Van 't Veld [68]. Sampling frequencies above 50 Hz provided a large stable region regarding variation in inherent system stability, linear controller gain, actuator bandwidth and control effectiveness uncertainty. An additional effect of the discrete nature of digital flight control systems is that the input response will be under influence of sampling, transport and computational delays. As already discussed, these can severely degrade closed loop performance or even cause instability.

3-5 Atmospheric disturbances

Wind and turbulence are two phenomena that can result in significant performance degradation within (I)NDI controllers. In [29] atmospheric disturbances were reported to negatively affect controller performance during a flight test of a NDI controller with Neural Networks. These effects were not included in the simulation model. Schierman et al. [57] commented that despite rigorous offline analysis, the controller using inner loop NDI was not able to cope with severe wind and turbulence conditions encountered during the flight test. In [42] performance degradation was observed due to high levels of turbulence during flight testing of an autoland NDI controller. Similar observations were made for INDI, Van Ekeren [66] remarked that increased tracking errors in flight tests compared to simulations could be in part attributed to turbulence.

Offline assessment of atmospheric disturbances using appropriate models is an integral part of successful flight control design [49]. In [37, 38, 39] wind and turbulence effects were offline assessed in the development of various controllers with inner-loop NDI. These proved to effectively attenuate atmospheric disturbances during flight tests. A point of attention is the control activity under turbulence [43]. Air data sensors pick up atmospheric turbulences that will propagate through the control laws resulting in high control activity. Air data measurements therefore need to be complemented with inertial mixing [49, 43].

3-6 Angular acceleration estimation

The incremental control method requires accurate feedback of the derivatives of the states i.e. the angular accelerations for conventional inner-loop rate control. Angular accelerometers for use in aerospace applications do exist [46] but are not commonly found in passenger aircraft. Most research on INDI has relied on some form of estimation. Numerous techniques exist, this section will be limited to methods that have been successfully applied in combination with INDI. In addition, a novel method will be developed based on the complementary filtering technique. Finally, the use of pairs of linear accelerometers are proposed as an alternative to dedicated angular accelerometers.

Differentiation

A straightforward technique is differentiation of the angular rates, assuming these are available as measurement. Although this is a fairly common approach in industry [46], the differentation process amplifies sensor noise which would propagate through the control laws without further processing. It has been suggested in literature that actuators act as low-pass filters thereby alleviating noise related issues. Noisy control signals can however cause excessive wear on the actuators and may increase the likelihood of failure.

Low-pass filtering

To attenuate sensor noise, differentiation is often applied in combination with low-pass filtering. In [62] low-pass filtering was applied before and after differentiation, this setup was flight tested as well. The washout filter proposed by Bacon et al. [3] was successfully flight tested in combintion with INDI on fixed and rotary-wing UAVs [69, 61, 66]. Filtering will however introduce lag in the closed loop system degrading performance and may cause synchronization issues, see also Section 3-7.

Linear predictive filtering

An alternative approach was proposed by Sieberling et al. [58] who developed a linear predictive filter using feedback of the commanded and obtained angular rates of the system. This approach avoids the phase lag and noise related issues associated with filtering and differentiation. Nevertheless, this filter requires training and assumes that the error in the predicted angular accelerations is neglectable small. Furthermore, the results were obtained under certain assumptions that may not hold for passenger aircraft.

Complementary filtering

A filtering strategy that could potentially reduce the noise, phase shift and prediction errors of above described methods is complementary filtering. This technique is often used in

flight control industry to combine measurements with complementary frequency characteristics [46]. In its broadest sense, a complementary filter combines two or more filters that are the mathematical complement of one other (i.e. they sum to identity). For this application, a second-order complementary filter is suggested, see Figure 3-1

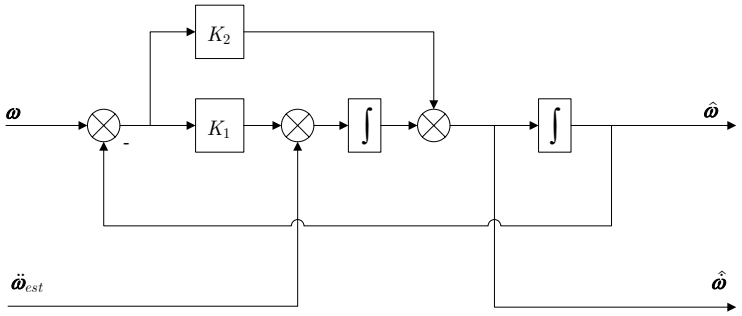

Figure 3-1: Second-order complementary filter structure

Where $\boldsymbol{\omega}$ are the measured angular rates acting as the low-pass signal. An estimation of the angular jerk $\ddot{\boldsymbol{\omega}}_{est}$ is used as high-pass signal. The latter is obtained from the incremental form of the Euler rotation equation, see Equation (7-6). Rearranging for $\dot{\boldsymbol{\omega}} - \dot{\boldsymbol{\omega}}_0$, the following relation is obtained:

$$\underbrace{\dot{\boldsymbol{\omega}} - \dot{\boldsymbol{\omega}}_0}_{\Delta\dot{\boldsymbol{\omega}}} \approx \boldsymbol{J}^{-1}(\boldsymbol{p})\boldsymbol{M}_{c_{\boldsymbol{\delta}}}(\boldsymbol{x}_0, \boldsymbol{p})\underbrace{(\boldsymbol{\delta} - \boldsymbol{\delta}_0)}_{\Delta\boldsymbol{\delta}} \tag{3-1}$$

Under the assumptions made for Equation (7-6), the angular jerk is obtained by dividing Equation (3-1) by the incremental time Δt:

$$\ddot{\boldsymbol{\omega}} \approx \boldsymbol{J}^{-1}(\boldsymbol{p})\boldsymbol{M}_{c_{\boldsymbol{\delta}}}(\boldsymbol{x}_0, \boldsymbol{p})\dot{\boldsymbol{\delta}} \tag{3-2}$$

Simulations were performed to assess the performance of the proposed complimentary filter using the high fidelity simulation setup developed in this thesis (see Chapters 6 and 7). The setup includes extensive actuator, sensor and filter models. The actuator rates $\dot{\boldsymbol{\delta}}$ are acquired via differentiation of the measured control deflections. Alternatively, these can also be estimated using actuator models. It should be stressed that $\boldsymbol{\omega}$ and $\ddot{\boldsymbol{\omega}}_{est}$ need to be time-synchronous. The outer loop of the closed loop setup (Figure 7-1) is slightly simplified, consisting of a first-order command filter ($\tau = 0.5$) and PI-controller with feedforward ($K_P = 7$, $K_I = 1$). To account for model mismatches a 10% error on the model parameters in $\boldsymbol{p}$ is selected. A conventional second-order washout filter ($\omega_{n_{fil}} = 20$ rad/s, $\zeta_{fil} = 1$) is used for comparison. Good results were obtained with filtering gains $K_1 = 100$ and $K_2 = 20$, see Figure 3-2. The complimentary filter reduces phase lag for approximately similar noise attenuation. The errors in the estimated pitch jerk were effectively regulated, see Figure 3-2b. Note that this error is in fact the second term on the right hand side of Equation (7-5) plus any high order terms, both normalized for the incremental time. As these terms are relatively low in frequency, their contribution can be included in the complimentary filtered response by selecting a filter crossover

frequency well above the frequency content of these terms. For visualization purposes, the pitch jerk obtained from the complimentary and washout filter were low-pass filtered due to noise.

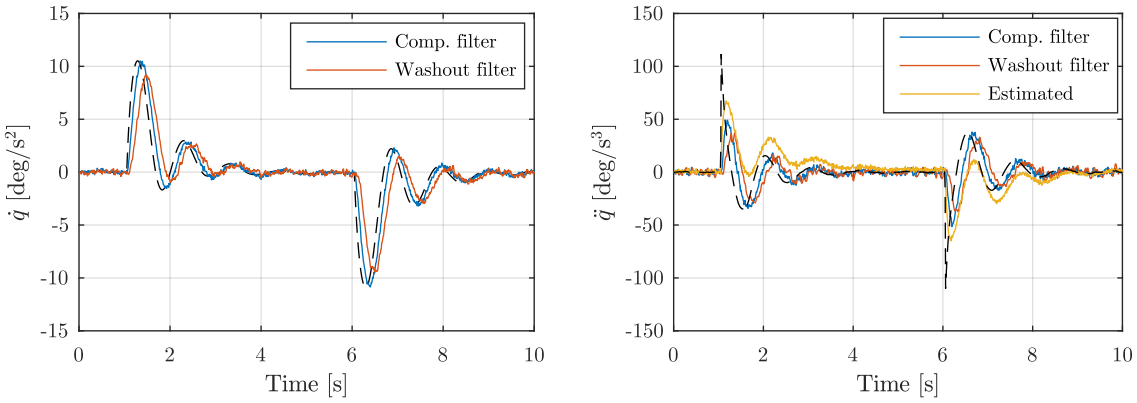

(a) Pitch acceleration **(b)** Pitch jerk

Figure 3-2: Closed loop response NDI to 5°/s box-cart input on pitch rate ($V_{tas} = 129$ m/s)

A second set of simulations was performed to assess the filter in the loop performance, see Figure 3-3. As expected, the reduced phase lag results in less oscillatory tracking response. The simulations demonstrate that the proposed complementary filter could be beneficial for improving INDI control performance in absence of dedicated angular accelerometers, requiring no additional modeling/sensors.

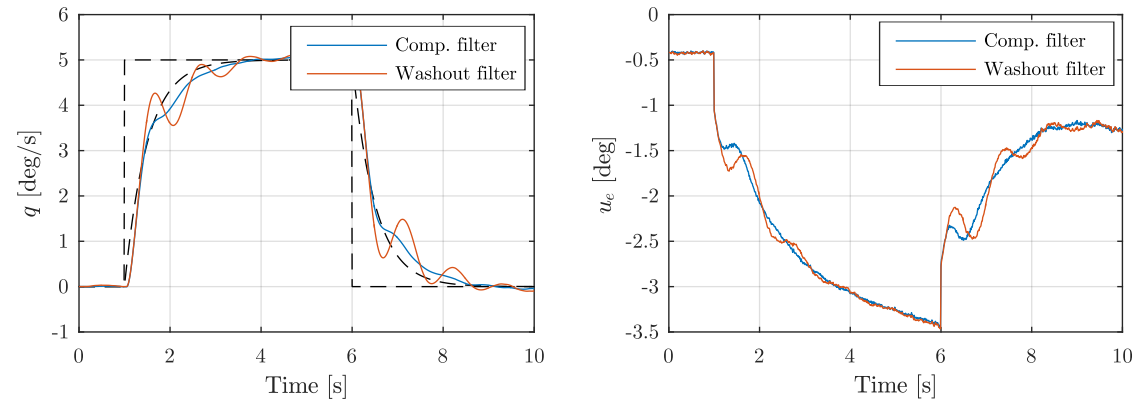

(a) Pitch rate **(b)** Elevator input signal

Figure 3-3: Closed loop response INDI filter-in-the-loop ($V_{tas} = 129$ m/s)

Linear accelerometers

The angular accelerations can be obtained from two pairs of strategically placed linear accelerometers. These are found in all modern passenger aircraft and rely on proven and well developed technologies in contrast to angular accelerometers [46]. The sensor pairs require placement parallel to the body axis of the aircraft with two axis coinciding and sufficient distance between the individual sensors along the non-coinciding axis. If these criteria are met

the angular accelerations can be obtained requiring only additional knowledge of the angular rates and the relative distance between the sensors. The PH-LAB is fitted with two side-by-side positioned linear accelerometers, see Table 5-3, allowing computation of the lateral angular accelerations:

$$\dot{p} = \frac{A_{z_{ahrs_2}} - A_{z_{ahrs_1}}}{y_{ahrs_1} - y_{ahrs_2}} g - rq \tag{3-3}$$

$$\dot{r} = \frac{A_{x_{ahrs_2}} - A_{x_{ahrs_1}}}{y_{ahrs_2} - y_{ahrs_1}} g + pq \tag{3-4}$$

To assess the performance of this technique, simulations were performed using the setup described previously. To account for sensor misalignments, kinematic position errors were included (5 cm in all three axis). In Figure 3-4 the open-loop aircraft response to a doublet input command is visualized. This command is simultaneously applied on aileron, elevator and rudder to excitate the errors induced by the misalignments.

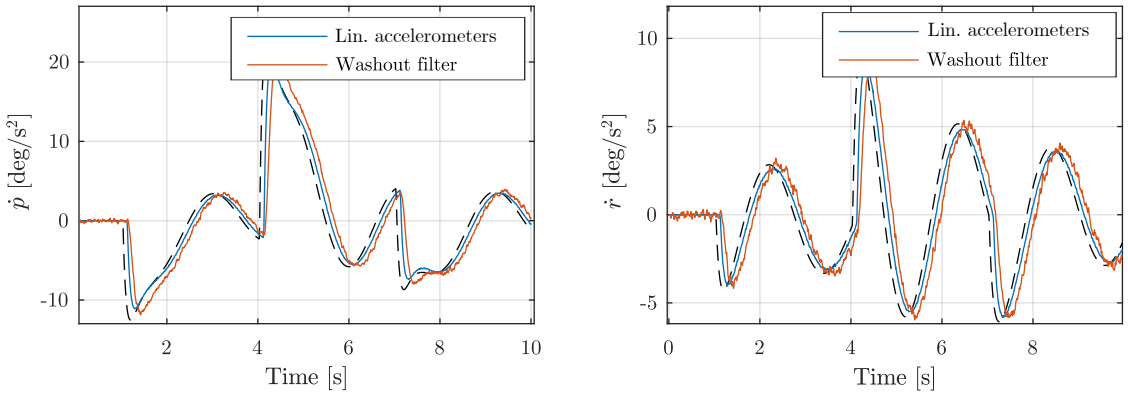

(a) Roll acceleration **(b)** Yaw acceleration

Figure 3-4: Open-loop response to 1° doublet input on elevator, aileron and rudder ($V_{tas} = 129$ m/s)

The kinematic position errors proofed to have a minor effect, a slight scaling of the response is observed. A significant improvement is obtained in terms of phase lag and noise compared to washout filters. A second set of simulations was performed with the filters in the loop, see Figure 3-5.

The reduced phase lag and noise result in less oscillatory tracking response and lower noise levels in the control signals. As expected, the sensitivity to relative position misalignment decreases with increased spacing between the sensors. However, maximizing this distance is not advisable as it will be more difficult to properly align the sensors relative to each other and alignment might be compromised under maneuvering due to fuselage bending. In case of the PH-LAB, with a spacing of 0.76 m, a sensor misalignment error of at least 5 cm does not compromise performance to a significant degree. The simulations demonstrate that pairs of linear accelerometers provide a high-performance and more implementation-ready alternative to dedicated angular accelerometers.

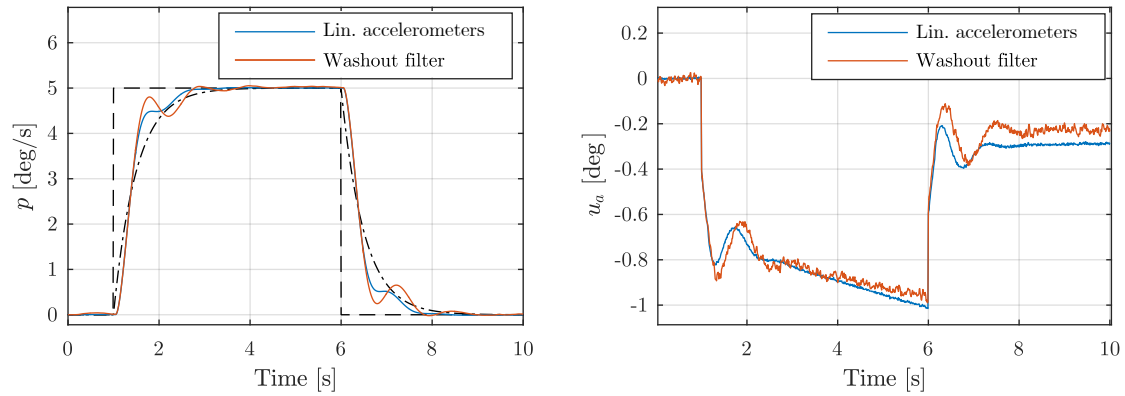

(a) Roll rate **(b)** Aileron input signal

Figure 3-5: Closed loop response INDI filter in the loop ($V_{tas} = 129$ m/s)

3-7 Signal synchronization

The incremental control method is based on a linearization around a specific point in time therefore requiring synchronous state derivative and control deflection feedback. In practice, these quantities are not always time-synchronous (e.g. due to filtering). Consider the general INDI control law in presence of actuator and sensor dynamics, see Figure 3-6.

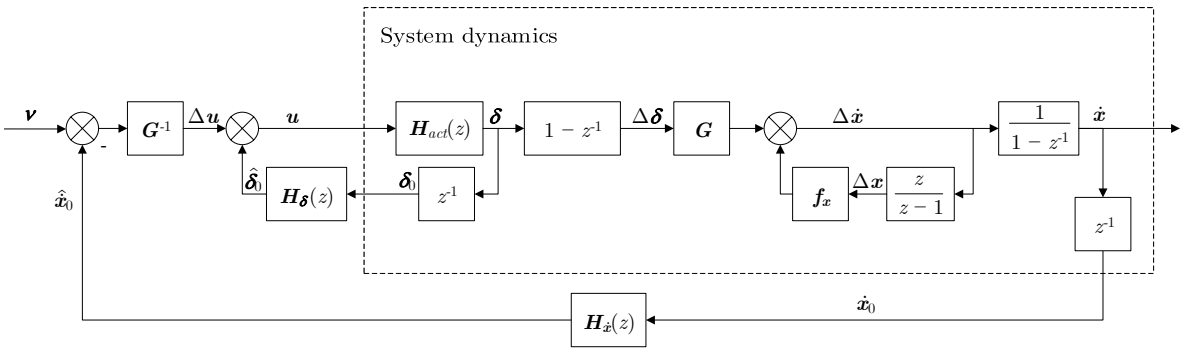

Figure 3-6: General INDI control law in presence of actuator and sensor dynamics

Where $\boldsymbol{H}_{act}$ are the actuator dynamics and $\boldsymbol{H}_{\boldsymbol{\delta}}$ and $\boldsymbol{H}_{\dot{\boldsymbol{x}}}$ the sensor dynamics of control deflection and state derivative, respectively. Note the inclusion of $\boldsymbol{f}_{\boldsymbol{x}}$, this is the partial derivative of $\boldsymbol{f}$ with respect to $\boldsymbol{x}$ i.e. the second term on the right hand side of Equation (2-8) normalized for the state increment $\Delta\boldsymbol{x}$. The state increment is assumed zero in the derivation of INDI under the assumption of small time increments and instantaneous control deflections. These assumptions do not fully hold for the platform under consideration in this thesis. Note that $\boldsymbol{f}_{\boldsymbol{x}}\Delta\boldsymbol{x}$ is also reffered to as the system dynamics increment [66]. The closed loop response of the system in Figure 3-6 is defined as follows:

$$\boldsymbol{H}_{\boldsymbol{\nu}\rightarrow\dot{\boldsymbol{x}}}(z) = \frac{\boldsymbol{H}_{act}(z)}{(\boldsymbol{I} - \boldsymbol{H}_{act}(z)\boldsymbol{H}_{\boldsymbol{\delta}}(z)z^{-1})(\boldsymbol{I} - \frac{z}{z-1}\boldsymbol{f}_{\boldsymbol{x}}) + \boldsymbol{H}_{act}(z)\boldsymbol{H}_{\dot{\boldsymbol{x}}}(z)z^{-1}} \tag{3-5}$$

It was already noted by Vlaar [69] that time differences between state derivative and control deflection feedback could lead to performance loss within INDI controllers. This effect has been more thoroughly inverstigated by Van 't Veld [68]. A surplus of state derivative feedback delay resulted in relatively fast system instability compared to a surplus of control deflection feedback delay. This effect was attributed to the difference in feedback sign (i.e. negative vs. positive).

Notice the presence of the actuator dynamics in the denominator of Equation (3-6). In the results obtained by Van 't Veld [68] it is observed that faster actuators may reduce closed loop stability in presence of unsynchronized signal feedback. This effect was however not explicitly discussed. For now, assume that $\boldsymbol{f}_{\boldsymbol{x}}\Delta\boldsymbol{x} = 0$ as it is more illuminating in revealing this effect mathematically. Equation (3-6) subsequently reduces to:

$$\boldsymbol{H}_{\boldsymbol{\nu}\rightarrow\dot{\boldsymbol{x}}}(z) = \frac{\boldsymbol{H}_{act}(z)}{\boldsymbol{I} - \boldsymbol{H}_{act}(z)\boldsymbol{H}_{\boldsymbol{\delta}}(z)z^{-1} + \boldsymbol{H}_{act}(z)\boldsymbol{H}_{\dot{\boldsymbol{x}}}(z)z^{-1}} \tag{3-6}$$

The output $\dot{\boldsymbol{x}}$ is then obtained as follows:

$$\dot{\boldsymbol{x}} = \boldsymbol{H}_{act}\boldsymbol{\nu} + \boldsymbol{H}_{act}(\boldsymbol{H}_{\boldsymbol{\delta}}\dot{\boldsymbol{x}}_0 - \boldsymbol{H}_{\dot{\boldsymbol{x}}}\dot{\boldsymbol{x}}_0) \tag{3-7}$$

Observe that if $\boldsymbol{H}_{\dot{\boldsymbol{x}}}$ is faster than $\boldsymbol{H}_{\boldsymbol{\delta}}$, the dynamic response of the second term on the right hand side of Equation 3-7 is in opposite direction of the virtual input $\boldsymbol{\nu}$, resulting in a relatively over-damped output response. In the reverse condition, the dynamic response of this term will be in the same direction as the virtual input, resulting in a relatively under-damped output response. The latter condition subsequently results in much faster system instability. If the actuators act as lag components, they will reduce the magnitude of the second term on the right hand side of Equation 3-7, increasing system stability. Note that filtering has a similar effect as actuators if applied in equal manner on state derivative and control deflection feedback.

To confirm the mathematical results, a stability analysis was performed on the system described in Figure 3-6, albeit in single-input single output form. To replicate a more realistic control setup, an outer proportional controller ($K_P = 2$) was added. The sampling frequency was set at 100 Hz and a value of 2 was chosen for $\boldsymbol{f}_{\boldsymbol{x}}$. The sensors were modeled as pure time delays with a baseline value of 100 ms. The actuator was modeled as a first-order lag. The system stability was assessed over a typical range of actuator bandwidth and sensor delay mismatch, see Figure 3-7. Note that the surplus of sensor delay is added to the baseline value.

Observe that a surplus of control deflection feedback delay results in a much larger stable region compared to a surplus of state derivative feedback delay. Further observe that above a certain minimum actuator bandwidth, faster actuators result in lower stability margins. The instable region for the lower actuator bandwidth range is an effect of the inclusion of $\boldsymbol{f}_{\boldsymbol{x}}$. Note that the closed loop stability is also a function of the linear controller gain, size of the $\boldsymbol{f}_{\boldsymbol{x}}$-matrix, $\boldsymbol{G}$-matrix uncertainty, sampling time and sensor delays [68]. Robustness analysis against synchronization mismatches should therefore be performed on a case-by-case basis.

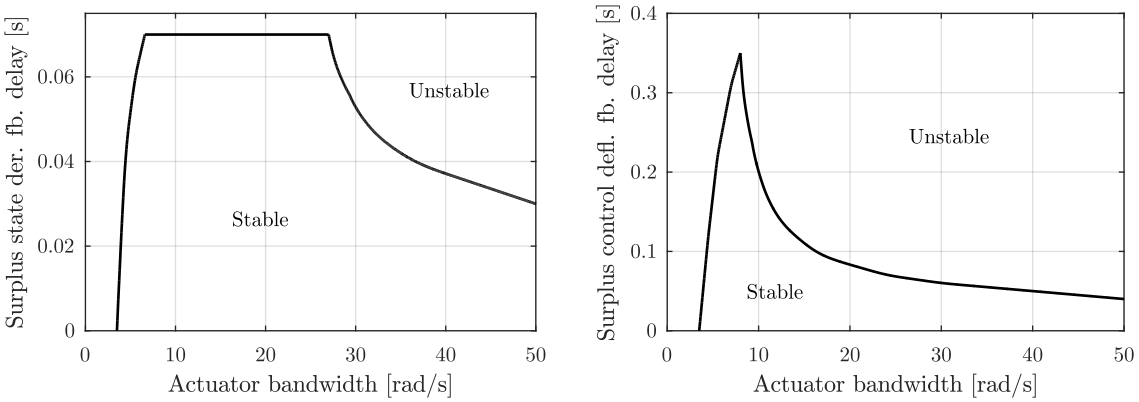

(a) Surplus state derivative feedback delay **(b)** Surplus control deflection feedback delay

Figure 3-7: Closed loop stability INDI in presences of actuators and unsynchronized signal feedback

Considering that small mismatches may already result in performance degradation, this is an important element in the design of INDI control laws.

In [61] it was shown that the closed loop response reduces to the actuator dynamics in case $\boldsymbol{H}_{\dot{\boldsymbol{x}}} = \boldsymbol{H}_{\boldsymbol{\delta}}$ and $\boldsymbol{f}_{\boldsymbol{x}}\Delta\boldsymbol{x} = 0$. This makes the closed loop response completely independent of the sensor dynamics and size of the incremental time step, see Equation 3-7. This clearly does not hold for real systems. Now assume that $\boldsymbol{H}_{\dot{\boldsymbol{x}}} = \boldsymbol{H}_{\boldsymbol{\delta}} = \boldsymbol{H}_{snsr}$ and $\boldsymbol{f}_{\boldsymbol{x}}\Delta\boldsymbol{x} \neq 0$. The closed loop response in Equation (3-6) subsequently reduces to:

$$\boldsymbol{H}_{\boldsymbol{\nu}\rightarrow\dot{\boldsymbol{x}}}(z) = \frac{\boldsymbol{H}_{act}(z)}{\boldsymbol{I} - \frac{z}{z-1}\boldsymbol{f}_{\boldsymbol{x}}(\boldsymbol{I} - \boldsymbol{H}_{act}(z)\boldsymbol{H}_{snsr}(z)z^{-1})} \tag{3-8}$$

Assuming that $\boldsymbol{f}$ is linear in $\boldsymbol{x}$, the output $\dot{\boldsymbol{x}}$ is then obtained as follows:

$$\dot{\boldsymbol{x}} = \boldsymbol{H}_{act}\boldsymbol{\nu} + \boldsymbol{f}_{\boldsymbol{x}}(\boldsymbol{x} - \boldsymbol{H}_{act}\boldsymbol{H}_{snsr}\boldsymbol{x}_0) \tag{3-9}$$

Observe that the second term on the right hand side of Equation (3-9) (i.e. the inversion error) increases with slower actuator and sensor dynamics and lower sampling frequencies. This exact effect was observed by Van Ekeren [66] in simulations performed on a fixed-wing sub-scale UAV model. Tracking errors due to neglecting the system dynamics increment scaled proportionally with the size of the combined delay of actuators, sensors and sampling. Now returning to the ideal case i.e. $\boldsymbol{H}_{snsr} = \boldsymbol{H}_{act} = \boldsymbol{I}$, Equation (3-9) reduces to the familiar form:

$$\dot{\boldsymbol{x}} = \boldsymbol{\nu} + \boldsymbol{f}_{\boldsymbol{x}}\Delta\boldsymbol{x} \tag{3-10}$$

3-8 Conclusions and recommendations

This chapter reviewed the literature on effects that violate the fundamental assumptions made for (I)NDI and result in significant performance loss within the control laws. Based upon this review, the following conclusions and recommendations can be made:

- NDI displays high sensitivity to model mismatches. Severe model mismatch due to system failures requires adaptive elements but may still not guarantee robustness. Although the adaptation of control laws is not considered in this thesis, model uncertainties may still result in considerable performance loss. Robustness to these uncertainties should be addressed using for example μ-synthesis, H_∞ loop shaping or via multi-model multi-objective optimization. INDI reduces the model sensitivity to the control effectiveness matrix. Robustness to uncertainties in this part of the model can be addressed in a similar manner as for NDI.

- Actuator dynamics and saturation effects violate some of the fundamental assumptions made for (I)NDI. Actuator lag can be addressed by careful tuning of the natural frequency of the reference model. Pseudo Control Hedging (PCH) is currently the most promising solution to actuator saturation effects. PCH aims to compensate for actuator limitations by means of modification of the reference model dynamics

- The following sensor deviations were found to result in performance loss within (I)NDI control laws: delay and lag, noise, bias and quantization errors. Especially delays have a detrimental effect on the controller performance and require careful offline analysis. Noise in sensor measurements can in general be reduced via filtering at the cost of the dynamic behavior of the sensor. Steady errors in the control variables due to biased measurements can be addressed via outer linear controllers with integral action.

- Low sampling frequencies violate the very small time increments assumption made for INDI, reducing controller performance. For the current application, the flight control computer samples the control laws with 100 Hz. This should be sufficient according to the currently available literature.

- Atmospheric disturbances may result in performance loss within (I)NDI. Careful offline assessment of wind and turbulence effects is key in addressing this issue. Note that the air data sensors pick up atmospheric turbulence that may propagate through the control laws. Air data measurements therefore need to be complemented with inertial mixing.

The following conclusions and recommendations are made with respect to the specific implementation aspects of INDI:

- A novel method based on the complimentary filtering technique has been proposed as a means to obtain more accurate angular acceleration estimates from angular rate measurements. The method has no additional dependencies other than the control surface deflection and control effectiveness, both already required for INDI. Closed loop simulations demonstrated that this filter performs well in comparison to conventional washout filters.

- INDI displays high sensitivity to time differences between state derivative and control deflection feedback. A surplus of state derivative delay results relatively fast in oscillations and system instability. For practical applications this sensitivity is somewhat reduced due to actuator and filter lag. It was shown mathematically and in a stability analysis that faster actuators may reduce stability under certain conditions in presence of unsynchronized signal feedback. This stresses the importance of synchronization for

systems with fast actuators. Robustness analysis against synchronization mismatches should be an integral part of INDI control law design.

- It has been shown mathematically that the size of the inversion error of INDI due to neglecting the so-called system dynamics increment scales with the combined delay of actuators, sensor, and sampling. This result conforms to observations made in simulations in previous research and stresses the importance of minimizing actuator, sensor and sampling delay.

Chapter 4

PH-LAB Fly-By-Wire system

Modern flight control systems use Fly-By-Wire (FBW) to operate the aircraft actuators via computer-generated commands. The full-authority FBW systems of modern passenger aircraft allow the aircraft dynamics to be tailored to a wide range of desired performance characteristics and handling qualities [49].

In recent years, the conventional mechanical flight control system of the PH-LAB has been supplemented with an electric FBW system [73, 45]. To reduce certification complexity and cost, the FBW system was designed with minimal impact on the original flight controls. By making use of the analog autopilot of the aircraft, only minor modifications to the control system were required. Nevertheless, this means that all limitations associated with the original autopilot are inherited by the FBW system as well. In Chapter 3, the physical limitations of actuators were identified as an important constraint to the design of dynamic inversion control laws. The focus of this chapter will therefore be on quantifying the limitations imposed on the input response by the FBW system, from which actuator models can be developed.

This chapter is structured as follows. In Section 4-1 a brief description of the original manual and automatic control system of the Cessna Citation II is provided. Section 4-2 discusses the design of the FBW system. In Section 4-3 the performance limitations of the FBW system will be assessed. Finally, in Section 4-4 some conclusions and recommendations are provided.

4-1 Manual and automatic control system [73, 45]

The flight control system of the PH-LAB is of a conventional reversible type meaning control column and rudder pedals are mechanically connected to ailerons, elevator and rudder via cables and bellcranks. The aircraft features a mechanical trim system in all three axis actuated from the cockpit, eliminating sustained control forces. The rudder trim tab also acts as a balancing tab deflecting in opposite direction at half the rate of the rudder when actuated. The elevator and rudder are of a horn-balanced design reducing the required control forces during actuation. High-lift devices in the form of electric Fowler flaps provide increased lift when extended (up to 40°). The aircraft is also fitted with hydraulic speedbrakes in the form

of slotted panels on top and bottom wing, these provide lift destruction and increased drag when activated.

The PH-LAB is fitted with a Honeywell SPZ-500c Integrated Flight Control System providing three axis automatic control. Important functionalities include the yaw damper which automatically applies rudder against transient motion in the yaw channel and the automatic elevator trim. The main components of the system are a flight director, autopilot computer and electric servo motors for ailerons, elevator, rudder and elevator trim tab. The servos are mechanically linked to the cable system via a drum and friction clutch. The latter disconnects the servo motors from the drum when the autopilot is disengaged allowing the drum to spin freely while the servo motors return to a zero position. The friction clutch also serves as a torque limiter allowing manual override of the autopilot via the control column, an important safety feature of the system. The autopilot computer is located in the nose compartment of the aircraft forming the control laws and the servo amplifiers. The servo amplifiers employ a current limiter restricting the amount of power that can be delivered to the servo motors. Data from the flight director and the aircraft sensor systems serve as input to the autopilot computer. The automatic elevator trim is activated when the servo torque is above a certain threshold for 1 or 2.5 seconds for upward or downward torque, respectively. The elevator trim tab is automatically adjusted such that excessive torque is removed above this threshold.

4-2 Fly-By-Wire system [73, 45]

The FBW system of the PH-LAB uses a modified autopilot computer allowing the system to accept control signals from an experimental FBW computer. Analog switches inserted between the autopilot control laws and servo amplifiers allow switching between the signals of the autopilot and the FBW computer, this way the functionality of the original autopilot is retained. The automatic elevator trim remains however always under the control of the autopilot. A useful property of this setup is that each control channel can be separately controlled by either the autopilot or the FBW computer. A dedicated cockpit control panel allows individual selection of the channels to be controlled by the FBW system. As a safety feature, the FBW system is only engaged if a match exists between the control channels selected on the control panel and in the experimental software. Furthermore, the autopilot computer requires a watchdog signal from the experimental software, in case of an interruption of this signal due to for example a software crash, the autopilot will be automatically disengaged.

Servo position controller

The FBW system employs a proportional controller that allows direct control over the deflection angle of the control surfaces $\boldsymbol{\delta}$, see Figure 4-1. The servo motor position $\boldsymbol{\delta}_s$ is used as feedback signal. The input signal $\boldsymbol{u}_s$ consists of a constant part for trimming the aircraft $\boldsymbol{\delta}_{s_0}$ and a varying part for maneuvering $\Delta\boldsymbol{u}$. The latter is the control signal computed by the FBW computer. Note that the dynamic inversion control laws compute the total control deflections. For implementation it is thus required to subtract the static part from the control inputs. The former are obtained by setting the virtual control input equal to zero at the initial computation [41]. By subtracting this value from the control inputs, only the deflections with respect to the trim condition are obtained. This implementation also prevents transient behavior at initialization of the experimental controller as the computed static part is typically slightly incorrect due to model uncertainties.

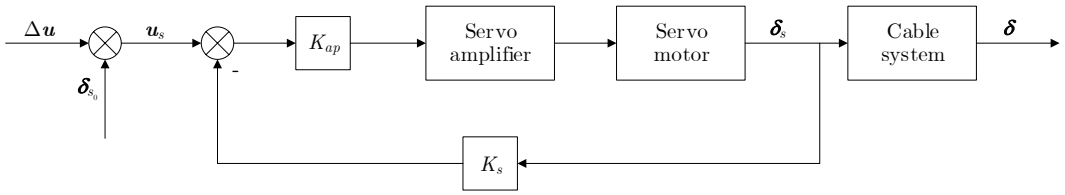

Figure 4-1: FBW system control laws [73]

Flight Test Instrumentation System

The PH-LAB is equipped with a custom-build Flight Test Instrumentation System (FTIS) [64, 52]. The FTIS acts as the communication hub between the various components of the FBW system and provides real-time monitoring, recording and processing capabilities. The main components of the FTIS include a real-time dSPACE computer and multiple analog and digital data acquisition boards interfacing to the available sensor systems. The FTIS is located in an instrumentation rack in the aft most position of the aircraft cabin. Data logging is either performed by the dSPACE computer or via an external computer connected to the system. The FBW computer is connected to the FTIS allowing access to all sensory data which can be used to compute a control signal. Synchronisation and communication between FTIS and the various software is obtained via the Delft University Environment for Communication and Activation (DUECA) [67].

Sidestick

A force-sensing sidestick positioned in the experimental pilot station allows manual control over the FBW system, see Figure 4-2. This manipulator is limited to 2-axis control i.e. pitch and roll for conventional control tasks. The sidestick output signal is proportional to the amount of force applied on the manipulator and is made available to the FBW computer via the FTIS. The sidestick features an autopilot disengage switch similar as found on the control column. Currently there is no manipulator available to manually augment the third control axis via the FBW system.

Experimental display

The experimental pilot station is equipped with a programmable display providing visualization of the primary flight instruments and task specific information. The display is connected to the FBW computer from which the visuals of the display are available as well.

4-3 Performance limitations [73]

The FBW system of the PH-LAB is a limited-authority system, meaning that the servo motors can only deflect the control surfaces to a limited degree. The components associated with the FBW system also have dynamic limitations. A specific point of attention is the stretch in the actuator cables due to aerodynamic loading of the control surfaces. This may reduce control effectiveness if not properly taken into account. This section will quantify the above limitations and proposes strategies to minimize performance loss.

Figure 4-2: Experimental pilot station PH-LAB

4-3-1 Actuator position

As mentioned in previous section, the FBW system employs two devices that limit the servo motor torque and subsequent force that can be applied to the cable system. With increasing deflection angle, aerodynamic forces on the control surfaces will increase accordingly. The limit torque of the servo motor therefore implies a limit control deflection, see Table 4-1. The values provided here are not "hard" limits as the aerodynamic forces on the control surfaces are a function of the flight and trim condition. Nevertheless, the corresponding limit values for the angular rates are indicative of the performance under typical flight conditions. Notice that the pitch authority is especially limited considering that typical short term steering tasks for passenger aircraft are executed with sustained pitch and roll rates of approximately $2.5°/s$ and $5°/s$, respectively. The reduced deflection limits result in relatively fast actuator saturation, see Figure 4-3. Notice the current limiter being activated around 5288 s and 5290 s.

Table 4-1: Maximum change in control deflection and maximum sustained angular rates PH-LAB

	$\Delta\delta_a$ [deg]	$\Delta\delta_e$ [deg]	$\Delta\delta_r$ [deg]	p [deg/s]	q [deg/s]
160 KIAS FL170 [73]	± 2.0	$+1.0/-0.5$	$+2.5/-3.0$	± 10	$+1.5/-1.0$
175 KIAS FL90	± 3.5	$+2.0/-1.0$	-	± 14	-

The current limiter of the servo amplifier employs a switching mechanism that lowers the current limit above barometric pressure altitudes of $13,400 \pm 1,100$ ft. To maximize performance, flight tests should ideally be executed below this altitude. The pitch authority of the FBW system can be increased by using the automatic elevator trim. The usefulness of this functionality is however limited for closed loop control due to the significant delay, effectively acting as an additional actuator system delay. To reduce the likelihood and severity of actuator saturation several measures can be taken. The sensitivity of the control manipulators should be relatively low such that maximum control input does not far exceed the capabilities of the FBW system. This also minimizes the signal noise of the manipulator and allows for more precise control within the limited control envelope. Furthermore, the pilots have to be made well aware of the limited authority and should modify their input behavior accordingly. Performance degradation due to actuator saturation can be prevented using adaptive control techniques.

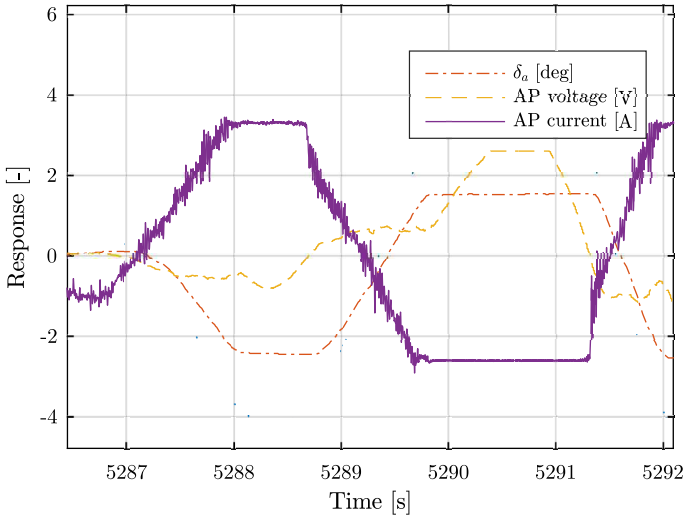

Figure 4-3: FBW system actuator saturation aileron

4-3-2 Actuator rate

The rate of deflection of the control surfaces are limited by the supplied voltage to the servo motors from the autopilot. This voltage is proportional to the rate of deflection of the control surfaces. The autopilot voltage is limited by the supplied input voltage of the FTIS and sidestick. These are ± 10 V and ± 2.5 V respectively hence the sidestick dictates the maximum supplied voltage to the servo motors, see Figure 4-3. The maximum rate of deflection of the actuators is estimated at $20°/s$, see Section 6-5.

4-3-3 Actuator dynamics

The intput-output response of the FBW system ($\boldsymbol{u}_s \rightarrow \boldsymbol{\delta}$) has been modelled by Zaal et al. [73] as a time delay and a small gain. The corresponding delay and gain values are 100 ms and 0.075 for the aileron channel and 60 ms and 0.045 for the elevator channel, respectively.

4-3-4 Actuator cable stretch

The transmission ratio between servo motor position and control surface deflection is not static due to the actuator cable system. Aerodynamic loading of the control surfaces and subsequent forces on the actuator cables may result in cable stretch [45]. It was however shown by Zaal et al. [73] that the transmission ratio (i.e. FBW input-output gain) could be modeled as a constant. The modeling data was however limited to a single airspeed and altitude.

The flight experiments in this research will be primarily limited to attitude tracking tasks with limited variations in airspeed and altitude. To this end, the FBW input-output gain is assumed constant during the individual experiments. Variations might nevertheless occur if the experiments are repeated for different flight conditions. A small error in the estimated FBW input-output gain is not considered critical at this stage of the development, this will

result in a minor increase/decrease in control effectiveness. For future applications it may be beneficial to include the cable system dynamics into the FBW control law by means of control surface deflection feedback. This will not only mitigate the issue of actuator cable stretch, the control law will regulate any other offsets between input and control surface deflection as well.

As the rudder channel was not modeled in [73], the FBW input-output gain F_{fbw} was determined from recent flight test data, see Figure 4-4 and Table 4-2. The flight data includes responses to a series of 3211 and doublet autopilot commands applied on the elevator and aileron. To remove any steady-state effects due to initial offsets between servo motor position and control surface deflection, the time derivatives of the control surface deflections were used. Observe that a constant gain provides a fairly good fit. Note that the values obtained by Zaal et al. [73] are significantly smaller. The reason for this large difference is unclear but might be attributed to different gain settings for K_{ap} and K_s or improper conversion of the raw synchro measurements.

Table 4-2: FBW system input-output gain (175 KIAS FL90)

	Aileron	Eevator	Rudder
K_{fbw}	0.70	0.60	0.55

4-4 Conclusions and recommendations

In this chapter the performance limitations of the PH-LAB FBW system have been quantified. The FBW system is not full-authority as typically found in modern passenger aircraft. This imposes several limitations on the input response and limits the control envelope in which the experimental controller has to operate. The control authority proofed to be especially limiting in the pitch axis, with maximum pitch rates below values typically used for maneuvering.

Several measures can be taken to maximize performance of the FBW system. First, flight tests should preferably be conducted below barometric altitudes of 13,400 ft. Above this altitude, the servo motors operate in a lower torque regime. Usage of the automatic elevator trim to improve authority is not considered beneficial for closed-loop control due to substantial time delays in this system. Low manipulator gains and proper pilot instruction could limit the likelihood and severity of actuator saturation. Control law adaptation to reduce performance degradation in presence of actuator saturation is considered specifically appropriate to include in the control setup.

The control laws currently implemented in the PH-LAB FBW system use the servo motor positions as feedback signal. The transmission ratio between servo motor position and control surface deflection varies due to actuator cable stretch. For quasi-steady airspeed and altitude conditions, this ratio can be assumed constant. A small estimation error of the transmission ratio is not considered critical, acting as a minor increase/decrease in control effectiveness. For future applications it is nevertheless advisable to change the feedback signal to the control surface deflections.

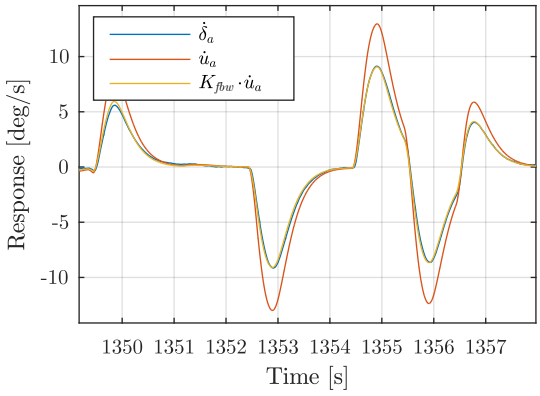

(a) Aileron

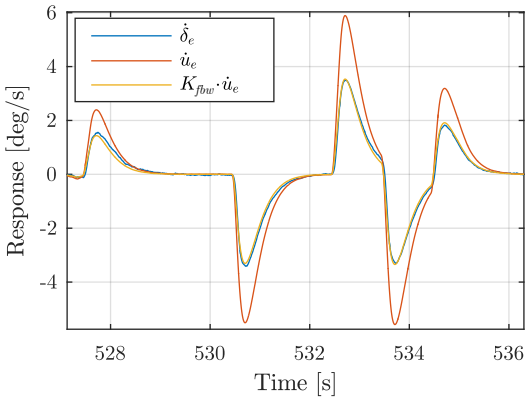

(b) Elevator

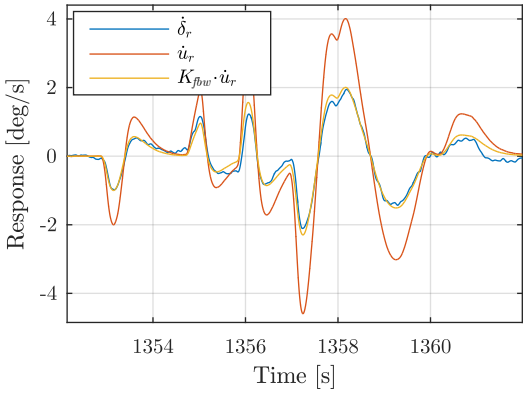

(c) Rudder

Figure 4-4: FBW input-output response (175 KIAS FL90)

Chapter 5

PH-LAB sensors

Augmented aircraft rely to a high degree on sensor measurements for stability and controllability [49]. The quality and accuracy of these sensors have a significant effect on the performance of the flight control system. Insufficient knowledge of the sensor deviations may result in serious setbacks [62, 40].

The PH-LAB is equipped with various sensors providing amongst others inertial and air data measurements [45]. Accurate airflow direction measurements can be obtained from the optional air data boom. Of particular interest to this research are the control surface deflection sensors, consdidering the control deflection feedback requirement for INDI. All sensors are connected to the Flight Test Instrumentation System (FTIS) [64, 52] allowing in-flight processing. In Chapter 3 the sensor deviations detrimental to (I)NDI were identified. The focus of this chapter is to quantify the relevant measurement errors of the PH-LAB sensors, from which sensor models can be developed.

The following sensor systems will be analyzed: Attitude and Heading Reference System (Section 5-1), Digital Air Data Computer (Section 5-2), airflow direction sensors (Section 5-3) and control deflection sensors (Section 5-4). Section 5-5 will provide some conclusions and recommendations. An overview of the sensor characteristics and relevant sensor positions can be found in Tables 5-2 and 5-3, respectively.

5-1 Attitude and Heading Reference System

The PH-LAB is equipped with two Rockwell Collins AHS-3000 Attitude and Heading Reference Systems (AHRS), providing processed inertial observations over the ARINC 429 data bus [55]. The system features solid-state digital quartz microelectromechanical systems (MEMS) sensors. Both AHRS are located side-by-side in the nose compartment of the aircraft.

Delay and lag

The AHRS signals are filtered in both the Attitude and Heading Computer and the ARINC data bus (8 Hz cut-off frequency). The nominal delay is specified at 117 ms and 110 ms for

the specific force and the attitude/angular rate signals, respectively. The angular rate delay has also been determined in flight data anlysis [68]. The time difference between autopilot input command and subsequent response of the angular rate signal served as estimate for the measurement delay. The validity of this approach is however uncertain considering that time delays in the actuator system were implicitly assumed zero, see also Section 5-4

Noise and Bias

The noise and bias characteristics of the AHRS signals have also been determined in [68]. The AHRS flight data was processed using a weighted two-sided moving average filter and subtracted from the equivalent pre-filtered data. The variance of the remaining data served as an estimate for the noise variance. An estimate for the bias was obtained by subtracting the averaged flight data of the first AHRS, from the equivalent data of the second AHRS. The analysis was performed over two relatively stationary parts of the flight and the worst case values were selected as final estimates. Note that the angular rate signals will require additional low-pass filtering to reduce sensor noise before the differentiation operation.

Position errors

During maneuvering flight, the measured specific forces might not correspond to the specific forces at the center of gravity of the aircraft [34]. Kinematic position errors arise due to position differences between sensors and aircraft center of gravity. These can be compensated for by applying the following correction:

$$\begin{aligned} A_{x_{cg}} &= A_{x_{ahrs}} + \frac{(x_{cg}-x_{ahrs})(q^2+r^2) - (y_{cg}-y_{ahrs})(pq-\dot{r}) - (z_{cg}-z_{ahrs})(pr+\dot{q})}{g} \\ A_{y_{cg}} &= A_{y_{ahrs}} + \frac{(y_{cg}-y_{ahrs})(r^2+p^2) - (z_{cg}-z_{ahrs})(qr-\dot{p}) - (x_{cg}-x_{ahrs})(qp+\dot{r})}{g} \\ A_{z_{cg}} &= A_{z_{ahrs}} + \frac{(z_{cg}-z_{ahrs})(p^2+q^2) - (x_{cg}-x_{ahrs})(rp-\dot{q}) - (y_{cg}-y_{ahrs})(rq+\dot{p})}{g} \end{aligned} \tag{5-1}$$

Note that this correction will in general reduce the accuracy of the observation. Errors associated with the additional required measurements will propagate through the observation of interest as well. Considering the flexible layout of the PH-LAB, it might be beneficial to relocate the AHRS to the instrumentation rack positioned close to the aircraft center of gravity.

5-2 Digital Air Data Computer

Air data observations are obtained via two Digital Air Data Computers (DADC) of different type. These are located in the nose compartment as well. The air data system uses a conventional pitot-static arrangement with a mirrored pair of pressure probes.

Delay and lag

Pitot-static systems are under influence of pneumatic lag due to tubing used to carry the sensed pressure at the pressure probes to the pressure transducers [34]. No technical specifications are available for the DADC, the dynamic response of the air data sensors is therefore assumed

equal to a first order lag with a time constant of 0.3 s. Note that this value is obtained from the ATTAS model [54], a similar twin-jet aircraft adapted for research.

Noise and bias

The noise and bias characteristics of the air data measurements of interest were determined following similar procedure as described in Section 5-1. Notice the particularly large bias of V_{tas} in Table 5-2, indicating erroneous calculation of V_{tas} in one of the DADC.

Position errors

Position errors can arise due to misalignment of the pitot tube relative to the local airflow but also due to aircraft induced flow perturbations [34]. The former tend to be insignificant below 10° angle of attack [72]. Errors due to aircraft induced flow perturbations are significant but cannot be easily compensated for. Similar as for the specific force measurements, position differences between sensor and aircraft center of gravity induce kinematic position errors. The PH-LAB pressure probes are located relatively close to the aircraft center of gravity (in lateral and vertical axis), errors induced by this small position offset were found to be insignificant, see Figure 5-1. In addition, the errors induced by the lateral offset could be accounted for by averaging the measurement of the first and second DADC, as these are individually connected to port and starboard pressure probes.

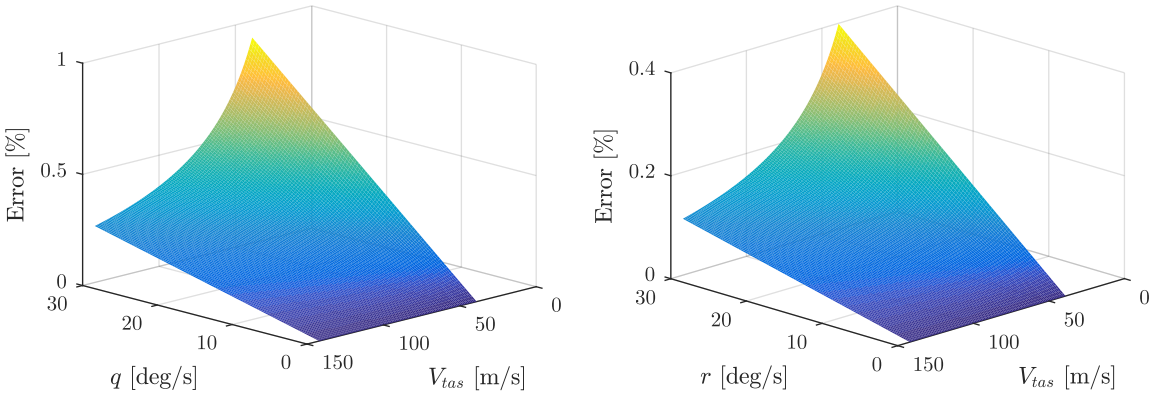

(a) Errors due to vertical sensor offset

(b) Errors due to lateral sensor offset

Figure 5-1: Kinematic position error airspeed (for $\alpha = \beta = 0$)

5-3 Airflow direction sensors

The angle of attack and angle of sidelip are comparatively difficult to measure accurately [34]. Current generation passenger aircraft are equipped with dedicated angle of attack sensors but sideslip sensors are less common. The PH-LAB only features an angle of attack sensor of limited accuracy, used by the stall warning device [7]. As the angle of attack and angle of sideslip are important quantities in the aerodynamic model, use will be made of the PH-LAB air data boom. This option allows measurements relatively free of aircraft induced flow perturbations.

The PH-LAB air data boom is fitted with vane-type airflow direction sensors directly mounted on synchro transducers, see Figure 5-2. No internal signal filtering is applied. The body-mounted angle of attack sensor is of a similar vane-type but paired with a potentiometer. The device is positioned on the starboard side of the fuselage near the leading edge of the wing. The signal is internally filtered, filter type and bandwidth are however unknown.

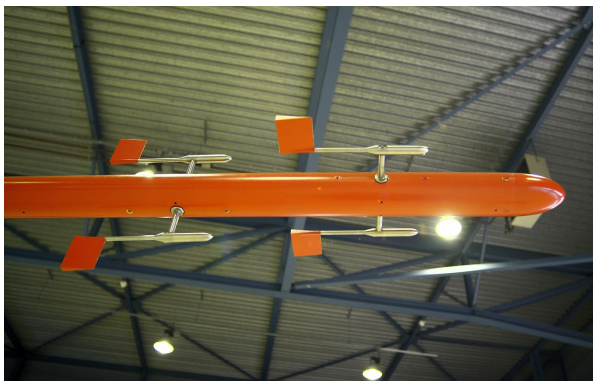

Figure 5-2: PH-LAB air data boom sensors

Delay and lag

The vanes are of a mass-balanced design, reducing the effect of accelerations and biases on the airflow direction measurements [34]. Due to the finite inertial characteristics of this design, the response cannot be considered instantaneous. The dynamic response is assumed equal to a first-order lag with a time constant of 0.1 s. Note that this value is taken from the ATTAS model [54]. From flight data analysis, a time difference was observed between the body angle of attack measurement and the equivalent boom measurement. A value for this difference was obtained via the argument maximum of the normalized cross-correlation function of the two signals (see Equation 5-2). The corresponding time difference equates to 0.18 s.

$$\tau = \arg\max_{t} \left(\frac{1}{\sigma_{\alpha_{boom}} \sigma_{\alpha_{body}}} \int \left(\alpha_{boom}(t) - \mu_{\alpha_{boom}}\right)^* \cdot \left(\alpha_{body}(t+\tau) - \mu_{\alpha_{body}}\right) \mathrm{d}t \right) \tag{5-2}$$

Noise and Bias

The noise characteristics of the airflow direction signals were obtained in similar manner as described in Section 5-1. As expected, the body angle of attack measurement is considerably less noisy compared to the equivalent boom measurement due to internal filtering of the former, see Table 5-2. The boom airflow sensors are calibrated relative to the nose boom. The boom points approximately 0.1° upwards compared to the waterline of the aircraft inducing a steady-state offset. It is advisable to compensate for this offset within the FTIS, for now this value is taken as a bias. Note that is not uncommon that steady-state offsets in the angle of sideslip measurement arise due to a non-straight fuselage [42]. The body mounted angle of attack sensor is calibrated using flight data of the AHRS, hence any bias associated with the AHRS is propagated through the angle of attack measurement as well.

Position errors

The airflow direction measurements are strongly effected by aircraft induced flow pertubations [34]. These can be significantly reduced by measuring the flow angles at a sufficient distance

in front of the aircraft. To get an idea of the magnitude of this effect, Figure 8-7a provides the response of the boom and body angle of attack measurement near the stall region. The difference between the two signals equates to more than 1.5° at high angles of attack. The effect is less pronounced in the normal flight regime but remains significant deeming the body angle of attack measurements unsuited for use without error correction. Kinematic position errors can be compensated for by using the following correction:

$$\alpha_{cg} = \alpha_{vane} - q\frac{x_{vane} - x_{cg}}{V_{tas}} \tag{5-3}$$

$$\beta_{cg} = \beta_{vane} + r\frac{x_{vane} - x_{cg}}{V_{tas}} - p\frac{z_{vane} - z_{cg}}{V_{tas}} \tag{5-4}$$

Note that during maneuvering elastic deformation of fuselage and air data boom may also result in position errors [34]. This does not only result in static errors, disturbances due to excitation of the boom structural eigenmodes will propagate through the airflow measurements as well. Analysis of flight data reveals that the PH-LAB boom also suffers from this problem, as visualized in Figure 5-3. For visualization purposes the response near the stall is provided where the boom is excitated by the buffet. The eigenmodes center around 10 Hz and a clear sinusoidal disturbance is visible in the time response of the angle of attack. In normal flight regimes the disturbances remain visible in the periodagram albeit with lower intensity. These disturbances can be reduced by complementing the airflow direction measurements with inertial mixing [43].

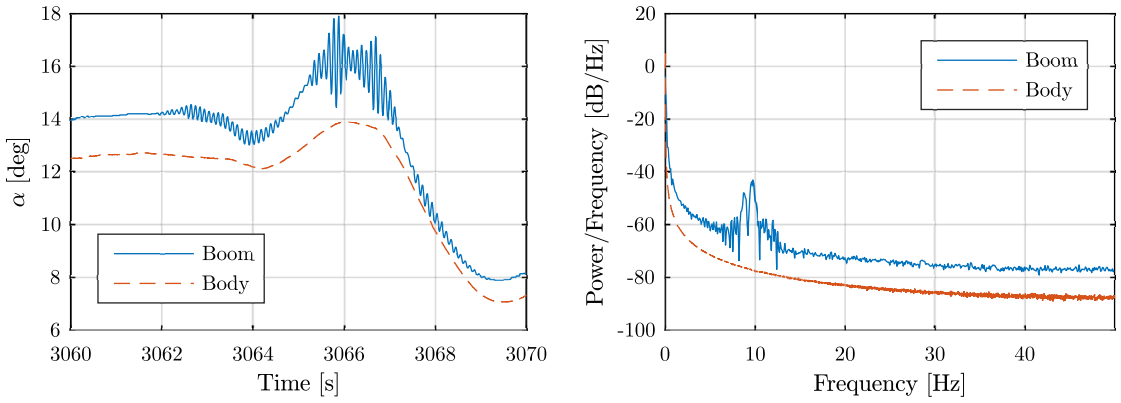

(a) Time response **(b)** Periodogram

Figure 5-3: Angle of attack measurement near stall

5-4 Control surface deflection sensors

The PH-LAB is equipped with sensors that measure the deflection angle of the control surfaces. The control surfaces are indirectly connected to synchro-type transducers via multiple linkage rods, resulting in a trigonometric relationship between measured and actual deflection. Conversion between the two is performed within FTIS by means of a polynomial regressor, which coefficients were determined via calibration. No internal signal filtering is applied.

The measurement of the aileron deflection follows from a single, starboard aileron synchro only. The control laws developed in this thesis require however observations of the total aileron deflection i.e. port plus starboard aileron deflection in the case of the PH-LAB. Furthermore, the relationship between port and starboard aileron deflection is nonlinear, a conversion polynomial has been determined via calibration as well. The relationship between total ($\delta_{a_{tot}}$) and starboard ($\delta_{a_{stbd}}$) aileron deflection can subsequently be derived, see Equation (5-5) and Table 5-1.

$$\delta_{a_{tot}} = c_0 + c_1\delta_{a_{stbd}} + c_2\delta^2_{a_{stbd}} + c_3\delta^3_{a_{stbd}} \tag{5-5}$$

Table 5-1: Coefficients conversion polynomial (for deflections in degrees)

c_0	c_1	c_2	c_3
$-1.366792 \cdot 10^{-1}$	2.025277	$1.146134 \cdot 10^{-2}$	$1.257941 \cdot 10^{-4}$

Delay and lag

The measurement delay of the control deflection signals was determined in [68]. The time difference between autopilot input command and the subsequent signal response of the control deflections served as a measure for the delay. This approach does however not account for possible delays in the actuator system nor does it allow to differentiate between actuator and sensor delay. This approach is therefore only valid for determining the relative time delay between angular rate and control deflection measurement (corresponding to 90 ms). Considering the absence of signal filtering, high sampling frequency and minimal delay inherent to synchro-type transducers [34], the control deflection measurement delay is assumed zero. For synchronization, the surplus of delay of the angular rate signals should be artificially added to the control deflection signals.

Noise and bias

The noise characteristics of the control deflection signals were determined in [68] as well. Notice in Equation (5-5) that for zero starboard aileron deflection the total (i.e. port) aileron deflection is non-zero, the subsequent offset c_0 is taken as a value for the bias.

5-5 Conclusion and recommendations

In this chapter the measurement deviations of the PH-LAB sensors have been quantified (see Table 5-2). The following measures are proposed to minimize performance degradation within (I)NDI controllers:

- Significant differences in time delay exist between angular rate and control surface deflection measurement. The incremental control method requires synchronous feedback of these two quantities. To this end, the surplus of angular rate delay needs to be artificially added to the control surface deflection measurement.
- Low-pass filtering is required to remove sensor glitches and minimize the amount of noise being propagated through the control laws. This is in particular important for the

unprocessed measurement signals (i.e. synchros) and the angular rates, the latter being differentiated to obtain angular accelerations.

- The PH-LAB sensors are not located in the vicinity of the aircraft center of gravity. Kinematic position errors in the specific force and airflow direction measurements therefore need to be compensated for. Errors in the airspeed measurement due to maneuvering proofed to be minor.
- The structural eigenmodes of the PH-LAB air data boom are excitated in flight. This results in a 10 Hz disturbance signal in the airflow direction measurements. These disturbances can be effectively reduced by complementing the airflow direction measurements with inertial mixing.
- The body angle of attack sensor was found to be of insufficient accuracy. The offset induced by aircraft induced flow perturbations has to be modeled if the body angle of attack sensor is to be used in future applications.
- The PH-LAB only features a starboard aileron deflection sensor. The incremental control method requires however feedback of the total aileron deflection. The nonlinear relation between port and starboard aileron deflection has been determined in calibration. From this relation the total aileron deflection could be derived.

Table 5-2: Sensor characteristics PH-LAB [68, 55]

Source	Signal	Noise (σ^2)	Bias	Resolution	Delay [ms]	Lag [ms]	Sampling freq. [Hz]
AHRS	$p, q, r, \dot{\theta}, \dot{\phi}, \dot{\psi}$ [rad/s]	$4.0 \cdot 10^{-7}$	$3.0 \cdot 10^{-5}$	$6.8 \cdot 10^{-7}$	90	-	52
	θ, ϕ [rad]	$1.0 \cdot 10^{-9}$	$4.0 \cdot 10^{-3}$	$9.6 \cdot 10^{-7}$	90	-	52
	A_x, A_y, A_z [g]	$1.5 \cdot 10^{-5}$	$2.5 \cdot 10^{-3}$	$1.2 \cdot 10^{-4}$	117	-	52
DADC	V_{tas}, V_{cas} [m/s]	$8.5 \cdot 10^{-4}$	2.5	$3.2 \cdot 10^{-2}$	-	300	8, 16[†]
	h [m]	$4.5 \cdot 10^{-3}$	$8.0 \cdot 10^{-3}$	$3.0 \cdot 10^{-1}$	-	300	16
	$\dot{h}$ [m/s]	$5.5 \cdot 10^{-4}$	$4.5 \cdot 10^{-2}$	$8.1 \cdot 10^{-2}$	-	300	16
	M [-]	$1.0 \cdot 10^{-8}$	$7.0 \cdot 10^{-7}$	$6.3 \cdot 10^{-5}$	-	300	8
FMS	V_{ground} [m/s]	$7.0 \cdot 10^{-4}$	$2.0 \cdot 10^{-1}$	-	-	-	2
	ψ [rad]	$5.5 \cdot 10^{-8}$	$7.0 \cdot 10^{-4}$	-	-	-	10
	χ [rad]	$7.0 \cdot 10^{-9}$	$6.0 \cdot 10^{-4}$	-	-	-	2
synchro	$\delta_a, \delta_e, \delta_r$ [rad]	$5.5 \cdot 10^{-7}$	$2.4 \cdot 10^{-3}$	-	$\sim$0	-	100
	$\alpha_{boom}, \beta_{boom}$ [rad]	$7.5 \cdot 10^{-8}$	$1.8 \cdot 10^{-3}$	$9.6 \cdot 10^{-5}$	-	100	100
analog	α_{body} [rad]	$4.0 \cdot 10^{-10}$	-	$1.0 \cdot 10^{-5}$	180	100	1000

[†] DADC No. 1 (V_{tas} only)

Table 5-3: Location relevant sensors in $\mathcal{F}_d$ [12]

	A_x, A_y, A_z	α_{boom}	β_{boom}	α_{body}	p_{tot}
x [m]	1.6256	-0.6985	-0.4140	4.4069	-
y [m]	$\pm$0.3810	-	-	-	$\pm$0.2972
z [m]	2.6670	-	3.2639	-	2.3114

Chapter 6

Aircraft model

The availability of mathematical models describing the aircraft and its subsystems is the prerequisite for the analysis and synthesis of flight control laws [49]. The accuracy and quality of these models have a considerable impact on the overall controller performance. This chapter covers the modeling of the aircraft and relevant subsystems and prepares the models for the assessment of the numerical design criteria (defined in Chapter 8).

The aircraft model is a high fidelity 6-DOF nonlinear model of the Cessna Citation I. The model was developed in the Delft University Aircraft Simulation Model and Analysis Tool (DASMAT) [36]. Note that the Citation II is a more recent iteration of the Citation I with increased seating capacity and improved flight performance [20]. The Citation II features more powerful engines, a longer fuselage and longer wings. Despite these differences, the Citation I model fits reasonably well to flight data of the Citation II [65]. The Relative Root Mean Square Error (RRMSE) for the longitudinal force and moment coefficients equate to 9% and 13% respectively. For the lateral force and moment coefficients the RRMSE equals 7% and 9% respectively.

The chapter is structured as follows. In Section 6-1 the reference frames used for the derivation of the model equations will be briefly discussed. The model equations will be derived in Section 6-2. In Sections 6-3 and 6-4 the aerodynamic and mass model will be discussed, respectively. Following the results obtained in Chapters 4 and 5, actuator and sensor models will be developed in Sections 6-5 and 6-6, respectively.

6-1 Reference frames [36]

Multiple reference frames are used to describe the aircraft motion and the forces and moments on the aircraft. In addition, a separate reference frame is used to describe the locations of the aircraft components.

Table 6-1: PH-LAB operating limitations [13]

Symbol	Minimum	Nominal	Maximum	Unit
m	3765 (BEW)	-	6622 (MTOW)	kg
x_{cg}	7.013 ($0.18\bar{c}$)	-	7.259 ($0.3\bar{c}$)	m
T	208.15	219.15	339.15	K
h	-304.8	10670	13106	m
V_{cas}	39	121	142	m/s
n	-1.32	-	3.3	g
δ_a	$-19, -34^{\dagger}$	-	$15, 34^{\dagger}$	deg
δ_e	-17	-	15	deg
δ_r	-22	-	22	deg

† Total aileron deflection

Earth-fixed reference frame $\mathcal{F}_E$

The earth-fixed reference frame or North-East-Down (NED) reference frame is a right-handed, rectangular Cartesian reference frame with the origin located in the aircraft center of gravity. The x-axis points towards North, the y-axis towards East and the z-axis points downwards parallel to the local direction of the gravitation. The NED reference frame is used as an inertial reference frame.

Body reference frame $\mathcal{F}_b$

The body reference frame is a right-handed, rectangular Cartesian reference frame with the origin located in the aircraft center of gravity. The orientation is fixed relative to the aircraft body with the xy-plane coinciding with the aircraft's plane of symmetry. The x-axis points forward in the direction of flight, the y-axis points starboard and the z-axis points downward under normal flight. The body reference frame is used for the derivation of the force and moment equations of motion. The transformation from $\mathcal{F}_b$ to $\mathcal{F}_E$ requires three consecutive Euler angle rotations: $\phi \rightarrow \theta \rightarrow \psi$. The resulting transformation matrix is defined as:

$$\mathbb{T}_{bE} = \begin{bmatrix} \cos(\theta)\cos(\psi) & \cos(\theta)\sin(\psi) & -\sin(\theta) \\ \begin{pmatrix}\sin(\phi)\sin(\theta)\cos(\psi)-\\ \cos(\phi)\sin(\psi)\end{pmatrix} & \begin{pmatrix}\sin(\phi)\sin(\theta)\sin(\psi)+\\ \cos(\phi)\cos(\psi)\end{pmatrix} & \sin(\phi)\cos(\theta) \\ \begin{pmatrix}\cos(\phi)\sin(\theta)\cos(\psi)+\\ \sin(\phi)\sin(\psi)\end{pmatrix} & \begin{pmatrix}\cos(\phi)\sin(\theta)\sin(\psi)-\\ \sin(\phi)\cos(\psi)\end{pmatrix} & \cos(\phi)\cos(\theta) \end{bmatrix} \tag{6-1}$$

Stability reference frame $\mathcal{F}_s$

The stability reference frame is a right-handed, rectangular Cartesian reference frame with the origin located in the aircraft center of gravity. The y-axis coincides with the equivalent axis of the body fixed reference frame. The x- and z-axis are defined by performing a plane rotation about the negative body y-axis over the angle of attack. The x-axis is parallel to the projection of the air-mass referenced velocity vector on the aircraft plane of symmetry. The stability reference frame is used to express the aerodynamic force and moment coefficients. The transformation matrix from $\mathcal{F}_b$ to $\mathcal{F}_s$ is defined as:

$$\mathbb{T}_{sb} = \begin{bmatrix} \cos(\alpha) & 0 & \sin(\alpha) \\ 0 & 1 & 0 \\ -\sin(\alpha) & 0 & \cos(\alpha) \end{bmatrix} \tag{6-2}$$

Aerodynamic reference frame $\mathcal{F}_a$

The aerodynamic reference frame is a right-handed, rectangular Cartesian reference frame with the origin located in the aircraft center of gravity. The x-axis is directed along the air-mass referenced velocity vector. The z-axis coincides with the equivalent axis of the stability fixed reference frame. The x- and y-axis are defined by performing a plane rotation about the positive stability z-axis over the angle of sideslip. The transformation matrix from $\mathcal{F}_s$ to $\mathcal{F}_a$ is defined as:

$$\mathbb{T}_{as} = \begin{bmatrix} \cos(\beta) & \sin(\beta) & 0 \\ -\sin(\beta) & \cos(\beta) & 0 \\ 0 & 0 & 1 \end{bmatrix} \tag{6-3}$$

Datum reference frame $\mathcal{F}_d$

The datum reference frame is a left-handed, rectangular Cartesian reference frame. The origin is located in the aircraft plane of symmetry, 2.39 m (94.0 in) forward and 0.381 m (15.0 in) below the front face of the forward pressure bulkhead [12]. The x-axis is in the plane of symmetry, the y-axis is perpendicular to this plane of symmetry and points to port, the z-axis points upwards under normal flight. The datum axis are anti-parallel to the body axes. This reference frame is used to define locations of characteristic points relative to the aircraft such as the center of gravity and the sensor positions.

6-2 Model equations

The combined translational and rotational dynamics of a rigid-body aircraft over a flat non-rotating earth are described by the Newton-Euler equations:

$$\dot{\boldsymbol{V}} = m^{-1}\big(\boldsymbol{F}_A(\boldsymbol{x},\boldsymbol{u},\boldsymbol{p}) + \boldsymbol{F}_T(\boldsymbol{x},\boldsymbol{u}_o,\boldsymbol{p})\big) - \boldsymbol{\omega}\times\boldsymbol{V} + \mathbb{T}_{bE}\begin{bmatrix}0 & 0 & g\end{bmatrix}^{\mathrm{T}} \tag{6-4}$$

$$\dot{\boldsymbol{\omega}} = \boldsymbol{J}(\boldsymbol{p})\big(\boldsymbol{M}_A(\boldsymbol{x},\boldsymbol{u},\boldsymbol{p}) + \boldsymbol{M}_T(\boldsymbol{x},\boldsymbol{u}_o,\boldsymbol{p}) - \boldsymbol{\omega}\times\boldsymbol{J}(\boldsymbol{p})\boldsymbol{\omega}\big) \tag{6-5}$$

Where $\boldsymbol{V} = [u,v,w]^{\mathrm{T}}$ are the inertial translational velocities and $\boldsymbol{\omega} = [p,q,r]^{\mathrm{T}}$ the angular rates, both in body axis. $\boldsymbol{F}_A$ and $\boldsymbol{M}_A$ are the aerodynamic forces and moments respectively, $\boldsymbol{F}_T$ and $\boldsymbol{M}_T$ are the forces and moments induced by the thrust. The vectors $\boldsymbol{u}$, $\boldsymbol{u}_o$, $\boldsymbol{x}$ and $\boldsymbol{p}$ are the aerodynamic controls, the throttle settings, the air-mass referenced aircraft states and the model parameters, respectively. $\mathbb{T}_{bE}$ is the transformation matrix from the NED frame to the body frame. The aircraft mass is denoted by m and assumed constant, g is the gravitational constant and $\boldsymbol{J}$ the inertia tensor:

$$\boldsymbol{J}(\boldsymbol{p}) = \begin{bmatrix} J_{xx} & 0 & -J_{xz} \\ 0 & J_{yy} & 0 \\ -J_{xz} & 0 & J_{zz} \end{bmatrix} \tag{6-6}$$

Note that it is assumed that the aircraft is symmetrical in the xy-plane i.e. $J_{xy} = J_{yz} = 0$. The rotational kinematic motion can be expressed in terms of the Euler angular rates following transformation of the body angular rates:

$$\begin{bmatrix} \dot{\phi} \\ \dot{\theta} \\ \dot{\psi} \end{bmatrix} = \mathbb{T}_{\Phi b} \begin{bmatrix} p \\ q \\ r \end{bmatrix} \tag{6-7}$$

Where $\mathbb{T}_{\Phi b}$ is the corresponding transformation matrix:

$$\mathbb{T}_{\Phi b} = \begin{bmatrix} 1 & \sin(\phi)\tan(\theta) & \cos(\phi)\tan(\theta) \\ 0 & \cos(\phi) & -\sin(\phi) \\ 0 & \sin(\phi)\sec(\theta) & \cos(\phi)\sec(\theta) \end{bmatrix} \tag{6-8}$$

The aerodynamic forces and moments are defined in terms of their respective coefficients in the stability reference frame:

$$\boldsymbol{F}_A^{s,cg_{ref}}(\boldsymbol{x}, \boldsymbol{u}, \boldsymbol{p}) = \frac{1}{2}\rho V_{tas}^2 S \begin{bmatrix} -C_D \\ C_Y \\ -C_L \end{bmatrix} \tag{6-9}$$

$$\boldsymbol{M}_A^{s,cg_{ref}}(\boldsymbol{x}, \boldsymbol{u}, \boldsymbol{p}) = \frac{1}{2}\rho V_{tas}^2 S \begin{bmatrix} bC_l \\ cC_m \\ bC_n \end{bmatrix} \tag{6-10}$$

Where ρ is the air density, V_{tas} the true airspeed, b the wing span, $\bar{c}$ the mean aerodynamic chord and S the wing surface area. C_D, C_Y and C_L are the non-dimensional drag, side force and lift coefficients respectively and C_l, C_m and C_n are the non-dimensional moment coefficients. The aerodynamic coefficients are defined in the stability reference frame with cg_{ref} as origin, the aft limit of the aircraft center of gravity. The force and moment equations in body axis with the center of gravity cg as origin are defined as follows:

$$\boldsymbol{F}_A^{b,cg}(\boldsymbol{x}, \boldsymbol{u}, \boldsymbol{p}) = \mathbb{T}_{sb}^{-1} \boldsymbol{F}_A^{s,cg_{ref}}(\boldsymbol{x}, \boldsymbol{u}, \boldsymbol{p}) \tag{6-11}$$

$$\boldsymbol{M}_A^{b,cg}(\boldsymbol{x}, \boldsymbol{u}, \boldsymbol{p}) = \mathbb{T}_{sb}^{-1} \boldsymbol{M}_A^{s,cg_{ref}}(\boldsymbol{x}, \boldsymbol{u}, \boldsymbol{p}) + (\boldsymbol{r}_{cg_{ref}} - \boldsymbol{r}_{cg}) \times \boldsymbol{F}_A^{b,cg}(\boldsymbol{x}, \boldsymbol{u}, \boldsymbol{p}) \tag{6-12}$$

Where $\mathbb{T}_{sb}$ is the rotation matrix from the body to the stability reference frame, $\boldsymbol{r}_{cg_{ref}}$ and $\boldsymbol{r}_{cg}$ are the reference and actual position of the center of gravity, respectively.

6-3 Aerodynamic model

The non-dimensional aerodynamic force and moment coefficients are modeled as ordinary polynomials. The force coefficients are parametrized as follows:

$$C_D = C_{D_0} + C_{D_{\delta_e}}\delta_e + C_{D_{\delta_r^2}}\delta_r^2 + C_{D_q}\frac{q\bar{c}}{V_{tas}} \tag{6-13}$$

$$C_Y = C_{Y_\beta}\beta + C_{Y_{\delta_a}}\delta_a + C_{Y_{\delta_r}}\delta_r + C_{Y_r}\frac{rb}{2V_{tas}} \tag{6-14}$$

$$C_L = C_{L_0} + C_{L_{\delta_e}}\delta_e + C_{L_q}\frac{q\bar{c}}{V_{tas}} \tag{6-15}$$

The moment coefficients are parametrized in similar fashion:

$$C_l = C_{l_\beta}\beta + C_{l_{\delta_a}}\delta_a + C_{l_{\delta_r}}\delta_r + C_{l_{\delta_{t_a}}}\delta_{t_a} + C_{l_p}\frac{pb}{2V_{tas}} + C_{l_r}\frac{rb}{2V_{tas}} \tag{6-16}$$

$$C_m = C_{m_0} + C_{m_{\delta_e}}\delta_e + C_{m_{\delta_{t_e}}}\delta_{t_e} + C_{m_q}\frac{q\bar{c}}{V_{tas}} \tag{6-17}$$

$$C_n = C_{n_\beta}\beta + C_{n_{\delta_a}}\delta_a + C_{n_{\delta_r}}\delta_r + C_{n_{\delta_{t_r}}}\delta_{t_r} + C_{n_p}\frac{pb}{2V_{tas}} + C_{n_r}\frac{rb}{2V_{tas}} \tag{6-18}$$

Note that due to space restrictions, less important coefficients (e.g. ground effect) have been left out. Terms like C_{Y_0} may in turn depend on the angle of attack, Mach number, altitude etc. Note that for the inverse model, terms associated with the trim deflections are assumed zero as are higher order control effector terms.

Multiplicative uncertainties are added to the aerodynamic coefficients and the rotational inertia. As an example, the perturbed side force coefficient $\widetilde{C}_Y$ is defined as follows:

$$\widetilde{C}_Y = C_Y(1 + \Delta C_Y) \tag{6-19}$$

Where C_Y is the nominal value of the side force coefficient and ΔC_Y the corresponding tolerance parameter. These are up to 10% for the longitudinal coefficients and up to 30% for the lateral coefficients following standard practice, see Table 6-2.

6-4 Mass model

The aircraft mass, rotational inertia and center of gravity differ to a significant degree between the Citation I and the Citation II [20]. To this end, a highly accurate mass model of the Citation II was adopted from De Visser [17]. The model is based on the weight and balance calculation procedure of the Citation II and takes into account the mass and position of passengers, payload and fuel. The contribution of the fuel mass is updated by means of

Table 6-2: PH-LAB parameter uncertainty ranges

Symbol	Minimum	Nominal	Maximum
$\Delta\tau_{sync}$	-0.3	0	0.3
ΔJ_{xx}	-0.1	0	0.1
ΔJ_{yy}	-0.1	0	0.1
ΔJ_{yy}	-0.1	0	0.1
ΔJ_{xz}	-0.3	0	0.3
ΔC_D	-0.1	0	0.1
ΔC_L	-0.3	0	0.3
ΔC_Y	-0.1	0	0.1
ΔC_{l_β}	-0.3	0	0.3
ΔC_{m_0}	-0.1	0	0.1
ΔC_{n_β}	-0.3	0	0.3
ΔC_{l_p}	-0.3	0	0.3
ΔC_{l_r}	-0.3	0	0.3
ΔC_{m_q}	-0.1	0	0.1
ΔC_{n_p}	-0.3	0	0.3
ΔC_{n_r}	-0.3	0	0.3
$\Delta C_{l_{\delta_a}}$	-0.3	0	0.3
$\Delta C_{l_{\delta_r}}$	-0.3	0	0.3
$\Delta C_{m_{\delta_e}}$	-0.1	0	0.1
$\Delta C_{n_{\delta_a}}$	-0.3	0	0.3
$\Delta C_{n_{\delta_r}}$	-0.3	0	0.3

feedback of the used fuel and a model of the geometry of the fuel tanks. The model requires initial values for the usable fuel mass, the mass and position of passengers and payload, and the aircraft Basic Empty Weight (BEW) and corresponding rotational inertia (see Table 6-3). The output of the model consists of the current aircraft mass, center of gravity position and the rotational inertia.

Table 6-3: PH-LAB geometry, rotational inertia and center of gravity position [13, 17]

Symbol	Quantity	Unit
S	30	m^2
b	13.35	m
$\bar{c}$	2.0569	m
J_{xx} (BEW)	12392.2	$kg{\cdot}m^2$
J_{yy} (BEW)	31501.1	$kg{\cdot}m^2$
J_{zz} (BEW)	41908.4	$kg{\cdot}m^2$
J_{xz} (BEW)	2252.2	$kg{\cdot}m^2$
$x_{cg_{ref}}$	7.259	m
$y_{cg_{ref}}$	0	m
$z_{cg_{ref}}$	3	m

6-5 Actuator model

To assess the effect of actuators on the closed loop performance, actuator models are included in the simulation environment. Furthermore, INDI requires feedback of the deflection angle of the control surfaces. In case these are not available as measurement or model dependency is preferred over sensor dependency, accurate actuator models are required for estimation.

Actuator dynamics are typically modeled as first or second order systems [36]. The original Citation I actuator model is first-order. The flight control system of the Citation II is similar to the Citation I nevertheless, differences still exist [50]. Furthermore, the dynamics and limitations associated with the FBW system are not included in this model. The input-output response of the FBW system has been previously modeled as an equivalent time delay and gain [73]. This model does however not include actuator position or rate limits. A component-level model of the FBW system has been developed by Lubbers [45]. The rudder channel was however not included in this model. Use of an actuator model with this degree of complexity would also not fare conceptually with the model-independent nature of INDI.

Considering the above, it was chosen to develop a first-order model of the PH-LAB actuator system using available flight test data. The flight test data used in the modeling process contains responses to a series of open loop 3211 and doublet commands applied by the autopilot on elevator and aileron, this way any dynamics of the FBW system are included as well. This approach also allows to make a clear distinction between lag and delay components. Besides a first-order lag component, the model includes actuator position and rate limits, and a transport delay:

$$\dot{\delta}(t) = S_{\dot{\delta}}\Big(K_{fbw}\omega_{act}u(t-\tau_{act}) - \omega_{act}S_{\delta}\big(\delta(t)\big)\Big) \tag{6-20}$$

$$S_{\delta}(x) = \begin{cases} \delta_{max} & \text{if} \quad x > \delta_{max} \\ x & \text{if} \quad \delta_{min} \leq x \leq \delta_{max} \\ \delta_{min} & \text{if} \quad x < \delta_{min} \end{cases} \tag{6-21}$$

$$S_{\dot{\delta}}(x) = \begin{cases} \dot{\delta}_{max} & \text{if} \quad x > \dot{\delta}_{max} \\ x & \text{if} \quad |x| \leq \dot{\delta}_{max} \\ -\dot{\delta}_{max} & \text{if} \quad x < -\dot{\delta}_{max} \end{cases} \tag{6-22}$$

Where K_{fbw} is the FBW input-output gain, δ is the deflection angle of the control effector, u the input, ω_{act} the actuator bandwidth and τ_{act} the transport delay. The saturation functions for actuator position and rate are S_{δ} and $S_{\dot{\delta}}$, respectively.

The actuator bandwidth is determined by fitting the measured deflection angle to the general step input time response of a first-order system:

$$\delta(t+\tau_{act}) = \delta_0 + K_{fbw}u_{step}(1-\mathrm{e}^{-t\omega_{act}}) \tag{6-23}$$

Where u_{step} is the step input size and δ_0 is the initial deflection angle. A nonlinear least square curve-fitting method is selected to find the optimum fit for ω_{act} for each step input command. The average value is taken as final estimate. Note that not all data proofed to be

usefull for modeling as during some maneuvers the actuators were saturated. The actuator bandwidth proofed to be very similar to the actuator model of the Citation I. The transport delay has been determined in previous research [68] although misidentified as sensor delay, see also Section 5-4.

For each step input command the maximum rate of deflection $\dot{\delta}_{max}$ is determined as well, the average is taken as a final estimate. Note that the actuator model does not include speed dependent position limiting.

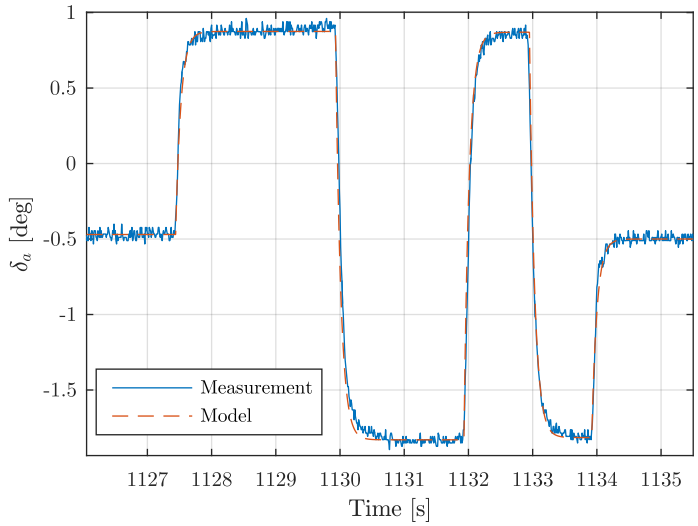

Figure 6-1: Response aileron deflection to 3211 input command (175 KIAS FL90)

Table 6-4: Actuator model parameters

	δ_{max} [deg]	δ_{min} [deg]	K_{fbw} [-]	$\dot{\delta}_{max}$ [deg/s]	τ_{act} [ms]	ω_{act} [rad/s]
Aileron	15	-19	0.70	19.7 ($\sigma = 4.81$)	39.8 ($\sigma = 7.91$)	12.4 ($\sigma = 2.30$)
Elevator	15	-17	0.60			
Rudder	22	-22	0.55			

6-6 Sensor models

The following sensor characteristics are modeled: noise, bias, delay, lag and quantization effects (see Table 5-2). The noise is modeled as a zero-mean Gaussian process. In addition, kinematic position errors are applied on the specific force and airflow direction signals. The disturbances induced by the flexibility of the air data boom are modeled as a 10 Hz sinusoidal signal.

Chapter 7

Control law design

This chapter covers the design and integration of the individual controller functions. This includes the construction of the actual synthesis of the controller components and signal processing algorithms. The individual functions are integrated in a standard controller architecture. These have been developed over the years at the institute of System Dynamics and Control (SR) of the German Aerospace Institute (DLR). For implementation the MATLAB/Simulink environment is used.

The controller is designed as a manual control system proving command augmentation and stabilization. The design is based upon earlier manual control functions developed for the VFW-614 ATTTAS [37] but uses Incremental Nonlinear Dynamic Inversion for the inner rate-loop. The objective of the controller is two-fold: Rate Control Attitude Hold (RCAH) and Attitude Control (AC). RCAH is governed between $\pm 27^\circ$ and $\pm 15^\circ$ for roll and pitch, respectively. AC is governed outside this range up to $\pm 35^\circ$ and $\pm 20^\circ$ for roll and pitch, respectively. The lateral tracking task includes the angle of sideslip as well. An important functionality of this controller is Pseudo Control Hedging (PCH), used for adaptation of the reference model output in case of actuator saturation

The chapter is structured as follows. Section 7-1 presents the design of the dynamic inversion inner rate-loop. The design of the outer loop is presented in Section 7-2. Finally in Section 7-3, the signal processing design will be presented.

7-1 Inner loop

This section will discuss the design of the inner loop, see Figure 7-1. (I)NDI is applied to the rotational dynamics of the aircraft. The control variables $\boldsymbol{y}$ are set equal to the body angular rates $\boldsymbol{\omega} = [p, q, r]^{\mathrm{T}}$. The aileron, elevator and rudder deflection are selected as input, i.e. $\boldsymbol{u} = [\delta_a, \delta_e, \delta_r]^{\mathrm{T}}$.

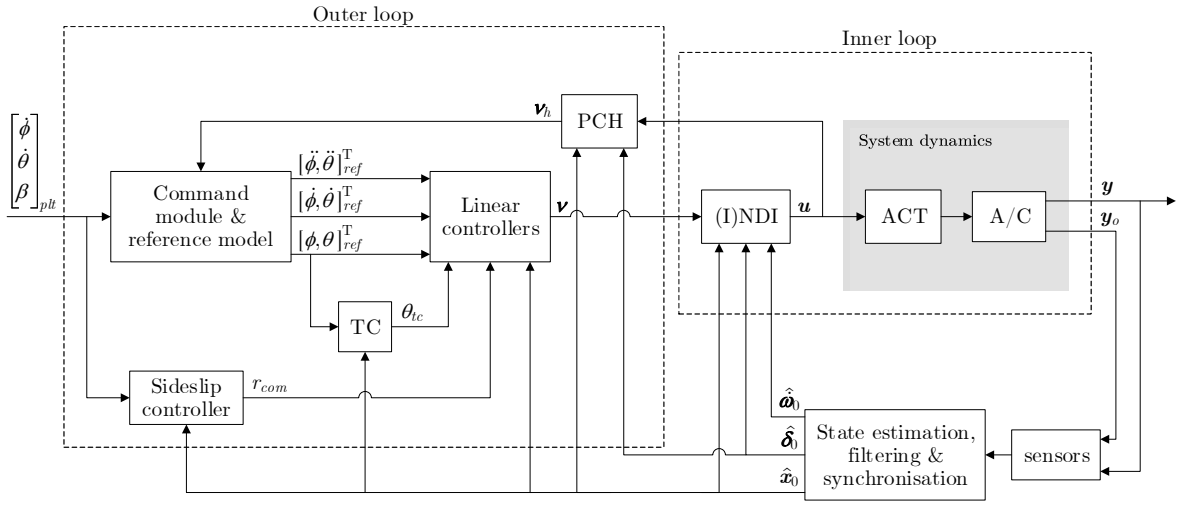

Figure 7-1: General controller structure

7-1-1 Angular rate NDI

The analytic relationship between the body angular rates and control surface deflections arises directly from Euler's rotation equations, see Equation (6-5). Neglecting the moment induced by the thrust $\boldsymbol{M}_T$, the aerodynamic moment $\boldsymbol{M}_A$ can be split into into an airframe dependent part $\boldsymbol{M}_a$ and a part dependent on the control effectors $\boldsymbol{M}_c$. These are assumed to be of the following form:

$$\boldsymbol{M}_a(\boldsymbol{x},\boldsymbol{p}) = \frac{1}{2}\rho V_{tas}^2 S \begin{bmatrix} bC_{l_a} \\ \bar{c}C_{m_a} \\ bC_{n_a} \end{bmatrix} \tag{7-1}$$

$$\frac{\partial \boldsymbol{M}_c(\boldsymbol{x},\boldsymbol{p},\boldsymbol{u})}{\partial \boldsymbol{u}} = \boldsymbol{M}_{c_{\boldsymbol{\delta}}}(\boldsymbol{x},\boldsymbol{p}) = \frac{1}{2}\rho V_{tas}^2 S \begin{bmatrix} bC_{l_{\delta_a}} & 0 & bC_{l_{\delta_r}} \\ 0 & \bar{c}C_{m_{\delta_e}} & 0 \\ bC_{n_{\delta_a}} & 0 & bC_{n_{\delta_r}} \end{bmatrix} \tag{7-2}$$

Where ρ is the air density, V_{tas} the true airspeed, S the wing surface area, b the wing span, $\bar{c}$ the mean aerodynamic chord, $\boldsymbol{x}$ the aircraft states and $\boldsymbol{p}$ the model parameters. Note that it is assumed that $\boldsymbol{M}_c$ is linear in $\boldsymbol{u}$. Equation (6-5) can be rewritten as follows:

$$\dot{\boldsymbol{\omega}} = \boldsymbol{J}^{-1}(\boldsymbol{p})\big(\boldsymbol{M}_a(\boldsymbol{x},\boldsymbol{p}) + \boldsymbol{M}_{c_{\boldsymbol{\delta}}}(\boldsymbol{x},\boldsymbol{p})\boldsymbol{u} - \boldsymbol{\omega} \times \boldsymbol{J}(\boldsymbol{p})\boldsymbol{\omega}\big) \tag{7-3}$$

Applying dynamic inversion to Equation (7-3), the following control law is obtained:

$$\boldsymbol{u} = \underbrace{\boldsymbol{M}_{c_{\boldsymbol{\delta}}}^{-1}(\hat{\boldsymbol{x}},\boldsymbol{p}^*)\boldsymbol{J}(\boldsymbol{p}^*)}_{(L_{\boldsymbol{G}}\boldsymbol{h})^{-1}} \Big(\boldsymbol{\nu} - \underbrace{\boldsymbol{J}^{-1}(\boldsymbol{p}^*)\big(\boldsymbol{M}_a(\hat{\boldsymbol{x}},\boldsymbol{p}^*) - \boldsymbol{\omega} \times \boldsymbol{J}(\boldsymbol{p}^*)\boldsymbol{\omega}\big)}_{L_{\boldsymbol{f}}\boldsymbol{h}}\Big) \tag{7-4}$$

7-1-2 Angular rate INDI

The incremental form of Euler's rotation equation is obtained following a first-order Taylor expansion of Equation (7-3) around the current point in time '0':

$$\dot{\boldsymbol{\omega}} \approx \dot{\boldsymbol{\omega}}_0 + \frac{\partial}{\partial \boldsymbol{\omega}}\Big(\boldsymbol{J}^{-1}(\boldsymbol{p})\big(\boldsymbol{M}_a(\boldsymbol{x},\boldsymbol{p}) + \boldsymbol{M}_{c_{\boldsymbol{\delta}}}(\boldsymbol{x},\boldsymbol{p})\boldsymbol{u} - \boldsymbol{\omega}\times\boldsymbol{J}(\boldsymbol{p})\boldsymbol{\omega}\big)\Big)\Big|_{\substack{\boldsymbol{\omega}=\boldsymbol{\omega}_0\\ \boldsymbol{u}=\boldsymbol{u}_0}} \underbrace{(\boldsymbol{\omega}-\boldsymbol{\omega}_0)}_{\Delta\boldsymbol{\omega}} + \frac{\partial}{\partial \boldsymbol{u}}\Big(\boldsymbol{J}^{-1}(\boldsymbol{p})\big(\boldsymbol{M}_a(\boldsymbol{x},\boldsymbol{p}) + \boldsymbol{M}_{c_{\boldsymbol{\delta}}}(\boldsymbol{x},\boldsymbol{p})\boldsymbol{u} - \boldsymbol{\omega}\times\boldsymbol{J}(\boldsymbol{p})\boldsymbol{\omega}\big)\Big)\Big|_{\substack{\boldsymbol{\omega}=\boldsymbol{\omega}_0\\ \boldsymbol{u}=\boldsymbol{u}_0}} \underbrace{(\boldsymbol{u}-\boldsymbol{u}_0)}_{\Delta\boldsymbol{u}} \tag{7-5}$$

Again assuming $\boldsymbol{\omega} - \boldsymbol{\omega}_0 = 0$, Equation (7-5) reduces to:

$$\dot{\boldsymbol{\omega}} \approx \dot{\boldsymbol{\omega}}_0 + \boldsymbol{J}^{-1}(\boldsymbol{p})\boldsymbol{M}_{c_{\boldsymbol{\delta}}}(\boldsymbol{x}_0,\boldsymbol{p})\Delta\boldsymbol{u} \tag{7-6}$$

Applying dynamic inversion to Equation (7-6) and adding the current control surface deflections $\boldsymbol{\delta}_0$, the following control law is obtained:

$$\boldsymbol{u} = \underbrace{\boldsymbol{M}_{c_{\boldsymbol{\delta}}}^{-1}(\hat{\boldsymbol{x}}_0,\boldsymbol{p}^*)\boldsymbol{J}(\boldsymbol{p}^*)}_{\boldsymbol{G}^{-1}}(\boldsymbol{\nu} - \underbrace{\hat{\dot{\boldsymbol{\omega}}}_0}_{\dot{\boldsymbol{x}}_0}) + \hat{\boldsymbol{\delta}}_0 \tag{7-7}$$

7-2 Outer loop [37]

This section will discuss the design of the outer loop, see Figure 7-1. The outer loop consists of the following components: command module & reference model, sideslip controller, Turn Compensation (TC), linear controllers and Pseudo Control Hedging (PCH).

7-2-1 Command module & reference model

The command module and reference model serve as attitude flight envelope protection and command filter, respectively. Furthermore, the command module blends two different control methods: rate control attitude hold (RCAH) and attitude control (AC). RCAH is active between 27° and −27° for roll and between 15° and −15° for pitch. When these limits are reached the feedforward term is deactivated and the pilot command signal is directly added to the saturated signal, see Figure 7-2. This way the attitude angles are directly governed by the pilot command input. AC is active up to ±35° for roll and ±20° for pitch, these are the limit values of the system. Note that for zero pilot input command in AC mode, the system will always command the aircraft back to the RCAH attitude limits. The purpose of this setup is to reduce violent behavior when the roll and pitch limits of the system are reached. The gain K_2 in the command module is required to achieve a smooth transition between AC and RACH. The reference model is a conventional second-order system smoothing the command signals to values achievable by the aircraft, see Equation (7-8).

$$H_{ref}(s) = \frac{K_1 K_2}{s^2 + K_1 s + K_1 K_2} = \frac{\omega_{n_{ref}}^2}{s^2 + 2\zeta_{ref}\omega_{n_{ref}} s + \omega_{n_{ref}}^2} \tag{7-8}$$

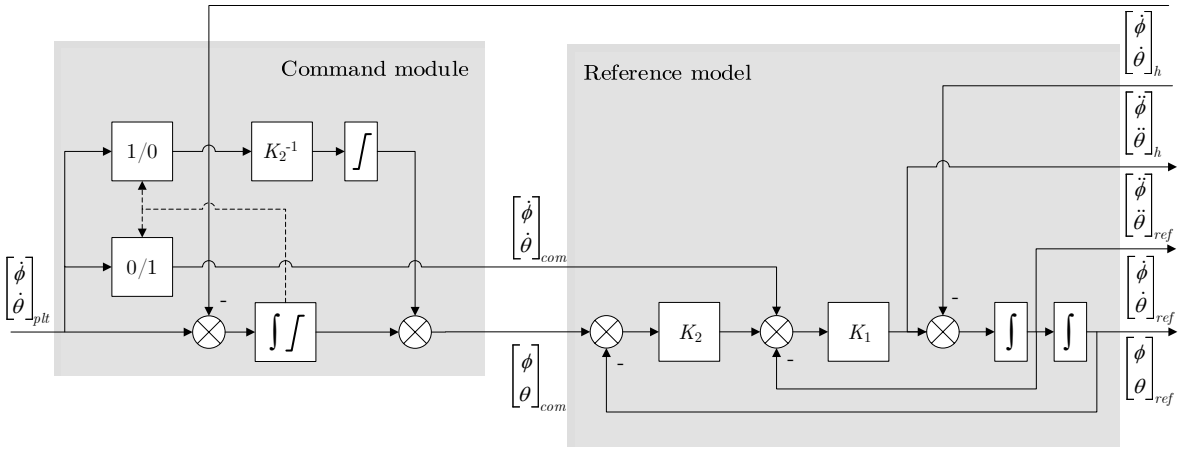

Figure 7-2: Command module & reference model [37]

7-2-2 Sideslip controller

For manual control, the angle of sideslip is preferred as outer loop control variable. Furthermore, as there is no means to manually control the yaw axis due to absence of a yaw input device, coordinated flight is only possible by means of direct sideslip augmentation. The control setup therefore includes a sideslip controller:

$$r_{com} = \frac{1}{V_{tas}}(wp - A_y) - \left(\frac{1}{s}K_{\beta_I}(\beta_{plt} - \beta) - K_\beta \beta\right) \tag{7-9}$$

The following approximation for w is used in absence of a direct measurement:

$$w = V_{tas}\sin(\alpha) \approx V_{tas}\alpha \tag{7-10}$$

7-2-3 Turn Compensation

The control setup includes a turn compensation (TC) module with the following control law:

$$\theta_{tc} = \Big(\cos\big(D(\phi_{ref})\big) - 1\Big)\frac{mg}{\frac{1}{2}\rho_0 V_{cas}^2 S C_{L_\alpha}} \tag{7-11}$$

Where D is the deadband function:

$$D(x) = \begin{cases} \phi_{ref} & \text{if} \quad |x| > \frac{\pi}{180} \\ 0 & \text{if} \quad |x| \leq \frac{\pi}{180} \end{cases} \tag{7-12}$$

7-2-4 Linear controllers

The linear controllers are defined in Equations (7-13) to (7-15). For the pitch and roll channel, the controllers operate up to the 2nd order time derivative.

$$\nu_{\dot{\phi}} = \left(K_{\phi} + \frac{K_{\phi_I}}{s}\right)(\phi_{ref} - \phi) + K_{\dot{\phi}}(\dot{\phi}_{ref} - \dot{\phi}) + K_{\ddot{\phi}}\ddot{\phi}_{ref} \tag{7-13}$$

$$\nu_{\dot{\theta}} = \left(K_{\theta} + \frac{K_{\theta_I}}{s}\right)(\theta_{ref} + \theta_{tc} - \theta) + K_{\dot{\theta}}(\dot{\theta}_{ref} - \dot{\theta}) + K_{\ddot{\theta}}\ddot{\theta}_{ref} \tag{7-14}$$

$$\nu_r = K_r(r_{com} - r) \tag{7-15}$$

Kinematic inversion of Equations (7-13) and (7-14) immediately results in:

$$\begin{bmatrix} \nu_p \\ \nu_q \\ \nu_r \end{bmatrix} = \mathbb{T}_{\Phi b}^{-1} \begin{bmatrix} \nu_{\dot{\phi}} \\ \nu_{\dot{\theta}} \\ \nu_{\dot{\psi}} \end{bmatrix} - \dot{\mathbb{T}}_{\Phi b} \begin{bmatrix} p \\ q \\ r \end{bmatrix} \tag{7-16}$$

7-2-5 Pseudo Control Hedging

Pseudo Control Hedging is implemented slightly differently as in [37], where hedging was only activated upon saturation of the actuator model. As the PH-LAB actuator model does not include speed dependent position limiting, activation upon model saturation is not desirable. In this setup, upon manual activation, compensation will be provided irrespective of actuator saturation.

Consider again Equation (2-17), substituting the results obtained in Section 7-1 for $\boldsymbol{G}$, the virtual control hedge $\boldsymbol{\nu}_h$ is obtained as follows:

$$\boldsymbol{\nu}_h = \underbrace{\boldsymbol{M}_{c_{\boldsymbol{\delta}}}(\hat{\boldsymbol{x}}_0, \boldsymbol{p}^*)\boldsymbol{J}^{-1}(\boldsymbol{p}^*)}_{\boldsymbol{G}}(\boldsymbol{u} - \hat{\boldsymbol{\delta}}) \tag{7-17}$$

Kinematic inversion of Equation (7-17) immediately results in:

$$\begin{bmatrix} \nu_{\dot{\phi}} \\ \nu_{\dot{\theta}} \\ \nu_{\dot{\psi}} \end{bmatrix}_h = \mathbb{T}_{\Phi b} \begin{bmatrix} \nu_p \\ \nu_q \\ \nu_r \end{bmatrix}_h + \dot{\mathbb{T}}_{\Phi b} \begin{bmatrix} p \\ q \\ r \end{bmatrix} \tag{7-18}$$

The compensation signal is subtracted from the reference signal $[\ddot{\phi}_{ref}, \ddot{\theta}_{ref}]^{\mathrm{T}}$, see Figure 7-2. The command module also requires hedging as the commanded attitude $[\phi_{com}, \theta_{com}]^{\mathrm{T}}$ is obtained via integration of the pilot rate command $[\dot{\phi}_{plt}, \dot{\theta}_{plt}]^{\mathrm{T}}$, leaving the commanded attitude unhedged would lead to undesired overshoot.

7-3 State estimation, filtering and synchronization

Good quality sensor signals are imperative to (I)NDI control. Not all signals provided by the PH-LAB sensor systems are processed and might contain disturbances that would propagate through the control laws without filtering. Inertial sensors are sensitive to structural vibrations while air data sensors pick up atmospheric turbulence. The flexibility of the PH-LAB air data boom also adds a 10 Hz disturbance to the airflow direction signals. The filtering techniques proposed here are in part taken from Looye and Joos [41].

The angular acceleration signals require additional attention as these are obtained via differentiation. Careful filtering of the angular rates is necessary to reduce sensor noise. The angular rate and control deflection signals also require synchronization.

7-3-1 Inertial data

The angular rates are filtered with a second-order low-pass filter [3]:

$$H_{fil}(s) = \frac{\omega_{n_{fil}}^2}{s^2 + 2\zeta_{fil}\omega_{n_{fil}} + \omega_{n_{fil}}^2} \tag{7-19}$$

The natural frequency $\omega_{n_{fil}}$ is set equal to 20 rad/s and the damping ratio ζ_{fil} is unity. The remainder of the inertial signals are filtered using first-order low-pass filters with a time constant of 50 ms.

7-3-2 Air data

All DADC and airflow direction signals (see Table 5-2) are combined with inertial measurements using a first-order complementary filter:

$$\hat{x} = \frac{1}{\tau_{fil}s + 1}x + \frac{\tau_{fil}s}{\tau_{fil}s + 1}x_i \tag{7-20}$$

Where x_i is the inertial equivalent of air data signal x. The filter time constant τ_{fil} is set equal to 1 s. Note that for some signals the derivative of the inertial signal is used as high-pass signal (i.e. substitute $\dot{x}_i$ for sx_i in Equation 7-20).

The inertial speed $\dot{V}_i$ is calculated from the linear accelerations ($\mathcal{F}_b \rightarrow \mathcal{F}_a$):

$$\dot{V}_i = \begin{bmatrix} a_x & a_y & a_z \end{bmatrix} \begin{bmatrix} \cos(\alpha)\cos(\beta) \\ \sin(\beta) \\ \sin(\alpha)\cos(\beta) \end{bmatrix} \tag{7-21}$$

The linear accelerations are obtained from the specific force measurements by addition of the gravitational component ($\mathcal{F}_E \rightarrow \mathcal{F}_b$):

$$\begin{bmatrix} a_x \\ a_y \\ a_z \end{bmatrix} = g \left(\begin{bmatrix} A_x \\ A_y \\ A_z \end{bmatrix} + \begin{bmatrix} -\sin(\theta) \\ \cos(\theta)\sin(\phi) \\ \cos(\theta)\cos(\phi) \end{bmatrix} \right) \tag{7-22}$$

The derivative of the inertial vertical speed $\ddot{h}_i$ is obtained from the linear accelerations ($\mathcal{F}_b \rightarrow \mathcal{F}_E$):

$$\ddot{h}_i = \begin{bmatrix} a_x & a_y & a_z \end{bmatrix} \begin{bmatrix} \sin(\theta) \\ -\cos(\theta)\sin(\phi) \\ -\cos(\theta)\cos(\phi) \end{bmatrix} \tag{7-23}$$

The altitude h is complemented with the complementary filtered vertical speed $\hat{\dot{h}}$. An approximation is used for the inertial Mach number M_i:

$$M_i \approx \frac{V_{tas}}{20.05\sqrt{(288.2 - 0.0065h)}} \tag{7-24}$$

The inertial angle of attack α_i is computed as follows:

$$\alpha_i = \theta - \gamma_a \tag{7-25}$$

Where γ_a is the air-mass referenced flight path angle:

$$\gamma_a = \sin\left(\frac{\dot{h}}{V_{tas}}\right) \approx \frac{\dot{h}}{V_{tas}} \tag{7-26}$$

The derivative of the inertial angle of sideslip $\dot{\beta}_i$ is obtained as follows:

$$\dot{\beta}_i = \frac{A_y g + g\sin(\phi)\cos(\theta)}{V_{tas}} - r\cos(\alpha) + p\sin(\alpha) \tag{7-27}$$

For comparative reasons the angle of sideslip is estimated as well. The estimated angle of sideslip β_{est} is obtained as follows:

$$\beta_{est} = \frac{1}{C_{Y_\beta}} \left(\frac{A_y mg}{\frac{1}{2}\rho_0 V_{cas}^2 S} - C_{Y_{rest}} \right) \tag{7-28}$$

Where $C_{Y_{rest}}$ and C_{Y_β} are determined by rearranging the side force equation of the aerodynamic model into the following form:

$$C_Y = C_{Y_\beta}(M, \alpha, ...)\beta + C_{Y_{rest}}(M, \alpha, \delta_r, ...) \tag{7-29}$$

A second-order complementary filter is used to prevent bias in case of long duration cross wind shear:

$$\hat{\beta}_{est} = \frac{K_1 s + K_2}{s^2 + K_1 s + K_2}\beta_{est} + \frac{s}{s^2 + K_1 s + K_2}\dot{\beta}_i \tag{7-30}$$

The filtering gains K_1 and K_2 are set equal to 1 and 0.2, respectively.

7-3-3 Control deflection

Synchronization between control deflection and angular acceleration feedback is achieved by applying equivalent filtering and artificially adding the surplus of angular rate delay to the control deflection signal [61, 69]:

$$\hat{\boldsymbol{\delta}}_0 = H_{fil}(s)H_{sync}(s)\boldsymbol{\delta} \tag{7-31}$$

Where H_{sync} is the frequency-domain equivalent of a pure time delay τ_{sync} corresponding to the surplus of angular rate delay. To account for variations in delay (e.g. due to sampling or unmodeled delays), a multiplicative uncertainty is added to τ_{sync}. Alternatively, the synchronized control deflections may be estimated using actuator models:

$$\hat{\boldsymbol{\delta}}_{0_{est}} = \frac{z^{-1}H_{act}(s)H_{fil}(s)H_{sync}(s)}{1 - z^{-1}H_{act}(s)H_{fil}(s)H_{sync}(s)}\Delta\boldsymbol{u} \tag{7-32}$$

Where H_{act} represents the actuator dynamics i.e. the frequency-domain equivalent of Equation (6-20). Note that z^{-1} is the increment delay, strictly this term is required as $\Delta\boldsymbol{u}$ is one incremental time step ahead of $\boldsymbol{\delta}_0$.

Chapter 8

Design optimization

This chapter covers the formulation of the design specifications and overall optimization of the integrated control system developed in Chapter 7. For the tuning of the control laws multi-objective optimization is used. The Institute of System Dynamics and Control (SR) of the German Aerospace Institute (DLR) developed the Multi-Objective Parameter Synthesis (MOPS) tool specifically for this purpose [32].

Multi-objective optimization allows a large set of criteria to be simultaneously addressed and aims to locate the best-compromise solution [43]. Scaling functions are used to assign relative importance to the criteria. Looye and Joos [41] developed a structured approach to multi-objective control law design whereby robustness is addressed using a multi-model approach in combination with local robustness criteria. The former is used to achieve robustness to parametric uncertainties in the synthesis model, the latter to unspecified uncertainties. This approach will be closely followed and adapted to the needs of the current project. Note that the optimization is performed separately for the longitudinal and lateral aircraft dynamics.

This chapter is structured as follows. In Section 8-1 the design specifications will be formulated and translated to numerical evaluable criteria. In Sections 8-2 and 8-3 the robustness and handling quality criteria will be further elaborated on. The tuning of the synthesis parameters is performed in Section 8-4. The resulting NDI and INDI design will be compered in Section 8-5. Finally in Section 8-6 some conclusions and recommendations are provided.

8-1 Design criteria [41]

Multi-objective optimization requires a set of computable criteria that can be used for optimization. The design criteria for the longitudinal and lateral synthesis parameters are defined in Tables 8-1 and 8-2, respectively. These are computed from nonlinear simulations and a linear analysis of the closed-loop system. The former are used to evaluate the reference tracking with criteria concerning overshoot, rise time, settling time and control effort. A second simulation is used to assess the disturbance rejection by means of a (cross)-wind step.

The criteria are formulated as min-max optimization problems and scaled such that a value smaller than 1 is considered satisfactory. The criteria corresponding to the nonlinear simulations are scaled by division of the corresponding demand value:

$$\hat{c}_{j,k}(\boldsymbol{T}) = \frac{c_{j,k}(\boldsymbol{T})}{d_j} \tag{8-1}$$

Where $c_{j,k}$ is the computed value of criterion j and model case k, and d_j the corresponding demand value. The tuning parameters are contained in $\boldsymbol{T}$, these are the linear controller gains and reference model parameters, see Equations (7-13) to (7-15) and Equation (7-8), respectively. The criteria corresponding to the linear analysis are scaled using 'good-bad' values [32]. With this scaling type, it is demanded that the criterion is at least equal to the 'bad-low' ('bad-high') value. The region between 'bad-low' ('good-high') and 'good-low' ('bad-high') is considered acceptable with linearly decreasing (increasing) scaling. Values larger (smaller) than 'good low' ('good high') are considered equally good and are subsequently scaled to 0. Notice that for some of the criteria in Tables 8-1 and 8-2 an inequality constraint is used such that no further optimization is performed after the demand value is obtained.

Table 8-1: Design criteria MOPS, longitudinal part. All simulations: symmetrical horizontal flight; $V_{tas} = 123$ m/s

Name	Description	Calculation	Bad-low/ good-high	Good-low/ bad-high	Demand	Type
Simulation 1: Box-cart: $\dot{\theta}_{plt} = 2.5°/s$ at $t = 1$ till $t = 6$ s						
osdthe [-]	Overshoot $\dot{\theta}$		-	-	0.5	c
rtdthe [s]	Rise time $\dot{\theta}$	0%→100%	-	-	0.75	c
stdthe [s]	Settling time $\dot{\theta}$	0.1°	-	-	4	m
osthe [-]	Overshoot θ		-	-	0.1	c
dbratio [s]	Dropb. r. $\frac{DB}{q_{ss}}$		0/0	0/0.1	-	m
stthe [s]	Settling time θ	0.1°	-	-	4	m
maxdde [deg/s]	Maximum $\dot{\delta}_e$	$\max\lvert\dot{\delta}_e\rvert$	-	-	20	m
Simulation 2: Wind step $w_{wind} = 16$ m/s at $t = 1$ s						
maxthe [deg]	Maximum θ	$\max\lvert\theta - \theta_0\rvert$	-	-	3.35	m
maxde [deg]	Maximum δ_e	$\max\lvert\delta_e\rvert$	-	-	15	m
Linear analysis:						
gmde [dB]	Gain margin δ_e		4/-	6/-	-	m
pmde [deg]	Phase margin δ_e		40/-	60/-	-	c
gmq [dB]	Gain margin q		4/-	6/-	-	m
pmq [deg]	Phase margin q		40/-	60/-	-	c
m=minimize, c=inequality constraint						

8-2 Robustness [41]

The robustness of the control law is addressed in two ways. A multi-model approach is used to achieve robustness to parametric uncertainties. The multi-model setup is created by adding

Table 8-2: Design criteria MOPS, lateral part. All simulations: symmetrical horizontal flight; $V_{tas} = 123$ m/s

Name	Description	Calculation	Bad-low	Good-low	Demand	Type
Simulation 1: Box-cart: $\dot{\phi}_{plt} = 5$ °/s at $t = 1$ till $t = 6$ s						
osdphi [-]	Overshoot $\dot{\phi}$		-	-	0.5	c
rtdphi [s]	Rise time $\dot{\phi}$	0%→100%	-	-	0.75	c
stdphi [s]	Settling time $\dot{\phi}$	0.1°	-	-	4	m
osphi [-]	Overshoot ϕ		-	-	0.1	c
rtphi [s]	Rise time ϕ	0%→100%	-	-	5	c
stphi [s]	Settling time ϕ	0.1°	-	-	4	m
maxdda [deg/s]	Maximum $\dot{\delta}_a$	$\max\lvert\dot{\delta}_a\rvert$	-	-	40	m
errbeta [deg]	Error β	$\int_0^T \lvert\beta\rvert \mathrm{d}t/T$	-	-	0.5	m
Simulation 2: Step $\beta_{plt} = 5°$ at $t = 1$ s						
osbeta [-]	Overshoot β		-	-	0.01	c
rtbeta [s]	Rise time β	10%→90%	-	-	4	m
stbeta [s]	Settling time β	0.1°	-	-	5	m
maxddr [deg/s]	Maximum $\dot{\delta}_r$	$\max\lvert\dot{\delta}_r\rvert$	-	-	20	m
errphi [deg]	Error ϕ	$\int_0^T \lvert\phi\rvert \mathrm{d}t/T$	-	-	0.5	m
Simulation 3: Wind step $v_{wind} = 16$ m/s at $t = 1$ s						
maxphi [deg]	Maximum ϕ	$\max\lvert\phi\rvert$	-	-	6.7	m
maxdr [deg]	Maximum δ_r	$\max\lvert\delta_r\rvert$	-	-	22	m
Linear analysis:						
gmda [dB]	Gain margin δ_a		4	6	-	m
pmda [deg]	Phase margin δ_a		30	60	-	c
gmdr [dB]	Gain margin δ_r		4	6	-	m
pmdr [deg]	Phase margin δ_r		30	60	-	c
gmp [dB]	Gain margin p		4	6	-	m
pmp [deg]	Phase margin p		30	60	-	c
gmr [dB]	Gain margin r		4	6	-	m
pmr [deg]	Phase margin r		30	60	-	c
m=minimize, c=inequality constraint						

a number of model cases with worst-case parameter combinations to the nominal case. These worst-cases are defined with respect to one of the design criteria defined in Tables 8-1 and 8-2. The optimization process addresses the criteria simultaneously for all model cases allowing for trade-off between criteria under worst-case and nominal parameter conditions. Note that this approach implicitly assumes that the controller is also robust to model cases in between those addressed. To this end also local robustness margins are included as optimization criteria. These are the minimum phase and gain margins at the sensor and actuator positions listed in Tables 8-1 and 8-2. Note that the local robustness criteria are also intended to achieve robustness to unspecified uncertainties (e.g. unmodeled dynamics and time delays).

8-3 Handling qualities

The controller is designed as an augmented manual control system, handling qualities are therefore an important design consideration. To optimize the longitudinal response for manual tracking tasks, the Gibson dropback criterion [22] (included in MIL-STD-1797A) and its updated version [48] are included as optimization criteria. A secondary goal of these criteria is to limit the risk of Pilot Induced Oscillations (PIO).

The Gibson dropback criterion is based on the analysis of the aircraft response to a positive box-car input on the pitch rate. The parameters involved in the criterion include the peak pitch rate, q_{peak}, and the attitude dropback, both normalized to the steady state pitch rate q_{ss}. The dropback DB is defined as the difference between the pitch attitude at the instance the input is removed θ_{out} and the steady state pitch attitude θ_{ss}, i.e. $DB = \theta_{out} - \theta_{ss}$. Note that a negative value of this difference is termed overshoot. The updated Gibson criterion uses a different dropback definition, focusing more on the mid-frequency range of the attitude response. The updated dropback $\Delta\theta$ is defined as the difference between the peak pitch attitude θ_{peak} and the steady state pitch attitude, i.e. $\Delta\theta = \theta_{peak} - \theta_{ss}$. The acceptable ranges for these parameters are visualized in Figure 8-8.

The most optimal tracking behavior is obtained with a dropback ratio $\frac{DB}{q_{ss}}$ of 0 s with values up to 0.1 s considered good, these are subsequently used as 'good-high' and 'bad-high' demand values, respectively. Satisfaction of *dbratio* and the pitch attitude overshoot criterion *osphi* also implies that the updated dropback ratio $\frac{\Delta\theta}{q_{ss}}$ falls within the desired region. This also applies to the pitch rate overshoot criterion *osdphi* and the pitch rate overshoot ratio $\frac{q_{peak}}{q_{ss}}$.

8-4 Parameter synthesis [41]

The parameter synthesis was performed in three successive steps. First the linear controller gains and reference model parameters were optimized. With the resulting tuning parameter set, a worst-case analyses was performed. Note that it was assumed that the worst-cases are to be found at the extremities of the parameter space. To this end, minimum or maximum values were selected for the parametric model uncertainties. The criteria were evaluated for all parameter combinations. To limit the number of combinations for NDI, tolerances on the moment of inertia and less relevant aerodynamic coefficients were left out.

The two criteria that proofed most sensitive to parameter variations were added as separate model cases to the nominal model to form a multi-model set. An additional parameter synthesis was performed for this set of model-cases. The results can be found in Tables 8-3 and 8-4. Note that the maximum uncertainty on the lateral moment coefficients has been slightly relieved to 20%, else a satisfactory design for the NDI controller could not be realized.

8-5 Assessment

The best-compromise solution for INDI and NDI will now be compared. Notice in Table 8-4 that for INDI a significantly lower integrator gain K_{ϕ_I} was selected by the optimizer compared to NDI. This behaviour can be attributed to the incremental nature of INDI as the calculated

Table 8-3: Controller synthesis parameters longitudinal part

Tuning parameter	INDI			NDI		
Linear controller gains:						
K_θ	7.76			8.99		
K_{θ_I}	0.500			3.73		
$K_{\dot{\theta}}$	3.02			5.18		
$K_{\ddot{\theta}}$	0.524			0.534		
Reference model parameters:						
ζ_{ref}	1.00			0.998		
$\omega_{n_{ref}}$	2.99			1.13		
Uncertain model parameters:						
	nominal	worst pmde	worst pmq	nominal	worst pmde	worst pmq
$\Delta\tau_{sync}$	0	-0.3	-0.3	0	0	0
ΔJ_{yy}	0	0.1	-0.1	0	0.1	-0.1
ΔC_L	0	0.1	-0.1	0	-0.1	0.1
ΔC_D	0	0.1	0.1	0	-0.1	-0.1
ΔC_{m_0}	0	0	0	0	-0.1	0.1
$\Delta C_{m_{\delta_e}}$	0	-0.1	0.1	0	0.1	0.1
ΔC_{m_q}	0	0	0	0	-0.1	-0.1

increment is added to the current input, basically acting as an integral term. Further notice that for the worst cases the optimizer pushed the synchronization uncertainty $\Delta\tau_{sync}$ to its minimum value. This behaviour was expected considering that a surplus of state derivative delay results in relatively fast system instability [68]. Steady-state offsets in the angular rate tracking were effectively regulated by the linear controllers. The steady errors in the sideslip tracking are the result of measurement bias. The settling time calculation was subsequently relieved to 0.2°. Note that the noise was deactivated during the optimization as this would cause inconsistencies between the different evaluations.

The values of the scaled criteria corresponding to the synthesis parameters defined in Tables 8-3 and 8-4 are visualized in Figures 8-1 and 8-2. Note that values smaller than 1 are considered satisfactory. Observe that for INDI all criteria are satisfied under nominal and worst case conditions. For NDI, some criteria could not be satisfied for the worst model cases. These include *stdthe* and *stthe* for the longitudinal part and *stdphi*, *stphi*, *osbeta* and *errphi* for the lateral part. Relieving the affected criteria under worst case parameters would be required to yield a satisfactory NDI design. For comparative reasons, this step was not undertaken. To assess the overall performance of the two designs, the mean and variance of the scaled criteria $\hat{c}_{j,k}$ were determined over the three model cases. The average of these values over all design criteria is found in Table 8-5.

Observe that INDI provides an average improvement of 5% (longitudinal case) and 7% (lateral case) over NDI with respect to the design criteria. Further notice the much lower variance for INDI, indicating smaller differences between the model cases and subsequent lower sensitivity to model mismatches.

Table 8-4: Controller synthesis parameters lateral part

Tuning parameter	INDI			NDI		
Linear controller gains:						
K_ϕ	5.51			7.91		
K_{ϕ_I}	1.34			7.02		
$K_{\dot{\phi}}$	4.80			6.48		
$K_{\ddot{\phi}}$	1.05			0.941		
K_r	1.62			3.22		
K_β	1.93			1.55		
K_{β_I}	0.977			0.709		
Reference model parameters:						
ζ_{ref}	1.00			0.741		
$\omega_{n_{ref}}$	1.35			1.27		
Uncertain model parameters:						
	nominal	worst gmda	worst pmp	nominal	worst gmda	worst gmp
$\Delta\tau_{sync}$	0	-0.3	-0.3	0	0	0
ΔJ_{xx}	0	-0.1	-0.1	0	0	0
ΔJ_{zz}	0	-0.1	-0.1	0	0	0
ΔJ_{xz}	0	0.3	-0.3	0	0	0
ΔC_Y	0	0.3	-0.3	0	0.3	0.3
ΔC_{l_β}	0	0	0	0	-0.2	-0.2
$\Delta C_{l_{\delta_a}}$	0	-0.2	0.2	0	0.2	0.2
$\Delta C_{l_{\delta_r}}$	0	0.2	0.2	0	0	0
ΔC_{l_p}	0	0	0	0	-0.2	0.2
ΔC_{l_r}	0	0	0	0	-0.2	-0.2
ΔC_{n_β}	0	0	0	0	-0.2	-0.2
$\Delta C_{n_{\delta_r}}$	0	0.2	0.2	0	0.2	0.2
$\Delta C_{n_{\delta_a}}$	0	0.2	0.2	0	0	0
ΔC_{n_p}	0	0	0	0	-0.2	-0.2
ΔC_{n_r}	0	0	0	0	0.2	-0.2

	Longitudinal case		Lateral case	
	INDI	NDI	INDI	NDI
$\mathrm{E}(\hat{\boldsymbol{c}})$	0.62	0.67	0.43	0.50
$\mathrm{E}(\mathrm{Var}(\hat{\boldsymbol{c}}_j))$	0.030	0.039	0.081	0.24

Table 8-5: Overall control law performance

The responses corresponding to the nonlinear simulations can be found in Figures 8-5 to 8-7. Note that the blue lines represent the responses of the nominal case and the grey area contains the responses of the worst cases. This area should be interpreted as the design uncertainty. As expected, the responses corresponding to the INDI controller show less sensitivity to parameter variations, with smaller deviations between the cases. The difference is most prominent in

Figure 8-6. The NDI controller is unable to regulate the roll angle error under sideslip for uncertain parameter conditions, with errors up to 1.4°.

The incremental controller displays superior disturbance rejection compared to NDI, with faster attenuation and lower overshoot in the attitude response, see Figures 8-4 and 8-7. This result conforms to observations made by Acquentella et al. [1].

8-6 Conclusion and recommendations

This chapter presented the design optimization of the integrated control system developed in Chapter 7. Multi-objective optimization was used for the tuning of the free control law parameters. Robustness to parametric and unspecified uncertainties was achieved using a multi-model approach in combination with local robustness criteria. Inclusion of the Gibson Dropback criterion ensured good handling qualities. Under the combined effect of actuators, sensors, filters, wind disturbance and model and synchronization mismatches, INDI provided a better compromise between command response, disturbance rejection and robustness compared to classical NDI.

Multi-objective optimization proofed to be very useful for comparing different control techniques. This method allows direct incorporation of a large set of robustness and performance criteria in the tuning process of the controller parameters. It was demonstrated that the method can be straightforwardly tailored for use with INDI by including additional criteria to address robustness to feedback signal synchronization mismatch. By comparing the best-compromise solution of INDI and NDI, the improved performance and robustness of INDI could be demonstrated from a more industry-like perspective.

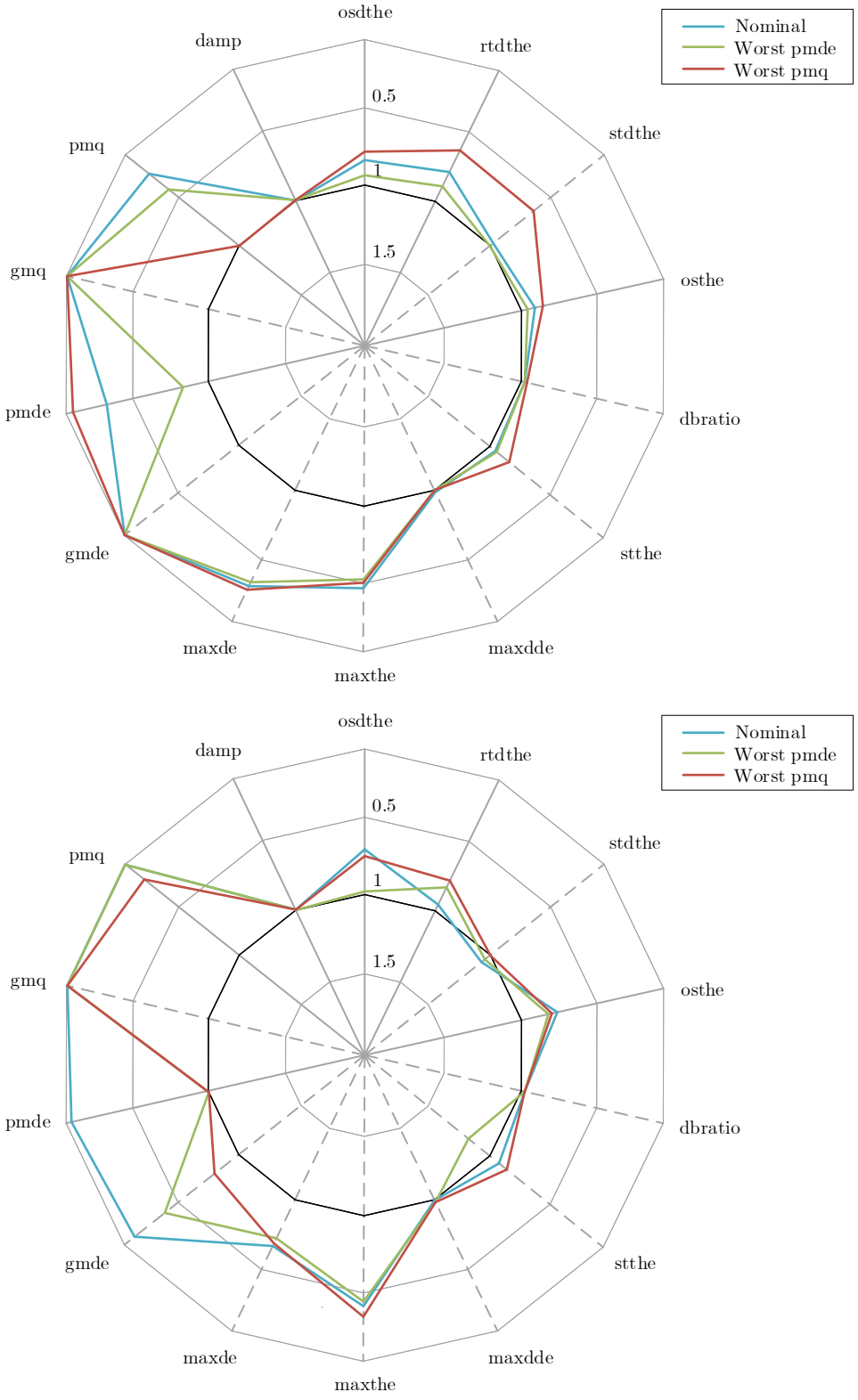

Figure 8-1: Performance diagram scaled criteria longitudinal part INDI (upper) and NDI (lower) (solid line = inequality constraint, dashed line = minimize)

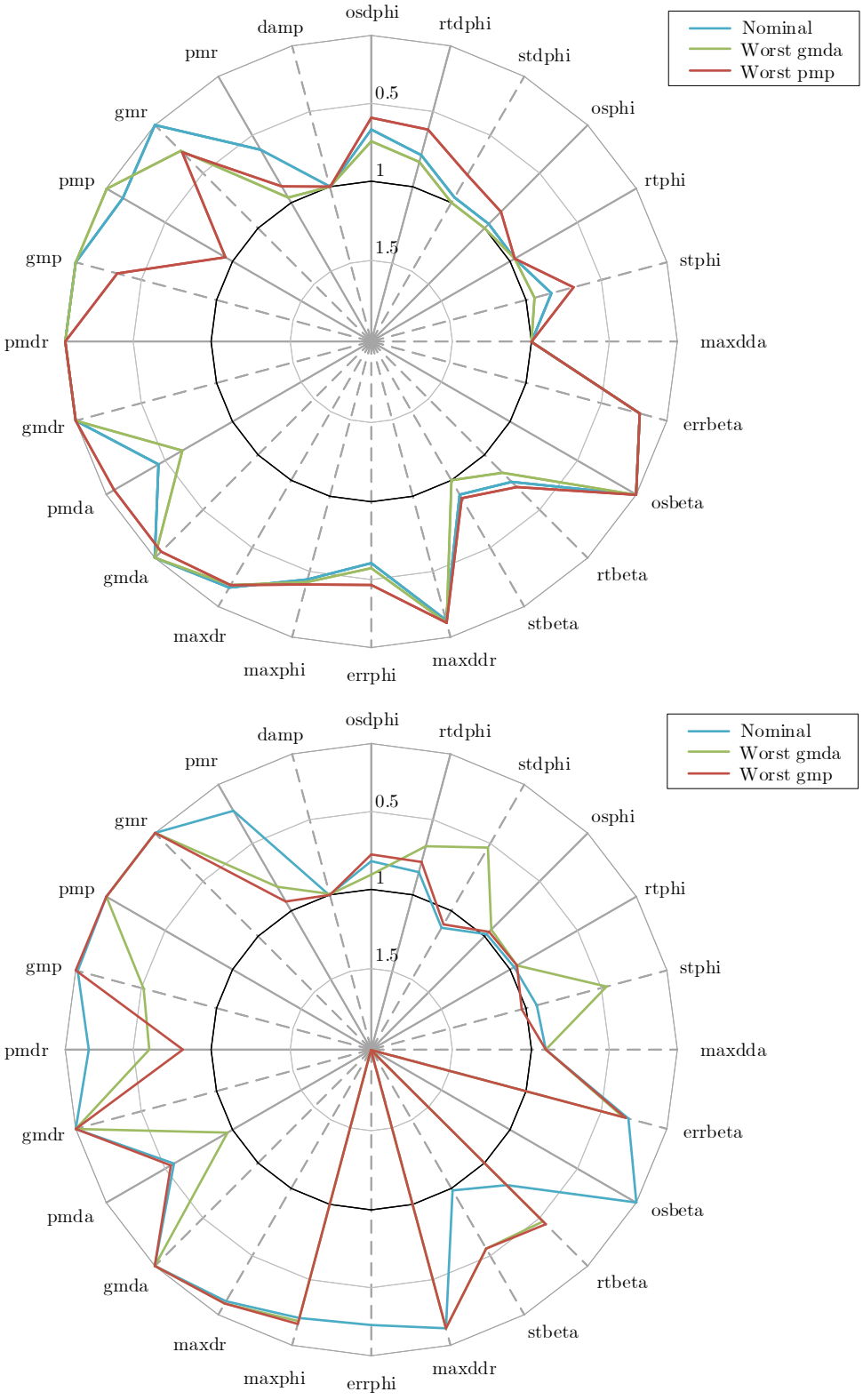

Figure 8-2: Performance diagram scaled criteria lateral part, INDI (upper) and NDI (lower) (solid line = inequality constraint, dashed line = minimize)

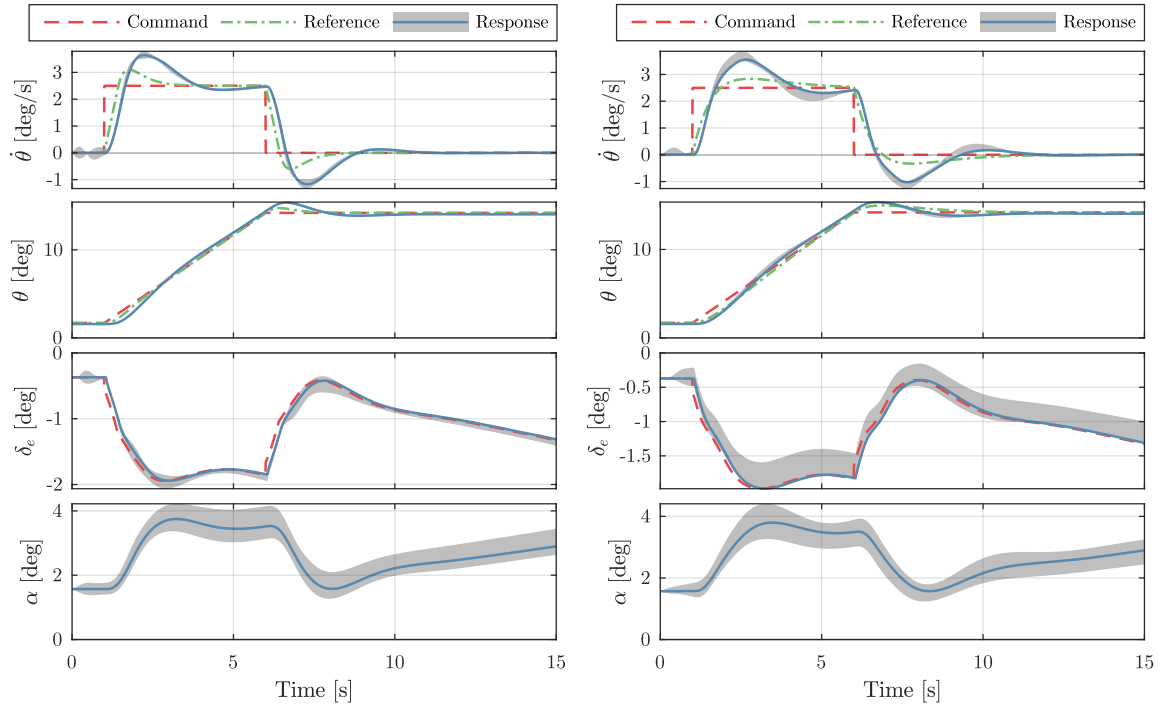

(a) INDI **(b)** NDI

Figure 8-3: Simulation 1 longitudinal part: tracking response to 2.5°/s pitch rate box-cart

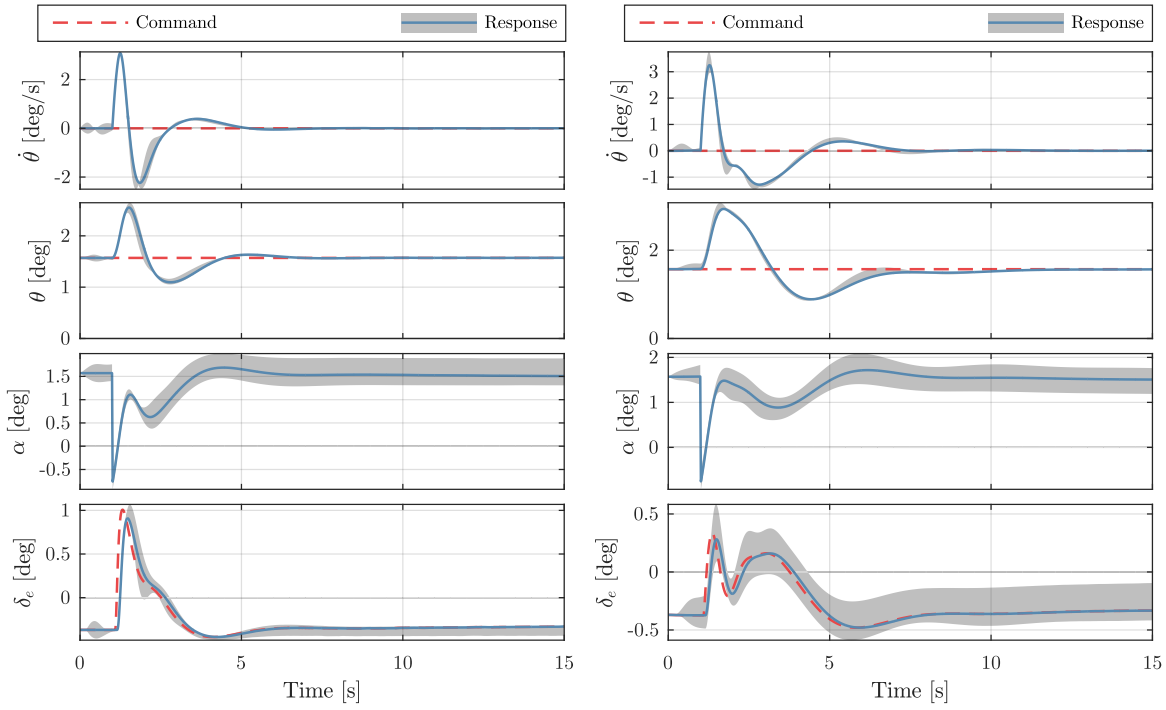

(a) INDI **(b)** NDI

Figure 8-4: Simulation 2 longitudinal part: tracking response to 16 m/s wind step

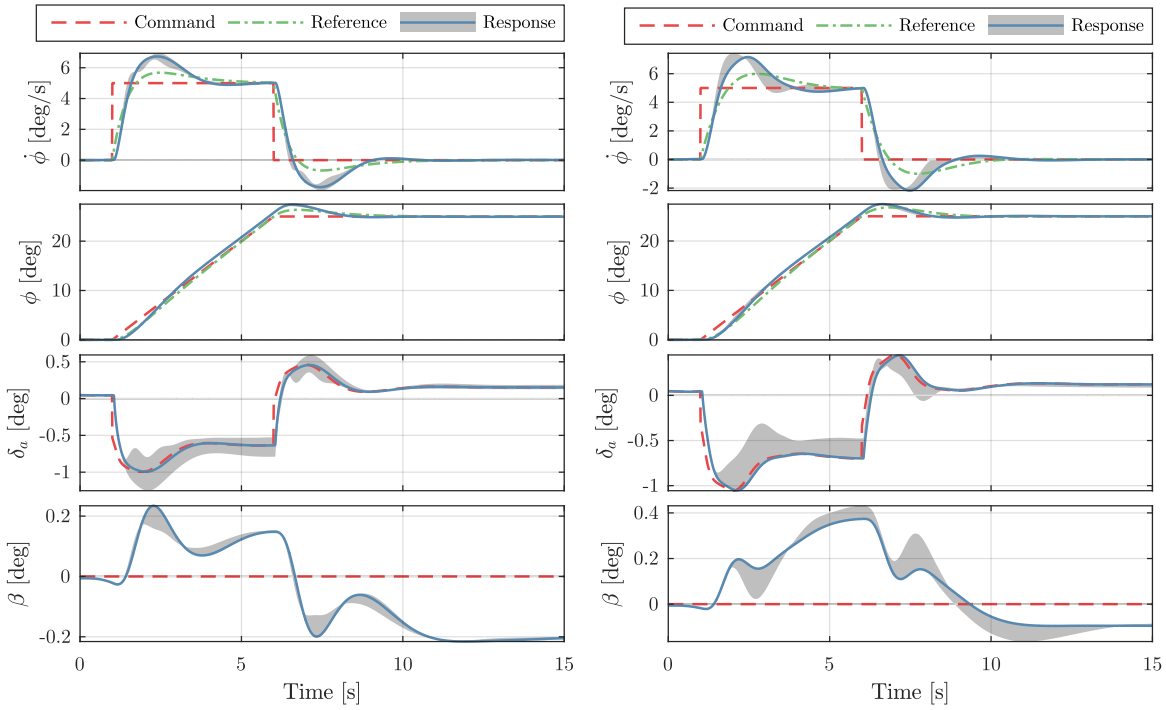

(a) INDI **(b)** NDI

Figure 8-5: Simulation 1 lateral part: tracking response to 5°/s roll rate box-cart

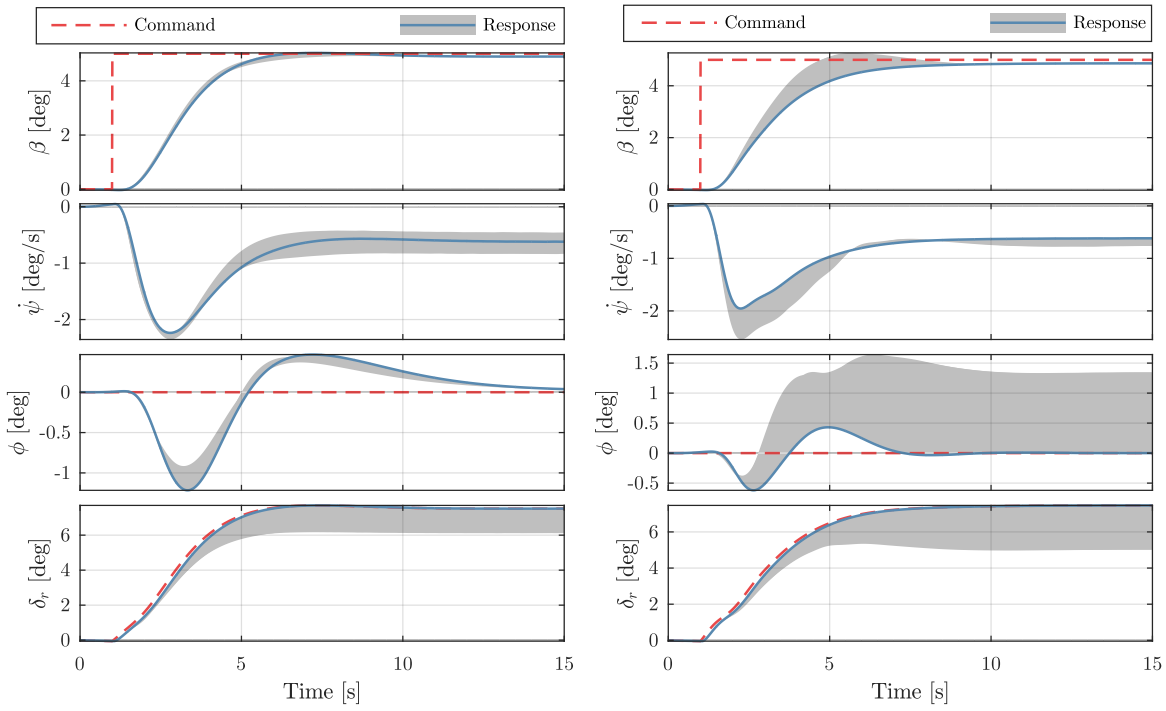

(a) INDI **(b)** NDI

Figure 8-6: Simulation 2 lateral part: tracking response to 5° sideslip step

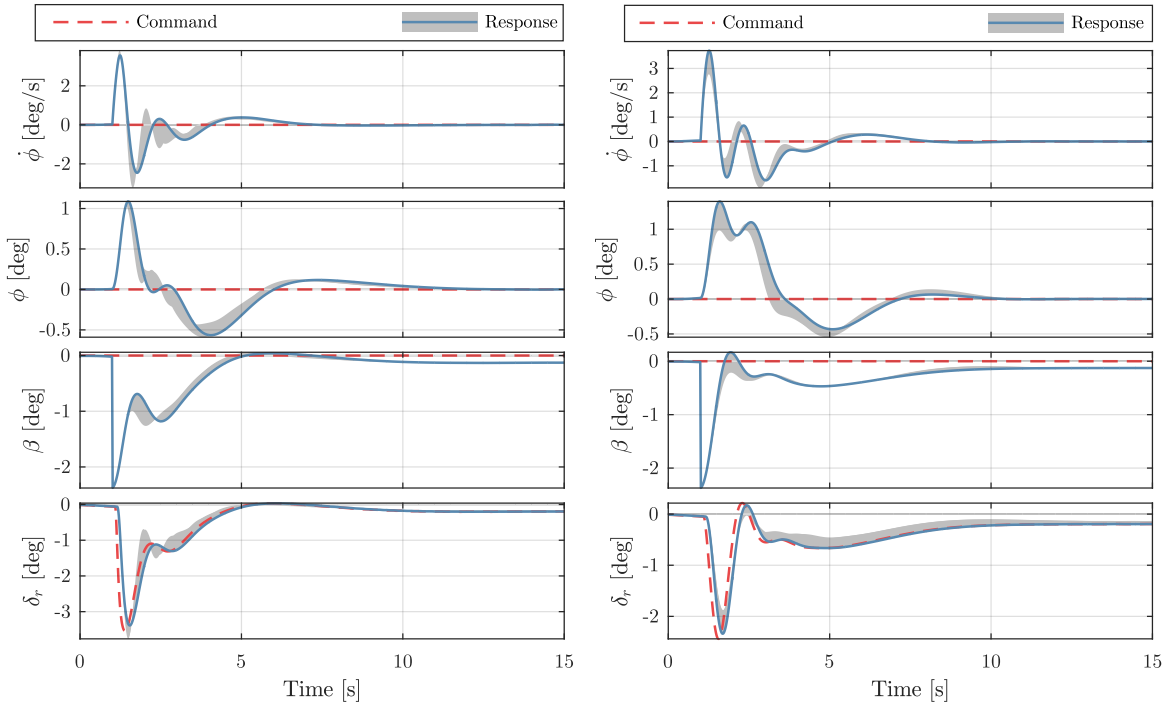

(a) INDI **(b)** NDI

Figure 8-7: Simulation 3 lateral part: tracking response to 16 m/s cross-wind step

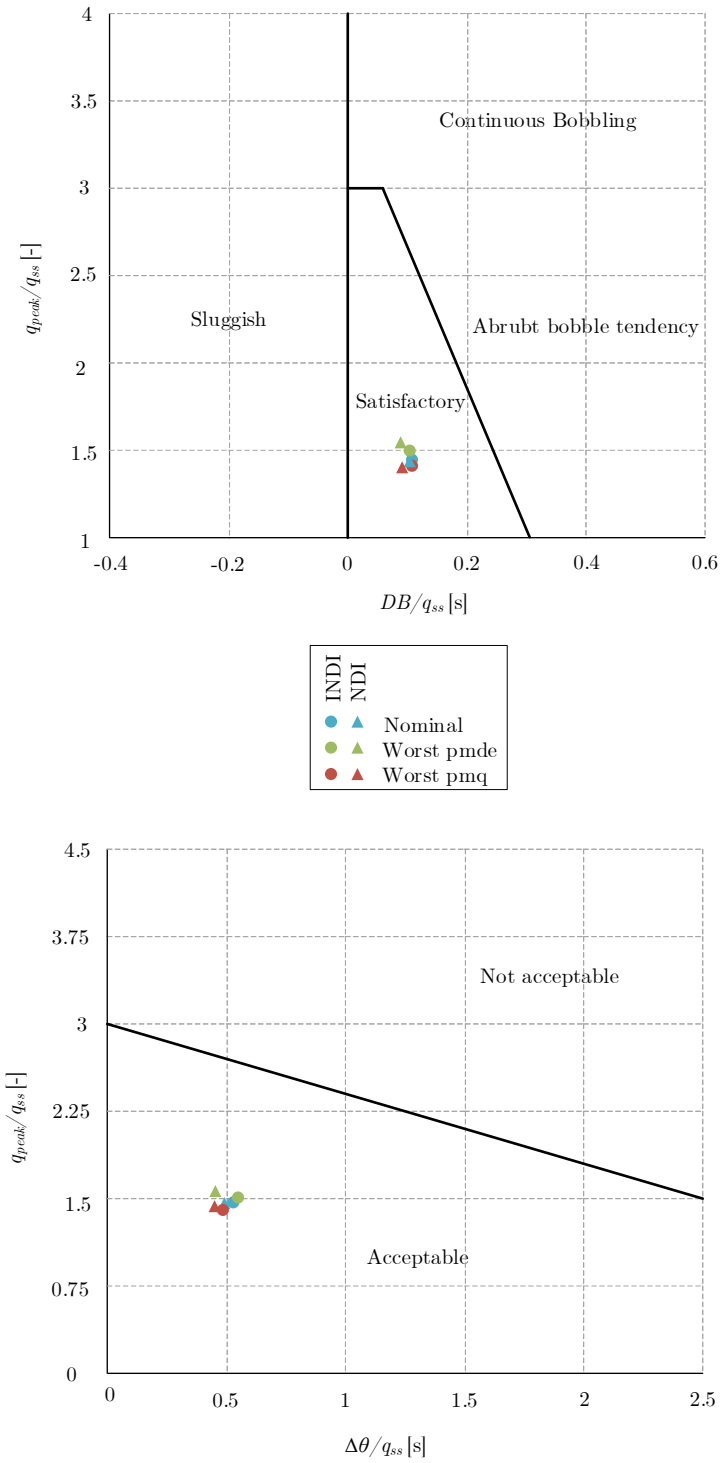

Figure 8-8: Gibson dropback criteria [22] (upper) & updated Gibson dropback criteria [48] (lower)

Chapter 9

Conclusions and recommendations

This chapter presents the conclusions and recommendations corresponding to the Master of Science Thesis: *Dynamic Inversion Flight Control Law Design for Fixed-Wing Aircraft: Design and Flight Testing of Incremental Nonlinear Dynamic Inversion based Control Laws for a Passenger Aircraft*. The research objective formulated for this thesis is to proof the concept of Incremental Nonlinear Dynamic Inversion (INDI) on a CS-25 certified aircraft in flight. INDI compares commanded and measured accelerations to compute increments on the current control deflections. This results in highly robust control solutions with respect to model uncertainties as well as changes in aircraft dynamic characteristics of failure cases during flight. At the same time, the complexity of the algorithms is similar to classical ones. By presenting the design and validation of manual attitude control functions based on INDI for a Cessna Citation II research aircraft, this thesis demonstrated that INDI can be successfully applied to a passenger aircraft and outperform classical Nonlinear Dynamic Inversion (NDI). Based on the preliminary studies, the following conclusions and recommendations can be made:

- Due to the angular acceleration feedback requirement, the INDI control signals are typically noisier compared to NDI, especially when using conventional estimation techniques. Noisy control signals may cause excessive wear on the actuators. Dedicated angular accelerometers, pairs of linear accelerometers or complimentary filtering are therefore proposed to obtain more noise free angular acceleration estimates. It was demonstrated that the linear accelerometer pair of the PH-LAB can be successfully used to obtain observations of the lateral angular accelerations with less phase lag and noise compared to conventional washout filters.

- A novel method based on the complimentary filtering technique has been proposed as a means to obtain more accurate angular acceleration estimates from angular rate measurements. The method has no additional dependencies other than the control surface deflection and control effectiveness, both already required for INDI. Closed loop simulations demonstrated that this filter performs well in comparison to conventional

washout filters. The results are also valuable for other control techniques that rely on angular acceleration feedback such as Incremental Backstepping (IBS).

- INDI displays high sensitivity to time differences between state derivative and control deflection feedback. A surplus of state derivative feedback delay results relatively fast in oscillations and system instability. For practical applications this sensitivity is somewhat reduced due to actuator and filter lag. It was shown mathematically and in a stability analysis that faster actuators may reduce stability under certain conditions in presence of unsynchronized signal feedback. This stresses the importance of synchronization for systems with fast actuators. Robustness analysis against synchronization mismatches should be an integral part of INDI control law design.

- It has been shown mathematically that the size of the inversion error of INDI due to neglecting the so-called system dynamics increment scales with the combined delay of actuators, sensor, and sampling. This result conforms to observations made in simulations in previous research and stresses the importance of minimizing actuator, sensor and sampling delay.

- Extensive robustness analysis revealed that INDI provides a highly robust control solution with respect to model uncertainties compared to classical NDI, even in presence of unsynchronized angular acceleration and control deflection feedback. Under the combined effect of actuators, sensors, filters, wind disturbance and model and synchronization mismatches, INDI provided a better compromise between command response, disturbance rejection and robustness compared to classical NDI.

- Multi-objective optimization proofed to be very useful for comparing different control techniques. This method allows direct incorporation of a large set of robustness and performance criteria in the tuning process of the controller parameters. It was demonstrated that the method can be straightforwardly tailored for use with INDI by including additional criteria to address robustness to feedback signal synchronization mismatch. By comparing the best-compromise solution of INDI and NDI, the improved performance and robustness of INDI could be demonstrated from a more industry-like perspective.

In addition to the *offline design*, the research paper presented the *assessment and clearance*, *rig testing* and *flight testing*. Based on results obtained in these steps, the following conclusions and recommendations can be made:

- Qualitative flight test with the INDI and NDI attitude control laws were performed on the Cessna Citation II PH-LAB, marking the first successful demonstration of INDI on a CS-25 certified aircraft. In presence of limited authority, uncertain control effectiveness and simulated engine failures, the system dynamics were canceled well by both controllers. The imposed reference dynamics were accurately tracked with nominal control effectiveness parameters, validating the simulation results.

- Pseudo Control Hedging (PCH) is a valuable addition to INDI in presence of actuator saturation. The flight test revealed that PCH was effective in reducing the saturation effect of the actuators. The use of PCH did however result in more noisy control responses. For future implementations it is advised to activate PCH only upon saturation.

This can for example be achieved via a simple algorithm that detects a misfit between commanded and actual control deflection. For control deflection feedback, models might in certain cases be preferred over measurements as PCH adapts the reference model to any bias between commanded and actual control deflection.

- In addition to engine failures, future flight test should focus on testing realistic failure scenarios such as jammed control surfaces or changes in mass distribution. Changes in dynamic behavior can be simulated by extending the flaps/gear or by activation of the spoilers. These are particularly valuable in showing the applicability of INDI as a fault tolerant flight control system.

- The theoretical advantage of nonlinear control techniques over linear methods should clearly manifest itself in the nonlinear flight regime. For future applications, flight tests at high angle of attack flight are considered specifically appropriate to include as experiment case.

- Due to the limited authority of the FBW system and nature of the Rate Control Attitude Hold and Attitude Control functions, it is important that the pilot has situational awareness what attitude is commanded to reduce the likelihood of saturating the system. The benefit of a roll angle marker was already demonstrated in flight. An additional marker on the primary flight display displaying the commanded pitch attitude is considered highly beneficial to improve input accuracy.

- It turned out to be difficult for the pilots to limit inputs on the force sidestick to one axis only. For future flight experiments it is therefore recommended to use computer-generated input signals in addition to pilot-generated input signals. The former have an advantage in terms of frequency-content and repeatability. This would allow for a better comparison of flight test results from different control laws and simulation results.

- For safety reasons and operational constraints, the flight test in this thesis were conducted at relatively high speed and altitude. It might be beneficial in future applications to conduct flight test below 13,400 ft and at lower airspeeds to maximize the authority of the FBW system.

- The servo position controller of the FBW system is responsible for perceived changes in control effectiveness due to actuator cable stretch. For future applications it might be beneficial to adjust this control law for control surface deflection feedback. This would mitigate the issues observed during the flight test with varying control effectiveness.

- The authority of the FBW system might be improved by relieving the (electronic) torque limitations on the servo motors, especially for the pitch channel. This would be highly valuable for future testing of advanced flight control laws, allowing more aggressive maneuvers and evaluation of the control laws over a wider performance envelope of the aircraft.

Appendix A

Flight test cards Flight #2

PH-LAB Flight Test Card

Flight #:	2
CASE #:	2.1.1
Wind / [kn]:	45
Wind / [deg]:	315

Observer:	
Gain Set:	NOMINAL
Optional Case:	NOMINAL
UUID:	8C2EA12

Flight Tag:	NDI_base_lat_lon_A

Synopsis:	NDI Base: 1. Check Pitch Up and Down, 2. Check Roll limits (RCAH, AC), 3. Check Roll Precision

Flight Condition:	V_CAS / [kn]	Flight Level	Flaps	Pre-Condition	Flight-Mode	Repetitions		
	200	150	0	Straight&Level	EFCS	1+		

Moding:	Enable	Reset	INDI	PCH	Cstar	Act_INDI	Act_PCH	Beta_Est	Alpha_B	doTurnC	OpenL	Long_cmd	Lat_cmd	AeroCg	doLimit
	1	E	0	0	0	1	1	0	0	0	0	1	1	1	0

Procedure:	1. De-activate EFCS	2. Reconfigure EFCS	3. Est. Flight Condition	4. Hands-off Stick	5. Activate EFCS

Start / [UTC]:	13:40
End / [UTC]:	13:~~43~~

NO TRANSIENTS !

Procedures:	0. Establish trimmed flight condition
	1. Pitch U: trim + 5°, Pitch D: trim -5° - at moderate rates, TRIM ON/OFF in the making
	2. Roll R to Limits (35°), release stick (A/C returns to 27.5°) - at moderate rates - repeat for L
	3. Roll R - Bank capture (5°, aim for precision) - at moderate rates - repeat for L
	4. Roll R - Bank capture (10°, aim for precision) - at moderate rates - repeat for L
	-
Comments:	Hard to pitch up, Push/Overshoot with TRIM Auto Trim PERFECT !! BANK is kept Roll is PERFECT NO CHALETS !! :)

PH-LAB Flight Test Card

Flight #:	2
CASE #:	2.1.3
Wind / [kn]:	
Wind / [deg]:	

Observer:	
Gain Set:	NOMINAL
Optional Case:	NOMINAL
UUID:	7D352B6

Flight Tag:	NDI_base_lat_lon_AeroCg_A

Synopsis:	NDI w/o AeroCg correction: 1. Check Pitch Up and Down, 2. Check Roll limits (RCAH, AC), 3. Check Roll Precision - see AoA increase

Flight Condition:	V_CAS / [kn]	Flight Level	Flaps	Pre-Condition	Flight-Mode	Repetitions		
	200	150	0	Straight&Level	EFCS	1+		

Moding:	Enable	Reset	INDI	PCH	Cstar	Act_INDI	Act_PCH	Beta_Est	Alpha_B	doTurnC	OpenL	Long_cmd	Lat_cmd	AeroCg	doLimit
	1	E	0	0	0	1	1	0	0	0	0	1	1	0	0

Procedure:	1. De-activate EFCS	2. Reconfigure EFCS	3. Est. Flight Condition	4. Hands-off Stick	5. Activate EFCS

Start / [UTC]:	13:55
End / [UTC]:	13:57

NO TRANSIENTS

Procedures:	0. Establish trimmed flight condition
	1. Pitch U: trim + 5°, Pitch D: trim -5° - at moderate rates — 3° overshoot
	2. Roll R to Limits (35°), release stick (A/C returns to 27.5°) - at moderate rates - repeat for L
	3. Roll R - Bank capture (5°, aim for precision) - at moderate rates - repeat for L
	4. Roll R - Bank capture (10°, aim for precision) - at moderate rates - repeat for L
	-
Comments:	NO TRIM (only Overshooting) DEP - Bank does matter holding the attitude

PH-LAB Flight Test Card

Flight #:	2
CASE #:	2.1.4
Wind / [kn]:	
Wind / [deg]:	

Observer:	
Gain Set:	CONSERVATIVE
Optional Case:	NOMINAL
UUID:	69BED8C0

Flight Tag:	NDI_base_lat_lon_AeroEst_cons_A

Synopsis:	NDI Base with estimated Aero: 1. Check Pitch Up and Down, 2. Check Roll limits (RCAH, AC), 3. Check Roll Precision

Flight Condition:	V_CAS / [kn]	Flight Level	Flaps	Pre-Condition	Flight-Mode	Repetitions		
	200	150	0	Straight&Level	EFCS	1+		

Moding:	Enable	Reset	INDI	PCH	Cstar	Act_INDI	Act_PCH	Beta_Est	Alpha_B	doTurnC	OpenL	Long_cmd	Lat_cmd	AeroCg	doLimit
	1	E	0	0	0	1	1	1	1	0	0	1	1	1	0

Procedure:	1. De-activate EFCS	2. Reconfigure EFCS	3. Est. Flight Condition	4. Hands-off Stick	5. Activate EFCS

Start / [UTC]:	14:00
End / [UTC]:	14:02

Procedures:	0. Establish trimmed flight condition
	1. Pitch U: trim ~~+5°~~ 2.5, Pitch D: trim ~~-5°~~ 2.5 - at moderate rates
	2. Roll R to Limits (35°), release stick (A/C returns to 27.5°) - at moderate rates - repeat for L
	3. Roll R - Bank capture (5°, aim for precision) - at moderate rates - repeat for L
	4. Roll R - Bank capture (10°, aim for precision) - at moderate rates - repeat for L
	-
Comments:	TRIM is not enabled NO RUDDER Movement → NO β → PERFECT

PH-LAB Flight Test Card

Flight #:	2
CASE #:	2.1.5
Wind / [kn]:	
Wind / [deg]:	

Observer:	
Gain Set:	NOMINAL
Optional Case:	NOMINAL
UUID:	D463A874

Flight Tag:	NDI_base_lat_lon_AeroEst_A

Synopsis:	NDI Base with estimated Aero: 1. Check Pitch Up and Down, 2. Check Roll limits (RCAH, AC), 3. Check Roll Precision

Flight Condition:	V_CAS / [kn]	Flight Level	Flaps	Pre-Condition	Flight-Mode	Repetitions		
	200	150	0	Straight&Level	EFCS	1+		

Moding:	Enable	Reset	INDI	PCH	Cstar	Act_INDI	Act_PCH	Beta_Est	Alpha_B	doTurnC	OpenL	Long_cmd	Lat_cmd	AeroCg	doLimit
	1	E	0	0	0	1	1	1	1	0	0	1	1	1	0

Procedure:	1. De-activate EFCS	2. Reconfigure EFCS	3. Est. Flight Condition	4. Hands-off Stick	5. Activate EFCS

Start / [UTC]:	14:03 / 12:11
End / [UTC]:	14:08 / 14:

NO TRIM

Procedures:	0. Establish trimmed flight condition
	1. Pitch U: trim ~~+5°~~, Pitch D: trim ~~-5°~~ - at moderate rates → 2. ONLY Roll
4.	2. Roll R to Limits (35°), release ~~stick (A/C returns to 27.5°) - at~~ moderate rates - repeat for L
2.	3. Roll R - Bank capture (5°, aim for precision) - at moderate rates - repeat for L → Continued movement
3.	4. Roll R - Bank capture (10°, aim for precision) - at moderate rates - repeat for L
	-
Comments:	NO AUTO-TRIM, MORE RESPONSIVE NO RUDDER ACTIVITY → PERFECT Roll: NOT STOPPING at gray indication CAPTURING !! OK

PH-LAB Flight Test Card

Flight #:	2
CASE #:	2.1.6
Wind / [kn]:	
Wind / [deg]:	

Observer:	
Gain Set:	NOMINAL
Optional Case:	NOMINAL
UUID:	82491A9F

Flight Tag:	NDI_base_lat_lon_OEI_A

Synopsis:	NDI Base with OEI: 1. Check Pitch Up and Down, 2. Check Roll limits (RCAH, AC), 3. Check Roll Precision

Flight Condition:	V_CAS / [kn]	Flight Level	Flaps	Pre-Condition	Flight-Mode	Repetitions		
	200	150	0	Straight&Level	EFCS	1+		

Moding:	Enable	Reset	INDI	PCH	Cstar	Act_INDI	Act_PCH	Beta_Est	Alpha_B	doTurnC	OpenL	Long_cmd	Lat_cmd	AeroCg	doLimit
	1	E	0	0	0	1	1	0	0	0	0	1	1	1	0

Procedure:	1. De-activate EFCS	2. Reconfigure EFCS	3. Est. Flight Condition	4. Hands-off Stick	5. Activate EFCS

Start / [UTC]:	14:15
End / [UTC]:	14:18

NO YOKE

Procedures:	0. Establish trimmed flight condition
	1. Pitch U: trim + 5°, Pitch D: trim -5° - at moderate rates, reduce pref. Engine to IDLE
	2. Observe, as FCL trims the A/C with rudder
	3. Roll R to Limits (35°), release stick (A/C returns to 27.5°) - at moderate rates - repeat for L
	4. Roll R - Bank capture (5°, aim for precision) - at moderate rates - repeat for L
	5. Roll R - Bank capture (10°, aim for precision) - at moderate rates - repeat for L
Comments:	RIGHT ENG → OEI → IDLE RUDDER SLIGHT LEFT → TRIM SEEMS TO WORK

ALIGNING PERFECT

PH-LAB Flight Test Card

Flight #:	2
CASE #:	2.1.8
Wind / [kn]:	
Wind / [deg]:	

Observer:	
Gain Set:	CONSERVATIVE
Optional Case:	NOMINAL
UUID:	278F2274

_ TRIMS
E: NOSE
A, R: CAN

Flight Tag:	INDI_lat_lon_A

AFTER WARDS

Synopsis:	INDI: 1. Check Pitch Up and Down, 2. Check Roll limits (RCAH, AC), 3. Check Roll Precision

NOM

Flight Condition:	V_CAS / [kn]	Flight Level	Flaps	Pre-Condition	Flight-Mode	Repetitions		
	200	150	0	Straight&Level	EFCS	1+		

Moding:	Enable	Reset	INDI	PCH	Cstar	Act_INDI	Act_PCH	Beta_Est	Alpha_B	doTurnC	OpenL	Long_cmd	Lat_cmd	AeroCg	doLimit
	1	E	1	0	0	1	1	0	0	0	0	1	1	1	0

Procedure:	1. De-activate EFCS	2. Reconfigure EFCS	3. Est. Flight Condition	4. Hands-off Stick	5. Activate EFCS

Start / [UTC]:	14:22	~~14:26~~ 14:26
End / [UTC]:	14:24	14:28

& MANUAL CALLS

~~STICK~~ NO YOKE MOVEMENTS

Procedures:	0. Establish trimmed flight condition 25
	1. Pitch U: trim ~~+5°~~, Pitch D: trim ~~-5°~~ - at moderate rates
	2. Roll R to Limits (35°), release stick (A/C returns to 27.5°) - at moderate rates - repeat for L
	3. Roll R - Bank capture (5°, aim for precision) - at moderate rates - repeat for L
	4. Roll R - Bank capture (10°, aim for precision) - at moderate rates - repeat for L
	-
Comments:	ROLL OSCILLATION! ~~45°~~

PH-LAB Flight Test Card

Flight #:	2
CASE #:	2.1.10
Wind / [kn]:	
Wind / [deg]:	

Observer:	
Gain Set:	NOMINAL
Optional Case:	OPTIONAL
UUID:	FEBC55AE

Flight Tag:	INDI_lat_opt_A

Synopsis:	INDI only lateral: 1. Check Roll limits (RCAH, AC), 2. Check Roll Precision

Flight Condition:	V_CAS / [kn]	Flight Level	Flaps	Pre-Condition	Flight-Mode	Repetitions		
	200	150	0	Straight&Level	EFCS	1+		

Moding:	Enable	Reset	INDI	PCH	Cstar	Act_INDI	Act_PCH	Beta_Est	Alpha_B	doTurnC	OpenL	Long_cmd	Lat_cmd	AeroCg	doLimit
	1	E	1	0	0	1	1	0	0	0	0	0	1	1	0

Procedure:	1. De-activate EFCS	2. Reconfigure EFCS	3. Est. Flight Condition	4. Hands-off Stick	5. Activate EFCS

Start / [UTC]:	14:30	38	40
End / [UTC]:	14:33	40	42

Procedures:	0. Establish trimmed flight condition
	1. Roll R to Limits (35°), release stick (A/C returns to ~~27.5°~~ 25°) - at moderate rates - repeat for L → CREEPING AWAY
	2. Roll R - Bank capture (5°, aim for precision) - at moderate rates - repeat for L
	3. Roll R - Bank capture (10°, aim for precision) - at moderate rates - repeat for L
	-
	-
Comments:	NO OSCILLATIONS at all. RESET STICK for All OK. ~~No~~ NO YOLTS Anti-Creeping

AIC oscillating

WORKS FULLY SMOOTHLY
CREEPS BACK → CTD ROLLS OFF / STICK - CTD Rolls
~~FAIL~~ DEAD-BAND VISIBLE → STICK is SENSITIVE

PH-LAB Flight Test Card

Flight #:	2
CASE #:	2.2.1
Wind / [kn]:	
Wind / [deg]:	

Observer:	
Gain Set:	CONSERVATIVE
Optional Case:	NOMINAL
UUID:	B669104C

Flight Tag:	NDI_base_lat_lon_cons_B

Synopsis:	NDI Base: 1. Check Pitch Up and Down, 2. Check Roll limits (RCAH, AC), 3. Check Roll Precision

Flight Condition:	V_CAS / [kn]	Flight Level	Flaps	Pre-Condition	Flight-Mode	Repetitions		
	240	150	0	Straight&Level	EFCS	1+		

Moding:	Enable	Reset	INDI	PCH	Cstar	Act_INDI	Act_PCH	Beta_Est	Alpha_B	doTurnC	OpenL	Long_cmd	Lat_cmd	AeroCg	doLimit
	1	E	0	0	0	1	1	0	0	0	0	1	1	1	0

Procedure:	1. De-activate EFCS	2. Reconfigure EFCS	3. Est. Flight Condition	4. Hands-off Stick	5. Activate EFCS

Start / [UTC]:	14:48
End / [UTC]:	14:53

NO TRANSLENT

Procedures:	0. Establish trimmed flight condition 25°
	1. Pitch U: trim + ~~5°~~, Pitch D: trim ~~-5°~~ - at moderate rates
	2. Roll R to Limits (35°), release stick (A/C returns to 27.5°) - at moderate rates - repeat for L
	3. Roll R - Bank capture (5°, aim for precision) - at moderate rates - repeat for L
	4. Roll R - Bank capture (10°, aim for precision) - at moderate rates - repeat for L
	-
Comments:	TRIM off: Pitch smooth and NORMAL Longit

PH-LAB Flight Test Card

Flight #:	2
CASE #:	2.2.4
Wind / [kn]:	
Wind / [deg]:	

Observer:	
Gain Set:	NOMINAL
Optional Case:	NOMINAL
UUID:	96E563CE

Flight Tag:	NDI_base_lat_lon_B

Synopsis:	NDI Base: 1. Check Pitch Up and Down, 2. Check Roll limits (RCAH, AC), 3. Check Roll Precision

1 226 afterwards 15:02

Flight Condition:	V_CAS / [kn]	Flight Level	Flaps	Pre-Condition	Flight-Mode	Repetitions		
	240	150	0	Straight&Level	EFCS	1+		

Moding:	Enable	Reset	INDI	PCH	Cstar	Act_INDI	Act_PCH	Beta_Est	Alpha_B	doTurnC	OpenL	Long_cmd	Lat_cmd	AeroCg	doLimit
	1	E	0	0	0	1	1	0	0	0	0	1	1	1	0

Procedure:	1. De-activate EFCS	2. Reconfigure EFCS	3. Est. Flight Condition	4. Hands-off Stick	5. Activate EFCS

Start / [UTC]:	14:54	56	15:00	15:02
End / [UTC]:	14:55	58	15:01	15:03

NO HOLDS / NO TRANS

Procedures:	0. Establish trimmed flight condition
	1. Pitch U: trim +5°, Pitch D: trim -5° - at moderate rates
	2. Roll R to Limits (35°), release stick (A/C returns to 27.5°) - at moderate rates - repeat for L
	3. Roll R - Bank capture (5°, aim for precision) - at moderate rates - repeat for L
	4. Roll R - Bank capture (10°, aim for precision) - at moderate rates - repeat for L
	-
Comments:	KEEPS ATTITUDE, DEAD-BAND expected ROLL PERFECT, Difference between CTD and actual Roll LOW CONTROL-ACTIVITY

PH-LAB Flight Test Card

Flight #:	2
CASE #:	2.2.7
Wind / [kn]:	
Wind / [deg]:	

Observer:	
Gain Set:	NOMINAL
Optional Case:	NOMINAL
UUID:	7F7AC1D1

Flight Tag:	NDI_PCH_lat_lon_B

Synopsis:	NDI with PCH: 1. Check Pitch Up and Down, 2. Check Roll limits (RCAH, AC), 3. Check Roll Precision - see Saturation limits

Flight Condition:	V_CAS / [kn]	Flight Level	Flaps	Pre-Condition	Flight-Mode	Repetitions		
	240	150	0	Straight&Level	EFCS	1+		

Moding:	Enable	Reset	INDI	PCH	Cstar	Act_INDI	Act_PCH	Beta_Est	Alpha_B	doTurnC	OpenL	Long_cmd	Lat_cmd	AeroCg	doLimit
	1	E	0	1	0	1	1	0	0	0	0	1	1	1	1

Procedure:	1. De-activate EFCS	2. Reconfigure EFCS	3. Est. Flight Condition	4. Hands-off Stick	5. Activate EFCS

Start / [UTC]:	
End / [UTC]:	

2DEG - LIMITS TRANSIENT

Procedures:	0. Establish trimmed flight condition
	1. Pitch U: trim +5°, Pitch D: trim -5° - at moderate rates, see if limitations hit
	2. Roll R to Limits (35°), release stick (A/C returns to 27.5°) - at moderate rates - repeat for L, observe > AoA
	3. Roll R - Bank capture (5°, aim for precision) - at moderate rates - repeat for L
	4. Roll R - Bank capture (10°, aim for precision) - at moderate rates - repeat for L
	-
Comments:	

PH-LAB Flight Test Card

Flight #:	2
CASE #:	2.2.14
Wind / [kn]:	
Wind / [deg]:	

Observer:	
Gain Set:	CONSERVATIVE
Optional Case:	NOMINAL
UUID:	2EBF4195

Flight Tag: INDI_lat_lon_cons_B

Synopsis: INDI: 1. Check Pitch Up and Down, 2. Check Roll limits (RCAH, AC), 3. Check Roll Precision

Flight Condition:	V_CAS / [kn]	Flight Level	Flaps	Pre-Condition	Flight-Mode	Repetitions		
	240 (→ 240)	150	0	Straight&Level	EFCS	1+		

Moding:	Enable	Reset	INDI	PCH	Cstar	Act_INDI	Act_PCH	Beta_Est	Alpha_B	doTurnC	OpenL	Long_cmd	Lat_cmd	AeroCg	doLimit
	1	E	1	0	0	1	1	0	0	0	0	1	1	1	0

Procedure:	1. De-activate EFCS	2. Reconfigure EFCS	3. Est. Flight Condition	4. Hands-off Stick	5. Activate EFCS

Start / [UTC]:	15:10	15:15	15:17
End / [UTC]:	15:12	15:16	

NO JOLTS, SMOOTH

Procedures:
0. Establish trimmed flight condition
1. Pitch U: trim + 5°, Pitch D: trim -5° - at moderate rates
2. Roll R to Limits (35°), release stick (A/C returns to 27.5°) - at moderate rates - repeat for L
3. Roll R - Bank capture (5°, aim for precision) - at moderate rates - repeat for L → TARGET RUNS OFF
4. Roll R - Bank capture (10°, aim for precision) - at moderate rates - repeat for L

-

Comments: MORE DAMPING, CONTROLS are good
GOOD
STICK Offset remains

PH-LAB Flight Test Card

Flight #:	2
CASE #:	2.2.17
Wind / [kn]:	
Wind / [deg]:	

Observer:	
Gain Set:	NOMINAL
Optional Case:	NOMINAL
UUID:	B752CF49

(Gain Set → CONSERVATIVE ROLL)

Flight Tag: INDI_lat_lon_B

Oscillation off

Synopsis: INDI: 1. Check Pitch Up and Down, 2. Check Roll limits (RCAH, AC), 3. Check Roll Precision

Flight Condition:	V_CAS / [kn]	Flight Level	Flaps	Pre-Condition	Flight-Mode	Repetitions		
	240	150	0	Straight&Level	EFCS	1+		

Moding:	Enable	Reset	INDI	PCH	Cstar	Act_INDI	Act_PCH	Beta_Est	Alpha_B	doTurnC	OpenL	Long_cmd	Lat_cmd	AeroCg	doLimit
	1	E	1	0	0	1	1	0	0	0	0	1	1	1	0

(doLimit → w Limits)

Procedure:	1. De-activate EFCS	2. Reconfigure EFCS	3. Est. Flight Condition	4. Hands-off Stick	5. Activate EFCS

Start / [UTC]:	15:13	15:25	28	31
End / [UTC]:	15:18	15:27	30	32

/34 + MANUAL MANEUVRES after that → Online Control

Procedures:
0. Establish trimmed flight condition → Turn induced → CG moving
1. Pitch U: trim + 5°, Pitch D: trim -5° - at moderate rates
2. Roll R to Limits (35°), release stick (A/C returns to 27.5°) - at moderate rates - repeat for L
3. Roll R - Bank capture (5°, aim for precision) - at moderate rates - repeat for L
4. Roll R - Bank capture (10°, aim for precision) - at moderate rates - repeat for L GOOD PITCH CONTROL

-

Comments: ROLL OSCILLATION; CG drifts → A/C follows → STICK
Some INPUT steps encountered

After STICK - Reset no Creeps, but small oscillations
Lowered Gain → Anti - Oscillation
Small oscillations PITCH is kept OK!!

PH-LAB Flight Test Card

Flight #:	2
CASE #:	2.3.2
Wind / [kn]:	
Wind / [deg]:	

Observer:	
Gain Set:	NOMINAL
Optional Case:	NOMINAL
UUID:	BC5010C1

Flight Tag:	INDI_lat_lon_OEI_C

Synopsis:	INDI with OEI: 1. Check Pitch Up and Down, 2. Check Roll limits (RCAH, AC), 3. Check Roll Precision

Flight Condition:	V_CAS / [kn]	Flight Level	Flaps	Pre-Condition	Flight-Mode	Repetitions		
	200	150	0	Straight&Level	EFCS	1+		

Moding:	Enable	Reset	INDI	PCH	Cstar	Act_INDI	Act_PCH	Beta_Est	Alpha_B	doTurnC	OpenL	Long_cmd	Lat_cmd	AeroCg	doLimit
	1	E	1	0	0	1	1	0	0	0	0	1	1	1	0

Procedure:	1. De-activate EFCS	2. Reconfigure EFCS	3. Est. Flight Condition	4. Hands-off Stick	5. Activate EFCS

Start / [UTC]:	15:40	15:42
End / [UTC]:	15:41	15:44

Procedures:	0. Establish trimmed flight condition
	1. Observe, as FCL trims the A/C with rudder, reduce pref. Engine to IDLE
	2. Roll R to Limits (35°), release stick (A/C returns to 27.5°) - at moderate rates - repeat for L
	3. Roll R - Bank capture (5°, aim for precision) - at moderate rates - repeat for L
	4. Roll R - Bank capture (10°, aim for precision) - at moderate rates - repeat for L
	-
Comments:	Engine de-ingested, Mod AILERON/RUDDER OSCILLATIONS !! NO LIMITS

Appendix B

Flight test cards Flight #3

PH-LAB Flight Test Card

PA

Flight #:	3
CASE #:	3.1.2
Wind / [kn]:	
Wind / [deg]:	

Observer:	RK
Gain Set:	NOMINAL
Optional Case:	NOMINAL
UUID:	64EC8D30

Flight Tag:	NDI_base_lat_lon_A

Synopsis:	NDI Base: 1. Check Pitch Up and Down, 2. Check Roll limits (RCAH, AC), 3. Check Roll Precision - w Pseudo-Autothrottle

Flight Condition:	V_CAS / [kn]	Flight Level	Flaps	Pre-Condition	Flight-Mode	Repetitions		
	200	150	0	Straight&Level	EFCS	1+		

Moding:	Enable	Reset	INDI	PCH	Cstar	Act_INDI	Act_PCH	Beta_Est	Alpha_B	doTurnC	OpenL	Long_cmd	Lat_cmd	AeroCg	doLimit
	1	E	0	0	0	1	1	0	0	0	0	1	1	1	0

Procedure:	1. De-activate EFCS	2. Reconfigure EFCS	3. Est. Flight Condition	4. Hands-off Stick	5. Activate EFCS

Start / [UTC]:	05:45	05:50
End / [UTC]:	05:49	05:52

TURBULENT AIR
NO CHOKES
Small Oscillation

Procedures:	0. Establish trimmed flight condition - Safety Pilot tries to maintain speed by throttle ~~0. Establish~~
	1. Pitch U: trim + 2.5°, Pitch D: trim -2.5° - at moderate rates — w/o TRIM / OK: Steady Pitch
	~~2. Roll R - Bank capture (5°, aim for precision) - at moderate rates - repeat for L~~
	3. Roll R - Bank capture (10°, aim for precision) - at moderate rates - repeat for L — keeps it → Repeat
	4. Roll R to Limits (35°), release stick (A/C returns to 27.5°) - at moderate rates - repeat for L — Transition ok
	-
Comments:	KEEPS ATT

PH-LAB Flight Test Card

Prio +

Flight #:	3
CASE #:	3.1.3
Wind / [kn]:	
Wind / [deg]:	

Observer:	
Gain Set:	NOMINAL
Optional Case:	NOMINAL
UUID:	8F795259

Flight Tag:	NDI_base_lat_lon_bank_A

Synopsis:	NDI Base: 1. Engage Roll at predefined bank angles (5°, 10°) - w Pseudo-Autothrottle

Flight Condition:	V_CAS / [kn]	Flight Level	Flaps	Pre-Condition	Flight-Mode	Repetitions		
	200	150	0	~~Straight&Level~~	EFCS	1+		

Roll ~~Pitch~~ & 5°/10° bank

Moding:	Enable	Reset	INDI	PCH	Cstar	Act_INDI	Act_PCH	Beta_Est	Alpha_B	doTurnC	OpenL	Long_cmd	Lat_cmd	AeroCg	doLimit
	1	E	0	0	0	1	1	0	0	0	0	1	1	1	0

Procedure:	1. De-activate EFCS	2. Reconfigure EFCS	3. Est. Flight Condition	4. Hands-off Stick	5. Activate EFCS

Start / [UTC]:	05:55	
End / [UTC]:	05:56	

OK !!

Procedures:	0. Establish trimmed flight condition, manually roll to +/-5° and engage NDI, manually roll to +/-10° and engage NDI
	1. Manually roll to +/-5° and engage NDI there, ~~manually roll to +/-10° and engage NDI there~~ — KEEPS it
	- L&R - Rolling
	-
	- WAIT NO PROBLEM
	-
Comments:	

PH-LAB Flight Test Card

P+

Flight #:	3
CASE #:	3.1.4
Wind / [kn]:	
Wind / [deg]:	

Observer:	
Gain Set:	NOMINAL
Optional Case:	NOMINAL
UUID:	65A321F3

Flight Tag:	NDI_base_lat_lon_rapid_A

Synopsis:	NDI Base: 1. Check Roll with quicker rates (5°, 10°) - w Pseudo-Autothrottle

Flight Condition:	V_CAS / [kn]	Flight Level	Flaps	Pre-Condition	Flight-Mode	Repetitions		
	200	150	0	Straight&Level	EFCS	1+		

Moding:	Enable	Reset	INDI	PCH	Cstar	Act_INDI	Act_PCH	Beta_Est	Alpha_B	doTurnC	OpenL	Long_cmd	Lat_cmd	AeroCg	doLimit
	1	E	0	0	0	1	1	0	0	0	0	1	1	1	0

Procedure:	1. De-activate EFCS	2. Reconfigure EFCS	3. Est. Flight Condition	4. Hands-off Stick	5. Activate EFCS

Start / [UTC]:	09:56
End / [UTC]:	10:08

NO YOLTS

OK

Procedures:	0. Establish trimmed flight condition - Safety Pilot tries to maintain speed by throttle → MAINTAINS OK
	1. Pitch U: trim + 5°, Pitch D: trim -5° - at RAPID rates CORRECTION
	2. Roll R - Bank capture (5°, aim for precision) - at RAPID rates - repeat for L
	3. Roll R - Bank capture (10°, aim for precision) - at moderate rates - repeat for L Little Overshoot
	-
	-
Comments:	

PH-LAB Flight Test Card

Flight #:	3
CASE #:	3.1.6
Wind / [kn]:	
Wind / [deg]:	

Observer:	
Gain Set:	NOMINAL
Optional Case:	NOMINAL
UUID:	16BE28E8

Flight Tag:	NDI_PCH_lat_lon_lOn_A

Synopsis:	NDI with PCH: 1. Check Pitch Up and Down, 2. Check Roll limits (RCAH, AC), 3. Check Roll Precision - see Saturation limits

Flight Condition:	V_CAS / [kn]	Flight Level	Flaps	Pre-Condition	Flight-Mode	Repetitions		
	200	150	0	Straight&Level	EFCS	1+		

Moding:	Enable	Reset	INDI	PCH	Cstar	Act_INDI	Act_PCH	Beta_Est	Alpha_B	doTurnC	OpenL	Long_cmd	Lat_cmd	AeroCg	doLimit
	1	E	0	1	0	1	1	0	0	0	0	1	1	1	1

Procedure:	1. De-activate EFCS	2. Reconfigure EFCS	3. Est. Flight Condition	4. Hands-off Stick	5. Activate EFCS

Start / [UTC]:	10:
End / [UTC]:	

YOLTS → OFF!

Procedures:	0. Establish trimmed flight condition - Safety Pilot tries to maintain speed by throttle
	1. Pitch U: trim + 2.5°, Pitch D: trim -2.5° - at moderate rates, see if limitations hit
	2. Roll R - Bank capture (5°, aim for precision) - at moderate rates - repeat for L
	3. Roll R - Bank capture (10°, aim for precision) - at moderate rates - repeat for L
	4. Roll R to Limits (35°), release stick (A/C returns to 27.5°) - at moderate rates - repeat for L
	-
Comments:	

No PCH Anyway

ACT - models OFF
working → (NDI 2

PH-LAB Flight Test Card

++

Flight #:	3
CASE #:	3.1.7
Wind / [kn]:	
Wind / [deg]:	

Observer:	
Gain Set:	NOMINAL
Optional Case:	NOMINAL
UUID:	4CD9F48E

Flight Tag:	NDI_PCH_lat_lon_lOn_ActOff_A

Synopsis:	NDI with PCH w/o ACT models: 1. Check Pitch Up and Down, 2. Check Roll limits (RCAH, AC), 3. Check Roll Precision - see AoA increase

Flight Condition:	V_CAS / [kn]	Flight Level	Flaps	Pre-Condition	Flight-Mode	Repetitions		
	200	150	0	Straight&Level	EFCS	1+		

Moding:	Enable	Reset	INDI	PCH	Cstar	Act_INDI	Act_PCH	Beta_Est	Alpha_B	doTurnC	OpenL	Long_cmd	Lat_cmd	AeroCg	doLimit
	1	E	0	1	0	1	0	0	0	0	0	1	1	1	1

Procedure:	1. De-activate EFCS	2. Reconfigure EFCS	3. Est. Flight Condition	4. Hands-off Stick	5. Activate EFCS

Start / [UTC]:	
End / [UTC]:	

Procedures:	0. Establish trimmed flight condition - Safety Pilot tries to maintain speed by throttle
	1. Pitch U: trim + 2.5°, Pitch D: trim -2.5° - at moderate rates, see if limitations hit
	2. Roll R - Bank capture (5°, aim for precision) - at moderate rates - repeat for L
	3. Roll R - Bank capture (10°, aim for precision) - at moderate rates - repeat for L
	4. Roll R to Limits (35°), release stick (A/C returns to 27.5°) - at moderate rates - repeat for L
	-
Comments:	

PH-LAB Flight Test Card

Flight #:	3
CASE #:	3.1.8
Wind / [kn]:	
Wind / [deg]:	

Observer:	
Gain Set:	CONSERVATIVE
Optional Case:	NOMINAL
UUID:	7964DF62

Flight Tag:	INDI_lat_lon_cons_A

Synopsis:	INDI: 1. Check Pitch Up and Down, 2. Check Roll limits (RCAH, AC), 3. Check Roll Precision

Flight Condition:	V_CAS / [kn]	Flight Level	Flaps	Pre-Condition	Flight-Mode	Repetitions		
	200	150	0	Straight&Level	EFCS	1+		

Moding:	Enable	Reset	INDI	PCH	Cstar	Act_INDI	Act_PCH	Beta_Est	Alpha_B	doTurnC	OpenL	Long_cmd	Lat_cmd	AeroCg	doLimit
	1	E	1	0	0	1	1	0	0	0	0	1	1	1	0

Procedure:	1. De-activate EFCS	2. Reconfigure EFCS	3. Est. Flight Condition	4. Hands-off Stick	5. Activate EFCS

Start / [UTC]:	10:02
End / [UTC]:	10:02

Procedures:	0. Establish trimmed flight condition - Safety Pilot tries to maintain speed by throttle
	1. Pitch U: trim + 2.5°, Pitch D: trim -2.5° - at moderate rates, see if limitations hit
	2. Roll R - Bank capture (5°, aim for precision) - at moderate rates - repeat for L
	3. Roll R - Bank capture (10°, aim for precision) - at moderate rates - repeat for L
	4. Roll R to Limits (35°), release stick (A/C returns to 27.5°) - at moderate rates - repeat for L
	-
Comments:	

PH-LAB Flight Test Card

Flight #:	3
CASE #:	3.1.9
Wind / [kn]:	
Wind / [deg]:	

Observer:	
Gain Set:	NOMINAL
Optional Case:	NOMINAL
UUID:	92BD91FD

Flight Tag:	INDI_lat_lon_lOn_A

Synopsis:	INDI: 1. Check Pitch Up and Down, 2. Check Roll limits (RCAH, AC), 3. Check Roll Precision

Flight Condition:	V_CAS / [kn]	Flight Level	Flaps	Pre-Condition	Flight-Mode	Repetitions		
	200	150	0	Straight&Level	EFCS	1+		

Moding:	Enable	Reset	INDI	PCH	Cstar	Act_INDI	Act_PCH	Beta_Est	Alpha_B	doTurnC	OpenL	Long_cmd	Lat_cmd	AeroCg	doLimit
	1	E	1	0	0	1	1	0	0	0	0	1	1	1	1

Procedure:	1. De-activate EFCS	2. Reconfigure EFCS	3. Est. Flight Condition	4. Hands-off Stick	5. Activate EFCS

Start / [UTC]:	
End / [UTC]:	

ROLLS OFF (MEDIATED)

Procedures:	0. Establish trimmed flight condition - Safety Pilot tries to maintain speed by throttle
	1. Pitch U: trim + 2.5°, Pitch D: trim -2.5° - at moderate rates, see if limitations hit
	2. Roll R - Bank capture (5°, aim for precision) - at moderate rates - repeat for L
	3. Roll R - Bank capture (10°, aim for precision) - at moderate rates - repeat for L
	4. Roll R to Limits (35°), release stick (A/C returns to 27.5°) - at moderate rates - repeat for L
	-
Comments:	

INDI w. ACT MEAS worked

PH-LAB Flight Test Card

Flight #:	3
CASE #:	3.1.10
Wind / [kn]:	
Wind / [deg]:	

Observer:	
Gain Set:	NOMINAL
Optional Case:	NOMINAL
UUID:	A49755EC

Flight Tag:	INDI_lat_lon_lOff_A

Synopsis:	INDI: 1. Check Pitch Up and Down, 2. Check Roll limits (RCAH, AC), 3. Check Roll Precision

Flight Condition:	V_CAS / [kn]	Flight Level	Flaps	Pre-Condition	Flight-Mode	Repetitions		
	200	150	0	Straight&Level	EFCS	1+		

Moding:	Enable	Reset	INDI	PCH	Cstar	Act_INDI	Act_PCH	Beta_Est	Alpha_B	doTurnC	OpenL	Long_cmd	Lat_cmd	AeroCg	doLimit
	1	E	1	0	0	1	1	0	0	0	0	1	1	1	0

Procedure:	1. De-activate EFCS	2. Reconfigure EFCS	3. Est. Flight Condition	4. Hands-off Stick	5. Activate EFCS

Start / [UTC]:	10:37
End / [UTC]:	10:40

ACCURATE, & NO YAWS!!

Procedures:	0. Establish trimmed flight condition - Safety Pilot tries to maintain speed by throttle
	1. Pitch U: trim + 2.5°, Pitch D: trim -2.5° - at moderate rates, see if limitations hit — Good reaction
	2. Roll R - Bank capture (5°, aim for precision) - at moderate rates - repeat for L
	3. Roll R - Bank capture (10°, aim for precision) - at moderate rates - repeat for L
	4. Roll R to Limits (35°), release stick (A/C returns to 27.5°) - at moderate rates - repeat for L
	-
Comments:	PITCH is not very good responding STICK is vidy responding

!!! MULTIPLE-Engs after 10:42 : PURE INDI Control A bit nervous, but controllable !! Problematic with Auto-Trim

PH-LAB Flight Test Card

Flight #:	3
CASE #:	3.1.11
Wind / [kn]:	~~205~~ 18
Wind / [deg]:	~~18~~ 203

Observer:	
Gain Set:	CONSERVATIVE
Optional Case:	NOMINAL
UUID:	BD52869

Flight Tag:	INDI_lat_lon_cons_lOn_ActOff_A

Synopsis:	INDI: 1. Check Pitch Up and Down, 2. Check Roll limits (RCAH, AC), 3. Check Roll Precision

Flight Condition:	V_CAS / [kn]	Flight Level	Flaps	Pre-Condition	Flight-Mode	Repetitions		
	200	150	0	Straight&Level	EFCS	1+		

Moding:	Enable	Reset	INDI	PCH	Cstar	Act_INDI	Act_PCH	Beta_Est	Alpha_B	doTurnC	OpenL	Long_cmd	Lat_cmd	AeroCg	doLimit
	1	E	1	0	0	0	1	0	0	0	0	1	1	1	1

Procedure:	1. De-activate EFCS	2. Reconfigure EFCS	3. Est. Flight Condition	4. Hands-off Stick	5. Activate EFCS

Start / [UTC]:	10:08	10:11	10:15	10:17	10:20	10:23			
End / [UTC]:	10:10	10:13	10:16	10:19	10:22				

Procedures:	0. Establish trimmed flight condition - Safety Pilot tries to maintain speed by throttle - EXTREMLY ALERT, as never tested
	1. Pitch U: trim + 2.5°, Pitch D: trim -2.5° - at moderate rates, see if limitations hit
	2. Roll R - Bank capture (5°, aim for precision) - at moderate rates - repeat for L
	3. Roll R - Bank capture (10°, aim for precision) - at moderate rates - repeat for L
	4. Roll R to Limits (35°), release stick (A/C returns to 27.5°) - at moderate rates - repeat for L
	-
Comments:	+8° instead of 6

PH-LAB Flight Test Card

Flight #:	3
CASE #:	3.1.12
Wind / [kn]:	
Wind / [deg]:	

Observer:	
Gain Set:	NOMINAL
Optional Case:	NOMINAL
UUID:	F7FABB1A

Flight Tag:	INDI_PCH_lat_lon_lOn_A

Synopsis:	INDI: 1. Check Pitch Up and Down, 2. Check Roll limits (RCAH, AC), 3. Check Roll Precision

Flight Condition:	V_CAS / [kn]	Flight Level	Flaps	Pre-Condition	Flight-Mode	Repetitions		
	200	150	0	Straight&Level	EFCS	1+		

Moding:	Enable	Reset	INDI	PCH	Cstar	Act_INDI	Act_PCH	Beta_Est	Alpha_B	doTurnC	OpenL	Long_cmd	Lat_cmd	AeroCg	doLimit
	1	E	1	1	0	1	1	0	0	0	0	1	1	1	1

Procedure:	1. De-activate EFCS	2. Reconfigure EFCS	3. Est. Flight Condition	4. Hands-off Stick	5. Activate EFCS

Start / [UTC]:	10:32
End / [UTC]:	

Procedures:	0. Establish trimmed flight condition - Safety Pilot tries to maintain speed by throttle
	1. Pitch U: trim + 2.5°, Pitch D: trim -2.5° - at moderate rates, see if limitations hit
	2. Roll R - Bank capture (5°, aim for precision) - at moderate rates - repeat for L
	3. Roll R - Bank capture (10°, aim for precision) - at moderate rates - repeat for L
	4. Roll R to Limits (35°), release stick (A/C returns to 27.5°) - at moderate rates - repeat for L
	-
Comments:	

PH-LAB Flight Test Card

Flight #:	3
CASE #:	3.1.14
Wind / [kn]:	
Wind / [deg]:	

Observer:	
Gain Set:	NOMINAL
Optional Case:	NOMINAL
UUID:	D789FEA6

Flight Tag:	INDI_lat_lon_lOff_OEI_A

Synopsis:	INDI: 1. Check Pitch Up and Down, 2. Check Roll limits (RCAH, AC), 3. Check Roll Precision

Flight Condition:	V_CAS / [kn]	Flight Level	Flaps	Pre-Condition	Flight-Mode	Repetitions		
	200	150	0	Straight&Level	EFCS	1+		

Moding:	Enable	Reset	INDI	PCH	Cstar	Act_INDI	Act_PCH	Beta_Est	Alpha_B	doTurnC	OpenL	Long_cmd	Lat_cmd	AeroCg	doLimit
	1	E	1	0	0	1	1	0	0	0	0	1	1	1	0

Procedure:	1. De-activate EFCS	2. Reconfigure EFCS	3. Est. Flight Condition	4. Hands-off Stick	5. Activate EFCS

Start / [UTC]:	10:28
End / [UTC]:	12:30

BOTH ENGINES
NO TRANSIENTS

Procedures:	0. Establish trimmed flight condition
	1. Reduce on THROTTLE to idle and see the rudder correcting attitude
	2. If feasible, some small pitch and roll maneuvres
	-
	-
	-
Comments:	

PERFECT

Good responding

Appendix C

Flight test results Flight #2

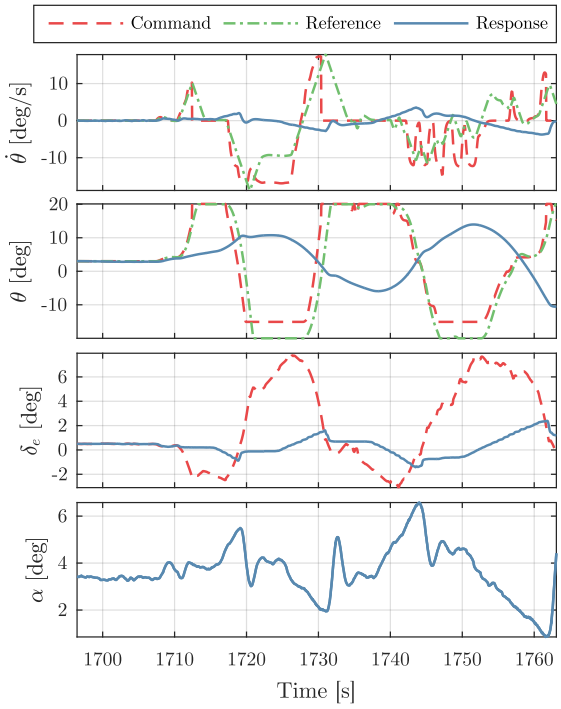

Figure C-1: Case #: 2.1.1 #1

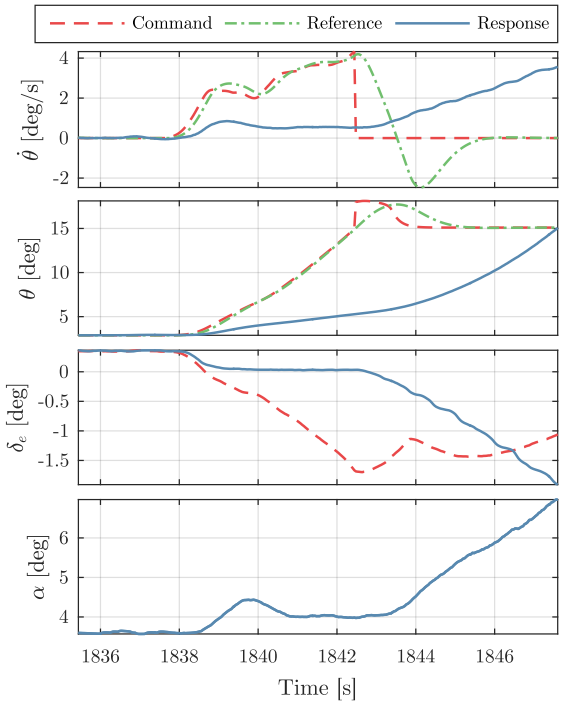

Figure C-2: Case #: 2.1.1 #2

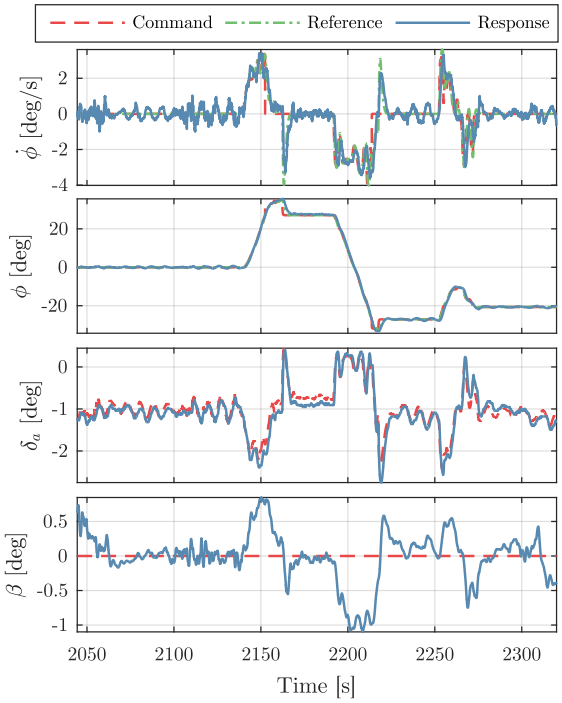

Figure C-3: Case #: 2.1.1 #3

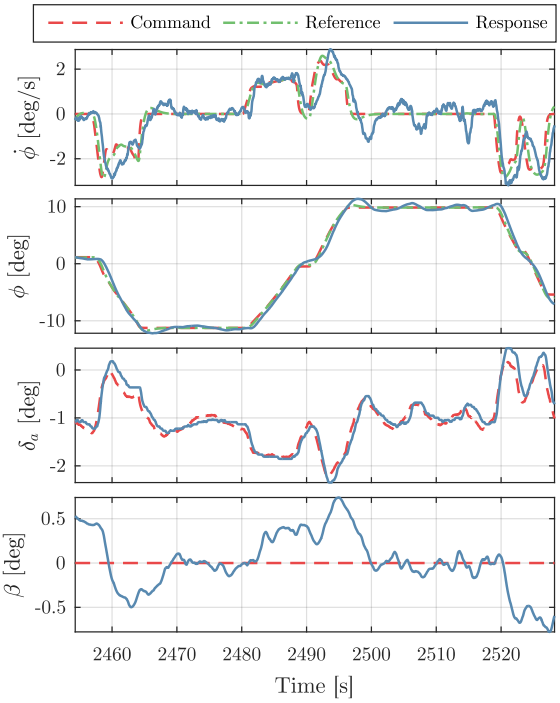

Figure C-4: Case #: 2.1.1 #4

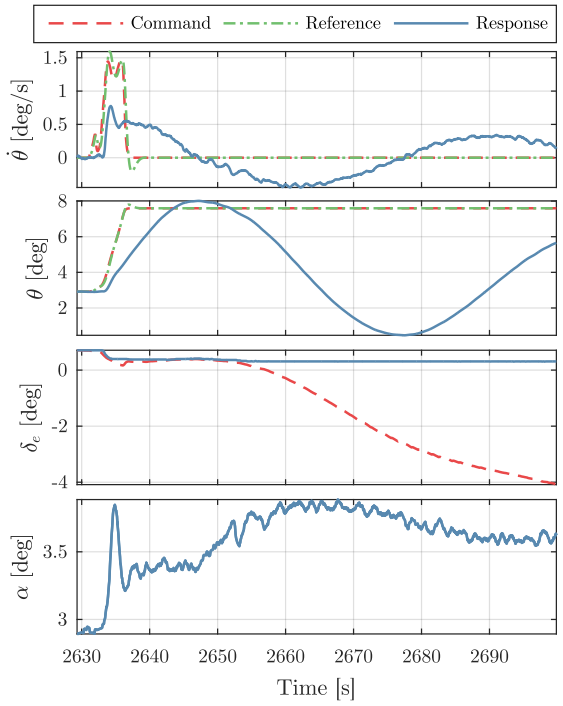

Figure C-5: Case #: 2.1.3 #1

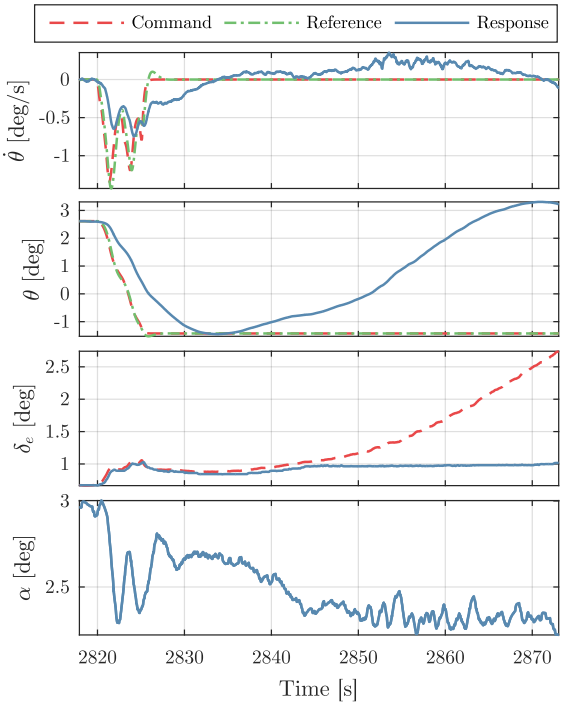

Figure C-6: Case #: 2.1.3 #2

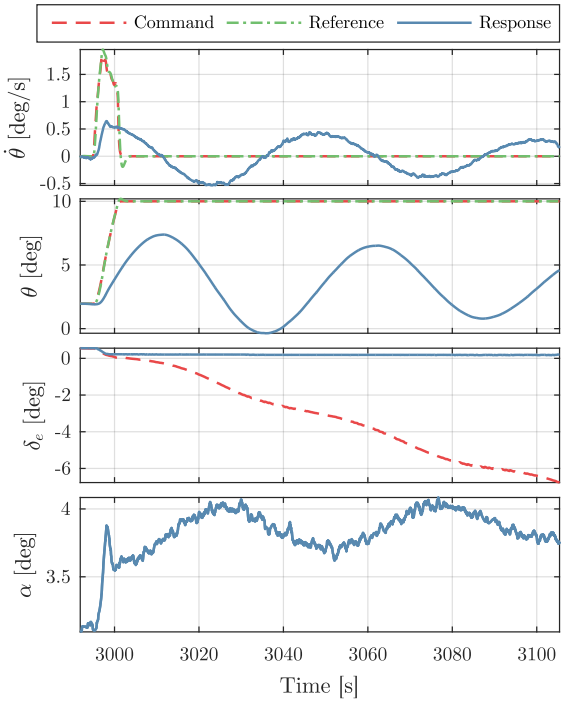

Figure C-7: Case #: 2.1.4 #1

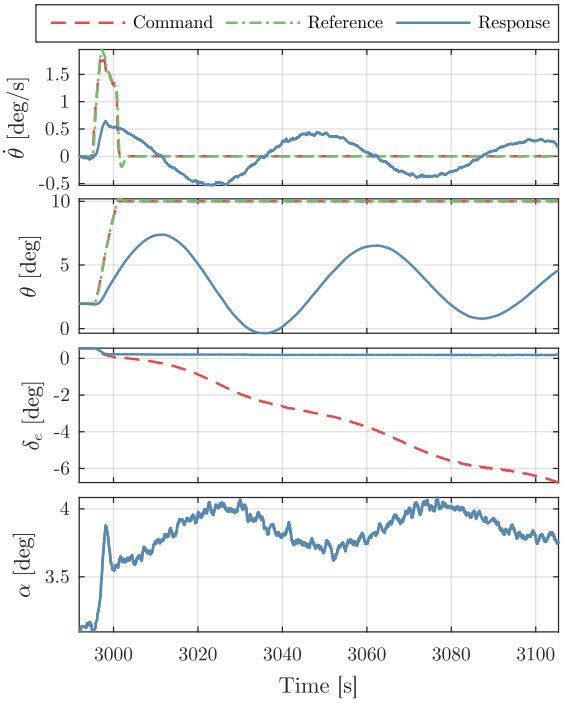

Figure C-8: Case #: 2.1.4 #2

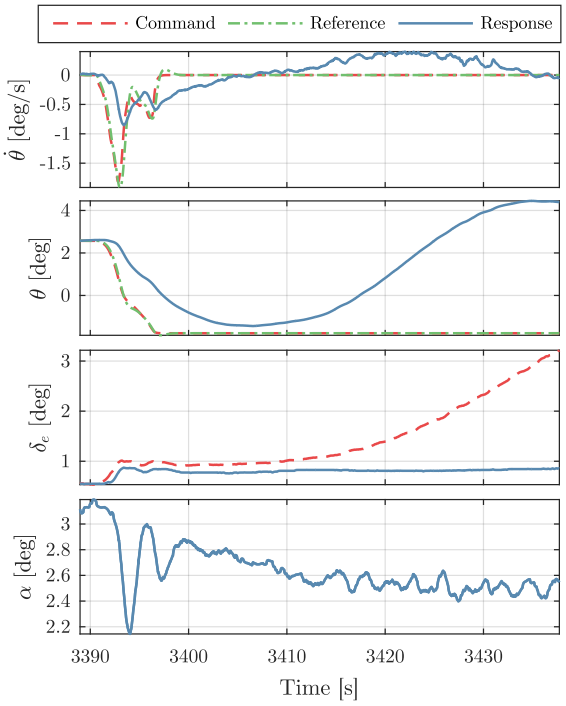

Figure C-9: Case #: 2.1.4 #3

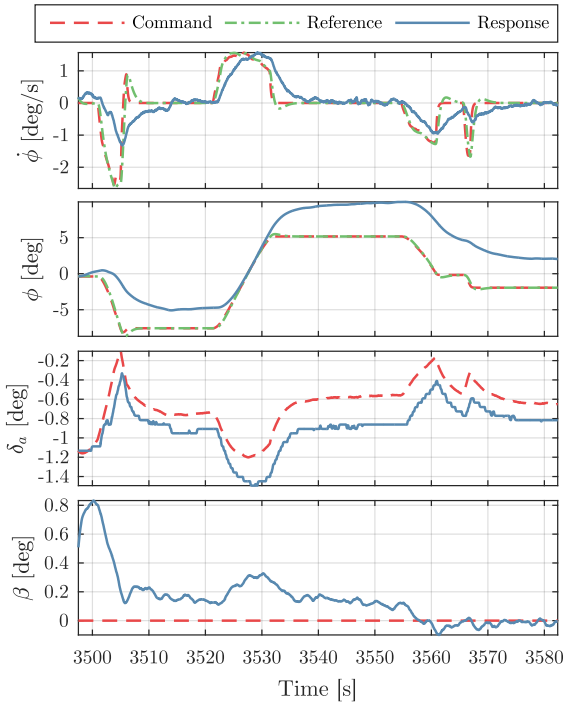

Figure C-10: Case #: 2.1.4 #4

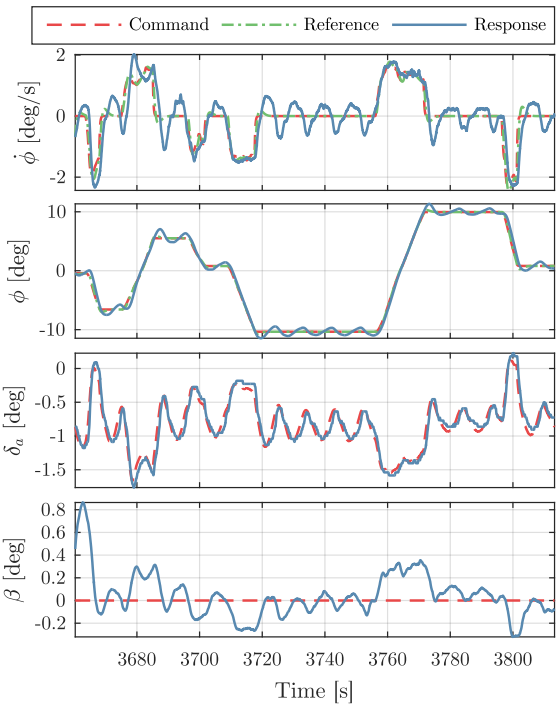

Figure C-11: Case #: 2.1.5

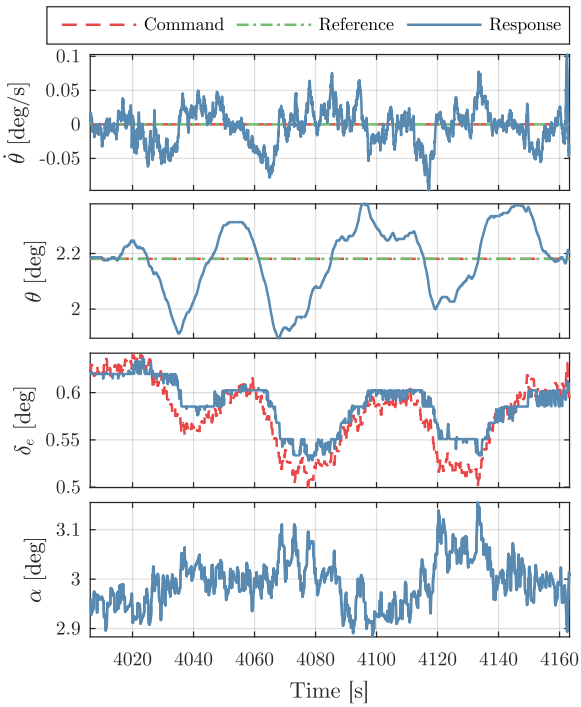

Figure C-12: Case #: 2.1.6

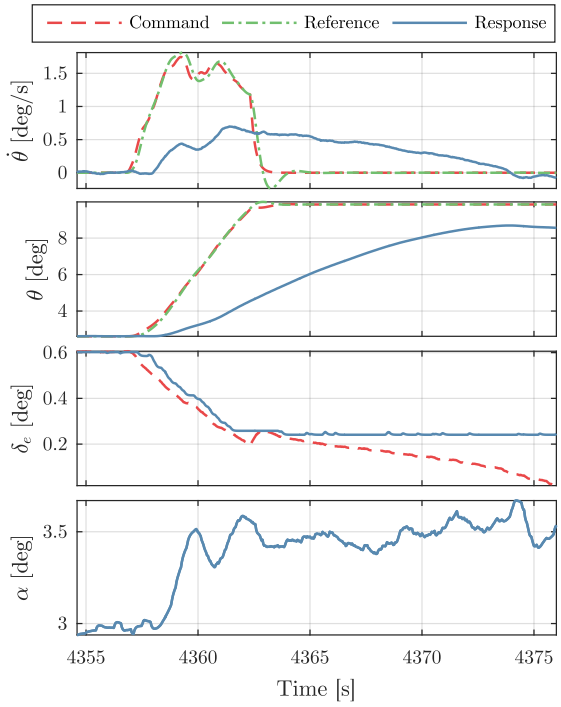

Figure C-13: Case #: 2.1.8 #1

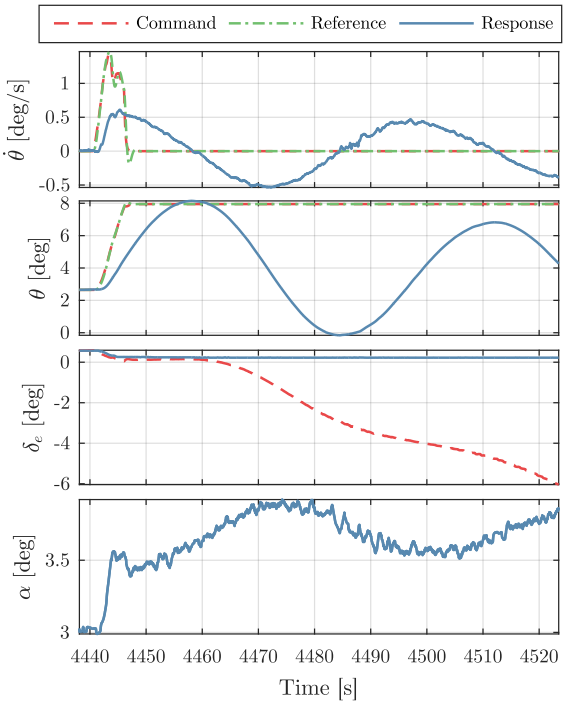

Figure C-14: Case #: 2.1.8 #2

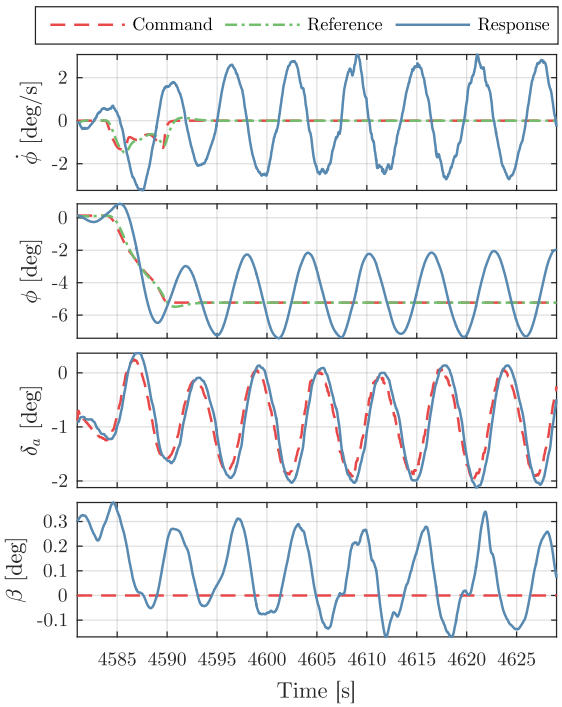

Figure C-15: Case #: 2.1.8 #3

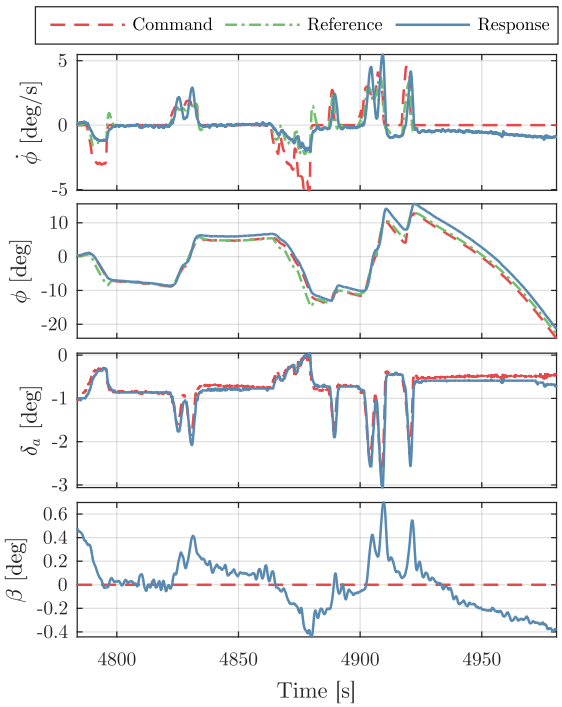

Figure C-16: Case #: 2.1.10 #1

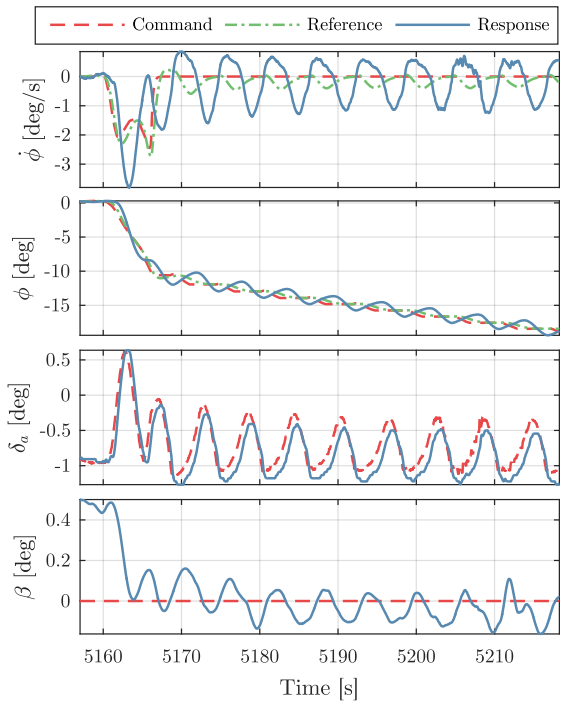

Figure C-17: Case #: 2.1.10 #2

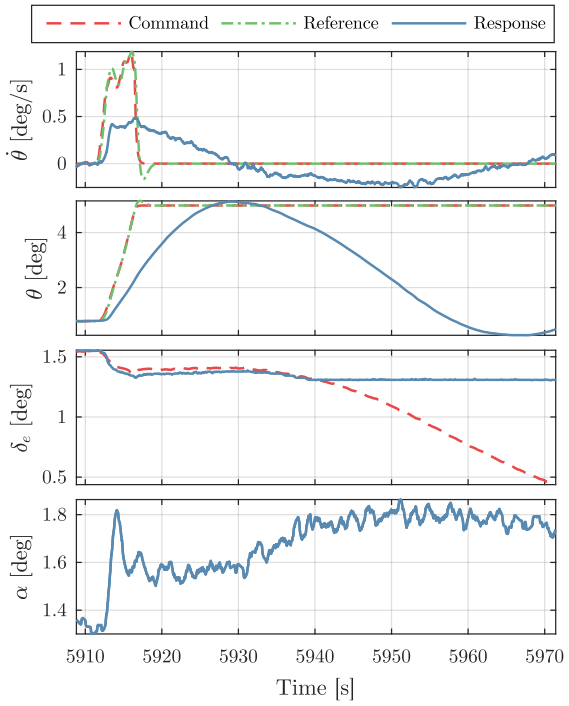

Figure C-18: Case #: 2.2.1

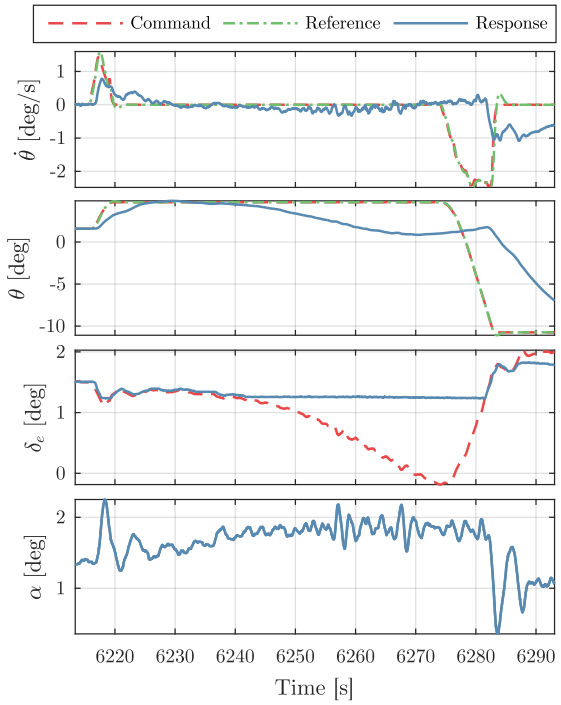

Figure C-19: Case #: 2.2.4

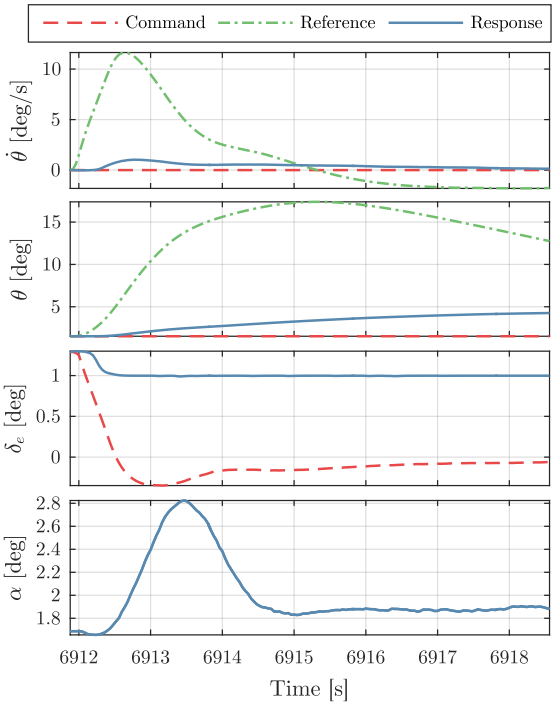

Figure C-20: Case #: 2.2.7 #1

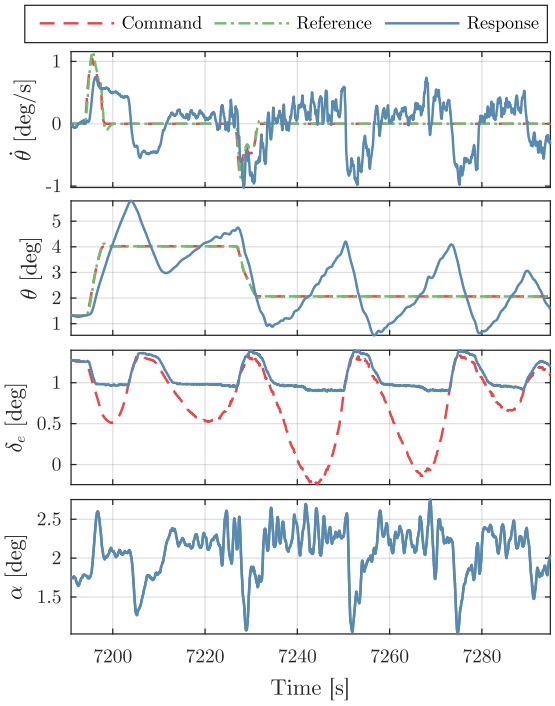

Figure C-21: Case #: 2.2.14 #1

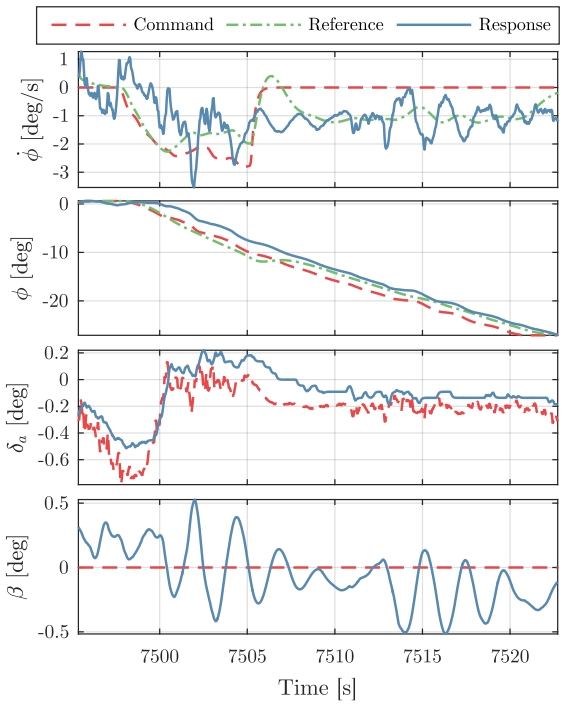

Figure C-22: Case #: 2.2.14 #2

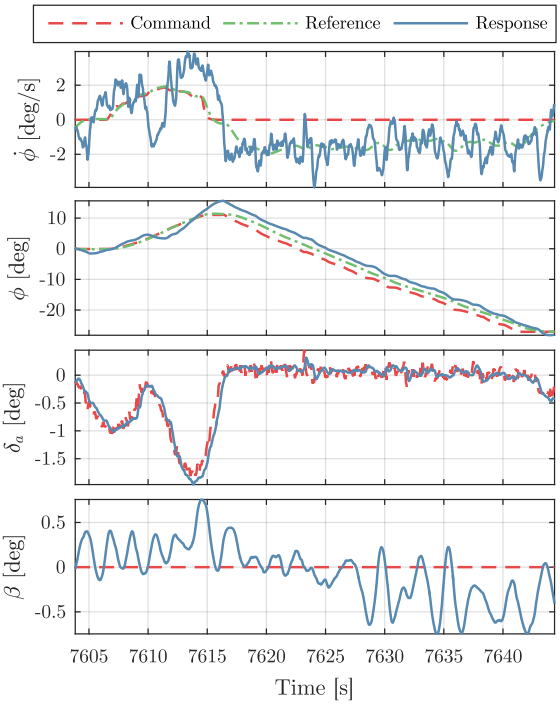

Figure C-23: Case #: 2.2.14 #3

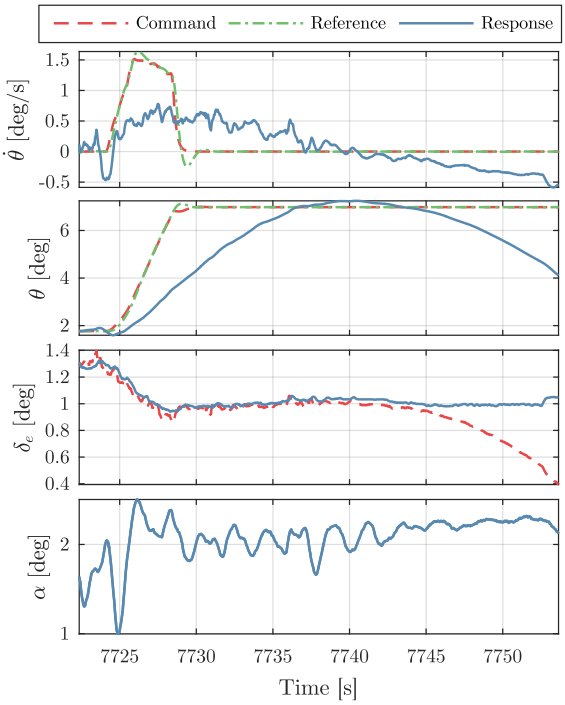

Figure C-24: Case #: 2.2.17 #1

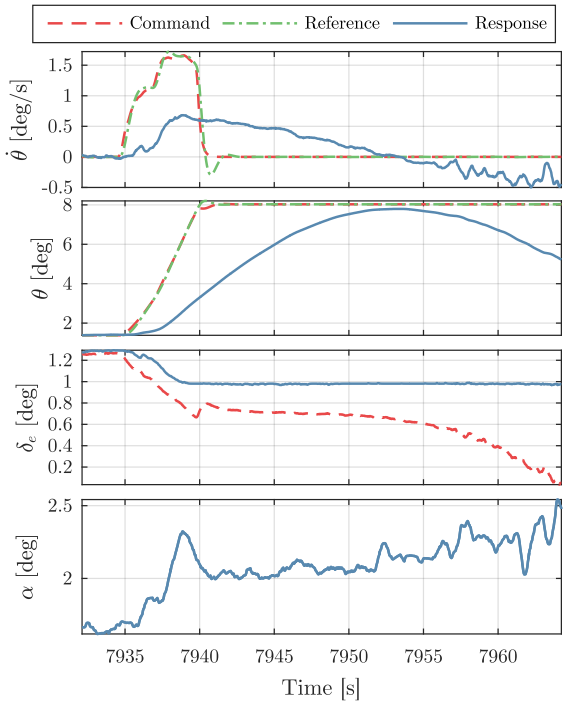

Figure C-25: Case #: 2.2.17 #2

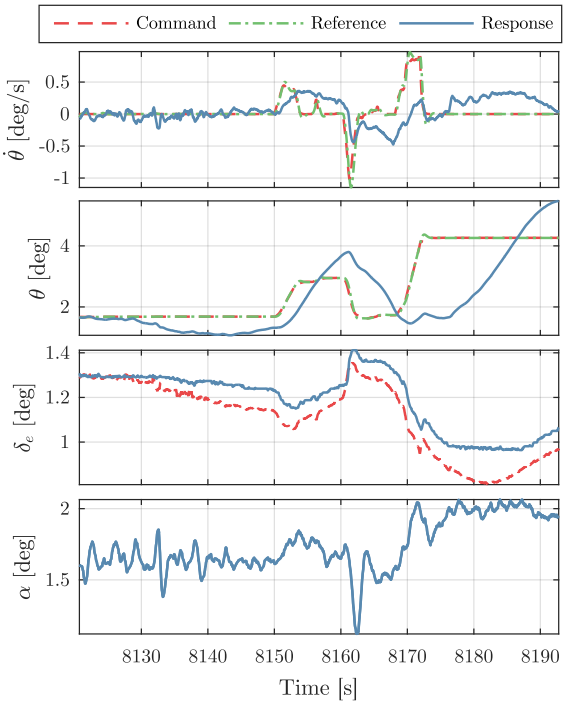

Figure C-26: Case #: 2.2.17 #3

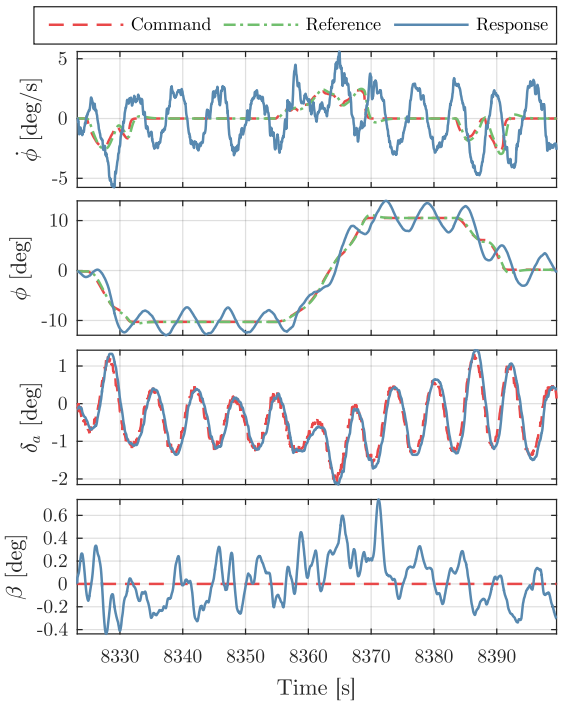

Figure C-27: Case #: 2.2.14 #4

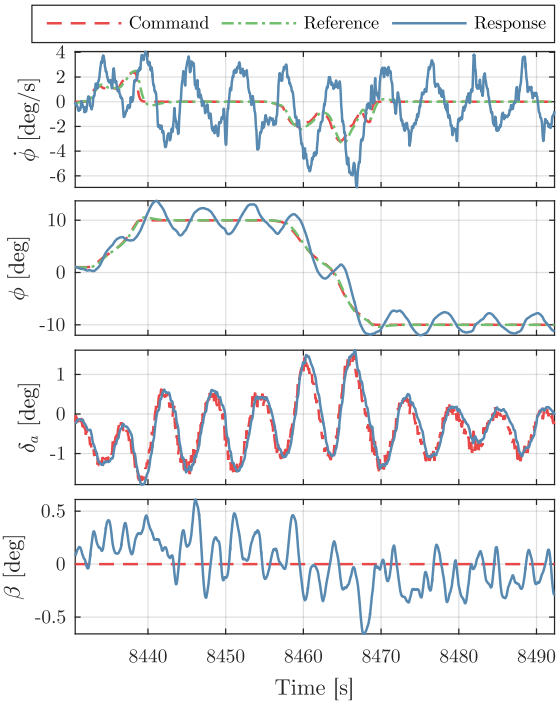

Figure C-28: Case #: 2.2.17 #5

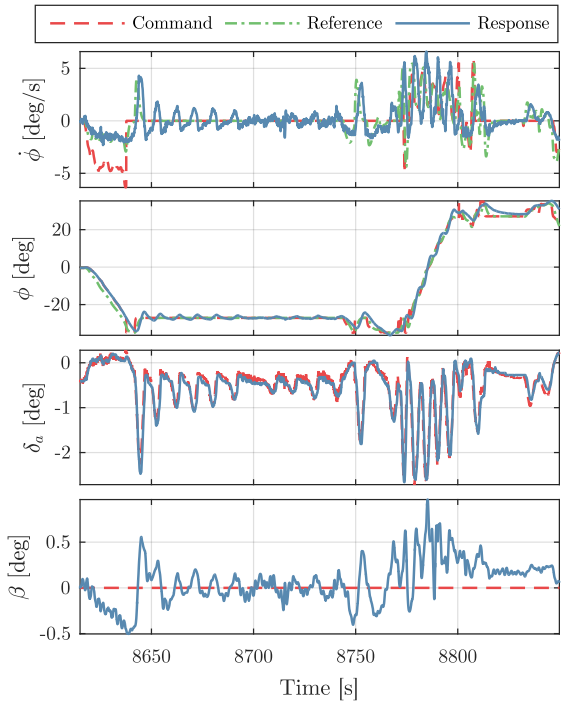

Figure C-29: Case #: 2.2.17 #6

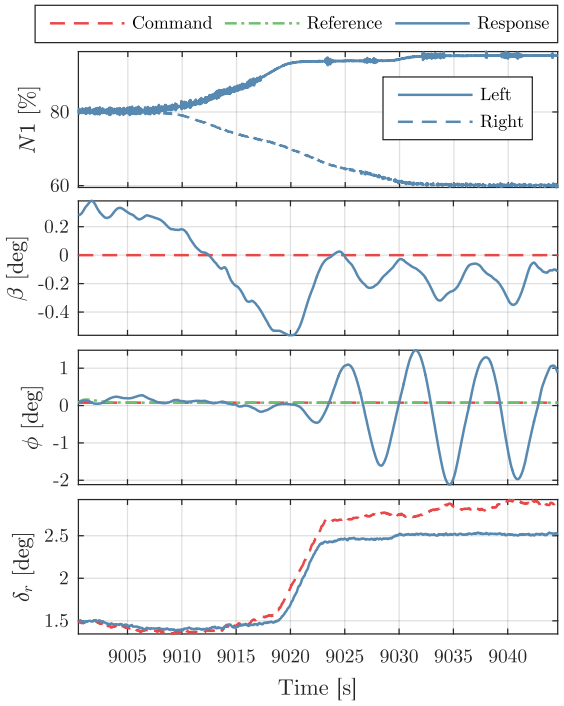

Figure C-30: Case #: 2.3.2 #1

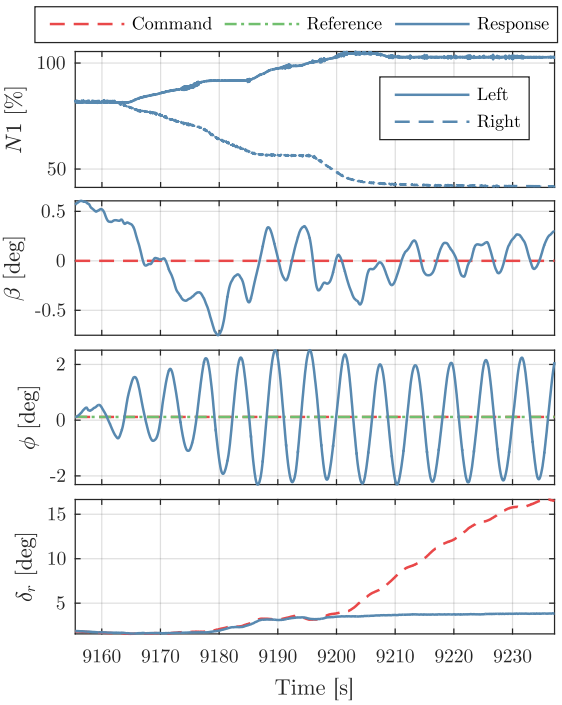

Figure C-31: Case #: 2.3.2 #2

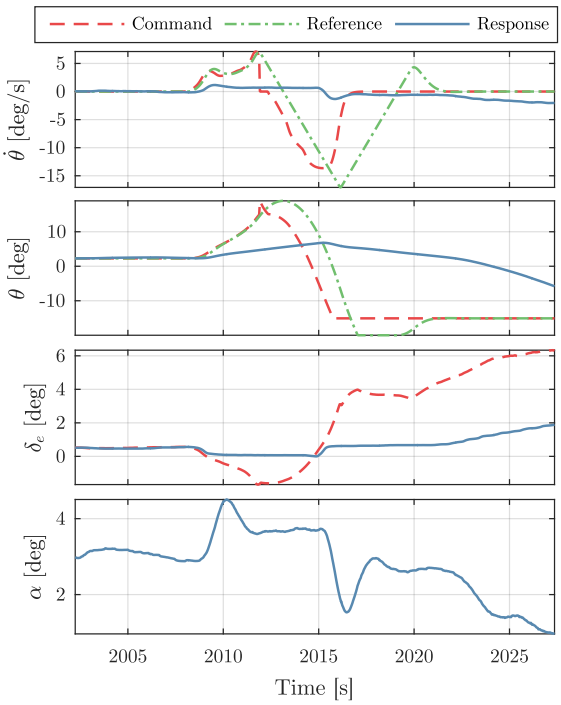

Figure C-32: Case #: 3.2.1 #1

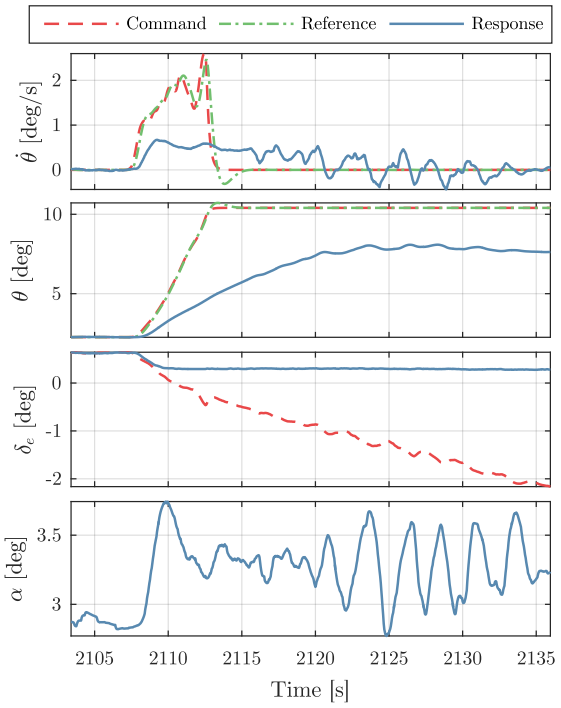

Figure C-33: Case #: 3.1.2 #2

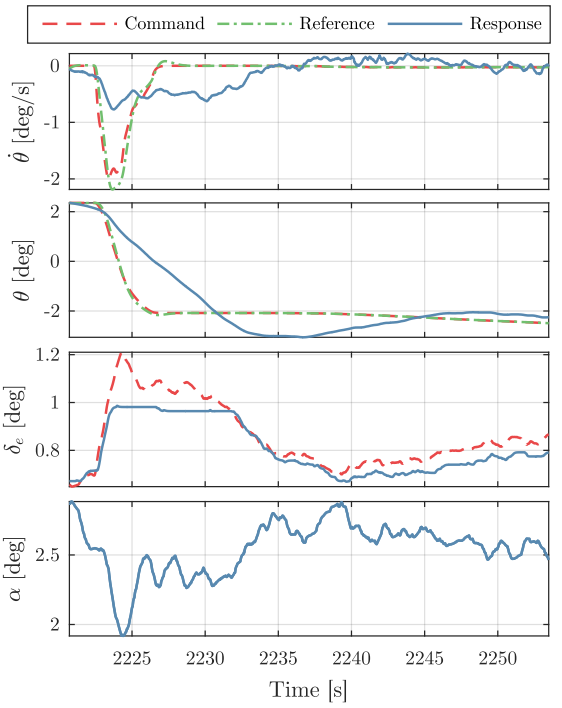

Figure C-34: Case #: 3.2.1 #3

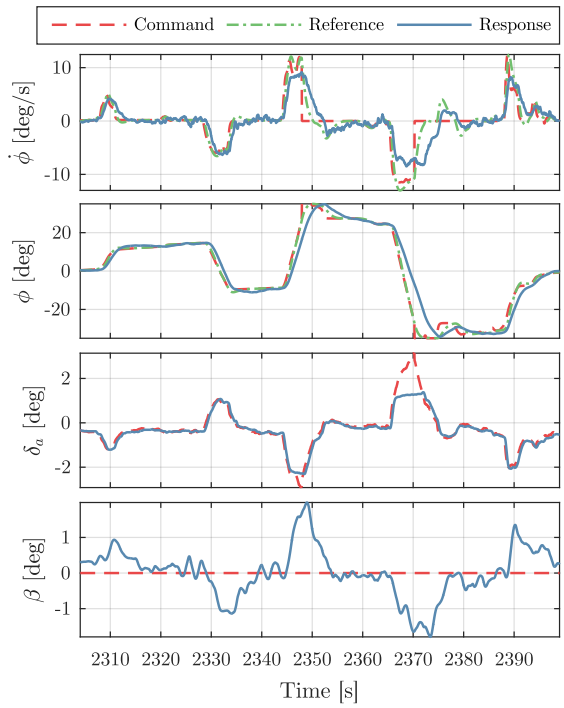

Figure C-35: Case #: 3.2.1 #4

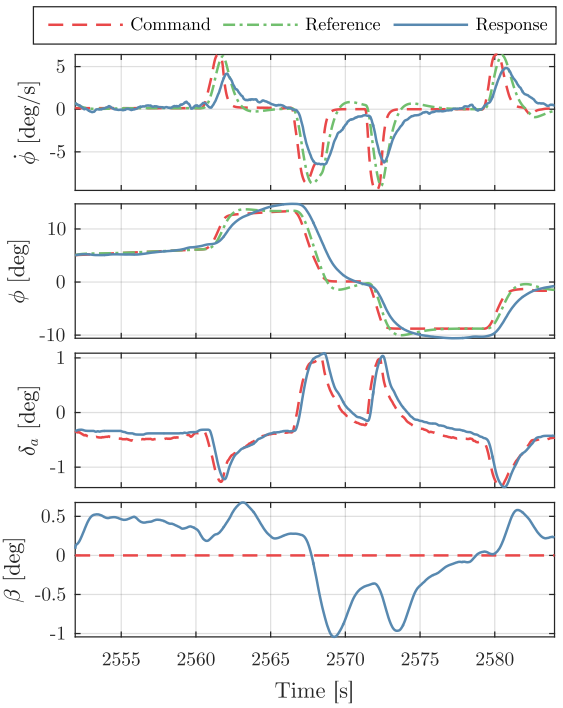

Figure C-36: Case #: 3.1.3

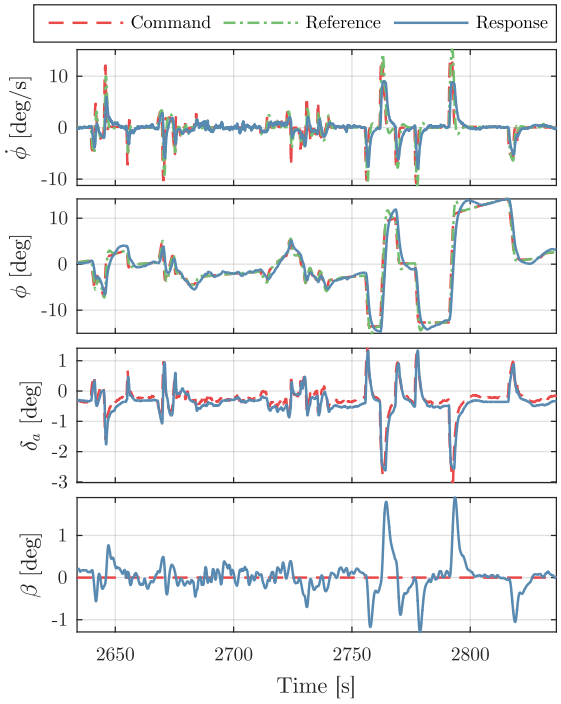

Figure C-37: Case #: 3.1.4

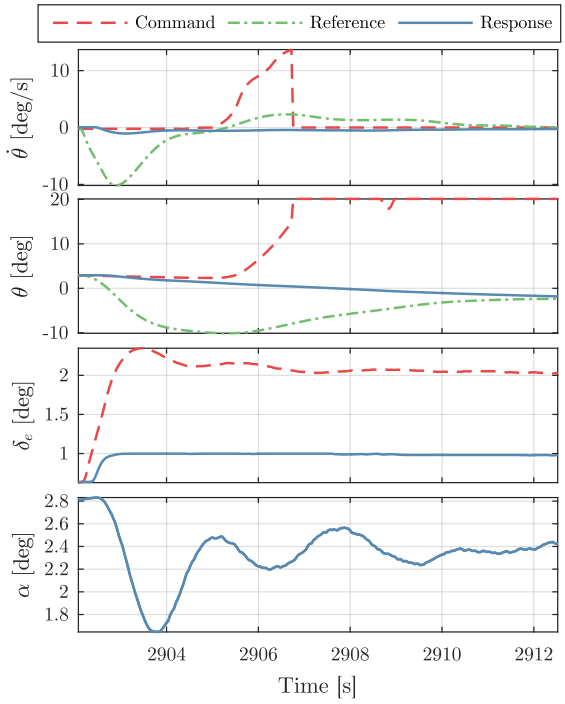

Figure C-38: Case #: 3.1.6 #1

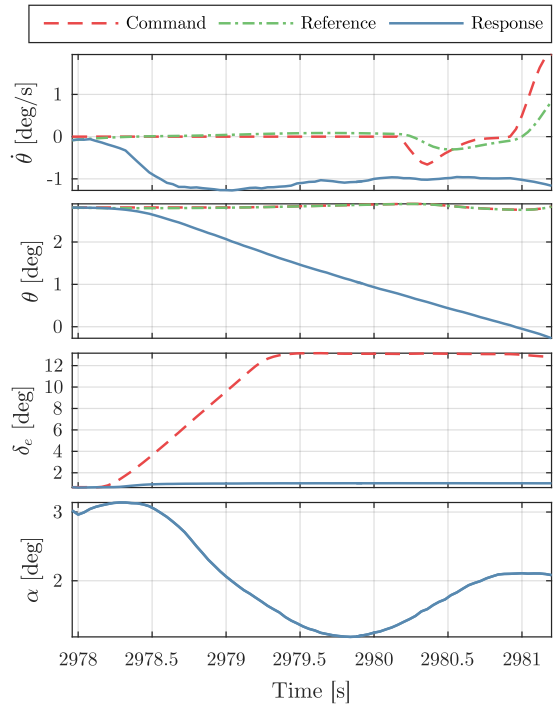

Figure C-39: Case #: 3.1.6 #2

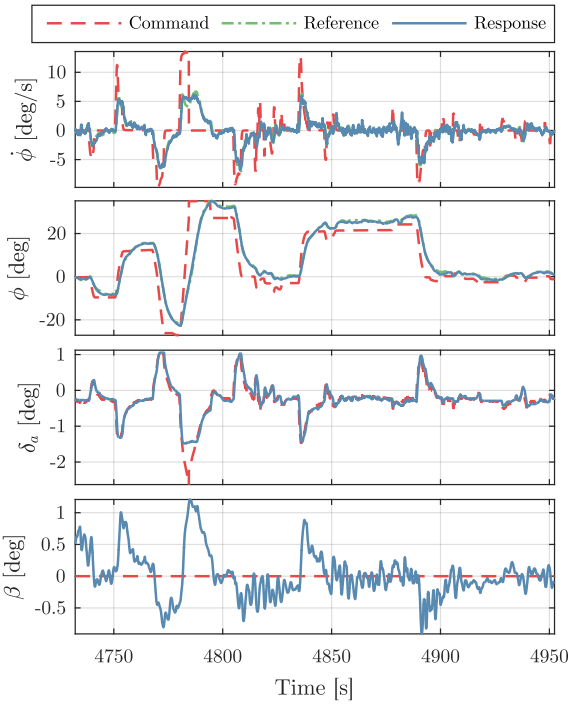

Figure C-40: Case #: 3.1.7

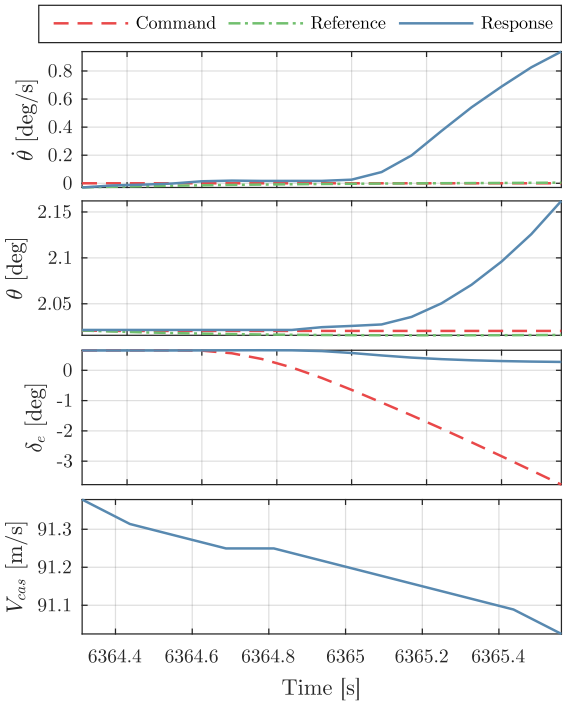

Figure C-41: Case #: 3.1.8

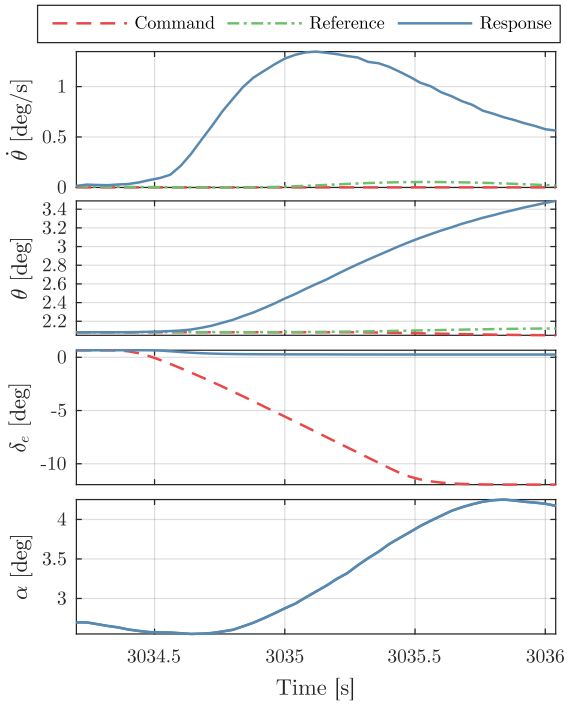

Figure C-42: Case #: 3.1.9 #1

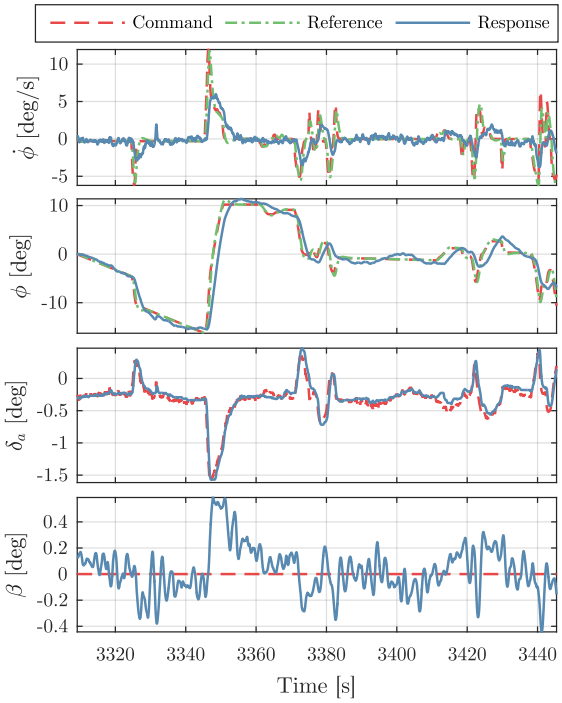

Figure C-43: Case #: 3.1.11 #1

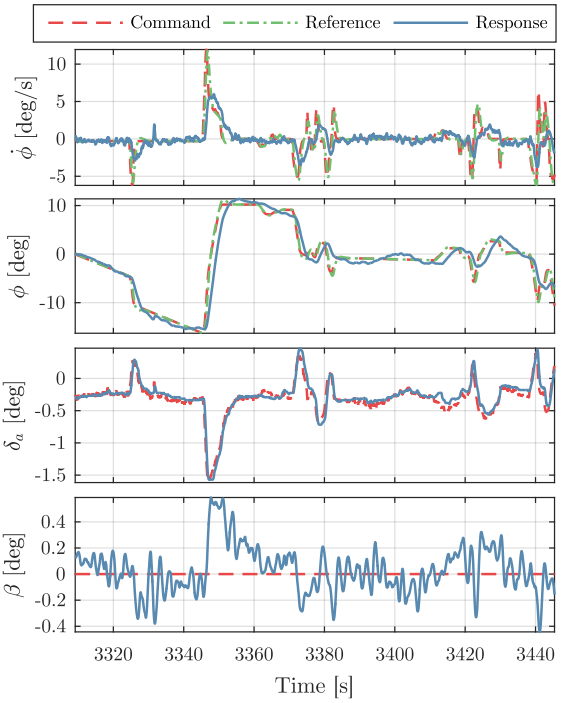

Figure C-44: Case #: 3.1.11 #2

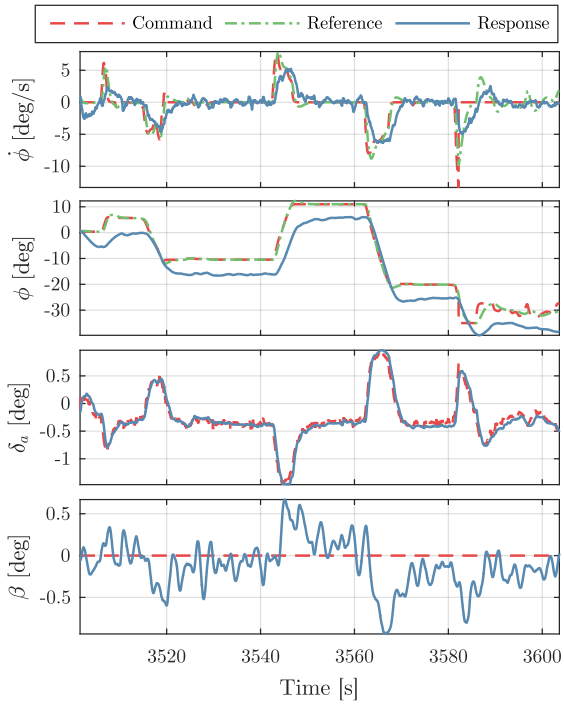

Figure C-45: Case #: 3.1.11 #2

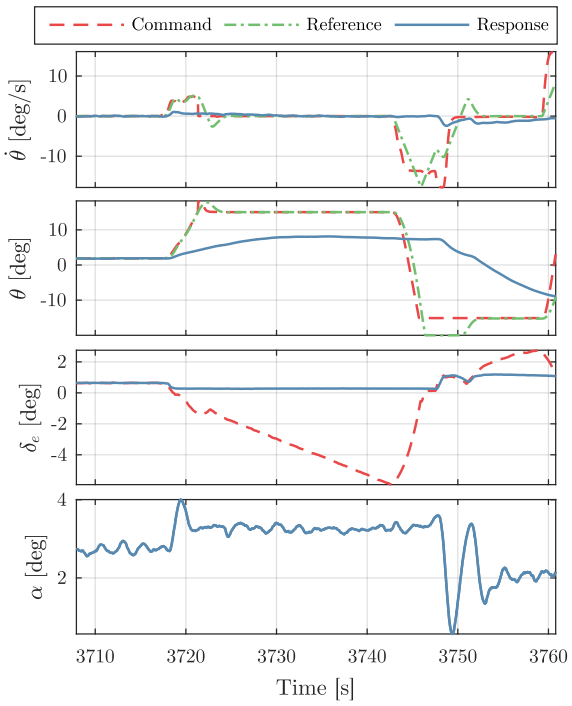

Figure C-46: Case #: 3.1.11 #3

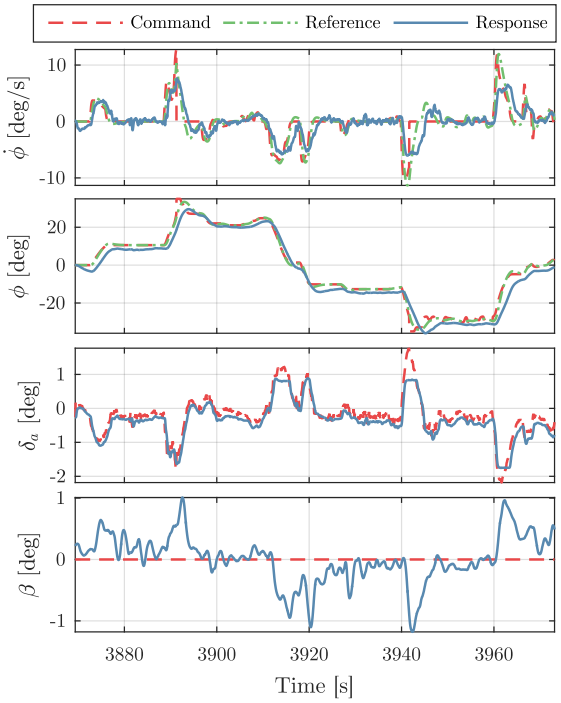

Figure C-47: Case #: 3.1.11 #4

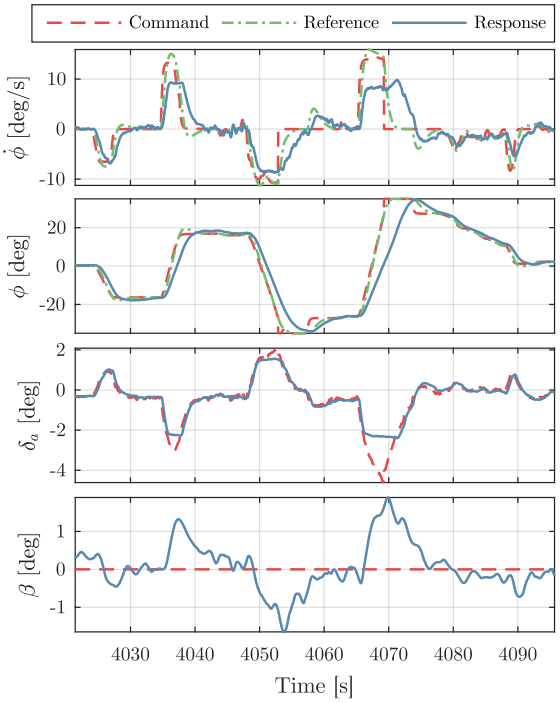

Figure C-48: Case #: 3.1.11 #5

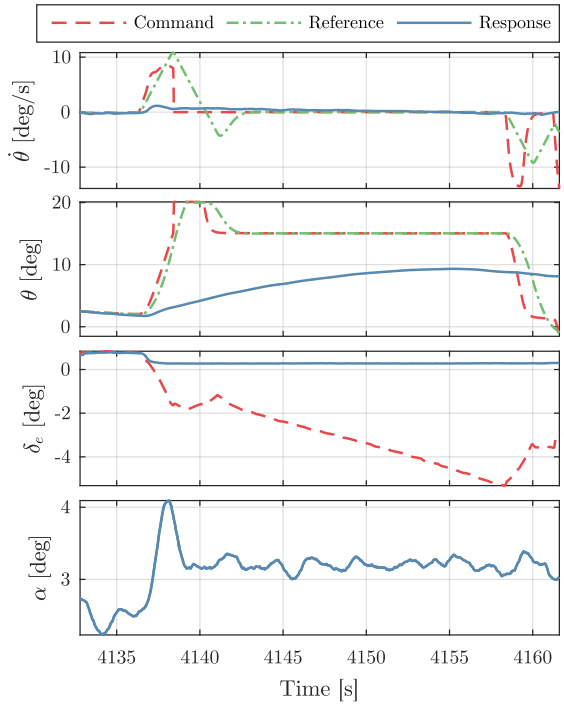

Figure C-49: Case #: 3.1.11 #6

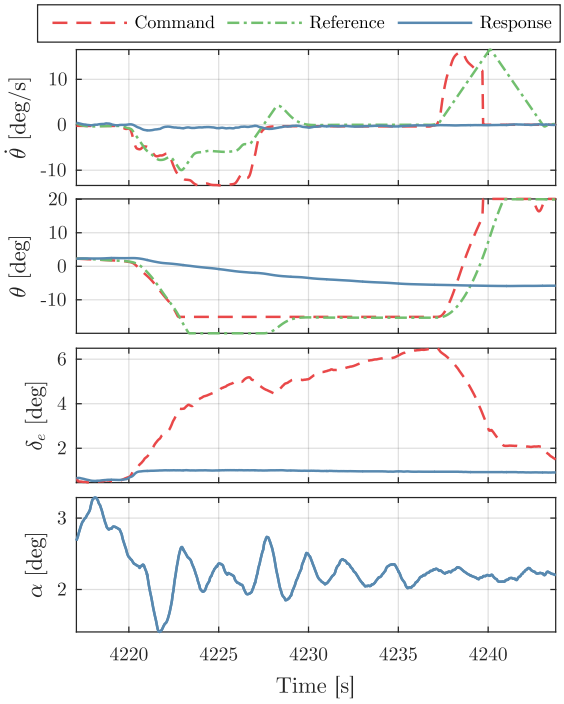

Figure C-50: Case #: 3.1.11 #7

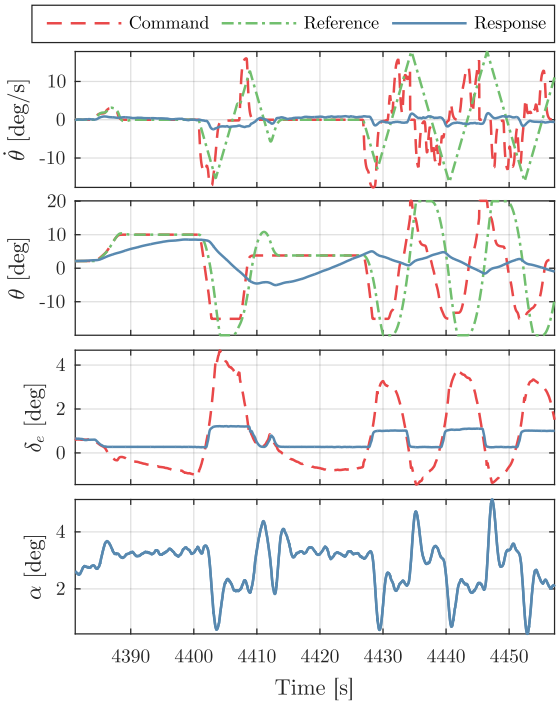

Figure C-51: Case #: 3.1.11 #8

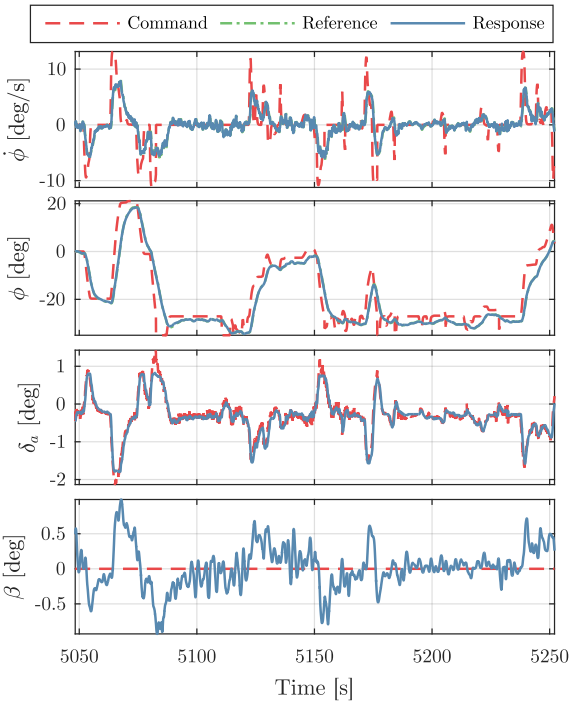

Figure C-52: Case #: 3.1.12

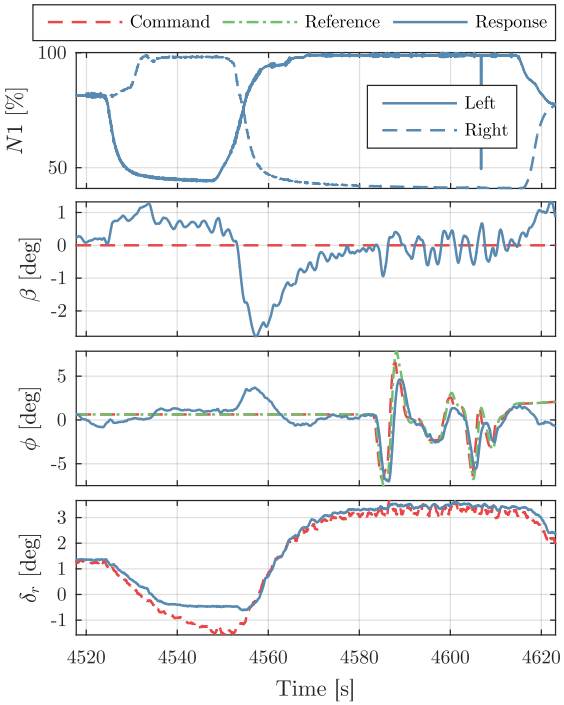

Figure C-53: Case #: 3.1.14

Appendix D

Flight test results Flight #3

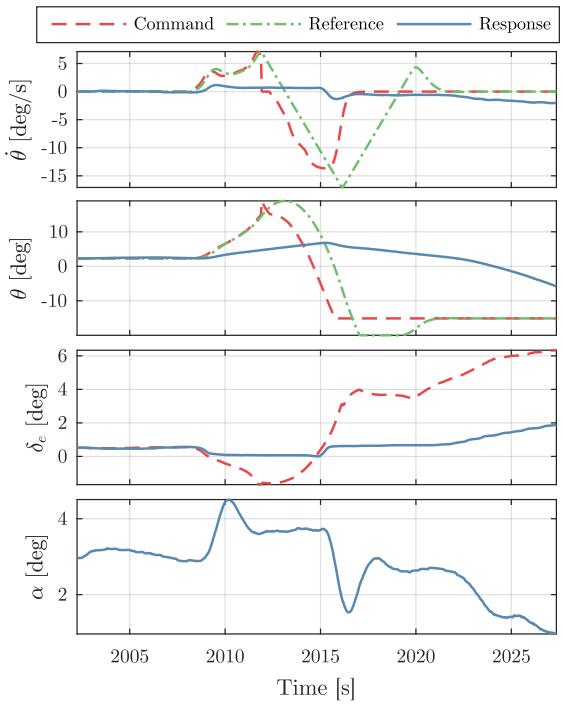

Figure D-1: Case #: 3.1.2 #1

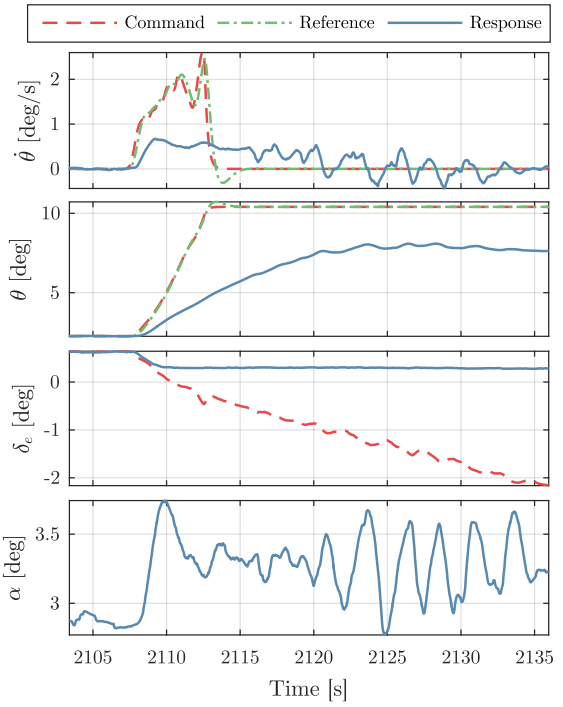

Figure D-2: Case #: 3.1.2 #2

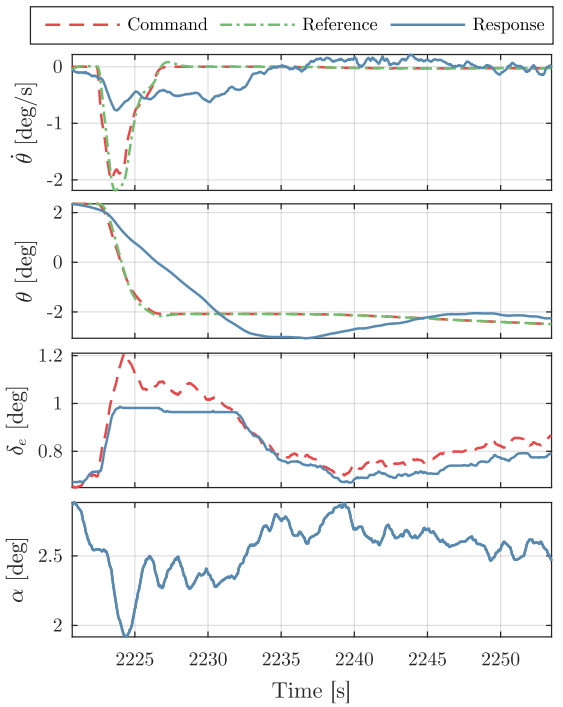

Figure D-3: Case #: 3.1.2 #3

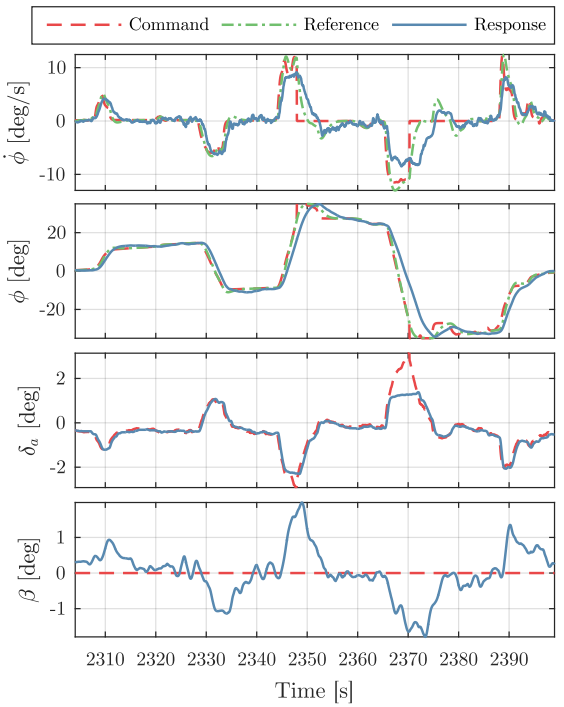

Figure D-4: Case #: 3.1.2 #4

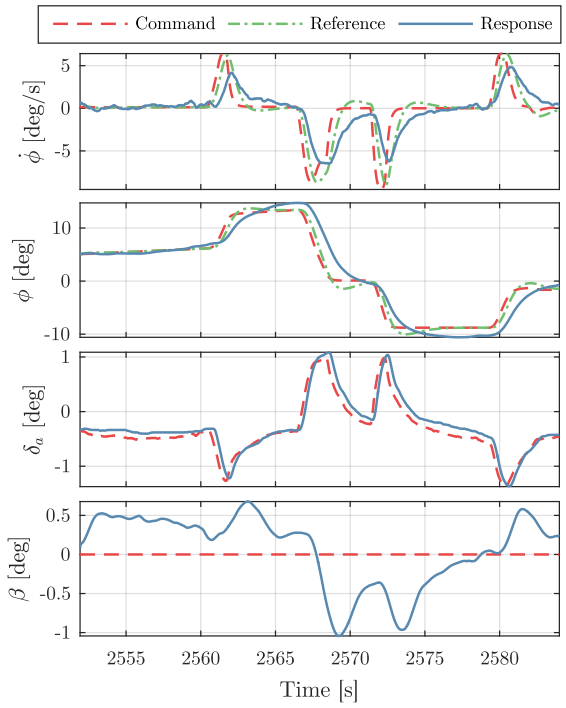

Figure D-5: Case #: 3.1.3

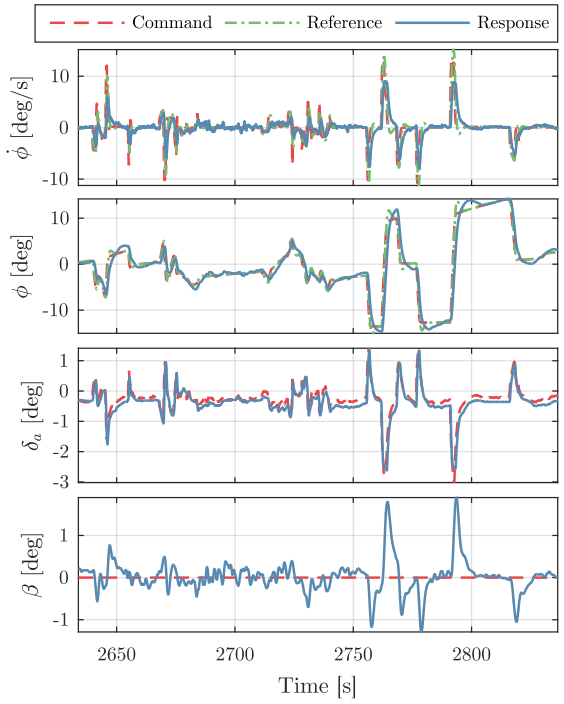

Figure D-6: Case #: 3.1.4

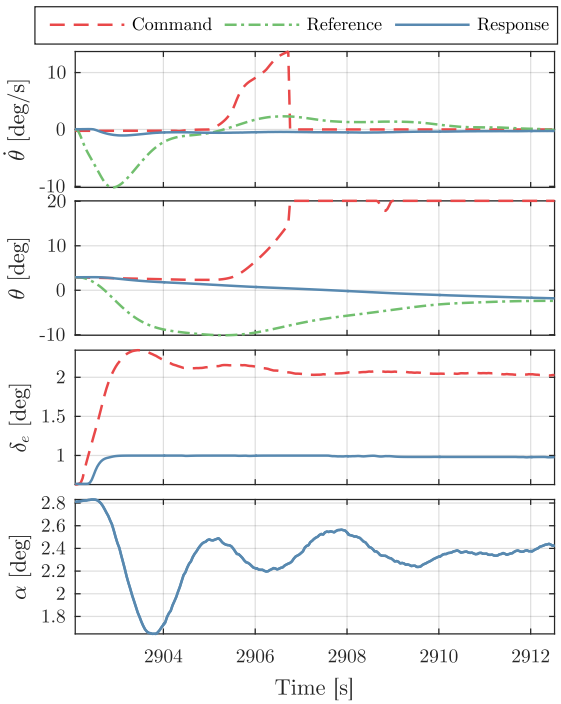

Figure D-7: Case #: 3.1.6 #1

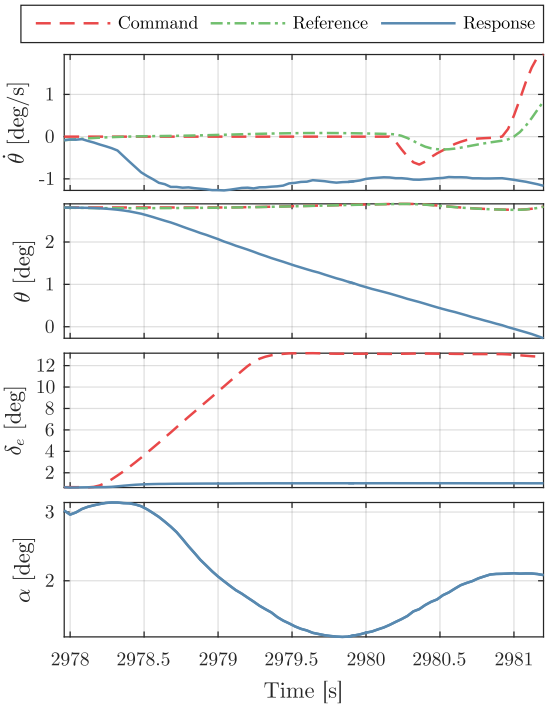

Figure D-8: Case #: 3.1.6 #2

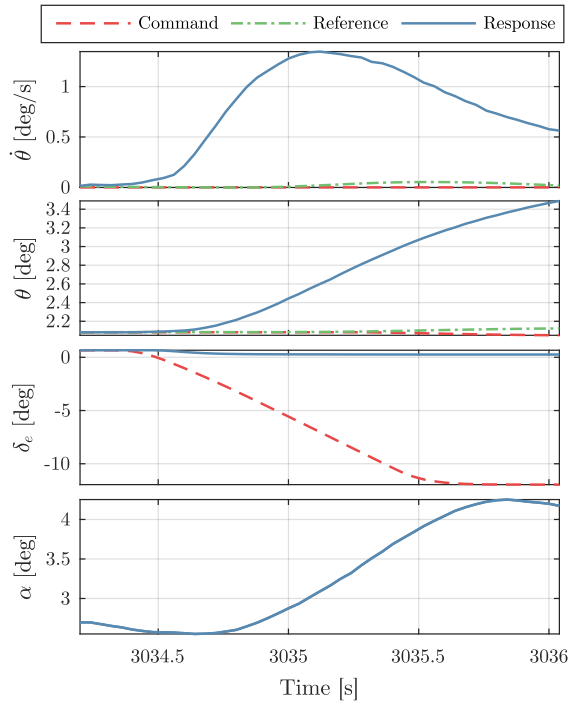

Figure D-9: Case #: 3.1.9

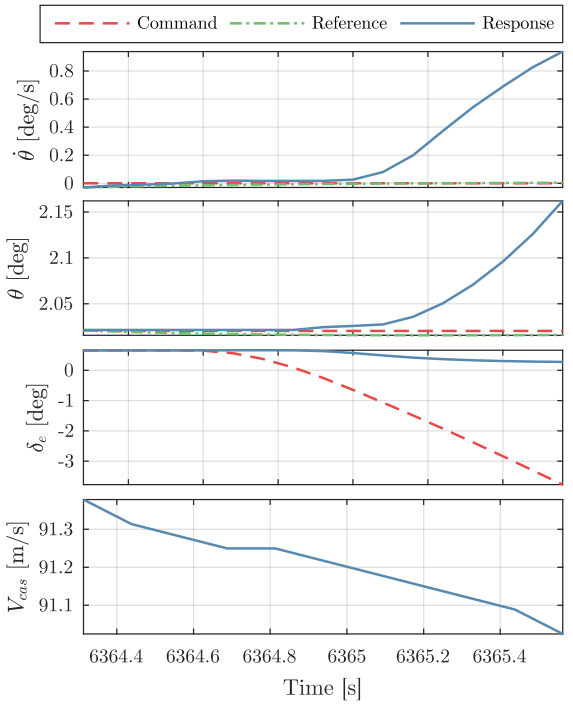

Figure D-10: Case #: 3.1.8

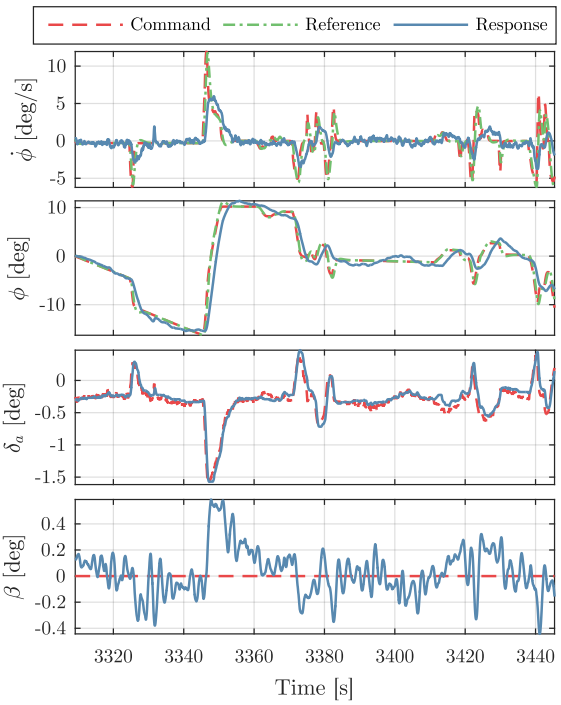

Figure D-11: Case #: 3.1.11 #1

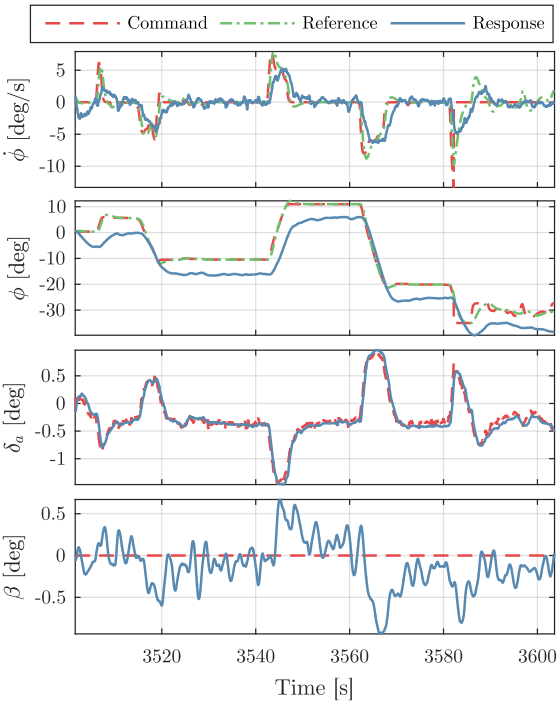

Figure D-12: Case #: 3.1.11 #2

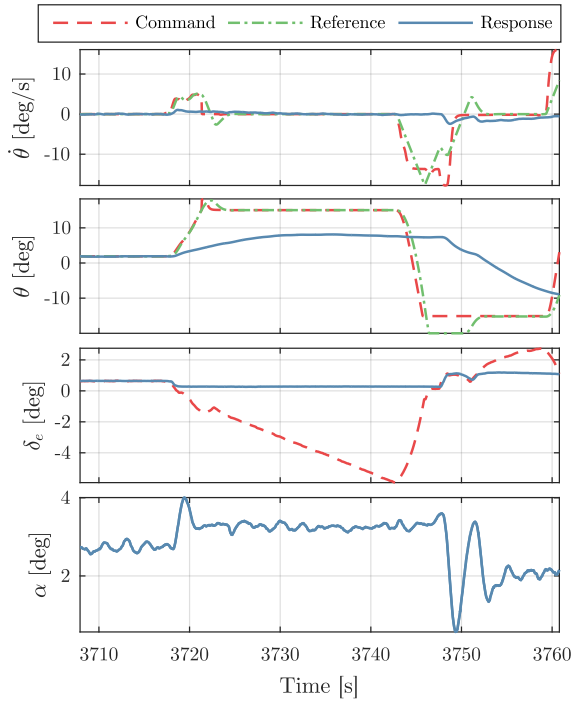

Figure D-13: Case #: 3.1.11 #3

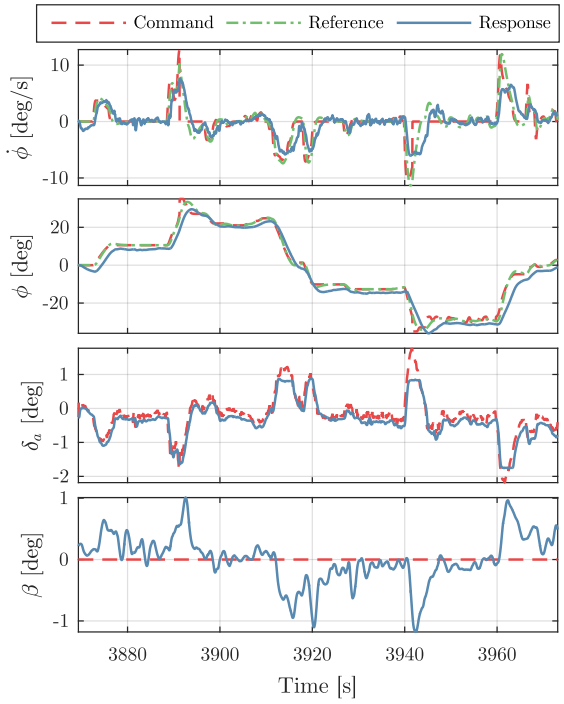

Figure D-14: Case #: 3.1.11 #4

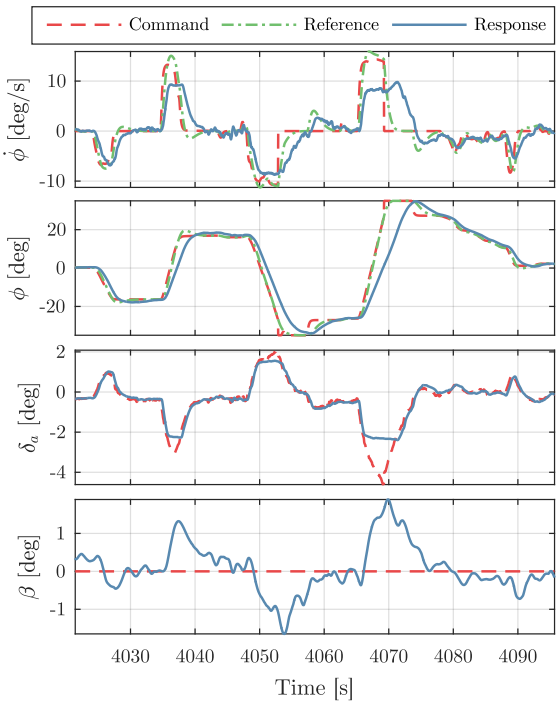

Figure D-15: Case #: 3.1.11 #5

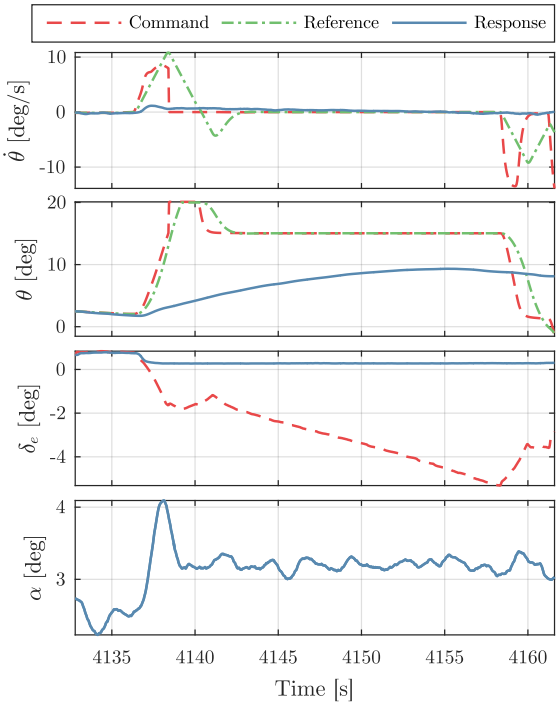

Figure D-16: Case #: 3.1.11 #6

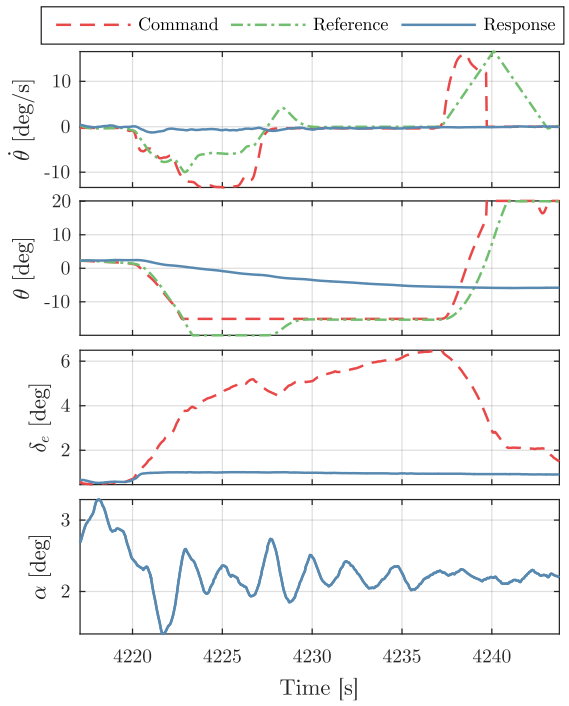

Figure D-17: Case #: 3.1.11 #7

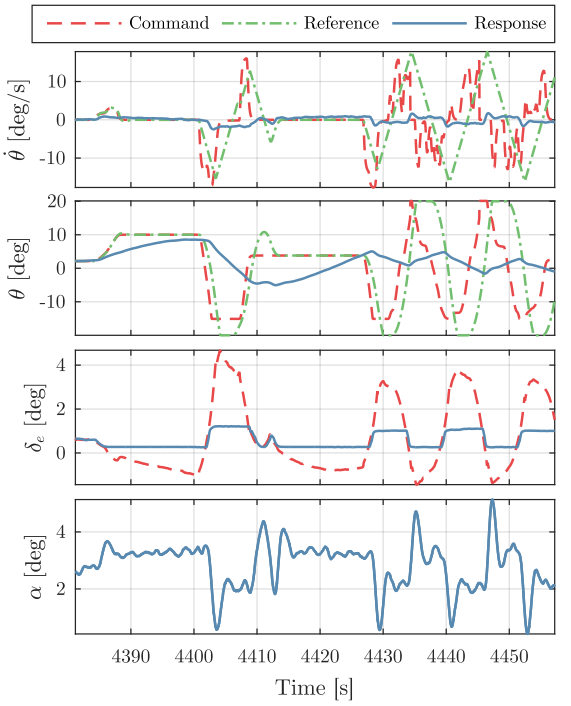

Figure D-18: Case #: 3.1.11 #8

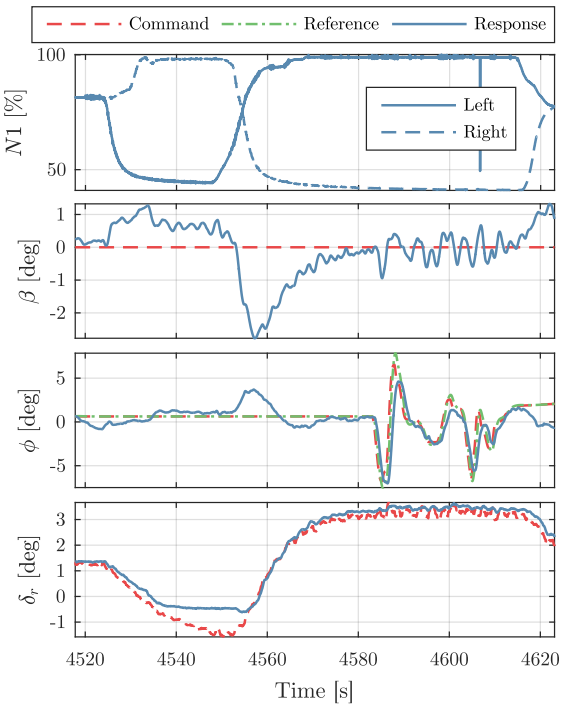

Figure D-19: Case #: 3.1.14

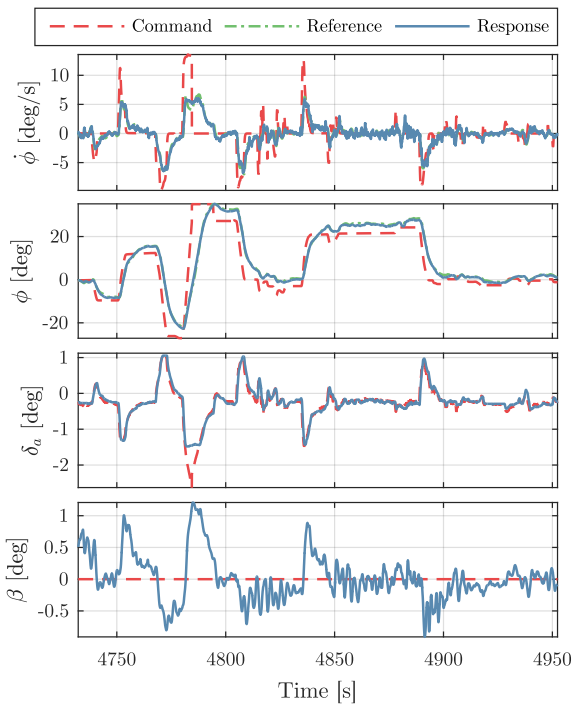

Figure D-20: Case #: 3.1.7

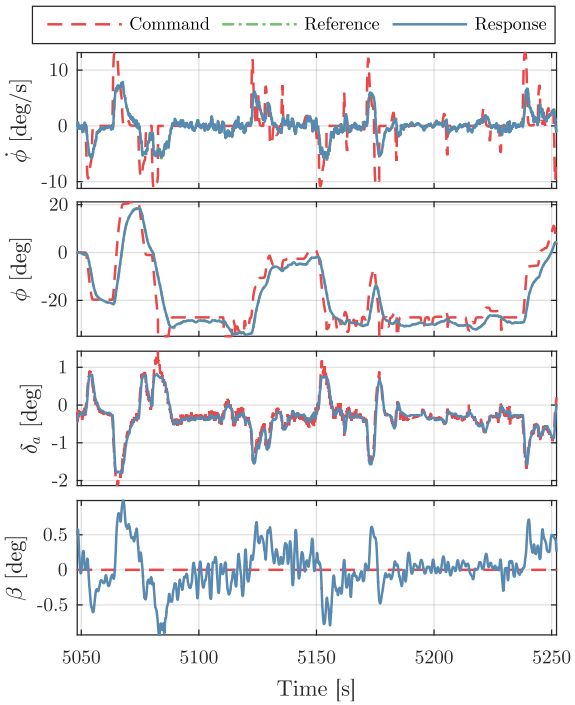

Figure D-21: Case #: 3.1.12

Bibliography

[1] P. Acquatella, W. Falkena, E.-J. van Kampen, and Q. P. Chu. Robust nonlinear spacecraft attitude control using incremental nonlinear dynamic inversion. In *AIAA Guidance, Navigation, and Control Conference*, pages 1–20, 2012.

[2] R. J. Adams and S. S. Banda. Robust flight control design using dynamic inversion and structured singular value synthesis. *IEEE Transactions on control systems technology*, 1 (2):80–92, 1993.

[3] B. J. Bacon, A. J. Ostroff, and S. M. Joshi. Reconfigurable ndi controller using inertial sensor failure detection & isolation. *IEEE Transactions on Aerospace and Electronic Systems*, 37(4):1373–1383, 2001.

[4] S. Baer. F-35a high angle of attack testing. In *AIAA Atmospheric Flight Mechanics Conference*, page 2057, 2014.

[5] G. G. Balas and J. Hodgkinson. Control design methods for good flying qualities. In *AIAA Atmospheric Flight Mechanics Conference*, pages 1–1, 2009.

[6] G. J. Balas. Flight control law design: An industry perspective. *European Journal of Control*, 9(2-3):207–226, 2003.

[7] R. J. M. Bennis. Non-linear State Estimation Techniques with Application to Dynamic Modelling of Angle of Attack Vane from Cessna Citation II Flight data. Master's thesis, Delft University of Technology, Faculty of Aerospace Engineering, 1998.

[8] Boeing Commercial Airplanes. Statistical Summary of Commercial Jet Airplane Accidents. Technical report, 2010.

[9] J. Bosworth. Flight results of the nf-15b intelligent flight control system (ifcs) aircraft with adaptation to a longitudinally destabilized plant. In *AIAA Guidance, Navigation and Control Conference and Exhibit*, page 6985, 2008.

[10] J. Bosworth and P. Williams-Hayes. Flight test results from the nf-15b intelligent flight control system (ifcs) project with adaptation to a simulated stabilator failure. In *AIAA Infotech@ Aerospace 2007 Conference and Exhibit*, page 2818, 2007.

[11] J. Burken, C. Hanson, J. Lee, and J. Kaneshige. Flight test comparison of different adaptive augmentations of fault tolerant control laws for a modified f-15 aircraft. In *AIAA Infotech@ Aerospace Conference and AIAA Unmanned... Unlimited Conference*, page 2056, 2009.

[12] Cessna Aircraft Company. *Cessna Citation II Maintenance Manual*, 1987.

[13] Cessna Aircraft Company. *Cessna Citation Flight Manual (Model 550)*, 1996.

[14] H. B. Chen and S. G. Zhang. Robust dynamic inversion flight control law design. In *Systems and Control in Aerospace and Astronautics, 2008. ISSCAA 2008. 2nd International Symposium on*, pages 1–6. IEEE, 2008.

[15] Civil Aviation Authority of the Netherlands (CAANL). Civil aviation safety data 1993-2007. Technical report, 2008.

[16] C. Cotting and T. Cox. A generic guidance and control structure for six-degree-of-freedom conceptual aircraft design. In *43rd AIAA Aerospace Sciences Meeting and Exhibit*, page 32, 2005.

[17] C. C. de Visser. *Global Nonlinear Model Identification with Multivariate Splines.* Phd thesis, Delft University of Technology, Faculty of Aerospace Engineering, June 2011.

[18] G. Di Francesco, M. Mattei, and E. D'Amato. Incremental nonlinear dynamic inversion and control allocation for a tilt rotor uav. In *AIAA Guidance, Navigation, and Control Conference*, page 0963, 2014.

[19] D. Enns, D. Bugajski, R. Hendrick, and G. Stein. Dynamic inversion: an evolving methodology for flight control design. *International Journal of Control*, 59(1):71–91, 1994. ISSN 0020-7179. doi: 10.1080/00207179408923070.

[20] European Aviation Safety Agency. *EASA.IM.A.207: Cessna 500, 550, S550, 560 and 560XL*, 2017.

[21] W. Falkena, C. Borst, Q. Chu, and J. Mulder. Investigation of practical flight envelope protection systems for small aircraft. *Journal of Guidance, Control, and Dynamics*, 34 (4):976–988, 2011.

[22] J. C. Gibson. Piloted handling qualities design criteria for high order flight control systems. *AGARD Criteria for Handling Qualities of Mil. Aircraft 15 p(SEE N 83-10054 01-08)*, 1982.

[23] P. Goupil and A. Marcos. Advanced diagnosis for sustainable flight guidance and control: The european addsafe project. Technical report, SAE technical paper, 2011.

[24] P. Goupil, J. Boada-Bauxell, A. Marcos, E. Cortet, M. Kerr, and H. Costa. Airbus efforts towards advanced real-time fault diagnosis and fault tolerant control. *IFAC Proceedings Volumes*, 47(3):3471–3476, 2014.

[25] C. Hanson, M. Johnson, J. Schaefer, N. Nguyen, and J. Burken. Handling qualities evaluations of low complexity model reference adaptive controllers for reduced pitch and roll damping scenarios. In *AIAA Guidance, Navigation, and Control Conference*, page 6607, 2011.

[26] C. D. Heise, G. P. Falconi, and F. Holzapfel. Hexacopter outdoor flight test results of an extended state observer based controller. *2014 IEEE International Conference on Aerospace Electronics and Remote Sensing Technology*, 2014. doi: 10.1109/icares.2014.7024373.

[27] International Civil Aviation Organization (ICAO). State of global aviation safety. Technical report, 2013.

[28] S. Jacklin. Closing the certification gaps in adaptive flight control software. In *AIAA Guidance, Navigation and Control Conference and Exhibit*, page 6988, 2008.

[29] E. Johnson and M. Turbe. Modeling, control, and flight testing of a small ducted fan aircraft. *AIAA Guidance, Navigation, and Control Conference and Exhibit*, 2005. doi: 10.2514/6.2005-6281.

[30] E. N. Johnson and A. J. Calise. Pseudo-control hedging: A new method for adaptive control. In *Advances in navigation guidance and control technology workshop*, pages 1–2, 2000.

[31] E. N. Johnson and S. K. Kannan. Adaptive trajectory control for autonomous helicopters. *Journal of Guidance, Control, and Dynamics*, 28(3):524–538, 2005.

[32] H.-D. Joos. A methodology for multi-objective design assessment and flight control synthesis tuning. *Aerospace Science and Technology*, 3(3):161–176, 1999.

[33] J. Koschorke, W. Falkena, E.-J. Van Kampen, and Q. P. Chu. Time delayed incremental nonlinear control. In *AIAA Guidance, Navigation, and Control (GNC) Conference*, page 4929, 2013.

[34] M. Laban. *On-Line Aircraft Aerodynamic Model Identification*. PhD thesis, Delft University of Technology, Faculty of Aerospace Engineering, 1994.

[35] Q. Lam, R. Hindman, W. Shell, and B. Ridgely. Investigation and preliminary development of a modified pseudo control hedging for missile performance enhancement. In *AIAA Guidance, Navigation, and Control Conference and Exhibit*, page 6458, 2005.

[36] C. A. A. M. v. d. Linden. *DASMAT-Delft University aircraft simulation model and analysis tool: a Matlab/Simulink environment for flight dynamics and control analysis*. Delft University Press, 1998.

[37] T. Lombaerts and G. Looye. Design and flight testing of manual nonlinear flight control laws. *AIAA Guidance, Navigation, and Control Conference*, Aug 2011. doi: 10.2514/6.2011-6469.

[38] T. Lombaerts and G. Looye. Design and flight testing of nonlinear autoflight control laws. In *AIAA Guidance, Navigation, and Control Conference*, page 4982, 2012.

[39] T. Lombaerts and G. Looye. Design and flight testing of nonlinear autoflight control laws incorporating direct lift control. *Advances in Aerospace Guidance, Navigation and Control*, page 549–568, 2013. doi: 10.1007/978-3-642-38253-6_32.

[40] T. Lombaerts, G. Looye, Q. Chu, and J. Mulder. Design and simulation of fault tolerant flight control based on a physical approach. *Aerospace Science and Technology*, 23(1): 151–171, 2012.

[41] G. Looye and H.-D. Joos. Design of robust dynamic inversion control laws using multi-objective optimization. In *Proceedings of the AIAA Guidance, Navigation and Control Conference*, 2001.

[42] G. Looye, D. Willemsen, J. Bauschar, and W. Moennich. Flight testing robust autoland control laws. *AIAA Guidance, Navigation, and Control Conference and Exhibit*, Jun 2001. doi: 10.2514/6.2001-4208.

[43] G. H. N. Looye. *An Integrated Approach to Aircraft Modelling and Flight Control Law Design*. Phd thesis, Delft University of Technology, Faculty of Aerospace Engineering, Jan. 2008.

[44] P. Lu and E.-J. van Kampen. Active fault-tolerant control for quadrotors subjected to a complete rotor failure. In *Intelligent Robots and Systems (IROS), 2015 IEEE/RSJ International Conference on*, pages 4698–4703. IEEE, 2015.

[45] B. Lubbers. A model of the Experimental Fly-By-Wire flight control system for the PH-LAB: Performing flight tests, system identification and parameter estimation. Master's thesis, Delft University of Technology, Faculty of Aerospace Engineering, 2009.

[46] S. Merhav. *Aerospace sensor systems and applications*. Springer, 2012.

[47] C. Miller. Nonlinear dynamic inversion baseline control law: Architecture and performance predictions. *AIAA Guidance, Navigation, and Control Conference*, Aug 2011. doi: 10.2514/6.2011-6467.

[48] D. G. Mitchell, R. H. Hoh, B. L. Aponso, and D. H. Klyde. Proposed incorporation of mission-oriented flying qualities into mil-std-1797a. Technical report, SYSTEMS TECHNOLOGY INC HAWTHORNE CA, 1994.

[49] D. Moorhouse, W. de Boer, C. Fielding, K.-U. Hahn, G. Hofinger, J.-F. Magni, and L. Verde. Flight control design-best practices. 2000.

[50] M. Mulder, B. Lubbers, P. Zaal, M. V. Paassen, and J. Mulder. Aerodynamic hinge moment coefficient estimation using automatic fly-by-wire control inputs. *AIAA Modeling and Simulation Technologies Conference*, Oct 2009. doi: 10.2514/6.2009-5692.

[51] D. Niedermeie and A. A. Lambregts. Fly-by-wire augmented manual control-basic design considerations. In *International Congress of the Aeronautical Sciences*, volume 100, page 7, 2012.

[52] J. Oliveira, Q. Chu, J. Mulder, H. Balini, and W. Vos. Output error method and two step method for aerodynamic model identification. In *AIAA Guidance, Navigation, and Control Conference and Exhibit*, page 6440, 2005.

[53] A. J. Ostroff and B. J. Bacon. Enhanced ndi strategies for reconfigurable flight control. In *American Control Conference, 2002. Proceedings of the 2002*, volume 5, pages 3631–3636. IEEE, 2002.

[54] REAL Consortium. RealATTAS Benchmark Definition. Technical Report BRPR-CT98-0627/TP-04v1, 2000.

[55] Rockwell Collins. *AHS-3000( ) Attitude Heading Reference System: installation manual*, 2005.

[56] J. Schaefer, C. Hanson, M. Johnson, and N. Nguyen. Handling qualities of model reference adaptive controllers with varying complexity for pitch-roll coupled failures. In *AIAA Guidance, Navigation, and Control Conference*, page 6453, 2011.

[57] J. Schierman, N. Gandhi, J. Hull, and D. Ward. Flight test results of an adaptive guidance system for reusable launch vehicles. *AIAA Guidance, Navigation, and Control Conference and Exhibit*, 2004. doi: 10.2514/6.2004-4771.

[58] S. Sieberling, Q. P. Chu, and J. A. Mulder. Robust Flight Control Using Incremental Nonlinear Dynamic Inversion and Angular Acceleration Prediction. *Journal of Guidance, Control, and Dynamics*, 33(6):1732–1742, 2010. ISSN 0731-5090. doi: 10.2514/1.49978.

[59] P. Simplício, M. Pavel, E. Van Kampen, and Q. Chu. An acceleration measurements-based approach for helicopter nonlinear flight control using incremental nonlinear dynamic inversion. *Control Engineering Practice*, 21(8):1065–1077, 2013.

[60] L. Slotine. *Applied Nonlinear Control*. Prentice Hall, 1991. ISBN 0130408905.

[61] E. J. Smeur, Q. Chu, and G. C. de Croon. Adaptive incremental nonlinear dynamic inversion for attitude control of micro air vehicles. *Journal of Guidance, Control, and Dynamics*, 2015.

[62] P. Smith and A. Berry. Flight test experience of a non-linear dynamic inversion control law on the vaac harrier. In *Atmospheric Flight Mechanics Conference*, page 3914, 2000.

[63] P. R. Smith. A Simplified Approach to Nonlinear Dynamic Inversion Based Flight Control. In *AIAA Atmospheric Flight Mechanics Conference and Exhibit*, pages 762–770, 1998.

[64] M. W. Soijer. *Software-Enabled Modular Instrumentation Systems*. Phd thesis, Delft University of Technology, Faculty of Aerospace Engineering, Nov. 2003.

[65] M. A. van den Hoek, C. C. de Visser, and D. M. Pool. Identification of a Cessna Citation II Model Based on Flight Test Data. In *Proceedings of the 4th CEAS Specialist Conference on Guidance, Navigation & Control, Warsaw, Poland*, 2017.

[66] W. van Ekeren. Incremental Nonlinear Flight Control for Fixed-Wing Aircraft: Design and Implementation of Incremental Nonlinear Flight Control Methods on the FASER UAV. Master's thesis, Delft University of Technology, Faculty of Aerospace Engineering, 2016.

[67] M. M. van Paassen, O. Stroosma, and J. Delatour. DUECA - Data-Driven Activation in Distributed Real-Time Computation. In *Proceedings of the AIAA Modeling and Simulation Technologies Conference and Exhibit, Denver (CO)*, number AIAA-2000-4503, Aug. 2000.

[68] R. C. van 't Veld. Incremental Nonlinear Dynamic Inversion Flight Control: Implementation on a CS-25 Certified Fixed-Wing Aircraft. Master's thesis, Delft University of Technology, Faculty of Aerospace Engineering, 2016.

[69] C. Vlaar. Incremental Nonlinear Dynamic Inversion Flight Control: Implementation and Flight Test on a Fixed Wing UAV. Master's thesis, Delft University of Technology, Faculty of Aerospace Engineering, 2014.

[70] R. Wacker, S. Munday, and S. Merkle. X-38 application of dynamic inversion flight control. 2001.

[71] G. P. Walker and D. A. Allen. X-35b stovl flight control law design and flying qualities. In *Biennial International Powered Lift Conference and Exhibit*, pages 5–7, 2002.

[72] W. Wuest. Agard flight test instrumentation series. volume 11. pressure and flow measurement. Technical report, ADVISORY GROUP FOR AEROSPACE RESEARCH AND DEVELOPMENT NEUILLY-SUR-SEINE (FRANCE), 1980.

[73] P. Zaal, D. Pool, A. I. t. Veld, F. Postema, M. Mulder, M. V. Paassen, and J. Mulder. Design and certification of a fly-by-wire system with minimal impact on the original flight controls. *AIAA Guidance, Navigation, and Control Conference*, Oct 2009. doi: 10.2514/6.2009-5985.